

ANNUAL REPORT 2014

Austrian SAXS Beamline at



Austrian Small Angle X-ray Scattering (SAXS) Beamline at ELETTRA

Annual Report 2014

Compiled by Sigrid Bernstorff & Heinz Amenitsch

Cover pictures taken from the user contributions:

R. Slunjski et al., pages 113-115 (front cover: background picture)

M. Buljan et al., pages 85 -87 (front cover: middle-right up)

D. Carboni et al., pages 124-126 (front cover: right up)

T.A. Grünewald et al., pages 62-63 (front cover: middle-right down)

M. Karlušić et al., pages 94-96 (front cover: right down)

C. Prehal et al., pages 101-102 (back cover: middle right up)

C. J. Schaffer et al., pages 107-108 (back cover: right up)

M. Karlušić et al., pages 94-96 (back cover: middle right down)

K. Salamon et al., pages 103-104 (back cover: right down)

Table of Contents

› Preface	
› The SAXS-Group	1
› The SAXS-Beamline in General	3
› Application for Beamtime at ELETTRA	7
› List of Users and Institutes in 2014	10
› List of Performed Experiments	19
› User Statistics	23
› Experimental Possibilities at the SAXS-beamline	
1. New developments and instrumentation	27
2. Accessible SAXS and WAXS ranges	30
3. Calibration of the s-axis and flat field correction	31
4. Available sample manipulation stages	33
5. Available detectors	40
6. Offline SAXS support laboratory	43
› User Contributions	
1. Life Sciences	46
2. Materials Science	82
3. Chemistry	116
› Publications	131
› Author Index	147

Preface



Frank Uhlig
Head Institute of Inorganic Chemistry and Dean of
Faculty of Technical Chemistry, Chemical & Process
Engineering and Biotechnology
Graz University of Technology

After the changes for the Austrian Beamlines at ELETTRA in 2012 and the significant upgrade of our scientific equipment in 2013 we were now able to perform our own research as well as provide the support for the external users of our beamline on a much higher level, leading to a further increasing productivity of our beamlines. Within 2014 we were again able to initiate novel projects not only within our own university but also by attracting new partners from Austria and beyond as well as within the CERIC-ERIC framework.

Also in 2014 we were able to significantly increase the quality of the available scientific equipment and hence the quality of the scientific output of the Austrian Beamlines at ELETTRA. The most visible sign for this was the restructuring of our chemistry lab in Trieste including the purchase of an urgently needed glovebox system providing now a much more professional environment for our users but also for our own research activities.



Picture 1. Newly renovated chemistry lab of the Austrian Beamlines at ELETTRA

I want to especially thank our Italian partners at ELETTRA and also our collaborators within the CERIC-ERIC framework for their outstanding support and their collaboration. Together with the Czech Republic, Italy, Romania, Serbia and Slovenia, Austria is one of the founding

members of the CERIC-ERIC infrastructure consortium. Our Austrian commitment to CERIC-ERIC consists on one hand of the AUSTRIAN SAXS Beamline in Trieste and on the other hand of our light and X-ray scattering laboratories at the Institute for Inorganic Chemistry in Graz. Within the last 1 ½ years, the first international researchers were not only using our facilities at ELETTRA but also our scattering labs in Graz.



Picture 2 . Users in the CERIC-ERIC scattering labs at Graz University of Technology in Austria

For the upcoming years, we expect from our ongoing collaboration with ELETTRA but also with our partners within the CERIC-ERIC network new impulses for the European scenery of infrastructures, science and technology.



Alfonso Franciosi
President and Chief Executive Officer
Elettra-Sincrotrone Trieste S.C.p.A.

Over the years the relation between Elettra-Sincrotrone Trieste and the Austrian scientific community has been a shining example of what international scientific collaborations should be about. This new report compiled by our colleagues of the Technical University of Graz (TUG), who are responsible for the Austrian programs involving the SAXS and DXRL beamlines at Elettra, show an impressive scientific production. The continued success of Austrian researchers in their beamtime applications at Elettra, with a success rate that almost doubles the average success rate, and the implementation of a new important joint venture, the Central European Research Infrastructure Consortium (CERIC-ERIC), testify both to the quality of Austrian science, and to the creativity and effectiveness of the TUG personnel at Elettra.

Last year the users of Elettra were able to take full advantage of the increase in machine stability and reproducibility resulting from the top-up operating mode, and the number of proposals received directly by Elettra remained at the record-breaking level of the previous year. To these one has to add the proposals that came through the CERIC-ERIC channel, and this resulted in a substantial increase (10%) of the number of proposals received.

The new x-ray fluorescence (XRF) beamline in collaboration with the International Atomic Energy Agency (IAEA) was opened to users in the Fall of 2014 and has been working since for users supported by IAEA and general users, offering GIXRF, XAS, XRF, TXRF capabilities. The superconductive wiggler, that is to provide photon energies up to 25 keV, was successfully tested on the storage ring at high field (3.5 T) during top-up operation. Liquid helium consumption was so low that we expect a single refilling per year. The new beamline for high pressure diffraction studies (XPRESS) has been opened to the first users, while the official opening of the second diffraction beamline for structural biology (XRD2) is expected for the end of the year. Both XPRESS and XRD2 have been constructed in collaboration with the Indian Institute of Science in Bangalore and utilize the superconductive wiggler radiation.

Additional corrector magnets are now installed on the XAFS, SISSI, SYRMEP and MCX bending magnet beamlines. This type of device makes the source points of the bending magnet beamlines independent of the position and angle of the beam from the adjacent insertion device, therefore increasing the flexibility and reproducibility of the electron trajectory.

A variety of important upgrades have taken place on a number of Elettra beamlines. For example, a new high performance VG Scienta DA30 electron spectrometer and a VLEED

detector for spin resolution have been added to the APE facility, in collaboration with the NFFA initiative of IOM-CNR; a special spin-filter for imaging of magnetic materials has been added to the Nanospectroscopy experimental station, in collaboration with the Forschungszentrum Jülich; the optics of the SISSI beamline has been upgraded.

The competitiveness and continued excellence of our research center depends on our ability to continually explore all options for upgrading our facilities and the research services that we can offer our users. A number of preliminary studies for a long-term upgrade of the Elettra light source have begun in 2014. The goal was to explore the technical feasibility of converting the existing storage ring to a minimum emittance source, provisionally designated as Elettra 2.0, that could be housed in the existing Elettra tunnel, utilizing the existing top-up capable injection system, and preserving as much as possible the source points of the existing beamlines, in order to minimize the required infrastructural changes and, therefore, the cost and installation time.

Our machine physicists and engineers have examined a number of different technical solutions for the lattice of Elettra 2.0, from a 4-bend achromat to a 9-bend achromat, and our initial costs/benefits analysis made us tentatively select a 6-bend achromat lattice, that would allow us to achieve an emittance of 250 pm-rad, i.e., 28 times lower than the present Elettra emittance, and still utilize the existing injection system. The performance of the upgraded Elettra based on such a lattice is significant, with an increase of a factor of 20 in beam brilliance at 1 keV.

Implementation of the new fourth-generation FERMI source has continued with the optimization of FEL-1 in collaboration with external users and, in parallel, the commissioning of the two-stages, FEL-2 facility. In 2014 FERMI was in operation for 6640 hours, with 60% of the time devoted to beamline *commissioning* and users' experiments and 40% devoted to machine physics studies and to the commissioning of FEL-2. As part of the program of the commissioning of FERMI, 16 user experiments were successfully performed using FEL 1 and the Diffraction and Projection Imaging (DiProI) beamline (7 experiments), Elastic and Inelastic Scattering – TIMEX (EIS-TIMEX) beamline (2 experiments), and the Low Density Matter (LDM) beamline (7 experiments). In addition, a first experiment using FEL-2 was realized using EIS-TIMEX. It involved time-resolved absorption spectroscopy at the silicon L_{2,3} edge in the 12.4 nm range. As a result of the fourth call for proposals for FERMI, 68 experimental proposals were received, bringing the total to 193. The FERMI Proposal Peer Review Panel is expected to select 15-10 proposals out of the last 68 received, with an oversubscription on 3.4-4.5.

FEL-1 routinely achieved energies of several hundreds $\mu\text{J}/\text{pulse}$ and design specifications were achieved or surpassed throughout the operating wavelength range and down to the minimum design wavelength of 20 nm. Useful intensities (of the order 10 $\mu\text{J}/\text{pulse}$) were utilized experimentally down to 10 nm. The commissioning of FEL-2 has continued, yielding high-quality spectra in the 10 nm range with pulse energies as high as 100 μJ per pulse, and 10 μJ per pulse (the nominal value) at 4 nm. As a result of this progress, the use of FEL-2 for energies up to 310 eV was in the fourth call for proposals, generating immediate widespread interest. Proposed experiments exploit the unique properties of the FERMI radiation, stemming from the seeded character of the FEL emission and from the polarization control afforded by the FERMI APPLE II undulators, for two colors, pump-probe experiments, transient-grating inelastic scattering experiments, four-wave mixing, studies of magnetization dynamics, etc. Construction continues for the EIS-TIMER, TeraFERMI and MagneDyn

beamlines, which should gradually become operational in 2015-2016. A new hutch adjacent to the TeraFERMI hutch is also under construction to house the table-top laser sources and experimental stations of the T-ReX laboratory, which will be operated as a user facility complementary to FERMI.

CERIC-ERIC, hosted by Italy, with statutory seat in Trieste and Elettra-Sincrotrone Trieste, currently includes Austria, the Czech Republic, Italy, Romania, Serbia and Slovenia. Croatia, Hungary and Poland participate as observers pending membership. CERIC-ERIC offers a common entry point and integrated services for international users, a single proposal evaluation system, free and open access by quality selection only, and will implement common support and logistic services as required, joint intellectual property rights and industrial policy, and joint educational and outreach activities across the different facilities. Three CERIC-ERIC calls for multi-technique proposals have already been published, offering access to several of the Elettra beamlines, the Austrian SAXS and TUG Laboratories, the Czech Materials Science beamline and the Prague Laboratory, the Budapest Neutron Center, the TEM Magurele Laboratory in Romania, and the national Slovenian NMR Center. The last call introduced an important change, namely the possibility to submit single-instrument proposals for those facilities where there are no other channels for open access available. These include the Light Scattering Laboratory and SAXS facility in Graz, HRTEM and EPR facilities in Bucharest, XPD, Near Ambient Pressure XPS and FESEM facilities in Prague and the Tandem accelerator facility in Zagreb.

Some of the new strategic directions opening up for us and for our partners with the ongoing developments at Elettra and FERMI will be addressed by a number of thematic events, including two workshops that will take place in sequence as part of the XXIII Elettra Users' Meeting: *New synchrotron radiation and optical techniques for nanoscale microscopy of biological systems: from single molecules to cells* (December 9-10), and *Multicolor FEL pulses and coherent control on the attosecond time scale opening new science perspectives* (December 10-11). Such workshops will serve the purpose of engaging a broader user community, and our partner institutions will have prominent roles in the above events.

We thank our Austrian partners at the Technical University of Graz for their professionalism and steady dedication over the years. We at Elettra look forward to expanding the scope and depth of our collaboration and exploring together the frontiers that the new upgraded Elettra, FERMI and CERIC-ERIC will open for all of us.

The SAXS Group

SCIENTISTS: Heinz Amenitsch ¹⁾
e-mail: amenitsch@elettra.eu

Sigrid Bernstorff ²⁾
e-mail: bernstorff@elettra.eu

Benedetta Marmioli ¹⁾
e-mail: benedetta.marmioli@elettra.eu

POST DOC: Krunoslav Juraic ¹⁾ (since 1.5.2014)
e-mail: kjuraic@irb.hr

SCIENTIFIC ASSISTANT: Barbara Sartori ¹⁾
e-mail: barbara.sartori@elettra.eu

PHD STUDENT: Max Burian ¹⁾ (since 1.10.2014)
e-mail: burian@tugraz.at

TECHNICIAN: Christian Morello ²⁾
e-mail: christian.morello@elettra.eu

1) Until 30.9.2012: Institute for Biophysics and Nanosystems Research, Austrian Academy of Sciences, Schmiedlstraße 6, 8042 Graz, Austria

Since 1.10.2012: Institute of Inorganic Chemistry, Graz University of Technology, Faculty of Technical Chemistry, Chemical and Process Engineering, Biotechnology - TCVB, Stremayrgasse 9/IV, 8010 Graz, Austria

Tel 0043-316-873 32145

Fax 0043-316-873 32102

WEB: <http://ac.tugraz.at>

and: Institute Outstation c/o Elettra - Sincrotrone Trieste

2) Elettra - Sincrotrone Trieste, Strada Statale 14, km 163.5, 34149 Basovizza (TS), Italy

Tel 0039-040-375 8572

Fax 0039-040-938 0902

WEB: <http://www.elettra.eu>

The SAXS-Beamline in General

Small Angle X-ray Scattering has become a well known standard method to study the structure of various objects in the spatial range from 1 to 1000 Å, and therefore instruments capable to perform such experiments are installed at most of the synchrotron research centers. The high-flux SAXS beamline at ELETTRA is mainly intended for time-resolved studies on fast structural transitions in the sub-millisecond time region in solutions and partly ordered systems with a SAXS-resolution of 10 to 1400 Å in real-space.

The photon source is the 57-pole wiggler whose beam is shared and used simultaneously with a Macromolecular Crystallography beamline. The wiggler delivers a very intense radiation between 4 and 25 keV of which the SAXS-Beamline accepts 3 discrete energies, namely 5.4, 8 and 16 keV. The beamline optics consists of a flat double crystal monochromator and a double focusing toroidal mirror.

A versatile SAXS experimental station has been set-up, and an additional wide-angle X-ray scattering (WAXS) detector monitors simultaneously diffraction patterns in the range from 1 to 9 Å. The sample station is mounted move-able onto an optical table for optimising the sample detector distance with respect to SAXS resolution and sample size.

Besides the foreseen sample surrounding the users have the possibility to install their own specialised sample equipment. In the design phase, besides technical boundary conditions, user friendliness and reliability have been considered as important criteria.

The optimisation of the beamline with respect to high-flux and consequently high flux density, allows to perform the following experiments:

- Low Contrast Solution Scattering
- Grazing Incidence Scattering and Surface Diffraction
- Micro-Spot Scanning
- X-ray Fluorescence Analysis
- Time-Resolved Studies $\geq 11 \mu\text{s}$
- Simultaneously Performed Small- and Wide-Angle Measurements (SWAXS) on:
 - Gels
 - Liquid Crystals
 - (Bio) Polymers
 - Amorphous Materials
 - Muscles

Furthermore, using 5.4 and 16 keV energies, the beamline is widely applicable also to very thin, e.g. single muscle fibers, and optically thick (high Z) specimen, as often used in e.g., material science and solid state physics.

THE INSERTION DEVICE

The wiggler for the SAXS beamline consists of three 1.5 m long segments, each having 19 poles. The device can work with a minimum gap of 20 mm, which corresponds to $K=20$ at 2 GeV. The main parameters of the wiggler are:

- Critical Energy 4.1 keV
- Radiation Power 8.6 kW
- Flux 3.5×10^{14} ph/s/mrad/0.1%BW (at 400 mA)

The wiggler radiation cone has a horizontal width of 9 mrad. From this the SAXS-beamline accepts vertically 0.3 mrad, and horizontally +/-0.5 mrad at a 1.25 mrad off-axis position. The resulting source size for 8 keV photons is $3.9 \times 0.26 \text{ mm}^2$ (horiz. x vert.).

THE OPTICS

The optics common with the diffraction beamline consists of:

- C-Filter and Beryllium window assembly to reduce the power load on the first optical elements by a factor of 2 and to separate the beamline vacuum from the storage ring.
- Beam defining slit chamber which allows to define the SAXS beam on three sides before the monochromator in order to reduce the straylight in the downstream beamline sections.

The SAXS beamline optics consists of:

- A double-crystal monochromator consisting of four individual chambers, in which three interchangeable asymmetric Si(111) crystal pairs are used to select one of three fixed energies. Each of the crystal pairs is optimised for the corresponding energy to accomplish a grazing angle of 2° . The energy resolution $\Delta E/E$ of the monochromator is in the range of $0.7 - 2.5 \cdot 10^{-3}$.
- A baffle chamber after the monochromator is used as an adjustable straylight fenditure.
- A segmented toroidal mirror focuses the light in horizontal and vertical direction with a $1/2.5$ magnification onto the SAXS-detector.
- An aperture slit reduces the straylight after the monochromator and the toroidal mirror.
- A guard slit defines the illuminated region around the focal spot. The spot size on the detector is 1.6 mm horizontally and 0.6 mm vertically. The calculated flux at the sample is in the order of 10^{13} ph/s at 400 mA. For a maximum sample size of $5.4 \times 1.8 \text{ mm}^2$ correspondingly a flux density of 10^{12} ph/s/ mm^2 has been calculated.

SAMPLE STAGE

The multipurpose sample stage allows to perform fast time-resolved relaxation studies based on temperature- or pressure-jumps as well as stopped flow experiments. Shear jump relaxation experiments are planned. Specifically, T-jumps can be induced by an infra-red light pulse (2 ms) from an Erbium-Glass laser, raising the temperature about 20°C in an aqueous sample volume of $10 \mu\text{l}$. A hydrostatic pressure cell with a maximal accessible angular range of 30° for simultaneous SAXS and WAXS measurements is available. P-jumps are realised by switching fast valves between a low and a high pressure reservoir, increasing or decreasing the hydrostatic pressure in the range from 1 bar to 2.5 kbar within a few ms. A Differential Scanning Calorimeter (DSC) allows for DSC-scans simultaneously to SWAXS measurements. In an overview, the following sample manipulations are possible (for further details, see pages 30-38):

- Temperature Manipulations: Ramps, Jumps and Gradient Scans
- Pressure Manipulation: Scan and Jumps
- Stopped Flow Experiments
- SWAXS Measurements Applying Mechanical Stress
- Calorimetric measurements

Scientific Applications	<p>Low Contrast Solution Scattering, Grazing Incidence Surface Diffraction, Micro-Spot Scanning, X-ray Fluorescence Analysis, Time-Resolved Studies $\geq 11 \mu\text{s}$ and Simultaneously Performed Small- and Wide-Angle Measurements (SWAXS) on:</p> <p style="text-align: center;">Gels Liquid Crystals (Bio) Polymers Amorphous Materials Muscles</p>																											
Source characteristics	<p><u>Wiggler (NdFeB Hybrid):</u></p> <table border="0" style="width: 100%;"> <tr> <td style="width: 60%;">Period</td> <td style="text-align: right;">140 mm</td> </tr> <tr> <td>No. full poles</td> <td style="text-align: right;">57</td> </tr> <tr> <td>Gap</td> <td style="text-align: right;">20 mm</td> </tr> <tr> <td>B_{max}</td> <td style="text-align: right;">1.607 T</td> </tr> <tr> <td>Critical Energy ϵ_c</td> <td style="text-align: right;">4.27 keV</td> </tr> <tr> <td>Power (9 mrad)</td> <td style="text-align: right;">8.6 kW</td> </tr> <tr> <td>Effective source size FWHM</td> <td style="text-align: right;">$3.9 \times 0.26 \text{ mm}^2(\text{h} \times \text{v})$</td> </tr> </table>	Period	140 mm	No. full poles	57	Gap	20 mm	B_{max}	1.607 T	Critical Energy ϵ_c	4.27 keV	Power (9 mrad)	8.6 kW	Effective source size FWHM	$3.9 \times 0.26 \text{ mm}^2(\text{h} \times \text{v})$													
Period	140 mm																											
No. full poles	57																											
Gap	20 mm																											
B_{max}	1.607 T																											
Critical Energy ϵ_c	4.27 keV																											
Power (9 mrad)	8.6 kW																											
Effective source size FWHM	$3.9 \times 0.26 \text{ mm}^2(\text{h} \times \text{v})$																											
Optics	<table border="0" style="width: 100%;"> <tr> <td style="width: 30%;"><u>Optical elements:</u></td> <td style="width: 35%;"><i>Double crystal monochromator:</i></td> <td style="width: 35%;"><i>Mirror:</i></td> </tr> <tr> <td></td> <td>Si (111) asym. cut, water cooled.</td> <td>two-segment, toroidal, Pt coated.</td> </tr> <tr> <td><u>Distance from source:</u></td> <td>18.4 m</td> <td>26.5 m</td> </tr> <tr> <td>Acceptance</td> <td colspan="2">1 mrad/0.3 mrad (h x v)</td> </tr> <tr> <td>Energy (3 selectable)</td> <td colspan="2">5.4, 8, 16 keV (0.77, 1.54, 2.3 Å)</td> </tr> <tr> <td>Energy resolution $\Delta E/E$</td> <td colspan="2">$0.7\text{-}2.5 \times 10^{-3}$</td> </tr> <tr> <td>Focal spot size FWHM</td> <td colspan="2">$1.2 \times 0.6 \text{ mm}^2(\text{h} \times \text{v})$</td> </tr> <tr> <td>Spot at Sample FWHM</td> <td colspan="2">$5.4 \times 1.8 \text{ mm}^2(\text{h} \times \text{v})$</td> </tr> <tr> <td>Flux at sample</td> <td colspan="2">$7.5 \times 10^{12} \text{ ph s}^{-1}(2 \text{ GeV}, 300 \text{ mA}, 8 \text{ keV})$</td> </tr> </table>	<u>Optical elements:</u>	<i>Double crystal monochromator:</i>	<i>Mirror:</i>		Si (111) asym. cut, water cooled.	two-segment, toroidal, Pt coated.	<u>Distance from source:</u>	18.4 m	26.5 m	Acceptance	1 mrad/0.3 mrad (h x v)		Energy (3 selectable)	5.4, 8, 16 keV (0.77, 1.54, 2.3 Å)		Energy resolution $\Delta E/E$	$0.7\text{-}2.5 \times 10^{-3}$		Focal spot size FWHM	$1.2 \times 0.6 \text{ mm}^2(\text{h} \times \text{v})$		Spot at Sample FWHM	$5.4 \times 1.8 \text{ mm}^2(\text{h} \times \text{v})$		Flux at sample	$7.5 \times 10^{12} \text{ ph s}^{-1}(2 \text{ GeV}, 300 \text{ mA}, 8 \text{ keV})$	
<u>Optical elements:</u>	<i>Double crystal monochromator:</i>	<i>Mirror:</i>																										
	Si (111) asym. cut, water cooled.	two-segment, toroidal, Pt coated.																										
<u>Distance from source:</u>	18.4 m	26.5 m																										
Acceptance	1 mrad/0.3 mrad (h x v)																											
Energy (3 selectable)	5.4, 8, 16 keV (0.77, 1.54, 2.3 Å)																											
Energy resolution $\Delta E/E$	$0.7\text{-}2.5 \times 10^{-3}$																											
Focal spot size FWHM	$1.2 \times 0.6 \text{ mm}^2(\text{h} \times \text{v})$																											
Spot at Sample FWHM	$5.4 \times 1.8 \text{ mm}^2(\text{h} \times \text{v})$																											
Flux at sample	$7.5 \times 10^{12} \text{ ph s}^{-1}(2 \text{ GeV}, 300 \text{ mA}, 8 \text{ keV})$																											
Experimental apparatus	<p><u>Resolution in real space:</u> 10-1400 Å (small-angle), 1- 9 Å (wide-angle)</p> <p><u>Sample stage:</u> temperature manipulations: ramps, jumps and gradient scans, pressure manipulation: scan and jumps, stop flow experiments, SWAXS measurements applying mechanical stress, SWAXS measurements applying magnetic fields. In-line calorimetric measurements simultaneously with SWAXS.</p> <p><u>Detectors:</u> 1D gas-filled detectors for simultaneous small- and wide-angle (Gabriel type), 2D CCD (Photonic Science) and Mar300 Image Plate for small-angle, Vantec-1D (Bruker AXS), Pilatus 2D detector.</p>																											
Experiment control	<p><u>Beamline control:</u> Program-units written in LabView for Windows</p> <p><u>1 D detector control:</u> PC-card and software from Hecus X-ray Systems GmbH, Graz.</p> <p><u>2 D detector control:</u> Software from corresponding detector system.</p>																											

CURRENT STATUS

The beamline has been built by the Institute for Biophysics and Nanosystems Research (IBN), Austrian Academy of Science in collaboration with staff members from Sincrotrone Trieste, and is in user operation since September 1996. The set-up of the beamline started at the beginning of January 1995 with the installation of the support structure. Until the end of 1995, the 8 keV single energy system had been realised. The upgrade to the full three energy system was finished in spring 1998. Time resolved experiments require fast X-ray detectors and data acquisition hard- and software. Depending on the desired resolution in time and in reciprocal space, on isotropic or anisotropic scattering of the sample, one-dimensional position sensitive (delay-line type) or two-dimensional Pilatus detectors are employed.

In August 2002 our chemistry and X-ray laboratory went into operation. The chemistry unit serves mainly for sample preparation and analysis for both, in house research and external user groups, whereas the X-ray laboratory allows on-site testing of samples before moving on to the SR beamline (see page 43).

In May 2008 we extended about 3 m also our experimental hutch. It is now possible to increase the sample to detector distance and therefore improve our minimum SAXS resolution or maximise the flux density at sample position for certain experiments.

On 1st October 2012 the beamline was transferred from the Institute of Biophysics and Nanosystems Research, Austrian Academy of Sciences, to the Institute of Inorganic Chemistry, Graz University of Technology.

Application for Beamtime at ELETTRA

1. Beamtime Policy at SAXS beamline

According to the agreement from 21. November 2013 regarding the co-operation between the TU Graz and Sincrotrone Trieste, at the Austrian SAXS-beamline the available beamtime of about 5000 hours/year is distributed as follows:

- 35% for Austrian Users, type: "CRG" (Collaborating Research Group)
- 35% for Users of Sincrotrone Trieste (General Users (GU))
- 30% is reserved for beamline maintenance and in-house research

In both user beamtime contingents also any industrial, proprietary and confidential research can be performed according to the "General User Policy" of Sincrotrone Trieste.

To apply for CRG and GU user beamtime proposals must be submitted according to the rules of Sincrotrone Trieste. The international review committee at ELETTRA will rank the proposals according to their scientific merit assessment. Based on this decision beamtime will be allocated according to the specific quotes for the beamtimes (CRG/GU) either for the following semester ("normal application") or for the next two years ("long term application"). However, at the moment no more than a maximum of 10% of the beamtime will be assigned to "long term" projects.

2. How to apply for beamtime

2A. Applications for SAXS-beamtime only

There are two deadlines each year for proposals, namely 15. September and 15. March. Accepted proposals will receive beamtime either in the then following first or second half year period, respectively. The Application Form must be completed on-line according to the following instructions.

ELETTRA USERS OFFICE

Strada Statale 14 - km 163.5

34012 Basovizza (Trieste), ITALY

Tel: +39 040 375 8628 / 8538- fax: + 39 040 375 8565

e-mail: useroffice@elettra.trieste.it

INSTRUCTIONS GIVEN BY THE USERS OFFICE

(see also <http://www.elettra.trieste.it/userarea/apbt.html>)

1. Read carefully the General Guidelines.

2. Connect to the Virtual Unified Office: <https://vuo.elettra.trieste.it/pls/vuo/guest.startup> using your favorite browser with JavaScript enabled.
3. Select the Virtual Unified Office link. Login with your ID and password. If you are a new user fill in the registration form with your data and choose your institution with the search button; in case your institution does not appear in the list, please contact useroffice@elettra.trieste.it giving all the details about it. When registered, you will receive an acknowledgment with your ID and password. You can change your password, if you wish. In case you forget your password, please don't register again but contact useroffice@elettra.trieste.it. At any moment you can select the help button and view more detailed instructions. By inserting your ID and password you will be able to continue.
4. Select the proposals button in the User functions group.
5. Select add and fill in on-line the proposal form. Please, type your proposal in English. Repeat this procedure for each proposal you intend to submit.
6. In case of continuation proposal: a) attach the experimental report of previous measurements; b) give your previous proposal number.
7. When finished, submit the proposal electronically, selecting the save button.
8. Print all safety forms (related to your proposal form).
9. Sign the safety form(s).
10. Mail all printed and signed safety form(s) to the (real) Users Office.

2B. Applications for a combination of SAXS-beamtime AND access to other laboratories (CERIC-ERIC proposals)

CERIC, the Central European Research Infrastructure Consortium, is a distributed research facility, set up as an ERIC, by Austria, Czech Republic, Italy, Romania, Serbia, Slovenia and open to other interested countries.

The specific scope of this ERIC concerns the offer as an integrated service to external researchers of the access to synchrotron light and other analytical techniques notably for materials preparation and characterization, structural investigations and imaging in Life Sciences, Nanoscience and Nanotechnology, Cultural Heritage, Environment, Chemistry and Materials Science.

CERIC-ERIC integrates the most competitive instrumental, technical and research resources complementary analytical and preparation methods like NMR, Synchrotron light, Neutrons, electron Microscopy and other Surface and Interface analytical instruments. For a detailed description on the available facilities visit CERIC's website.

Access to its services is awarded free of charge to any researcher upon submission of a proposal to be selected by an external international peer review committee. Proposals should address challenging scientific or technological problems that require the use of several methods offered by the partners for sample growth and characterization. CERIC-ERIC

features a completely innovative approach focusing on the scientific or technological value of the project allowing to request access to different integrated facilities in a single step, through a single access point.

How to Apply

Detailed information can be found at
<http://www.c-eric.eu/index.php?n=Users.Homepage>

NOTE:

For administrative questions related to the proposal submission, contact
useroffice@elettra.trieste.it

For scientific or technical questions related to the possibility of performing a given SAXS experiment, contact bernstorff@elettra.eu or amenitsch@elettra.eu

Users and institutes performing experiments in 2014

Austria

Austrian Centre of Industrial Biotechnology, Graz

HERRERO ACERO Enrique

TSCHELIESSNIG Rupert Hans

Graz University of Technology, Institute of Inorganic Chemistry, Graz

AMENITSCH Heinz

BINDER, Judith

BURIAN Max

KRIECHBAUM Manfred

JURAIC Krunoslav

MARMIROLI Benedetta

MEISENBICHLER Christian

SARTORI Barbara

TORVISCO GOMEZ Ana

UHLIG Frank

ZEPPEK Cathrin

Graz University of Technology, Institute for Chemistry and Technology of Organic Materials, Graz

DUNST Sebastian

EHMANN Heike M.A.

GOLLAS Bernhard

KALTENHAUSER Verena

LEIMGRUBER Simon

REISHOFER David

TRIMMEL Gregor

VIEIRA Luciana

Johannes Kepler University, Institute of Semiconductor and Solid State Physics, Linz

HEISS Wolfgang

SYTNIK Mykhailo Aleksandr

Medical University of Graz, Institute of Biophysics

KORNMUELLER Karin

LEHOFER Bernhard

PRASSL Ruth

Montanuniversity Leoben, Department of Physics

LECHNER Rainer T.

MORAK Roland

PARIS Oskar

PREHAL Christian

SHARIFI RAJABI Parvin

University of Natural Resources and Life Sciences, Department of Nanobiotechnology,
Vienna

KURZHALS Steffen
VAN OOSTRUM Peter D. J.
VIRK Mudassar Mumtaz
LASSENBERGER Andrea
ZIRBS Ronald
VONDERHAID Iris
REIMHULT Erik

University of Natural Resources and Life Sciences, Department of Material Sciences and
Process, Engineering, Vienna

GRUENEWALD Tilman A.
JORDAN Barbara
LICHTENEGGER Helga C.
RENNHOFER Harald

University of Vienna, Faculty of Physics

BAUER Paulus S.
CAPONE Barbara
WINKLER Paul M.

University of Vienna, Faculty of Physics, Dynamics of Condensed Systems, Vienna

AKBARZADEH Johanna

Brazil

University of Sao Paulo, Institute of Physics, Sao Paul

ITRI Rosangela

Croatia

Institute of Physics, Zagreb

DELAČ MARION Ida
KRALJ Marko
KREGAR Z.
KRSTULOVIĆ N.
SALAMON Krešimir
SKENDEROVIĆ H.

"Ruđer Bošković" Institute, Zagreb

BAN D'ETAT C.
BOGDANOVIĆ-RADOVIĆ Ivancica
BULJAN Maya
CAR T.
DUBČEK Pavo
GRACIN, Davor
JAKŠIĆ Milko
JERČINOVIĆ Marko

KARLUŠIĆ Marko
MELJANAC D.
NEKIĆ Nikolina
PIVAC Branko
RADIĆ Nikola
ŠANTIĆ Branko
SIKETIĆ Z.
SLUNJSKI R.

Brno University of Technology, Institute of Physical Engineering, Brno
MĚCH Rostislav

Denmark

University of Copenhagen, Department of Pharmacy, Faculty of Health and Medical Sciences, Copenhagen

AZMI Intan Diana Mat
ØSTERGAARD Jesper
STÜRUP Stefan
GAMMELGAARD Bente
MICHAELSEN Maria
SASSENE Philip Jonas
YAGHMUR Anan

University of Copenhagen, Nanomedicine Laboratory, Centre for Pharmaceutical Nanotechnology and Nanotoxicology, Copenhagen

MOGHIMI S.M.

Finland

University of Helsinki, Viikki Drug Discovery and Development Technology Center

BURMESTER Mechthild

University of Helsinki, Centre for Drug Research, and School of Pharmacy, University of Eastern Finland, Kuopio

URTTI Arto

France

CIMAP, CEA-CNRS-ENSICAEN-UCBN, Caen

LEBIUS H.

Institute Laue-Langevin, Grenoble, and Université Grenoble Alpes, IBS, Grenoble

PETERS J.
MARTINEZ N.

Université Paris VII, Paris Diderot - Lab of Matière et systèmes complexes (UMR 7057), Paris

CARN Florent

Germany

DESY, HASYLAB, Hamburg

FUNARI Sergio

VALERIO Joana

INM, Leibniz-Institute for New Materials, Saarbrücken

PERRE Emilie

PRESSER Volker

SCHREIBER Anna

WEINGARTH Daniel

Martin-Luther University Halle-Wittenberg, Institute of Chemistry, Chair of Macromolecular Chemistry, Halle

BINDER Wolfgang H.

DöHLER Diana

MICHAEL Philipp

NEUMANN Steve

Technical University of Berlin, Institute for Chemistry

FINDENEKG G.H.

MEISSNER Jens

Technische Universität München, Dept. of Physics, Lehrstuhl für Funktionelle Materialien, Garching

ABDELSAMIE Amr

BIESSMANN Lorenz

INDARI Efi Dwi

KÖRSTGENS Volker

MÜLLER-BUSCHBAUM Peter

RUI Yichuan)

SCHAFFER Christoph J.

SCHLIPF Johannes

SU Bo

WANG Tianyi

University Duisburg-Essen, Faculty for Physics and CENIDE, Duisburg

SCHLEBERGER M.

University of Göttingen, Institute for X-ray Physics

HEMONNOT Clement

KOESTER Sarah

GRACEFFA Rita

SALDANHA Oliva

University of Munich, Department of Chemistry and Center for NanoScience, Munich
BEIN Thomas
DOCAMPO Pablo
HANUSCH Fabian

University of Ulm, Institute of Optoelectronics
MEISCH T.
SCHOLZ F.

Greece

University of Athens, Physics Department
CORDOYIANNIS G.

India

Amity University, Center for Spintronic Materials, Noida
GUPTA Ajay
SHARMA Gagan
SHARMA Kavita

UGC-DAE Consortium for Scientific Research, University Campus, Indore
GUPTA Mukul
PANDIT Pallavi
REDDY Raghavendra Varimalla

Israel

Hebrew University of Jerusalem, Institute of Chemistry and the Fritz Haber Research Center
HARRIES Daniel
MOSENKIS Jonathan
SAPIR Liel
SUKENIK Shahar

Italy

Center for Life Nano Science@Sapienza, Italian Institute for Technology, Rome
COLAPICCHIONI V.

CNR (National Research Council), Institute of Biomedicine and Molecular Immunology, Palermo
BUFFA V.
ROMANCINO D.
BONGIOVANNI A.

CNR (National Research Council), Institute of Biophysics, Palermo

BULONE Donatella
CARROTTA Rita
LIBRIZZI Fabio
MANGIONE Maria Rosalia
MANNO Manno
MARTORANA Vincenzo
NOTO Rosina
RACCOSTA Samuele
SAN BIAGIO Pier Luigi
VILASI Silvia

Elettra-Sincrotrone Trieste S.C.p.A., Trieste

BERNSTORFF Sigrid
DE MARCH Matteo
DEKA Jashmini
GIROD Matthias
IANESELLI Luca
MORELLO Christian
ONESTI Silvia Caterina Elvira

INSTM - Consorzio Interuniversitario Nazionale per la Scienza e Tecnologia dei
Materiali & Elettra-Sincrotrone Trieste

CASALIS Loredana
PARISSE Pietro

IOM - CNR National Laboratorio TASC, Trieste

RADIVO Andrea
SOVERNIGO Enrico
TORMEN Massimo

Italian Institute of Technology, Drug Discovery and Development Unit, Genova

MOGLIANETTI Mauro

Universita di Cagliari, Dip. di Scienze Chimiche e Geologiche, Monserrato

NOBILI Francesco
CASULA Maria Francesca
LOCHE Danilo

Università "G.D'Annunzio" di Chieti - Pescara

SINIBALDI Raffaele

Università di Milano, Dipartimento di Biotecnologie Mediche e Medicina Trasla-
zionale, Segrate

BELLINI Tommaso
CERBINO Roberto
NAVA Giovanni

University of Padova, Department of Chemical Sciences, Padova

FAVARO Marco

University of Padova, Department of Pharmaceutical Sciences, Padova

GRIGOLETTO Antonella

PASUT Gianfranco

Università di Palermo, Scienze e Tecnologie Biologiche Chimiche e Farmaceutiche,
Palermo

PALUMBO PICCIONELLO Antonio

Polytechnic University delle Marche, Department of Life and Environmental Sciences,
Ancona

CARDUCCI Federica

MARIANI Paolo

MOSCATELLI Silvia

ORTORE Maria Grazia

RICCI Caterina

SPINOZZI Francesco

“Sapienza” University of Rome, Department of Molecular Medicine

CARACCIOLO Giulio

PALCHETTIS.

POZZI Daniela

“Sapienza” University of Rome, Department of Physics

BOMBOI Francesca

SCIORTINO Francesco

Università di Sassari, Laboratorio di Scienza dei Materiali e Nanotecnologie, CR-
INSTM, Alghero

CARBONI Davide

INNOCENZI Plinio

MALFATTI Luca

PINNA Alessandra

University of Trieste, Department of Chemical and Pharmaceutical Sciences, & Center
of Excellence for Nanostructured Materials, & INSTM, Trieste

BONASERA Aurelio

SYRGIANNIS Zois

Portugal

Universidade do Porto - REQUIMTE, Departamento de Ciências Químicas, Faculdade
de Farmácia, Porto

NUNES Claudia

PINHEIRO Marina

REIS Salette

Singapore

National University of Singapore, Mechanobiology Institute
GRENCI Gianluca

Slovakia

Comenius University, Faculty of Pharmacy, Bratislava
BUCSI Alexander
DEVINSKY F.
HUBCIK Lukas
UHRIKOVA Daniela

Slovenia

Jožef Stefan Institute, Department for Nanostructured Materials, Ljubljana
ČEH Miran

Jožef Stefan Institute, Ljubljana
LAVRIC Marta
MILAVEC Jerneja
POVSE JESENEK Dalija
RESETIC Andraz
TRCEK Maja

Jozef Stefan International Postgraduate School, Ljubljana
ABINA A.
PUC Uros

Jožef Stefan Institute, Condensed Matter Physics Department, Ljubljana, and Jožef Stefan International Postgraduate School Ljubljana, and University of Maribor, Faculty of Natural Sciences and Mathematics, Maribor
ZIDANŠEK Alexander

Jožef Stefan Institute, Ljubljana, and University of Maribor, Faculty of Natural Sciences and Mathematics, Maribor
KRALJ Samo

Spain

CSIC - Consejo Superior de Investigaciones Cientificas - Instituto de Ciencia de Materiales, Barcelona
BUENO LOPEZ Dolores
MASCIOCCHI Norberto
MORENO-CALVO Evelyn

Sweden

Lund University, Division of Materials Engineering, Department of Mechanical EngineeringMaterials, Lund

SURREDDI Kumar Babu

United Kingdom

Diamond Light Source, Didcot

CACHO-NERIN Fernando

USA

Syracuse University, Department of Chemistry, Syracuse, NY

RUHLANDT-SENGE Karin

WEBB Jr Cody Cliffdon

List of Performed Experiments

2014 (first half year)

Proposal	Proposer	Institute	Country	Title	Research Field
20135121	DE MARCH Matteo	Elettra – Sincrotrone Trieste S.C.p.A.	Italy	Low resolution crystallography	Life Sciences
20135165	ZEPPEK Cathrin	TU Graz, Institute of Inorganic Chemistry	Austria	Time resolved in-situ GISAXS of 9-ANTHRACENY2SiH ₂ in PMMA	Chemistry
20135176	LECHNER Rainer T.	Montanuniversitaet Leoben, Dep. of Physics	Austria	Investigation of the growth of organic hierarchic nanocrystals using a novel synthesis method by in-situ SWAXS	Materials Science
20135183	KARLUSIC Marko	Ruder Bošković Insitute, Zagreb	Croatia	Morphology of ion tracks in amorphous thin films and multilayers	Materials Science
20135192	UHRIKOVA Daniela	Comenius Uni., Faculty of Pharmacy	Slovakia	Polymorphic behaviour of pH responsive drug nanocarriers	Life Sciences
20135199	WINKLER Paul	Universität Wien - Fakultät für Physik	Austria	Application of SAXS to the study of biogenic nanoparticle formation	Materials Science
20135219	TRIMMEL Gregor	TU Graz, Inst. for Chem. and Technology of Organic Materials	Austria	A time resolved GISWAXS study on the structural changes in nanoimprinted polymer patterns for the preparation of inorganic/organic hybrid solar cells	Materials Science
20135239	CARN Florent	Uni. Paris VII, Lab of Matière et systèmes complexes	France	Controlled Clustering of Nanoparticles Into Nanorods Mediated by Semi-flexible or flexible Polyelectrolyte	Materials Science
20135245	PARIS Oskar	Montanuniversitaet Leoben, Dep. of Physics	Austria	Bridging aggregation of silica nanoparticles with proteins: Kinetics and structure	Materials Science
20135333	MICHAELSEN Maria	Uni. of Copenhagen, Dep. of Pharmaceutics and Analytical Chemistry	Denmark	Structural transitions of lipid-based mixed micelles in a simulated intestinal milieu studied by combined time-resolved SAXS and stopped flow technique	Life Sciences
20135355	BULJAN Maja	Ruder Bošković Insitute, Zagreb	Croatia	Structural properties of self-assembled core/shell Ge/Ni clusters for magneto-optical applications	Materials Science
20135374	MALFATTI Luca	Uni. Sassari, Dep. of Materials Science & Nanotechnology, Alghero	Italy	pore organisation into crystalline mesostructured thin films based on 3-Glycidoxy-propyl-trimethox-ysilane	Materials Science
20135387	BURMESTER Mechthild	Uni. of Helsinki, Viikki Drug Discovery & Development Technology Center	Finland	Structural characterization of cubosomes and hexosomes: the effects of lipid composition, model drug, matrix components and storage conditions on stability	Life Sciences
20135359	PARIS Oskar	Montanuniversitaet Leoben,, Dep. of Physics	Austria	In-situ SAXS Studies of Electrical Double-Layer Capacitors: the Role of Ion Size	Materials Science
20135407	GOLLAS Bernhard	TU Graz, Inst. for Chem. and Technology of Organic Materials	Austria	Structure and dynamics of the electrode/electrolyte interface in deep eutectic solvents.	Chemistry
20135419	DEKA Jashmini	Elettra - Sincrotrone Trieste S.C.p.A.	Italy	Oligonucleotide modified Gold Nanoparticles as a Platform for studying Enzymatic Reaction and Ionic Strength effects on DNA	Life Sciences

20135413	MANNO Mauro	CNR - Istituto di Biofisica, Palermo	Italy	Effect of protein lipidation on the structural properties of exosome vesicles released by skeletal muscle cells	Life Sciences
20135441	JURAIC Krunoslav	Ruder Bošković Insitute, Zagreb	Croatia	Simultaneous GISAXS/GIWAXS experiment of Nanostructured Zinc Oxide Thin Films for Organic Photovoltaics	Materials Science
20135461	DUBCEK Pavo	Ruder Bošković Insitute, Zagreb	Croatia	Pulsed laser dewetting of aluminium	Materials Science
20135470	SARTORI Barbara	TU Graz, Dept. of Inorganic Chemistry	Austria	Effect of different salts on the formation of mesostructured nanoparticles synthesized in the gas phase	Materials Science
inhouse research	BERNSTORFF Sigrid & MÜLLER-BUSCHBAUM Peter	Elettra-Sincrotrone Trieste & TU München, Dept. of Physics	Italy & Germany	Morphology of hybrid Perovskite thin films by 2-step synthesis	Materials Science
inhouse research	AMENITSCH Heinz & LICHTENEGGER Helga	TU Graz & Uni. of Natural Resources & Life Sciences, Dep. of Material Sciences & Process Engineering, Vienna	Austria	Core-Shell Structure of Monodisperse Poly(ethylene glycol)-Grafted Iron Oxide Nanoparticles Studied by SAXS	Materials Science
inhouse research	BERNSTORFF Sigrid & RADIC Nikola	Elettra-Sincrotrone Trieste & Ruder Bošković Insitute, Zagreb	Italy & Croatia	A 2D and 3D arrays of Ni nanoparticles formed by magnetron sputtering	Materials Science
inhouse research	AMENITSCH Heinz & CARACCIOLIO Giulio	TU Graz & Sapienza Uni. di Roma, Dep. of Chemistry	Austria & Italy	Role of cholesterol on the transfection barriers of cationic lipid/DNA complexes	Life Sciences
inhouse research	AMENITSCH Heinz & POZZI Daniela	TU Graz & Sapienza Uni. di Roma, Dep. of Chemistry	Austria & Italy	Killing cancer cells with nanotechnology: novel poly(I:C) loaded liposome-silica hybrid nanoparticles	Life Sciences
inhouse research	AMENITSCH Heinz & RUHLANDT Karin	TU Graz & Uni. of Syracuse, Dep. of Chemistry, Syracuse, NY	Austria & USA	Mechanism of Formation of HKUST-1, a Copper Containing Metal-Organic Framework (MOF) Depending on Reagents and Solvents	Chemistry
inhouse research	BERNSTORFF Sigrid & BINDER Wolfgang	Elettra-Sincrotrone Trieste & Martin Luther Uni. Halle-Wittenberg, Halle	Italy & Germany	Autocatalysis in self-healing polymers: investigation of time-dependent nano-cluster formation via SAXS	Chemistry
inhouse research	AMENITSCH Heinz & NUNES Claudia	TU Graz & Uni. of Porto, Dep. of Chemistry, Faculty of Pharmacy	Austria & Portugal	Evaluation of anti-tuberculosis drugs on the biophysical properties of the membrane studied 3D model systems.	Life Sciences
inhouse research	AMENITSCH Heinz & BONASERA Aurelio	TU Graz & Uni. Trieste, Dep. of Farmaceutical Sciences	Austria & Italy	XRD From powders to devices	Life Sciences
inhouse research	AMENITSCH Heinz & SYRGIANNIS Zois	TU Graz & Uni. Trieste, Dep. of Farmaceutical Sciences	Austria & Italy	Self-Structuring Photosynthetic Sensitizer-Catalyst nanotrajectories for High Quantum Efficient Water Oxidation	Life Sciences

2014 (second half year)

Proposal	Proposer	Institute	Country	Title	Research Field
20140026	ORTORE Maria Grazia	Università Politecnica delle Marche - Dipartimento Scienze Applicate ai Sistemi Complessi	Italy	Amyloid beta peptide aggregation influenced by curcumin-like compounds	Life Sciences
20140055	MÜLLER- BUSCHBAUM Peter	Technische Universität München - Physik Dept.	Germany	The role of solvent-additives on the crystallization behavior of polymer- fullerene layers for organic photovoltaics	Materials Science
20140086	MARIANI Paolo	Uni. Politecnica delle Marche, Dep. of Life and Environmental Sciences, Ancona	Italy	DNA nanostars: phase behaviour and structural investigation by SAXS	Life Sciences
20140108	MORENO-CALVO Evelyn	Consejo Superior de Investigaciones Cientificas, Institute for Materials Science	Portugal	Characterization of the nanostructure of rich-cholesterol vesicles with application in nanomedicine	Life Sciences
20140125	SARAH Koester	Uni. Goettingen, Institute for X-ray Physics	Germany	Probing nanostructural changes in red blood cells in microflow by SAXS	Life Sciences
20140151	PRASSL Ruth	Medical Uni. of Graz, Institute of Biophysics	Austria	Effects of high hydrostatic pressure on low density lipoprotein (LDL) and its core lipid transition	Life Sciences
20140187	GUPTA Ajay	Amity University, Center for Spintronic Materials	India	Role of surface and interfaces in determining the properties of polymer films in nanoconfined geometry	Materials Science
20140189	LICHTENEGGER Helga	Universität für Bodenkultur, Institut für Physik und Materialwis- senschaft, Vienna	Austria	Investigating thermoresponsive polymer brushes on iron oxide nanoparticles by time resolved SAXS	Materials Science
20140190	LICHTENEGGER Helga	Universität für Bodenkultur, Institut für Physik und Materialwis- senschaft, Vienna	Austria	The influence of bio-resorbable Mg implants on bone chemistry and mineralization - SAXS	Life Science
20140234	PARIS Oskar	Montanuni. Leoben, Dep. of Physics	Austria	Humidity driven deformation of mesoporous silica thin films: The influence of film thickness and film perfection	Materials Science
20140274	ZIDANSEK Aleksander	Jozef Stefan Institute, Ljubana	Slovenia	Structure of soft nanocomposites exhibiting crystal-type ordering	Materials Science
20140311	RUHLANDT Karin	Syracuse Uni., Dep. of Chemistry, Syracuse, NY	USA	Mechanism of Formation of HKUST- 1, a copper containing metal organic framework (MOF) depending on reagents and solvents.	Chemistry
20140383	PREHAL Christian	Montanuni. Leoben, Inst. of Physics, Leoben	Austria	Ion electrosorption in nanoporous supercapacitors studied by in-situ SAXS	Materials Science
20140387	KORNMUELLER Karin	Medical Uni. of Graz, Institute of Biophysics	Austria	Self-assembling designer peptides as bio-inspired nanomaterials: supramolecular structure and membrane-activity	Life Sciences

20140418	LIBRIZZI Fabio	CNR - Istituto di Biofisica, Palermo	Italy	Kinetic study of amyloid-like oligomers formation in Concanavalin A	Life Sciences
20140430	BULJAN Maja	Ruder Bošković Insitute, Zagreb	Croatia	Preparation of Ge/Si core/multishell quantum dot lattices in an alumina matrix	Materials Science
20140436	MARMIROLI Benedetta	TU Graz, Institute of Inorganic Chemistry	Austria	Feasibility study of the early stage interaction of silica nanoparticles with Lysozyme using a free jet micromixer in combination with SAXS	Life Sciences
20140477	KARLUSIC Marko	Ruder Bošković Insitute, Zagreb, Croatia	Croatia	Swift heavy ion tracks in mixed amorphous materials	Materials Science
20140517	JURAIC Krunoslav	TU Graz, Institute of Inorganic Chemistry	Austria	Structural properties of TiO ₂ nanotubes arrays formed on ZnO substrate for dye sensitized solar cells	Materials Science
20140518	YAGHMUR Anan	Univ. of Copenhagen, Dep. of Pharmaceutics & Analytical Chemistry	Denmark	Stability of model drug-encapsulated cubosomes and hexosomes in human plasma	Life Sciences
CERIC 20142017	WINKLER Paul	Universität Wien, Fakultät für Physik	Austria	Determining growth and structural parameters of organic nanoparticles by in-situ light scattering	Materials Science
CERIC 20142013	FAVARO Marco	Uni. Padova, Dep of Chemical Sciences	Italy	Structural and chemical characterization of hollow graphene nanospheres and of hybrid metal oxides-graphene oxide - based composites.	Materials Science
Inhouse	BERNSTORFF Sigrid & RADIC Nikola	Elettra-Sincrotrone Trieste & Ruder Bošković Insitute, Zagreb	Italy & Croatia	Phase and morphology of tantalum nitride films deposited by reactive magnetron sputtering	Materials Science
Inhouse	BERNSTORFF Sigrid & DUBCEK Pavo	Elettra-Sincrotrone Trieste & Ruder Bošković Insitute, Zagreb	Italy & Croatia	Aluminium nanoparticles for improved photovoltaic cell	Materials Science
Inhouse	AMENITSCH Heinz & GOLLAS Bernhard	TU Graz, Inst. for Chem. and Technology of Organic Materials	Austria	Structure and dynamics of the electrode/electrolyte interface in deep eutectic solvents	Chemistry
Inhouse	BERNSTORFF Sigrid & FUNARI Sergio	Elettra-Sincrotrone Trieste & HASYLAB at DESY, Hamburg	Italy & Germany	Simultaneous time-resolved SWAXS and DSC determination of lipid membranes fluidity in the presence of osmolytes (urea and trimethylamine N-oxide (TMAO))	Life Sciences
Inhouse	AMENITSCH Heinz & BONASERA Aurelio	TU Graz & Uni. Trieste, Dep. of Farmaceutical Sciences	Austria & Italy	From powders to devices	Life Sciences
Inhouse	AMENITSCH Heinz & SYRGIANNIS Zois	TU Graz & Uni. Trieste, Dep. of Farmaceutical Sciences	Austria & Italy	Self-Structuring Photosynthetic Sensitizer-Catalyst nanotrajectories for High Quantum Efficient Water Oxidation	Life Sciences
Inhouse	AMENITSCH Heinz & HODZIC Aden	TU Graz & Elettra-Sincrotrone Trieste	Austria & Italy	Stability of pharmaceutical formulations	Life Sciences
Inhouse	AMENITSCH Heinz & BURIAN Max	TU Graz	Austria	Structural Characterization of RuPom/Pyridin Complexes	Life Sciences

User Statistics

1. Number of submitted proposals and assigned shifts from 1995 until December 2015

The Austrian SAXS-beamline at ELETTRA opened to users in September 1996. Since then many experiments have been performed related to the fields of life science, materials science, physics, biophysics, chemistry, medical science, technology and instrumentation.

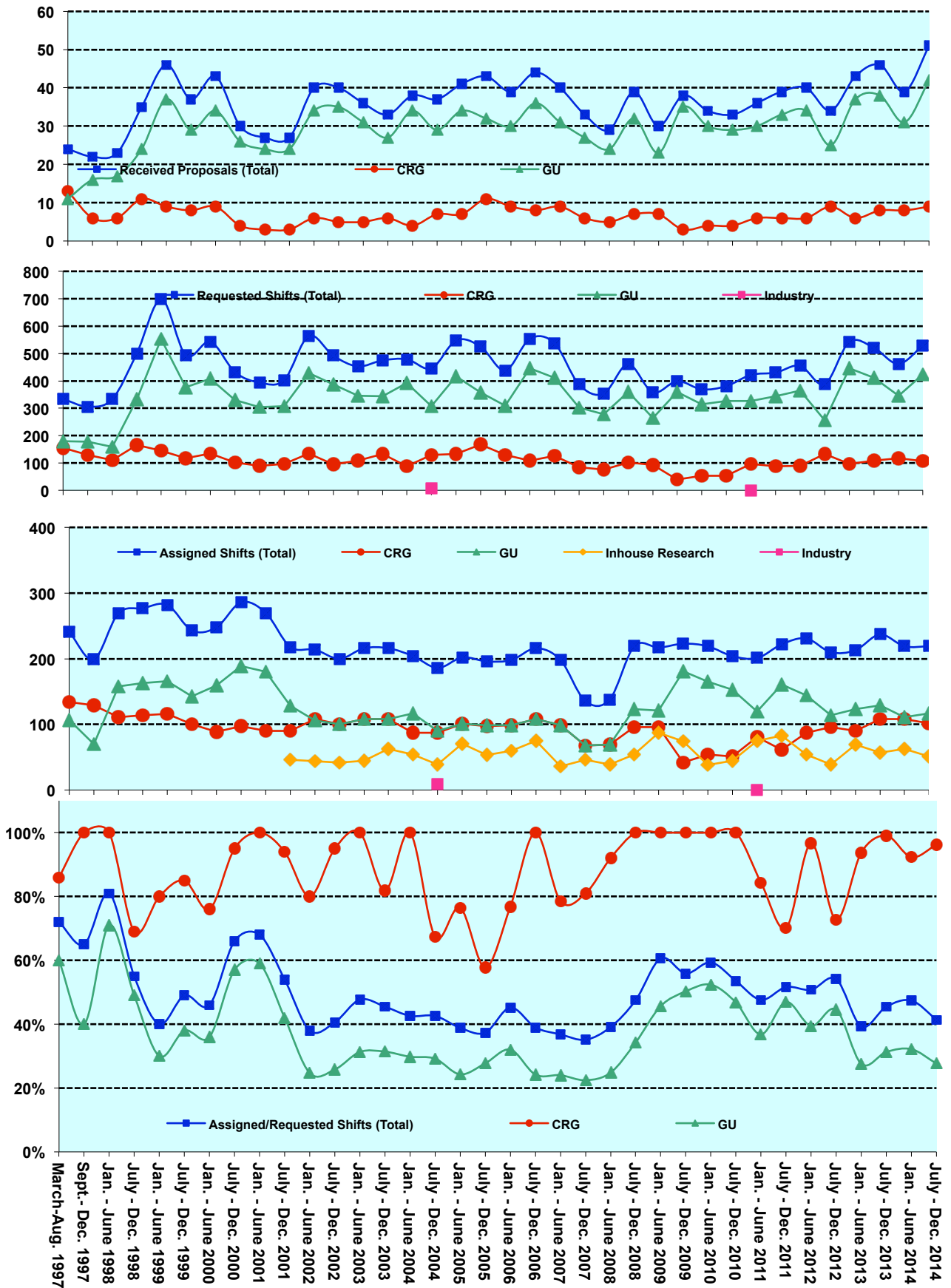
The assignment of beamtime at this beamline is done separately for the group of "General Users" (GU) and the "Collaborating Research Group" (CRG), i.e., the Austrian users. Beamtime was assigned to the proposals of each group in the order of the rating received by the Scientific Committee, and up to the maximum number of shifts available to each group according to the contract between the Technical University of Graz and the "Sincrotrone Trieste". Until December 1997 up to 30 % of the beamtime was given to CRG, up to 55 % to GU, and 15% was reserved for maintenance purposes. From January 98 to June 2001 the quota for beamtime was up to 35 % for CRG, up to 50 % for GU, and again 15% reserved for maintenance purposes. From July 2001 on the two contingents for user proposals from CRG and GU receive up to 35% of the beamtime each. The remaining 30 % of beamtime are used for inhouse research projects as well as for maintenance purposes. From July 2014 on, access to the Austrian SAXS-beamline can also be obtained by submitting a proposal via the new CERIC-ERIC channel (see page 8).

Figure 1 gives an overview of the numbers of received proposals, the numbers of requested and assigned shifts, as well as the percentage between assigned and requested shifts during the last years. As can be seen in Fig.1, the request for beamtime at the SAXS-beamline increased strongly until the first half year of 1999. Then, probably due to the high rejection rates, the number of submitted proposals decreased somewhat during 2001, which resulted in a better ratio of accepted / rejected proposals. This oscillating behaviour of beamtime request can also be seen for the period 2002 – 2015 where after higher numbers of submitted proposals slightly reduced request periods follow. The numbers for the second semester of 2007 and first of 2008 reflect also that, due to the long shut-down from 1.10.2007 to 3.03.2008 (for the new booster-electron-injector installation) less proposals were submitted, and less beamtime was available.

In 2014, in total 90 proposals (17 from CRG, and 73 from GU) were submitted. From these 2 CRG and 18 GU proposals were submitted by "new" usergroups, i.e. groups which so far had never beamtime at the SAXS beamline. From these, 6 GU and both CRG proposals were accepted by the review committee. In addition 7 CERIC-proposals were submitted for the second semester of 2014, from which two (both from new user groups) were accepted for beamtime.

Figure 1 (Next page). The statistical information about the beamtime periods since end of 1995 are given for the groups "CRG", and "GU" separately, as well as for both together ("Total"). Shown are, for all beamtime periods (from top to bottom):

- Number of received proposals, • Number of requested shifts,
- Number of assigned shifts, and • Relation between assigned and requested shifts



2. Provenience of users

During 2014, 208 users from 64 institutes in 19 countries have performed experiments at the SAXS beamline. In Fig. 2 are shown both the provenience of these users, and of their respective institutes. Each user or institute was counted only once, even though many users performed experiments in both beamtime periods of 2014.

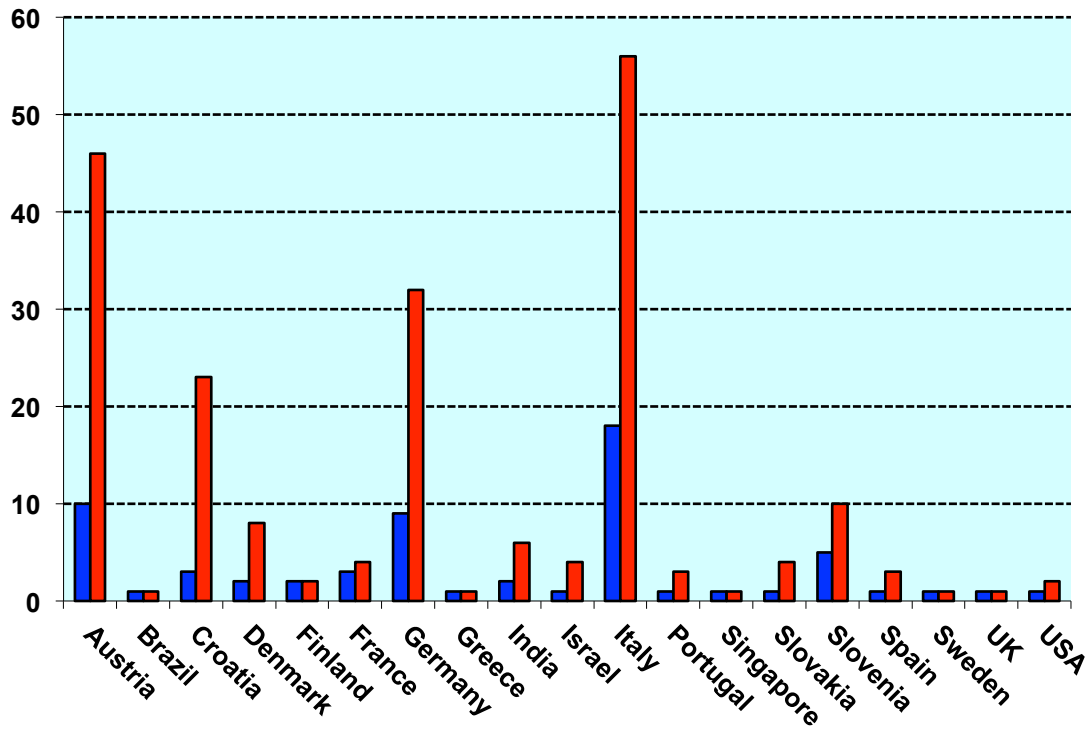


Figure 2. Nationality of the Austrian SAXS beamline users in the year 2014. The number of users (red) and the corresponding number of institutes (blue) are shown for each country.

3. Documentation of experimental results

As could be expected, with the start of user-operation at the SAXS-beamline the number of contributions to conferences started to increase strongly. With a delay of one year - the average time needed for paper publications - also the number of publications increased accordingly, as can be seen in Fig. 3.

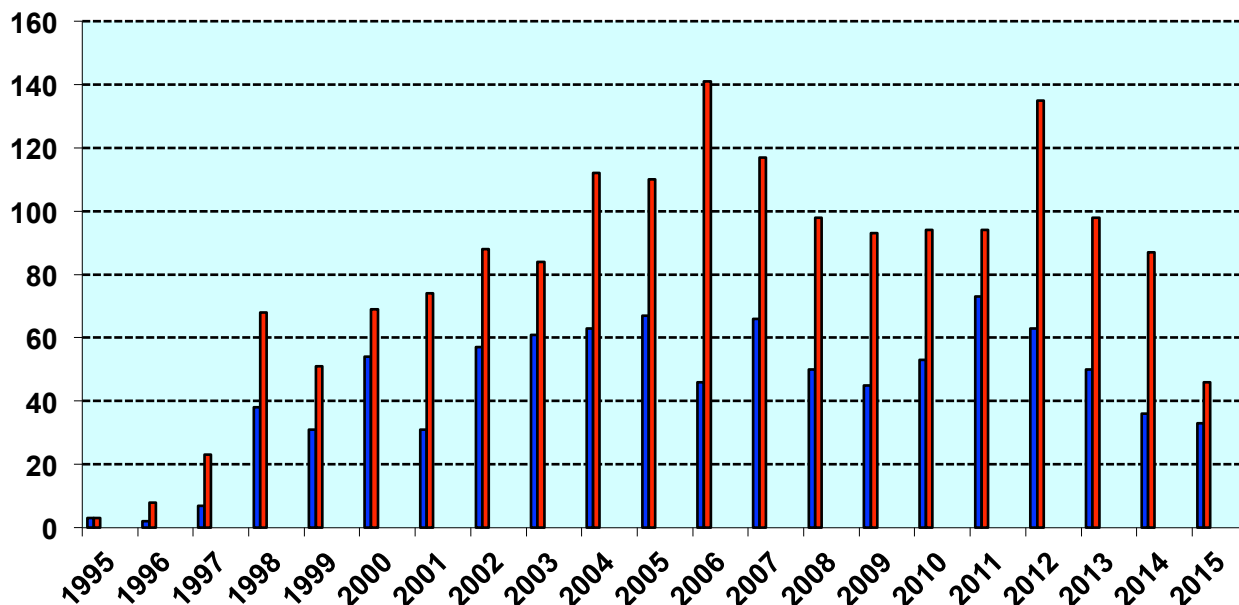


Figure 3. Number of conference contributions (red) and refereed paper publications (blue) for the years 1995-2014, and until August 2015.

In addition, from 1995 until August 2015, the following documentations based on instrumentation of the SAXS-beamline, or on data taken with it, have been produced:

Technical Reports on Instrumentation: 5
Contributions to Elettra Newsletters: 15
Contributions to Elettra Highlights: 50
Habil Thesis: at least 4
PhD Thesis: at least 103
Master Thesis: at least 44
Bachelor Thesis at least 1

Experimental Possibilities at the SAXS-beamline

1. NEW DEVELOPMENTS AND INSTRUMENTATION

Several improvements in the beamline software were done during the last year. One is related to the implementation of an automatic SAXS data reduction system (SAXS dog), and the other is related to the upgrade of the beamline Labview (version 6i) control programs mainly related to the Pilatus detector control (a more user friendly and intuitive interface) and its integration with the motors and temperature controls.

The SAXSDOG project

The simultaneous use of both of the 2D image detectors (Pilatus 1M and 100k) significantly limited the possibility of online data evaluation since standard data processing software for azimuthal integration, such as FIT2D [1], was causing a computational bottle neck. Together with support from Graz, we therefore developed and fully implemented the online data integrating software SAXSDOG. It outsources the azimuthal integration of the recorded images onto our fast 16 core CPU server such that integration rates of up to 80 images per second can be reached. At the beginning of a new user session, the calibration and image masking is done via FIT2D [1] and is then imported in the SAXSDOG client program LEASH. The client software then loads the calibration onto the SAXSDOG server, which automatically integrates every newly created image in a designated folder. The final 1D data as well as main integral parameters such as the integrated intensity, invariant and correlation length are visualized in real time. Additionally, the entire software package can also be run in client mode, which emulates a server process and therefore does not require a dedicated SAXSDOG server. This enables the use of SAXSDOG for users at home where even on standard PCs integration speeds of 20 images/second are easily achievable. The software is written in Python and is available upon request.

[1] A P Hammersley, S O Svensson, and A Thompson, H Graafsma, Å Kwick, and J P Moy, "Calibration and correction of distortions in 2D detector systems", Rev. Sci. Instr., (SRI-94), 66, 2729-2733 (1995)

Improved Labview SAXS beamline control

List of improvements:

- The secondary beamshutter can now also be operated via the main SWAXS detector program
- The dataloger signal monitor was integrated into the main SWAXS detector program
- Automatic scans of the GISAXS grazing angle of incidence, with optimized exposure times
- Simple and automated procedures for temperature and position scans synchronized with the SWAXS detector program
- Simplified procedure to start "ALBULA", the program for automatic displaying the just acquired detector tiff images



Figure 1. Main SWAXS Labview VI program for detector control

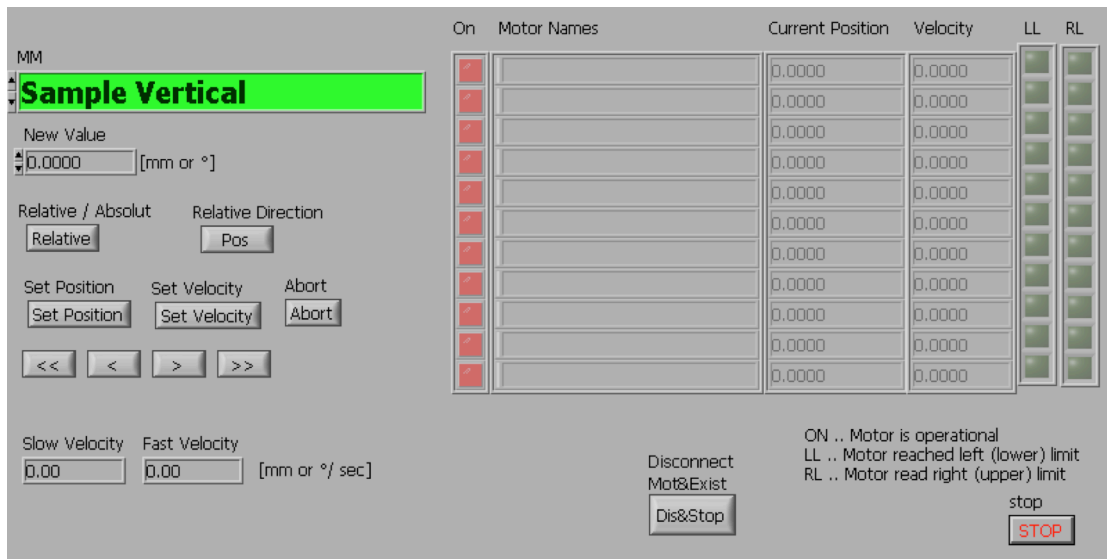


Figure 2. Sub control panel Newport motors main Labview VI control program.

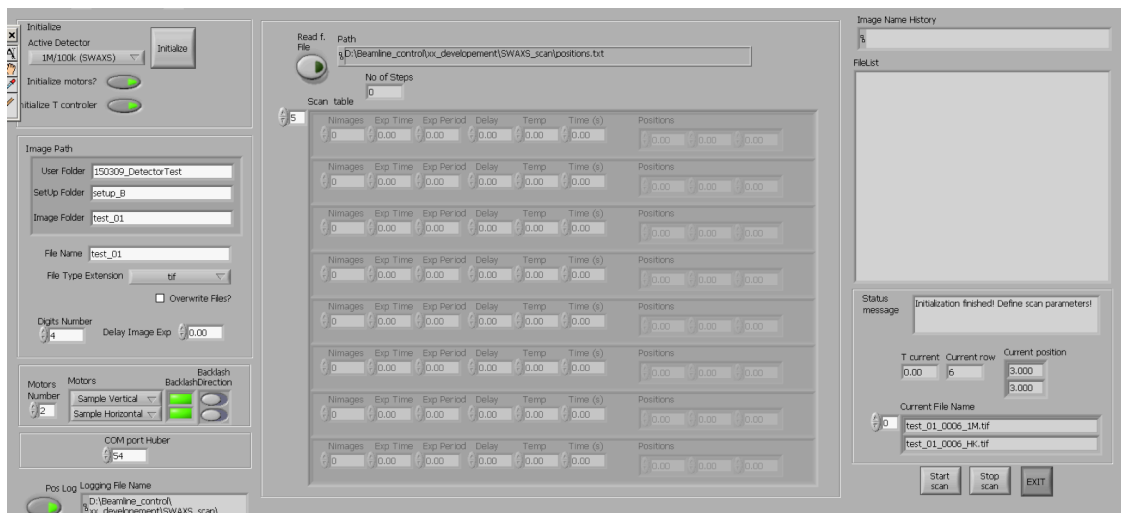


Figure 3. Sub control panel of SWAXS Scan Labview VI program for synchronization between Pilatus detectors, motor controllers and temperature controllers

Combined UV-Vis – stopped –flow experiment

In order to study both, structural changes on the nanometer scale as well as opto-electronic transients in the UV/VIS regime, we expanded our existing BioLogic SFM 400 “Stopped-Flow” system. We are now able to perform the same experiments under perfectly comparable conditions for both *in-situ* SAXS and UV/VIS absorption experiments, making this the technique of choice for reactions involving photoactive compounds occurring in the order of ms.

Wavelength	190-1000	nm
Time resolution	12.5	ms
Min. Dead-Time	25	ms
Min. Dead-Volume	80	μl/shot
Sample-Compartments	4	-

Important: Specifications are subject to sample conditions, especially sample viscosity and the number of mixing-processes.

Glove box

A new UNILab Pro Glove Box Workstation from M.Braun is now available in the Chemistry Lab. The glovebox is filled with high purity nitrogen, and is available for the manipulation of sensitive samples. Oxygen and moisture sensors are continuously monitoring the O₂ and H₂O content in the box. The attainable purity level is less than 1 ppm for both H₂O and O₂. Inside the glovebox are available a -20°C freezer, a precision balance and a stirring / heating plate. Two antechambers with a sliding tray, a small one (150mm diameter) for small parts, and a larger one (390mm diameter, 600mm length) for bigger items, allow to bring samples and also additional equipment into and out of the working atmosphere without affecting the inner environment



2. ACCESSIBLE SAXS AND WAXS RANGES

The accessible **SAXS-range** depends on the requirements of each specific experiment: the required SAXS resolution (minimum q -value needed) defines the minimum possible sample-to-detector distance, which in turn limits the maximum reachable q -value due to the limited detector and vacuum-tube sizes. Also the required time-resolution can limit the effectively accessible SAXS-range, depending of the active size of the most suitable detector from our pool (see pages 27-28, 37-38). Therefore, first-time users should contact their local contact in usefull time before coming to ELETTRA in order to design their experiment accordingly.

Generally, the sample-to-detector distance can vary between a minimum of ca. 20 cm, and a maximum of 3 m. Thus, depending on the photon energy, maximum SAXS resolutions of 2000 Å (5.4 keV), 1400 Å (8 keV) or 630 Å (16 keV) are available.

Simultaneous SAXS- and WAXS-measurements can be performed using two different detectors at the same time. The accessible **WAXS-range** depends on the requirements for each specific experiment, namely on the choice of the sample holder, and the vacuum chamber needed for the SAXS-range. A maximum angular range (2θ) of about $20^\circ - 80^\circ$ can be possible.

A specially designed vacuum chamber (SWAXS-nose, see Annual Report of 1996/97, p. 32) allows to use both scattering areas below (for SAXS) and above (for WAXS) the direct beam, respectively. The overall length of the SWAXS-nose in the horizontal direction, measured from the sample position, is 512 mm and the fixed sample to WAXS-detector distance is 324 mm. With a SAXS camera-length of ≤ 1.25 m an overlap in the d -spacings covered by the SAXS- and WAXS-detectors, respectively, is possible: then, the common regime lies around 9 Å d -spacing.

3. CALIBRATION OF THE S-AXIS AND FLAT FIELD CORRECTION

At the SAXS beamline various standards are used for the angular (s-scale) calibration of the different detectors:

- Rat tail tendon for the SAXS detector - high resolution (rtt*.dat)
- Silver behenate for the SAXS detector – medium and low resolution (agbeh*.dat)
- Para-bromo benzoic acid for the WAXS detector – WAXS range 1 and 2 (pbromo*.dat)
- Combination of Cu, Al foils and Si powder for the WAXS detector – WAXS range 2 and higher

In Figure 1 a typical diffraction pattern of rat tail tendon is shown, depicting the diffraction orders (from the first to the 14th order) measured with a "high" resolution set-up (2.3 m) and the delay-line gas detector. The d-spacing is assumed to be 650 Å, but this value can vary depending on humidity up to 3%. Thus, the rat tail tendon is often used only to determine the position of the direct beam (zero order), while the absolute calibration is performed using the diffraction pattern of Silver behenate powder. Fig. 2 depicts a diffraction pattern of Silver behenate measured with "medium" resolution set-up (1.0 m) from the first to the 4th order (repeat spacing 58.4 Å) [1].

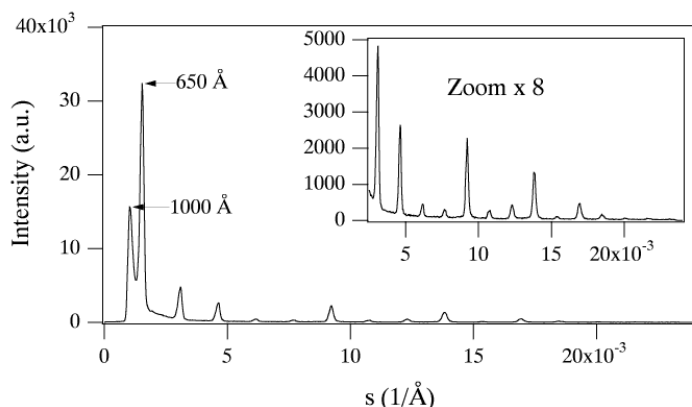


Figure 1. SAXS diffraction pattern of the collagen structure of rat tail tendon fibre at a distance of 2.3 m

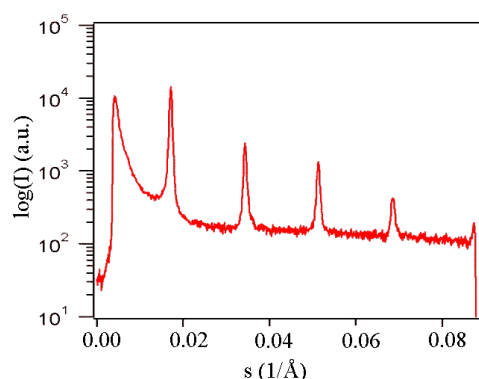


Figure 2. SAXS diffraction pattern of Ag behenate powder at a distance of 1.0 m

In Figure 3 a typical WAXS pattern of p-bromo benzoic acid is shown. The diffraction peaks are indexed according to the values given in Table 2, taken from [2].

d-spacing/Å	rel. intensity	d-spacing/Å	rel. intensity
14.72	18000	4.25	490
7.36	1200	3.96	2380
6.02	330	3.84	10300
5.67	980	3.74	26530
5.21	6550	3.68	1740
4.72	26000	3.47	760

Table 2. d-spacings and relative intensities of p-bromo benzoic acid according to [2].

p-bromo benzoic acid: calculated intensities

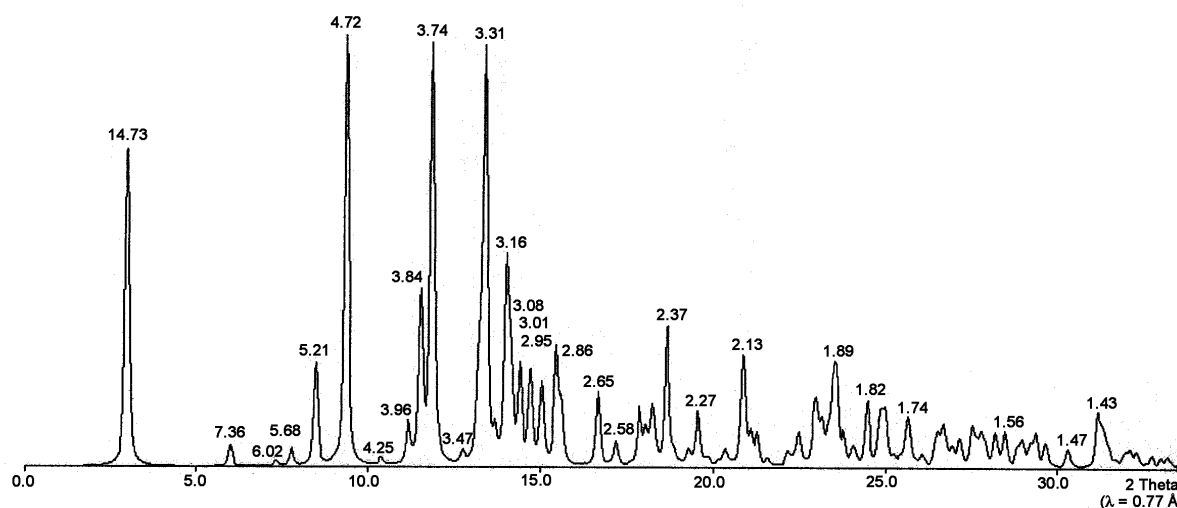


Figure 3. Calculated diffraction pattern of p-bromo benzoic acid. d-spacings are given in Å.

The s-scale for both, the SAXS and the WAXS range, can be obtained by linear regression, i.e., the linear relation between the known s-values of the calibrant versus the measured peak positions has to be found.

A further correction is regarding the flat field response (efficiency) of the detectors. For this correction, the fluorescence light of various foils are used to illuminate the detectors rather homogeneously:

At 8 keV: iron foil (100 µm thick), fluorescence energy: 6.4 keV K_{α} , 7.1 keV K_{β} (effic*.dat)

At 16 keV: copper foil (> 100 µm thick), fluorescence energy: 8.028 keV $K_{\alpha 2}$, 8.048 keV $K_{\alpha 1}$, 8.905 keV K_{β} (effic*.dat)

The measured scattering patterns are corrected for the detector efficiency simply by dividing them by the fluorescence pattern. Note: The average of the detector efficiency data should be set to unity and a small threshold should be applied to avoid any division by zero.

[1] T.N. Blanton et. al., Powder Diffraction 10, (1995), 91

[2] K. Ohura, S. Kashino, M. Haisa, J. Bull. Chem. Soc. Jpn. 45, (1972), 2651

4. AVAILABLE SAMPLE MANIPULATIONS STAGES

1. General

Usually the sample is mounted onto the sample alignment stage which allows the user to place the sample into the beam with a precision of $5\mu\text{m}$ (resolution: $1\mu\text{m}$). In Fig. 5 the ranges for vertical and horizontal alignment as well as the maximum dimensions of the sample holders are given. The maximum weight on the sample stage is limited to 10 kg. In case the envelope dimensions of a sophisticated sample station provided by the users are slightly larger than those given in Fig. 5, the user can ask the beamline responsible for a check up of his space requirements. If it does not fit at all to these specifications, user equipment can also be mounted directly onto the optical table, which allows much larger spatial dimensions.

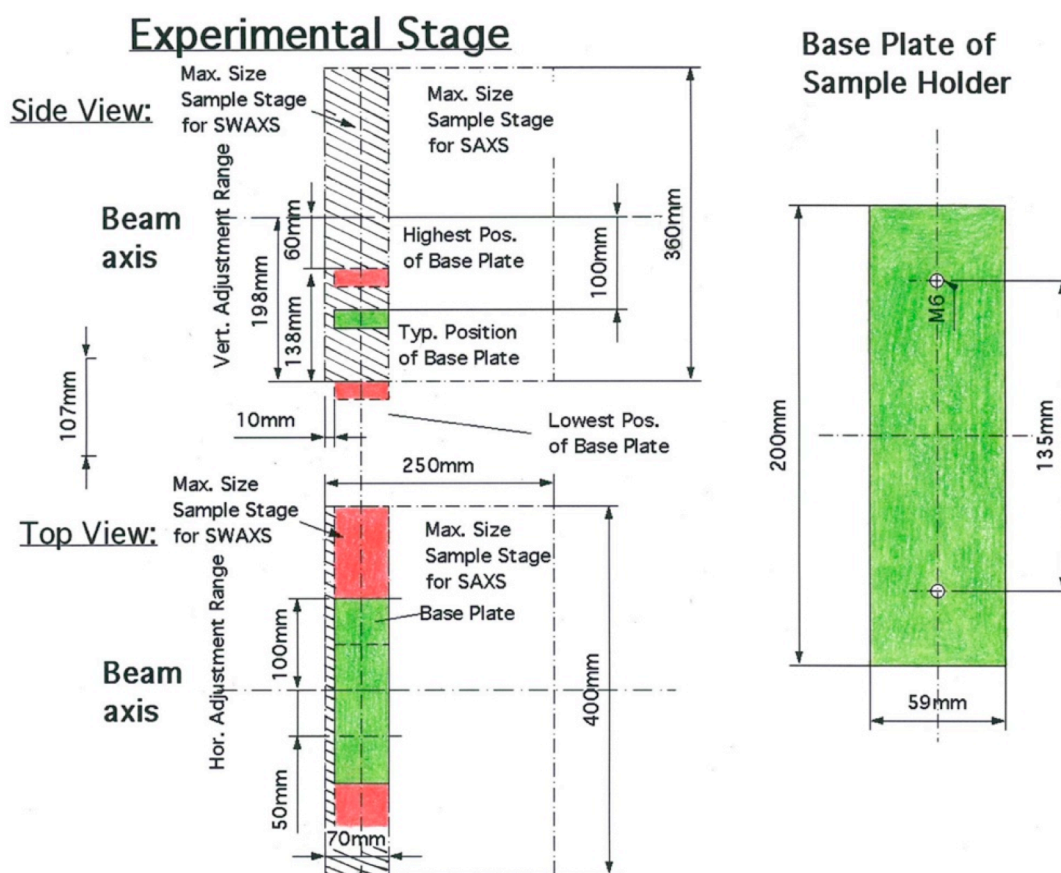


Figure 5. Maximum dimensions and alignment range of the sample holder to be mounted via a base-plate onto the standard alignment stage (left), and dimensions of the base-plate (right).

2. Sample Holders

As standard equipment for liquid samples Paar capillaries (diameter: 1 and 2 mm) are used thermostated with the KPR (Peltier heating/cooling) sample holders (Anton Paar, Graz, Austria). For use in these sample holders flow through capillaries and Gel holders are standard equipment. Temperature scans can be performed with KPR (-30 – 70 °C). Typically the precision and the stability of this systems is 0.1 °C. Additionally thermostats for temperature control or cooling proposes can be used at the beamline (-40 – 200 °C). Helium and Nitrogen gas bottles are available at the beamline, for other gases please contact the beamline responsible.

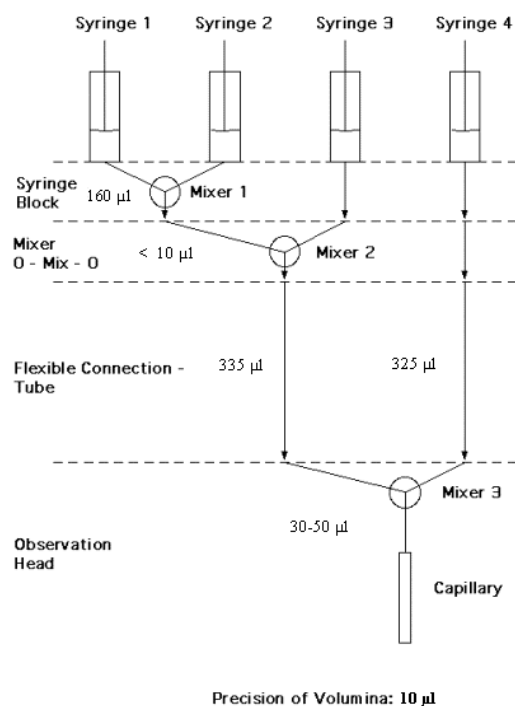
Multiple-sample holders can be mounted onto the standard sample manipulator. At present holders are available for measuring in automatic mode up to 30 solid samples at ambient temperature or up to 4 liquid or gel samples in the temperature range 0 – 95 °C.

3. Online Exhaust System

At the experimental station is available a custom-built fume cover and chemical exhaust system for toxic gases. Thus it is possible to e.g. study in-situ chemical reactions, during which toxic gases might develop.

4. Stopped Flow Apparatus

A commercial stopped flow apparatus (manufactured by Bio-Logic, Paris, France), especially designed for Synchrotron Radiation SAXS investigations of conformation changes of proteins, nucleic acids and macromolecules, is available. The instrument consists of a 4-syringe cell with 3 mixer modules manufactured by Bio-Logic. Each syringe is driven independently from the others by an individual stepping-motor, which allows a high versatility of the mixing sequence (flow-rate, flow duration, sequential mixing). For example, injection sequences using one or up to 4 syringes, unequal filling of syringes, variable mixing ratio, reaction intermediate ageing in three- or four-syringe mode etc.. The solution flow can be entirely software-controlled via stepping motors, and can stop in a fraction of a millisecond.



The software allows the set-up of the shot volumes of each of the 4 syringes in a certain time interval. Up to 20 mixing protocols can be programmed. Additionally macros for the repeated execution of individual frames can be defined. Furthermore, the input and output trigger accessible for user operation can be programmed. In the usual operation modus the start of rapid mixing sequence is triggered from our X-ray data-acquisition system (input trigger).

After the liquids have been rapidly mixed, they are filled within few ms into a 1 mm quartz capillary - situated in the X-ray beam- , which is thermostated with a water bath. Depending on the diffraction power of the sample time resolutions of up to 10 ms can be obtained.

A special set-up is available to allow also the operation without flexible tube connection. This allows for smaller dead volumes.

Figure 6. Sketch of the stop flow system.

The main parameter of the system are:

- Thermostated quartz capillary (1 mm)
- Temperature stability 0.1 °C
- Total sample used per mixing cycle (shot volume): 100 µl
- Maximum 2θ angle of 45°
- Total Volume 8 ml
- Dead volume 550 µl
- Flow rate: 0.045 – 6 ml/s
- Duration of flow 1 ms to 9999 ms/Phase
- Dead time: 1 ms
- Reservoir volume: 10 ml each

Further information can be found at the webpage: <http://www.bio-logic.fr/>

SFM- 20 Stopped flow module

A SFM-20 stopped-flow module (Bio-Logic) is available for single mixing rapid kinetics experiments at the beamline. This system is dedicated to kinetics or conformational studies on biological samples, such as protein folding, enzyme kinetics, water (or solute) transport across the membranes of small vesicles.

The two glass, gas tight syringes (10 ml) are controlled by independent stepper motors; the instrument can be set to obtain completely variable mixing ratio, and can be used to mix solutions of different viscosity.

The SFM-20 is controlled from a PC using the included Bio-Kine software and a USB connected control module. The software provides powerful and simple menus to design mixing sequence and multi-concentration experiments.

This new device has the big advantage of a smaller dead volume with respect to the old device SFM4, which is now dedicated mainly to material sciences, in which the sample volume is not a critical factor.

Specifications:

- *dead time*: 0.6 ms
- *Mixing ratio*: 1:1 to 1:40
- *Priming volume*: 50 µl per syringe
- *Flow rate range*: 0.003 to 5.8 ml/s
- *Mixing ratio*: fully variable from 1:1 to 1:40
- *Minimum injection volume in stopped-flow mode*: 10-30 µl depending on the syringe

5. Grazing Incidence Small Angle X-ray Scattering

Grazing incidence studies on solid samples, thin film samples or Langmuir-Blodgett-films can be performed using a specially designed sample holder, which can be rotated around 2 axes transversal to the beam. Furthermore the sample can be aligned by translating it in both directions transversal to the beam. The precisions are 0.001 deg for the rotations and 5 µm for the translations. Usually the system is set to reflect the beam in the vertical direction.

According to the required protocol and the actual assembly of the rotation stages ω , θ , 2θ and φ scans can be performed.

6. Temperature Gradient Cell

A temperature gradient cell for X-ray scattering investigations on the thermal behaviour of soft matter manybody-systems, such as in gels, dispersions and solutions, has been developed. Depending on the adjustment of the temperature gradient in the sample, on the focus size of the X-ray beam and on the translational scanning precision an averaged thermal resolution of a few thousands of a degree can be achieved.

7. Flow-through Cell

The flow through cell works in a simple manner: Special quartz capillaries (Glas Technik & Konstruktion, Schönwalde/Berlin) of 1.5 mm diameter and wide openings of about 3 mm at each end, can be inserted into the standard Anton Paar sample holder, which allows various temperature treatments (T-range 25-300 or $-30-70$ °C, respectively). Thin tubes are connected directly to the capillary ends and a constant flow is achieved by a peristaltic pump.

8. IR-Laser T-Jump System for Time-Resolved X-ray Scattering on Aqueous Solutions and Dispersions

The Erbium-Glass Laser available at the SAXS-beamline (Dr. Rapp Optoelektronik, Hamburg, Germany) delivers a maximum of 4 J per 2ms pulse with a wavelength of $1.54 \mu\text{m}$ onto the sample. The laser-beam is guided by one prism onto the sample, which is filled in a glass capillary (1 or 2 mm in diameter) and Peltier or electronically thermostated in a metal sample holder (A. Paar, Graz, Austria). With a laser spotsize of maximal 7 mm in diameter a sample-volume of maximal $5.5 \mu\text{l}$ or $22 \mu\text{l}$, respectively, is exposed to the laser-radiation. In a water-solutions/dispersions with an absorption coefficient of $A = 6.5 \text{ cm}^{-1}$ T-jumps up to 20°C are possible.

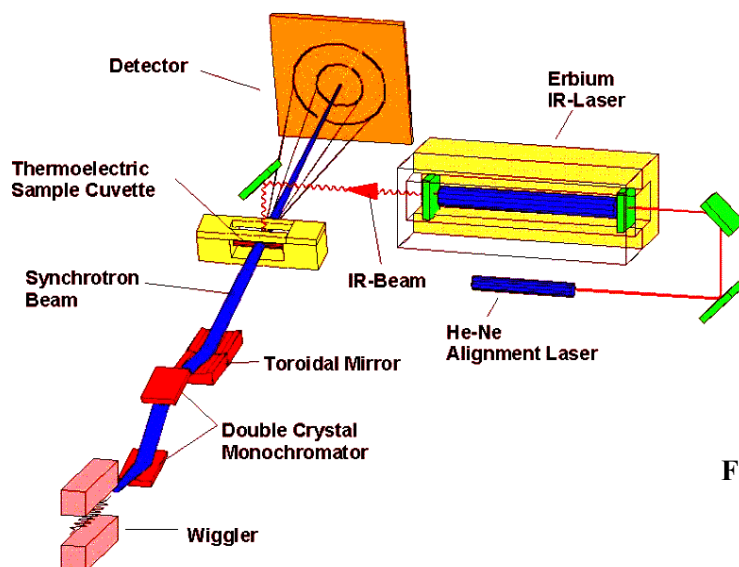


Figure 7. Sketch of the T-jump set-up

9. High Pressure Cell System

SWAXS measurements of samples under pressure can be performed from 1 to 2500 bar, from 0 to 80 °C in the scattering angle region up to 30 degrees, both in the static or time-resolved mode, e.g. p-jump or p-scan, with a time-resolution down to the ms range. Precise pressure scans of any speed within a broad range (e.g. ca. 1.0 bar/s - 50 bar/s in the case of water as pressurising medium, and a typical sample volume) can be performed. Alternatively, dynamic processes can be studied in pressure-jump relaxation experiments with jump amplitudes up to 2.5 kbar/10ms in both directions (pressurising and depressurising jumps).

In most applications diamond windows of 0.75 mm thickness (each) are used. The transmission of one pair (entrance and exit window) is 0.1 at 8 keV, i.e. lower than 0.3, the value for the originally used 1.5 mm thick Be-windows. However the loss in intensity is more than compensated for by the considerably lower background scattering of diamond thus leading to higher q-resolution in the experiments.

The sample thickness can be 0.6-4.0 mm, with a volume of approximately 0.5-3 mm³ completely irradiated by pin-hole collimated (< 1.0 mm diameter) X-rays.

The pressure cell system is flexible and can be built according to the needs of the particular experiment. Normally, a liquid (water, ethanol or octanol) is used as pressurising medium. But in principle, also gaseous media can be employed as well. N₂ has been successfully tested, and measurements in supercritical CO₂ became frequent.

Beside bulk measurements on samples in transmission set-up, also grazing incidence experiments using silicon wafer with highly aligned samples on its surface inserted in the high-pressure cell have been carried out successfully.

10. Oxford Cryostream Cooler

The Cryostream cooler creates a cold environment only a few millimeters from the nozzle position. The temperature and the flow of the nitrogen gas stream is controlled and regulated by a Programmable Temperature Controller based on an 'in stream' heater and a thermo-sensor before it passes out over the sample.

The system has been especially developed for X-ray crystallography to perform diffraction experiments on e.g. shock frozen bio-crystals. However, the programmable temperature controller allows further implication for SAXS-experiments, e.g., rapid temperature drops in solvents. The design of the Cryostream Cooler facilitates:

- Nitrogen stream temperatures from -190 to 100 °C
- Stability of 0.1 °C,
- Refill without any disturbance of the temperature at the sample
- Temperature ramps can easily be carried out remotely controlled with scan rates up to 6 °C/min
- Individual temperature protocols can be cycled
- T-jumps in both directions can be performed by rapid transfer of the sample in a pre-cooled or -heated capillary using a fast syringe driver reaching a minimum temperature of -80 °C. Here, typical scan rates are about 15 °C/sec with a total process time in the order of 10 sec.

Further information can be found at the webpage: <http://www.oxfordcryosystems.co.uk/>

11. In-line Differential Scanning Calorimeter (DSC)

The in-line micro-calorimeter built by the group of Michel Ollivon (CNRS, Paris, France) allows to take simultaneously time-resolved synchrotron X-ray Diffraction as a function of the Temperature (XRDT) and high sensitivity DSC from the same sample.

The microcalorimetry and XRDT scans can be performed at any heating rate comprised between 0.1 and 10 °C/min with a 0.01 °C temperature resolution in the range -30/+130 °C. However, maximum cooling rates are T dependent and 10°C/min rates cannot be sustained below 30°C since cooling efficiency is a temperature dependent process. Microcalorimetry scans can be recorded independently, and also simultaneously, of X-ray patterns. The microcalorimeter head can also be used as a temperature controlled sample-holder for X-ray measurements while not recording a microcalorimetry signal. Isothermal microcalorimetry is also possible when a time dependent thermal event such as meta-stable state relaxation or self-evolving reaction, is expected. The sample capillaries have a diameter of 1.5 mm and are filled over a length of 10 mm.

12. Tension Cell

Together with the external user group Schulze-Bauer/Holzapfel the research team constructed a general-purpose tension cell. This particular cell was designed for *in-situ* tensile testing with the particular feature that the sample could be completely immersed in a solvent (e.g. physiological solution), which is of particular interest for the blood vessel or collagen fiber testing. The sample container can be attached to a thermal bath to control the temperature in the range from 5 to 95 °C. A screw with an appropriate opening for the passage of the X-ray beam can adjust the optical thickness of the sample container continuously and optimize the set-up for different sample geometries.

The fully remote controlled system allows to control not only the fiber extension from 0 to 50 mm, but also it records simultaneously the force signal in the range from 0 to 25 N and as an option the optically determined Video extensometer signal to measure the transversal contraction of the sample.

13. Domed Hot Stage

The domed hot stage (model DHS1100 from Anton Paar, Graz, Austria) for in-situ temperature studies operates in the temperature range from 25 to 1100°C, and gas connections allow sample measurements in vacuum or inert gas to avoid oxidation or other chemical reactions of the sample at high temperatures.

The special, dome-shaped X-ray window is made of graphite, which exhibits an excellent combination of good mechanical properties, high temperature resistance and X-ray transmission. Moreover a custom made cover with Kapton windows has been constructed which allows GISAXS measurements at lower temperatures with reduced window background. This cell allows e.g. for variable humidity environment or inert gas flow. Below 200 °C heater temperature, the instrument can be run without dome. The hot stage is light weight, and can be mounted onto our goniometer cradle for GISAXS measurements on thin films or surfaces, as well as on the XY stage for transmission measurements. A transmission cell for 1.5 mm diameter capillaries has been constructed.

Due to the design of dome, heater and sample fixing, very low angles of incidence can be reached and the following types of X-ray measurements can be carried out: grazing incidence small angle scattering, pole figures, grazing incidence diffraction as well as grazing incidence in-plane diffraction. The main applications for the DHS 1100 are to investigate the temperature dependence of crystalline textures, crystal stress and strain, temperature-induced phase transitions as well as structural properties of thin films.

5. AVAILABLE DETECTORS

1. 2D “Pilatus 3 1M” and “Pilatus 100K” detector systems

The two Pilatus Detector Systems from Dectris Ltd. (Baden, Switzerland) can be used simultaneously for SAXS (Pilatus 3 1M, [1]) and WAXS (Pilatus 100K, [2]) measurements. Both detectors operate in "single photon counting" mode and are based on the CMOS hybrid pixel technology: the X-rays are directly transformed into electric charge, and processed in the CMOS readout chips. This rather new design has no dark current or readout noise, a high dynamic range of 20 bits (~1 million counts), and an excellent point spread function of < 1 pixel. The data are stored in TIF format and can be directly processed with FIT2D [3].

Technical specifications:

	Pilatus3 1M	Pilatus 100K
Area [mm ²]	168.7 x 179.4	83.8 x 33.5
Number of detector modules	2 x 5	1
Pixel size [μm ²]	172 x 172	172 x 172
Number of pixels	981 x 1043 = 1 023 183	487 x 195 = 94 965
Intermodule gap	x: 7 pixels, y: 17 pixels, 7.2 % of total area	-
Dynamic range [Bits]	20 (1:1,048,573)	20 (1:1,048,573)
Counting rate per pixel [incoming X-ray photons/sec]	10 ⁷	> 2 x 10 ⁶
Readout time [ms]	0.95	2.7
Maximum framing rate [Hz]	500	300
Point-spread function [FWHM]	1 pixel	1 pixel
Data formats	Raw data, TIF, EDF, CBF	Raw data, TIF, EDF, CBF
External trigger / gate	5V TTL, 3 different modes	5V TTL, 3 different modes

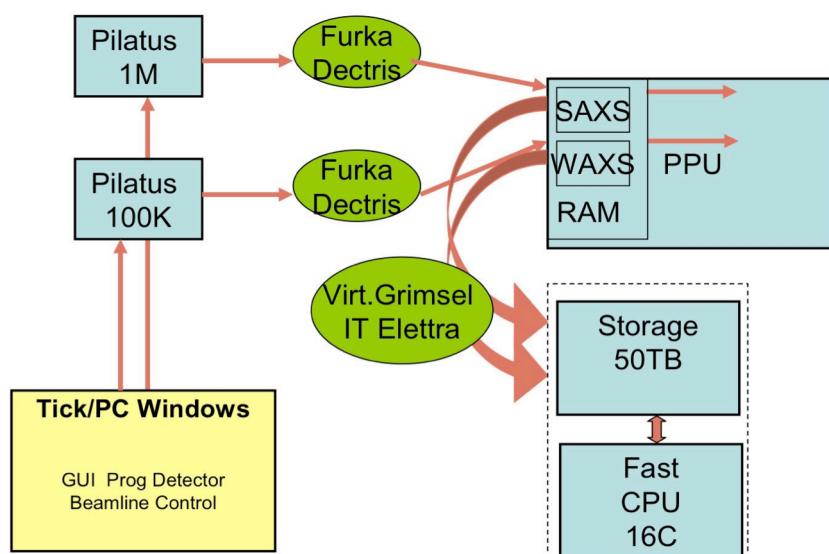
[1] https://www.dectris.com/pilatus3_specifications.html#main_head_navigation

[2] <http://www.dectris.com/sites/pilatus100k.html>

[3] A.P. Hammersley, "Fit2D: an introduction and overview", ESRF Internal Report, ESRF97HA02T, 1997

In order to use the Pilatus Detectors properly and to cope with the high data throughput, we have installed a big 50 TB server at the SAXS beamline. The current system architecture is shown in Fig. 1. The data acquisition is initiated by sending a command from the detector GUI running on the beamline control computer to the detector camserver. The detector acquires single or multiple images, which are automatically transferred from the detector CPU-RAM-disk to the mini PPU RAM-disk by a demon FURKA. The ELETTRA-IT group installed an additional demon which stores the data locally at the PPU and transfers the data to the 50 TB SAXS-server. For online post processing a new tool SAXSDOG running on the fast CPU core of the 50TB SAXS-server was developed by our group together with support

from the SAXS group in Graz in order to integrate the data on the fly, and additional options are foreseen to visualize the data as soon they arrive. These options are currently tested and optimized partly also during user operation of the beamline.



Schematic of the data transfer scheme for the Pilatus SWAXS set-up

2. 2D Image Plate

The Mar300 Image Plate detector with a circular active area of 300mm in diameter is the largest-area detector available to users of the beamline, with a spatial resolution (pixel size) of 150 μ m. This detector has two modes of operation (180mm or 300mm), depending on the desired active area, which result in image sizes of 1200x1200 and 2000x2000, respectively. They are stored in the mar image format (16 bit for compactness, with higher precision extensions for values out of range), and can be processed and converted using the Fit2D program [1]. Typical applications are those that need a large Q-range with high dynamic range (typical values of 10^5), i.e. solution scattering from proteins and nanoparticles, temperature-step scans, slow processes like nanoparticle formation, mesophase formation, etc. The exposure time for the Image Plate is given in seconds, with typical values between 1 and 60. Readout time depends on the chosen active area (for 180mm mode, about 130 seconds; for 300mm mode, about 210 seconds), and therefore it is not suitable for samples where high time resolution is needed. Exposure information, number of images in the series and other information is automatically written to a summary file after each image.

So far the detector cannot be triggered by an external trigger input. Controlling an additional (external) device or experiment can only be done by hardware wiring of the TTL shutter signal.

3. 2D CCD-Camera System

The CCD (Phtotonic Science, GemStar/XIDIS model) is a high resolution and sensitivity camera, providing a high dynamic range (16 bit) and advanced features such as on-camera binning and external triggering. The camera is fully software-controlled using the Image Pro Plus software, and connects to the controlling computer via a Hi-Speed USB interface.

Camera specifications:

Sensitive area	82 x 74 mm (110 mm diagonal)
Image size	2048 x 2048
Pixel size	43 μ m
Dynamic range	16 bit (20 bit in exposure fusion mode)
Binning	x1, x2, x4, x8 (independent X and Y, on-chip and in software)
Interface	external triggering, external gating (3.3V TTL)
Intensifier gain	12 bit (0-4095 levels, approx 200:1 max gain)
Exposure time	<1ms to 30 min
Frame rate	at x1 binning, ~800 ms readout time per frame at x8 binning (on-chip), ~145 ms readout time per frame
Image format	16bit TIFF native (Image Pro Plus allows exporting to other formats as well)

4. 1D Vantec Detector

Two identical one-dimensional high-count rate capable Vantec-1 Detectors from BrukerAXS Inc. are available. They have each an active area of 50 x 16 mm, and can be used together mounted in-line to increase the active area. They have a spatial resolution of about 50 μ m, which is smaller than the resolution obtained by the presently used Gabriel Type Gas detectors. Moreover its new gas amplification principle based on the Microgap technology [1] allows much higher count rates compared to the old system. Now the main limitation is the data acquisition system with its maximum integral count rate of about 1 MHz. In the present data acquisition system HCI (Hecus X-ray Systems, Graz, Austria) the detector has the following performance:

- Minimal time resolution: 11 μ s
- Maximum No. of frames: 512 (depending on the no. of channels)
- Maximum integral count rate: 1 MHz

5. 1D Gabriel-type Detector System

Two 1D Gabriel-type detectors are available, which feature both 1024 pixels. The smaller detector has an entrance window size of 8 x 100 mm, and an active length of 86.1 mm with a resolution of 0.135 mm/channel. The larger detector has an entrance window size of 10 x 150 mm, and an active length of 134 mm with a resolution of 0.159 mm/channel. They can be used simultaneously, and are run with the data acquisition system HCI (Hecus X-ray Systems, Graz, Austria). This detector system has the following performance:

- Minimal time resolution: 11 microsec
- Maximum No. of frames: 512
- Maximum integral count rate: 40 kHz

6. OFFLINE SAXS SUPPORT LABORATORY

The laboratory consists of two rooms: the chemistry lab, which has been renewed during 2013, serves mainly for sample preparation and analysis for both, in house research and external SAXS user groups. In the X-ray laboratory is available a SWAXS camera for simultaneous small and wide-angle scattering (Hecus X-ray Systems, Graz, Austria), which allows on-site testing of samples before moving on to the SR beamline.



Figure 4. View of the Chemistry laboratory (left) and X-Ray laboratory (right).

Standard glassware, syringes and needles of different sizes, μ -pipettes (p10 - p100 - p200 - p1000), as well as some standard chemical reagents (e.g., chloroform, ethanol, methanol) and deionized water (milli-RO and ultrapure milli-Q water) is available.

The chemistry lab is further equipped with:

- micro centrifuge (max. 13200 rpm; model 5415D from Eppendorf, Hamburg, Germany)
- Chemical fume hood, equipped with a carbon filter for general organic solvents (model GS8000 from Strola, Italy)
- vacuum drying oven (min. pressure 1 mbar; max. T: 200 °C, precision +/- 0.4 °C; Binder WTB, Tuttlingen, Germany)
- balance (min.-max.: 0.001 - 220 g; model 770 from Kern & Sohn, Balingen, Germany)
- Magnetic stirrer with heating plate and thermometer, temp max 260 °C
- vortex for microtubes (model REAX from Heidolph, Schwabach, Germany)
- two water baths :
 - Unistat CC, freely programmable in the range from -30 to 100°C (Huber, Offenburg, Germany);
 - Lauda M3, available for heating only (Lauda-Könighofen, Germany)
- ultrasonic bath with water heater (VWR International, Milano, Italy)
- Ultrasonic processor equipped with a 3 mm probe (Sonics VCX130, SY-LAB Geräte GmbH, Germany)
- HPLC pump, Pharmacia LKB; working range, 0,01-9,99 ml/min, 0,1-40MPa
- HPLC pump, Gilson 307; working range, 0,01- 5 ml/min, 0,1-60MPa
- three-syringe pump, low pressure; flow rate range, 1 μ l/hr – 2120 ml/hr (TSE Systems GmbH, Germany)

- four-syringe pumps, high pressure: P max ~ 60 bar (Harvard Apparatus, Holliston, Massachusetts, USA)
- three high pressure infusion modules: P max ~ 690 bar (Teledyne Isco, Lincoln, NE, USA)
- fridge (+ 4°C) and freezer (- 20 °C)
- Ultra low freezer (-80°C) (KW Apparacchi Scientifici, Italy)
- **UV-VIS spectrometer:** Besides a standard 10 mm path length cuvette holder, the UV-VIS spectrophotometer (Cary 60, Agilent Technologies) is equipped with a Slide-Mounted External Specular Reflectance accessory which allows specular reflectance measurements to be made at a fixed angle of 30°. This accessory is suitable for studies of the film thickness on metallic substrates and measurements of epitaxial film thickness. Interchangeable masks for examining small samples or small areas of large samples are provided (3 mm, 6 mm and 13 mm diameters).
A dedicated cuvette for UV-Vis measurements in combination with the stop-flow apparatus, to study the kinetics of fast reactions, is now available in the Chemistry Lab. A couple of optic fibers (Ocean Optics type QP600-1-XSR, wavelength range 180-900nm) can be connected to the stop-flow observation head and to the Agilent Cary 60 UV-Vis spectrophotometer for data collection.
The instrument can also be used for *in situ* measurement on liquid samples, through two optic fibers: a Torlon fiber probe, diameter 10 mm, for aggressive solutions, and a μ probe, 3.5 mm diameter, 10 mm fixed path length, for smaller volumes (approx. 500 μ l).
Specifications: double beam Czerny-Turner monochromator, wavelength range 190–1100 nm, fixed spectral bandwidth 1.5 nm, minimum scan rates of 24,000 nm/min (full wavelength scan time <3s), maximum measurement rate 80 data points/sec
- **FT-IR spectrometer** (Alpha-T, Bruker Optics): equipped with the following modules for the analysis of different types of samples:
 - standard sample holder for transmission measurements,
 - single reflection diamond ATR sampling module for powder and solid analysis, which, due to the wide free working area around the crystal (approx. 350°), allows the analysis of large samples. Specifications: One-reflection Diamond crystal, spectral range: 375 - 7,500 cm^{-1} , working distance (max. sample height): >20 mm
 - sampling module for contactless reflection measurements in front of the spectrometer. Specifications: spectral range: 375-7.500 cm^{-1} , measurement spot: 6 mm diameter, appr. 15 mm in front of the spectrometer

User Contributions

Life Sciences

THE INTERNAL NANOSTRUCTURE OF CUBOSOMES AND HEXOSOMES IS MAINTAINED IN HUMAN PLASMA

I. D. M. Azmi¹, J. Østergaard¹, H. Amenitsch², S. Stürup¹, B. Gammelgaard¹, A. Urtti^{3,4}, S. M. Moghimi⁵, A. Yaghmur¹

- 1.) Department of Pharmacy, Faculty of Health and Medical Sciences, University of Copenhagen, Universitetsparken 2, DK-2100 Copenhagen, Denmark
- 2.) Institute of Inorganic Chemistry, Graz University of Technology, Stremayerg. 6/IV, 8010 Graz, Austria
- 3.) Centre for Drug Research, University of Helsinki, FIN-00014 Helsinki, Finland
- 4.) School of Pharmacy, University of Eastern Finland, FIN-70211 Kuopio, Finland
- 5.) Nanomedicine Laboratory, Centre for Pharmaceutical Nanotechnology and Nanotoxicology, University of Copenhagen, DK-2100 Copenhagen, Denmark

Lyotropic liquid crystalline particles with well-ordered internal nanostructures are promising nanocarrier candidates in cancer therapy. Among these soft nanoparticulate systems, cubosomes (an aqueous dispersion with internal bicontinuous cubic (V_2) phase) and hexosomes (an aqueous dispersion with internal H_2 phase) are attractive nanocarriers for delivery of anticancer drugs [1-4]. They displayed nanostructures closely related to those observed in biological membranes and are tailored for solubilizing amphiphilic, hydrophobic, and hydrophilic drugs in their highly ordered self-assembled interiors. A prerequisite for successful development of such formulations is their stability and integrity after administration. Here, we have addressed the possible use of synchrotron small angle X-ray scattering (SAXS) to examine the structural events occurring upon prolonged direct contact of these lyotropic liquid crystalline colloidal dispersions with human plasma.

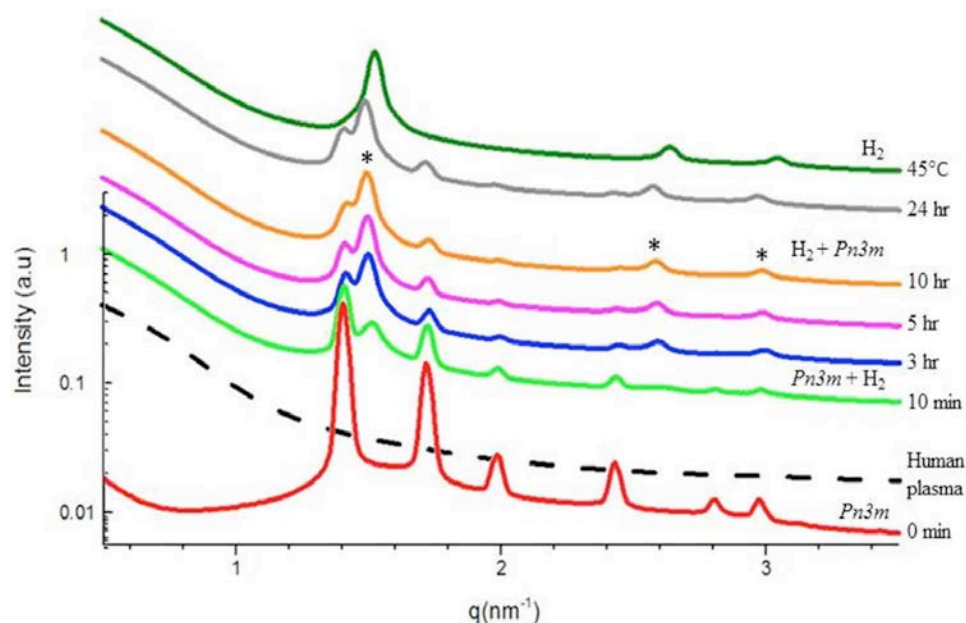


Figure 1. SAXS pattern at 37°C and 45°C for an aqueous dispersion based on phytantriol (PHYT) and F127 (10:1, v/v) mixed with human plasma at a volume ratio of 1:1. The SAXS measurements were performed at different incubation time up to 24hr. The reflections of the identified internal inverted type hexagonal (H_2) phase were denoted by the symbol (*). The scattering intensity was shifted vertically for better visibility

In this work, the dispersed samples comprised of PHYT were mixed with human plasma at a volume ratio of 1:1 and SAXS experiments were performed at different incubation times over a period of 24 hr. Interestingly, after 10 min of incubation, a weak peak at a q value of about 0.15 \AA^{-1} was detected, which indicated the formation of an additional phase. As further seen,

the cubic $Pn3m$ phase started to vanish after 3 hr of incubation; whereas the newly formed prominent H_2 phase evolved and its three characteristic reflections (10), (11) and (20) (marked with *), were clearly visible after 10 hr of incubation (Figure 1). The co-existence of the internal biphasic nanostructure (an inverted-type bicontinuous cubic phase of the symmetry $Pn3m$, denoted by Q^{224} with an inverted type hexagonal (H_2) phase having a lattice parameter of about 42.3 Å) was still observed after 24 hr of incubation. Both phases were stable and there was no indication to any significant effect of increasing the incubation time from 10 min to 24 hr on their structures: increasing the incubation time did not significantly affect the lattice parameters of both phases. The appearance of the H_2 phase after a certain time of incubation is most likely attributed to the interaction of the submicron sized particles with human plasma components. A slight increase in temperature to 45 °C led to a complete transition to a neat internal H_2 phase (formation of hexosomes). The reflections of the H_2 phase (marked by *) were slightly shifted to higher q values at 45 °C leading to a decrease in the lattice parameter from 42.3 Å to 41.3 Å due to the dehydration of the hydrophilic headgroup of phytantriol and the simultaneous influence of increasing temperature on its hydrophobic tail.

This study reveals the possible utilization of synchrotron SAXS for investigating the nanostructural events occurring upon the direct exposure of non-lamellar liquid crystalline particles to human plasma. The obtained results suggest that the investigated biological fluid human plasma affects the internal nanostructure of PHYT-based nanostructured aqueous dispersions, which induced the internal phase transition without disintegrating the dispersed particles to structureless forms.

References:

- [1] A. Yagmur, O. Glatter; Characterization and potential applications of nanostructured aqueous dispersions; *Adv. Colloid Interface Sci.* 147-148, 333-342 (2009)
- [2] C. Nilsson, B. Barrios-Lopez, A. Kallinen et al.; SPECT/CT imaging of radiolabeled cubosomes and hexosomes for potential theranostic applications; *Biomaterials* 34, 8491-8503 (2013)
- [3] I. D. Mat Azmi, L. Wu, P. P. Wibroe et al.; Modulatory effect of human plasma on the internal nanostructure and size characteristics of liquid crystalline nanocarriers; *Langmuir* 31, 5042–5049 (2015)
- [4] N.. M. Lakshmi, P. R. Yalavarthi, H. C. Vadlamudi, J. Thanniru, G. Yaga, K. Haritha; Cubosomes as targeted drug delivery systems - a biopharmaceutical approach; *Curr. drug discov. technol.* 11, 181-188 (2014)

POLYMORPHIC BEHAVIOUR OF PH RESPONSIVE DRUG NANOCARRIERS

A. Búcsi, L. Hubčík, F. Devínsky and D. Uhríková

Faculty of Pharmacy, Comenius University in Bratislava, Odbojárov 10, 832 32 Bratislava, Slovakia

Monoolein or glycerol monooleate (GMO) is a biodegradable polar lipid that has no marked toxic effects. In excess of water monoolein forms a bicontinuous cubic phase of $Pn3m$ symmetry that shows good stability in a wide range of temperatures [1]. The $Pn3m$ cubic phase of monoolein is formed by a curved bicontinuous lipid membrane extending in three dimensions, separating two congruent networks of water channels. Due to its unique structure and high stability in excess of water the $Pn3m$ cubic phase of monoolein is widely studied as a delivery system for drugs of various polarities [2]. The encapsulation and release of drugs from cubic phases can be controlled by the regulation of the diameter of the water channels by the addition of amphiphilic substances that incorporate into the lipid bilayer and change its curvature [3, 4].

N-alkyl-N,N-dimethylamine-N-oxides, C_nNO ($n=12-18$, even, n is the number of carbons in the alkyl substituent), are non-toxic surfactants widely used (mainly $C12NO$) in cosmetic and pharmaceutical formulations. The C_nNO molecules are zwitterionic at neutral values of pH. A strong polar N-O bond and a high electron density on oxygen allow protonization of C_nNO in acidic solution, and the surfactant becomes cationic C_nN^+OH .

The microstructure of both GMO and mixtures of $C_nNO+GMO+DNA$ in excess of water were examined using synchrotron small angle X-ray scattering (SAXS beamline) at the Elettra Sinchrotrone Trieste. Complexes were prepared in the range of molar ratios $0 < C_nNO:GMO \leq 0.4$, mixing the lipid and C_nNO in an organic solvent. The solvent was evaporated by a stream of nitrogen, and mixtures were dried under vacuum. A solution of single stranded DNA was used for the complexes preparation. pH was modulated in the range 4 – 7.

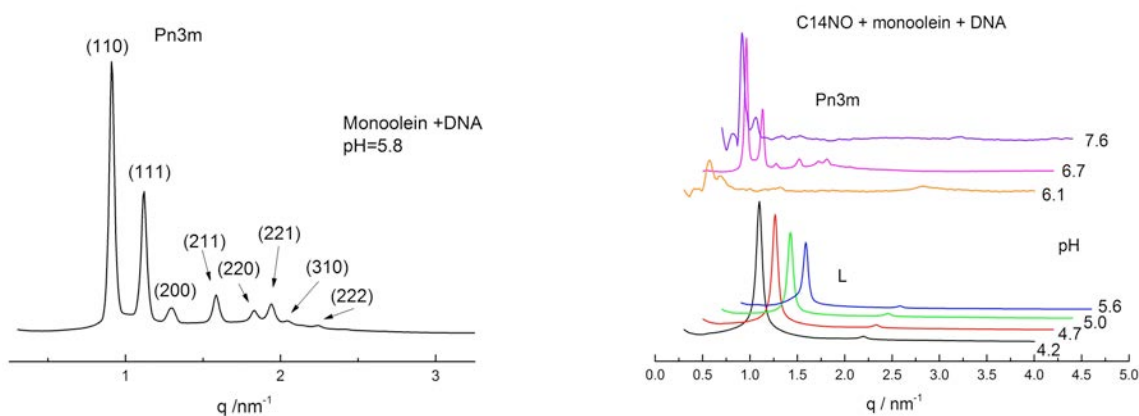


Figure 1. Left: **a)** SAXS pattern of monoolein (GMO) with DNA. **b)** Cubic to lamellar phase transition induced by pH in $C14NO + GMO + DNA$ at $C14NO:GMO=0.2$ mol/mol and $20^\circ C$

Fig. 1a shows SAXS pattern of GMO +DNA typical for the $Pn3m$ cubic phase with peaks at positions $\sqrt{2}$, $\sqrt{3}$, $\sqrt{4}$, $\sqrt{6}$, $\sqrt{8}$, $\sqrt{9}$, $\sqrt{10}$ and $\sqrt{12}$. The lattice parameter $a = 9.7$ nm (at $20^\circ C$) was determined as a reciprocal value of the slope of linear function $q/2\pi$ vs. $(h^2+k^2+l^2)^{1/2}$, where hkl are Miller indices. Our experimental data have shown that at neutral pH, the $Pn3m$ cubic

phase is preserved in CnNO+GMO+DNA complexes prepared at molar ratios $\text{CnNO:GMO} \leq 0.3$. CnNO modulates the lattice parameter of the $Pn3m$ cubic phase. The lattice parameter reaches values up to $a \sim 17$ nm in complexes prepared at a molar ratio $\text{CnNO:GMO} = 0.3$. At higher CnNO content ($\text{CnNO:GMO} = 0.4$ mol/mol) the cubic phase collapses into a lamellar phase with the repeat distance $d \sim 6$ nm.

Fig. 1b shows an example of pH induced polymorphism observed in the studied system. At $\text{pH} > 6$, we observed structures of three-dimensional symmetry. However due to the additive the lattice parameter a increased significantly. In C14NO+GMO+DNA we detected the $Pn3m$ cubic phase with the lattice parameter changing from 15.6 nm to 17.6 nm with pH increasing from 6.1 to 7.2, respectively. Scattering patterns have shown not well defined structures for complexes prepared in solutions at $\text{pH} \sim 6$. At acidic solutions with $\text{pH} < 6$, CnNO+GMO+DNA forms a lamellar phase with the repeat distance d modulated by pH. The repeat distance d decreased from 6.4 nm to 5.7 nm with pH changing in the range 5.6 - 4.2 for C14NO+GMO+DNA complexes. UV-VIS measurements proved the capability of the system to bind DNA. In acidic solutions, the fraction of bound DNA represented ~ 98 % of total the DNA, and $\sim 45 - 50$ % when complexes prepared in pH range 6 - 7.5. The observed structural changes, from cubic to lamellar phase follow the process of CnNO protonization modulated through pH of the bulk solution. Both the CnNO protonization and consequent DNA binding dramatically affect the curvature of the GMO lipid network.

Our experiments have shown that molecules of CnNO increase the lattice parameter of $Pn3m$ cubic phase of monoolein. This increase is caused mainly by changes of the diameter of the water channels and less by changes in the thickness of the lipid bilayer. Both the fraction of DNA bound in CnNO+GMO+DNA complexes and the cubic to lamellar phase transition can be modulated through the pH.

Acknowledgement: The Authors thank the SAXS beamline staff for their assistance and help with the experiments. The research leading to these results has received funding from the European Community's Seventh Framework Programme (FP7/2007-2013) under grant agreement n° 312284, and support from MŠ SR VEGA grant 1/1224/12

References:

- [1] K. Larsson, *Curr. Opin. Colloid Interface Sci.* **5**, 64-69 (2000)
- [2] J. C. Shah, Y. Sadhale, and D. M. Chilukuri, *Adv. Drug Deliv. Rev.* **47**, 229-250 (2001)
- [3] B. Angelov, A. Angelova, V. M. Garamus, G. Lebas, S. Lesieur, M. Ollivon, S. S. Funari, R. Willumeit, and P. Couvreur, *J. Am. Chem. Soc.* **129**, 13474-13479 (2007)
- [4] B. Angelov, A. Angelova, U. Vainio, V. M. Garamus, S. Lesieur, R. Willumeit, and P. Couvreur, *Langmuir* **25**, 3734-3742 (2009)

ROLE OF CHOLESTEROL ON THE TRANSFECTION BARRIERS OF CATIONIC LIPID/DNA COMPLEXES

G. Caracciolo¹, D. Pozzi¹ and H. Amenitsch²

1.) Department of Molecular Medicine, 'Sapienza' University of Rome, Viale Regina Elena 291, 00161 Rome, Italy

2.) Institute of Inorganic Chemistry, Graz University of Technology, Stremayerg. 6/IV, 8010 Graz, Austria

Nowadays, cationic liposomes (CLs), are among the most promising candidates for in vivo and ex vivo delivery of nucleic acids [1,2]. The low transfection efficiency (TE) of CL-DNA complexes (lipoplexes) is due to the multiple intracellular barriers that must be overcome to deliver exogenous DNA into the cell nucleus of the host cell and enable its expression. It has been suggested that a critical factor in lipid mediated gene transfection is the structural and phase evolution of lipoplexes upon interaction with plasma membrane. Lipoplexes structure rearrangement could result in important consequences on the DNA escape process and release into the cytoplasm. This factor together with liposomes cellular uptake mechanism and trafficking to lysosomes are critical for efficient delivery. Recently, it has been suggested that internalization pathways of lipoplexes are cholesterol-dependent and that cholesterol plays a major role on their intracellular trafficking [3]. The incorporation of cholesterol and cholesterol-derivatives in the lipoplex formulation has been shown to boost TE [4], but the precise reason why this occurs remains to be understood. To provide insights into the role of cholesterol on lipoplex cell transfection, here we investigated into the transfection mechanisms of cholesterol-containing lipoplexes. To this end, we used CLs made of the cationic 1,2-dioleoyl-3-trimethylammonium-propane (DOTAP) and the neutral dioleoylphosphocholine (DOPC), and we gradually replaced DOPC molecules by cholesterol. Furthermore, we investigated their interaction with plasma membrane by mixing CLs with mimicking anionic membrane models. Employing structural studies by synchrotron small angle X-ray scattering (SAXS), laser scanning confocal microscopy (LSCM), and TE measurements, we were able to elucidate the relation between efficiency and the transfection mechanism of cholesterol-containing lipoplexes.

To rationalize the TE behaviour of cholesterol-containing lipoplexes, we first characterized the phase organization of DOTAP–DOPC–cholesterol/DNA lipoplexes at the nanoscale. Figure 1(a) shows two representative synchrotron SAXS patterns of DOTAP–DOPC–cholesterol/DNA ($X_{\text{chol}} = 0$ and 0.5) at $\rho = 3$. The sharp peaks at q_{001} are due to alternating lipid bilayer–DNA–monolayer multilamellar structure. The broad peak marked by an arrow results from one-dimensional (1D) ordering of the DNA sandwiched between the lipid bilayers. We observed no Bragg peaks due to cholesterol monohydrate. Figures 1(b) and 1(c) show the variation of d and d_{DNA} as a function of the molar fraction of cholesterol, X_{chol} . Reduction in the DNA interhelical spacing are due to the reduction in membrane area where DNA condensation occurs (headgroup area of cholesterol is definitely smaller than that of DOPC). We observed then, that the interlamellar periodicity d decreases with increasing X_{chol} (Figure 1(b)), due to the reduced hydration layer of cholesterol molecules. When DOPC is replaced by cholesterol, the hydration repulsion layer is reduced, probably resulting in enhanced fusion of lipoplexes cationic membranes with anionic cellular membranes. Moreover we simulated the interactions of lipoplexes with the cellular membranes. We examined the structure of mixtures of the lipoplexes with negatively charged MM that have frequently been used as model systems of bio-membranes. It should be underlined that anionic lipid vesicles lack of many relevant elements of biological membranes such as proteins and receptors and are orders of magnitude smaller of cells. Synchrotron SAXS showed that, in 1:1 molar ratio mixtures with MM, DOTAP-DOPC/DNA lipoplexes retained their lamellar structure. On the other hand, DOTAP–cholesterol/DNA lipoplexes underwent a lamellar to hexagonal phase

transition (Figure 2). A correlation between membrane fusion and a lamellar–nonlamellar phase change has long been disputed in the literature and has been well explained with respect to both energetics and molecular mechanism. Hence, DOTAP–cholesterol/DNA lipoplexes are likely to easily fuse with cellular membranes, and, as a result of lipid mixing, the resultant aggregates should exhibit extensive phase coexistence and heterogeneity, thereby facilitating DNA release (Figures 4(b) and 4(c)) and leading to superior transfection efficiency [5].

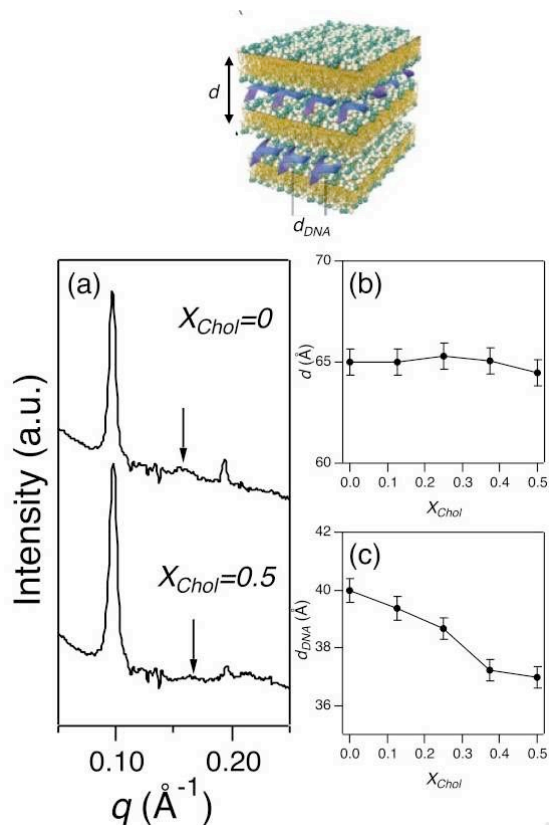


Figure 1. (a) Representative synchrotron SAXS patterns of lipoplexes. Lamellar periodicity (b) and DNA-DNA distance (c) of cholesterol-containing lipoplexes. At the top, a schematic of the multilamellar structure of lipoplexes is shown

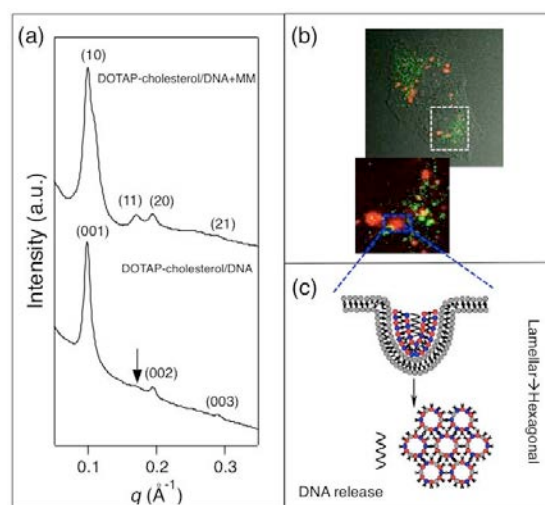


Figure 2. (a) Representative synchrotron SAXS patterns of DOTAP– cholesterol/DNA lipoplexes both plain (bottom scan) and in 1:1 molar ratio mixtures with MM showing a lamellar to hexagonal phase transition (upper scan). (b) Confocal images showing intracellular aspect of DOTAP– cholesterol/DNA lipoplexes after interaction with cellular membranes (irregular red patches). (c) Scheme describing the mechanism of interaction between DOTAP– cholesterol/DNA lamellar lipoplexes and MM (gray). MM molecules diffuse within DOTAP–cholesterol/DNA membranes pro- mote a lamellar-to-hexagonal phase transition and DNA is released

We have shown that cholesterol-containing lipoplexes can enter cells through different endocytosis pathways and largely avoid lysosomal degradation. Activation of multiple endocytic pathways and efficient endosomal escape may therefore explain the efficiency boost of cholesterol- containing lipoplexes. Synchrotron SAXS also showed that cholesterol-containing lipoplexes exhibit a lamellar-nonlamellar phase transition in mixture with biomembrane mimicking lipid formulations. Aside from being a proof of concept, this observation might explain the visualized abundant DNA release and, in turn, the superior transfection efficiency. These studies highlight the enrichment in cholesterol as a decisive factor for transfection. The intracellular mechanisms of action of cholesterol-containing

nanocarriers should be considered for the rational design of systems with superior delivery efficiency.

References:

- [1] C. R. Dass, Lipoplex-mediated delivery of nucleic acids: factors affecting in vivo transfection; *J. Mol. Med.* **82**, 579-591 (2004)
- [2] X. Guo and L. Huang, Recent Advances in Non-viral Vectors for Gene Delivery; *Acc. Chem. Res.* **45**, 971-979 (2012)
- [3] J. Rejman, V. Oberle, I. Zuhorn, and D. Hoekstra, Size-dependent internalization of particles via the pathways of clathrin- and caveolae-mediated endocytosis; *Biochem. J.* **377**, 159-169 (2004)
- [4] L. Xu and T. J. Anchordoquy, Effect of cholesterol nanodomains on the targeting of lipid-based gene delivery in cultured cells *Mol. Pharm.* **7**, 1311-1317 (2010)
- [5] D. Pozzi, F. Cardarelli, F. Salomone, C. Marchini, H. Amenitsch, G. La Barbera and Giulio Caracciolo, Role of cholesterol on the transfection barriers of cationic lipid/DNA complexes; *Appl. Phys. Lett.* **105**, 073701 (2014)

KILLING CANCER CELLS WITH NANOTECHNOLOGY: NOVEL POLY(I:C) LOADED LIPOSOME-SILICA HYBRID NANOPARTICLES

G. Caracciolo¹, D. Pozzi¹, V. Colapicchioni², S. Palchetti¹ and H. Amenitsch³

- 1.) Department of Molecular Medicine, 'Sapienza' University of Rome, Viale Regina Elena 291, 00161 Rome, Italy
- 2.) Center for Life Nano Science@Sapienza, Istituto Italiano di Tecnologia, Viale Regina Elena 291, 00161 Roma, Italy
- 3.) Institute of Inorganic Chemistry, Graz University of Technology, Stremayerg. 6/IV, 8010 Graz, Austria

Polyinosinic-polycytidylic acid (poly(I:C)), a synthetic double-stranded RNA (dsRNA) analog, has been studied for several years in view of its application in cancer immunotherapy. To date, it is well recognized that poly(I:C) is able to change cancer microenvironment and suppress tumor growth by innate and adaptive immune system activation [1]. Moreover, it has been demonstrated that poly(I:C) directly induces programmed cell death in different cancer cells. However, despite the adjuvant potential of poly(I:C) being widely known, its clinical application may be a double-edged sword [2]. This synthetic dsRNA suffers from being poorly immunogenic and toxic when administered systematically and in high dosages. Nevertheless, the combination of poly(I:C) with an adequate delivery system seems to be a promising strategy to lower the drug dosage required and to improve its therapeutic index by enhancing its efficacy and/or increasing its tolerability in the body. In this work, we have synthesized and thoroughly characterized a core-shell liposome-silica hybrid (LSH) nanoparticle (NP) made of a silica core surrounded by a multicomponent cationic lipid bilayer. Mesoporous silica NPs were employed due to their peculiar ability to enhance lateral bilayer fluidity compared with that of either liposomes or supported lipid bilayers formed on non-porous cores. Giving the superiority of multicomponent (MC) liposome in drug and gene delivery, the lipid shell was made by a four-component lipid system constituted by cationic lipids 1,2-dioleoyl-3-trimethylammonium-propane (DOTAP) and (3 β -[N-(N',N'-dimethylaminoethane)-carbamoyl]-cholesterol (DC-Chol) and neutral helper lipids dioleoylphosphocholine (DOPC) and dioleoylphosphatidylethanolamine (DOPE). In view of *in vivo* application, a NP variant with polyethylenglycole (PEG) 2k grafted to the lipid shell was also designed (Fig. 1).

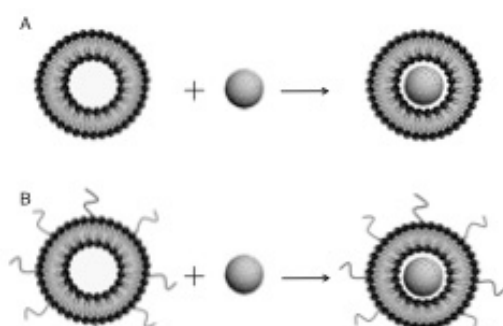


Figure 1. Schematic sketch describing the formation of liposome-silica hybrid (LSH) nanoparticles (NPs). (A) Multicomponent cationic liposomes were incubated with mesoporous silica nanoparticles. (B) Employment of pegylated liposomes results in the formation of pegylated LSH NPs

To promote efficient interaction with silica NPs membrane unilamellarity of cationic vesicles is required. The technique of choice to test unilamellarity of liposomes in diluted solution is high-resolution synchrotron small angle X-ray scattering (SAXS). SAXS experiments were performed at the Austrian SAXS beam line of the synchrotron light source ELETTRA (Trieste, Italy).

Fig. 2 shows the synchrotron SAXS curves of both bare and pegylated MC CLs. As evident, MC lipid vesicles (Fig. 2, bottom panel) exhibited only pure diffuse scattering, which is

typical of uncorrelated bilayers. The scattered intensity was therefore fitted with one of the simplest lipid bilayer models. The SAXS pattern of pegylated liposomes (Fig. 2, top panel) revealed a slight deviation from the form factor at low q ($q < 1 \text{ nm}^{-1}$). This observation is in line with previous studies showing that pegylated lipids can form phase-separated lamellae within lipid membranes. In Table 1 are reported the structural parameters of unpegylated and pegylated MC cationic liposomes.

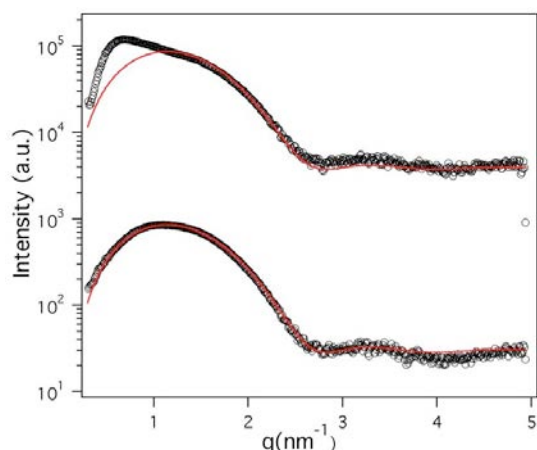


Figure 2. Bottom panel. Synchrotron SAXS pattern of unpegylated multicomponent cationic liposomes. Top panel. Synchrotron SAXS pattern of pegylated multicomponent cationic liposomes

Table 1. Structural parameters of unpegylated and pegylated MC cationic liposomes

	Unpegylated MC liposomes	Pegylated MC liposomes
d_B (nm)	4.42 ± 0.13	4.40 ± 0.15
d_C (nm)	0.87 ± 0.07	0.91 ± 0.09

To the best of our knowledge this is the first time that a liposome-silica hybrid system is employed as poly(I:C) delivery system and adjuvant. The anti-cancer activity of this core-shell hybrid nanoplatfrom was tested on the highly aggressive and androgen-independent prostate cancer cell line PC3, on which free poly(I:C) has only weak, if any, effect. Further validation was provided in MCF7 human breast adenocarcinoma cell line that is extensively used in cancer research. According to World Cancer Research Fund International (www.wcrf.org), prostate cancer and breast cancer are the fourth and the second most common cancers respectively, accounting for nearly 20 percent of all cancers. Notably, poly(I:C)-loaded LSH NPs were found to be highly efficient in eliminating cancer cells. At the lowest poly(I:C) dose, negative complexes were able to induce apoptosis in 40% of cancer cells. Remarkably, when cancer cells were treated with bare liposomes, a similar level of apoptosis required ten-fold the amount of poly(I:C).¹⁷ Our results thus suggest that LSH NPs represent excellent candidates for both in vitro and in vivo drug delivery applications [4].

References:

- [1] A. I. Chin, A. K. Miyahira, A. Covarrubias, J. Teague, B. Guo, P. W. Dempsey and G. Cheng, Toll-like Receptor 3-Mediated Suppression of TRAMP Prostate Cancer Shows the Critical Role of Type I Interferons in Tumor Immune Surveillance; *Cancer Research* **70**, 2595-2603 (2010)
- [2] K. Tewari, B. J. Flynn, S. B. Boscardin, K. Kastenmueller, A. M. Salazar, C. A. Anderson, V. Soundarapandian, A. Ahumada, T. Keler, S. L. Hoffman, M. C. Nussenzweig, R. M. Steinman and R. A. Seder, Chemical cross-linking of HIV-1 Env for direct TLR7/8 ligand conjugation compromises recognition of conserved antigenic determinants; *Vaccine* **28**, 7256-7266 (2010)
- [3] G. Pabst, M. Rappolt, H. Amenitsch and P. Lagner, Structural information from multilamellar liposomes at full hydration: full q -range fitting with high quality x-ray data; *Physical Review E* **62**, 4000 (2000)
- [4] V. Colapicchioni, S. Palchetti, D. Pozzi, E. S. Marini, A. Riccioli, E. Ziparo, M. Papi, H. Amenitsch and G. Caracciolo, Killing cancer cells with nanotechnology: novel poly(I:C) loaded liposome-silica hybrid nanoparticles; *J. Mat. Chem. B*, under review

SURFACE PASSIVATION IMPROVES THE SYNTHESIS OF HIGHLY STABLE AND SPECIFIC DNA-FUNCTIONALIZED GOLD NANOPARTICLES WITH VARIABLE DNA DENSITY

J. Deka¹, R. Měch², L. Ianeselli¹, H. Amenitsch³, F. Cacho-Nerin^{3,4}, P. Parisse⁵ and L. Casalis^{1,5}

- 1.) Elettra-Sincrotrone Trieste, s.s. 14 km 163.5 in Area Science Park, 34149 Basovizza, Trieste, ITALY
- 2) Institute of Physical Engineering, Brno University of Technology, Technická 2, 61669 Brno, Czech Republic
- 3) Graz University of Technology, Institute for Inorganic Chemistry, Stremayrgasse 9/V, A-8010 Graz, Austria
- 4) Diamond Light Source, Diamond House, Harwell Science and Innovation Campus, OX11 0DE Didcot, UK
- 5) INSTM – ST Unit, s.s. 14 km 163.5 in Area Science Park, 34149 Basovizza, Trieste, ITALY

Gold nanoparticles (AuNPs) show unique (size and/or shape dependent) electrical, catalytic, thermal and optical properties arising due to the collective behaviour of the electrons confined at the nano-scale, making them a promising candidate in the field of nanotechnology in general and nanobiotechnology in particular. Moreover, the ease of functionalization of AuNPs by promoting self-assembly of simple or complex (generally thiolated or aminated) molecules on its surface is an added advantage. On the other hand, single-stranded DNA (ssDNA) finds a vast application in both biological as well as non-biological fields such as sensing, photonics, optoelectronics and structural nanotechnology, due to the unique specificity of DNA-DNA hybridization. One of the major limiting steps for the ssDNA functionalization is the electric repulsion.

We have developed and reported a fast and efficient method for the synthesis of DNA functionalized AuNPs that is desirable in many applications related to nanobiotechnology [1]. We have investigated the effect of salt on the stability of the DNA functionalized AuNPs with their SAXS measurements in the presence/absence of salt; which was a significant part of the work. The studies demonstrated that the particles were very stable up to 1.0 M of NaCl concentration which is desirable in many biological studies. The SAXS patterns are shown in Fig. 1.

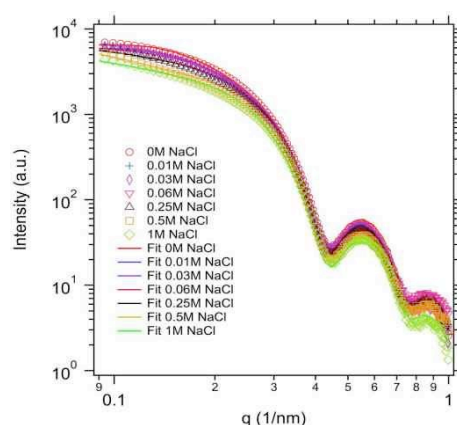


Figure 1. SAXS patterns of DNA1/TOEG6@AuNPs at various concentrations of NaCl and their respective fits using the form factor of spheres with Schultz distribution for their size distribution and a sticky hard sphere model for the structure factor

We can observe that R_{HS} changes from 14.4 nm to 11.7 nm passing from 0.03 to 0.06 M NaCl sign of a compaction of the DNA due to the screening of the counterions present in the solution. At the same time we can observe a trend for ϵ_{HS} that starts from negative values (sign of a repulsive interaction) at low concentration of salt, reaching positive values (sign of an

attractive interaction) at higher salt concentration confirming a better screening of the negative charges carried by the DNA backbone.

The SAXS study was also useful to determine the size of the functionalized nanoparticles, which, in the case of *cit@AuNPs*, were (17±2) nm from Small Angle Scattering X-ray (SAXS) analysis corresponding well to the (19±2) nm from Scanning Electron Microscopy (SEM) analysis.

In order to get an insight into the salt-stability of DNA1/TOEG6@AuNPs, SAXS based analyses were performed at various concentrations of salt, up to 1.0 M. For these measurements of commercially available 20 nm *cit@AuNPs* were used (Sigma-Aldrich Chemical Co.). The monodispersity of these particles was slightly higher than those produced in our lab, which made the commercial version more suitable for SAXS measurements. Analysis of the SAXS data reveals monodisperse particles with a size of (20±2) nm in good agreement with the specifications. The results did not reveal appreciable changes as a function of the salt concentration indicating very little or no interaction among the functionalized AuNPs even at 1.0 M NaCl concentration, which confirms their stability.

Table 1. Fit parameters obtained, for DNA/TOEG6@AuNP at various salt concentrations, from the fitting of the respective SAXS curves with Schultz distribution and a Sticky Hard Sphere model for the structure factor. R_s represents the radius of the AuNP core, σ_s is the width of radius distribution, R_{HS} is the radius of the hard sphere interaction, that can be approximated with the DNA/TOEG6 layer on top of the particles, p_{HS} is the volume fraction of the particles in the solution, λ_{HS} is a range parameter of the sticky potential (the potential extends till $\lambda_{HS} \times R_{HS}$) and ϵ_{HS} is the depth of the sticky interaction potential in $k_B T$ units. Due to the number of parameters involved in the fit we applied the following constraints: R_s , p_{HS} , σ_s and λ_{HS} have been kept equal for all the different salt concentration; R_{HS} has been kept between 11.7 and 14.4 nm, according to the minimum and maximum possible height for a mixed ssDNA and TOEG6 SAM according to the Daoud-Cotton model for polyelectrolyte brushes [2]; ϵ_{HS} has been left free

[NaCl]	R_s (nm)	R_{HS} (nm)	σ_s (nm)	p_{HS}	λ_{HS}	ϵ_{HS}
0 M	10.1±0.1	14.4±0.5	0.95±0.05	0.03±0.01	1.4±0.1	-0.80± 0.05
0.01 M	10.1±0.1	14.4±0.5	0.95±0.05	0.03±0.01	1.4±0.1	-0.47±0.05
0.03 M	10.1±0.1	14.4±0.5	0.95±0.05	0.03±0.01	1.4±0.1	-0.60±0.05
0.06 M	10.1±0.1	11.7±0.5	0.95±0.05	0.03±0.01	1.4±0.1	0.13± 0.02
0.25 M	10.1±0.1	11.7±0.5	0.95±0.05	0.03±0.01	1.4±0.1	0.56±0.05
0.50 M	10.1±0.1	11.7±0.5	0.95±0.05	0.03±0.01	1.4±0.1	1.5±0.3
1.0 M	10.1±0.1	11.7±0.5	0.95±0.05	0.03±0.01	1.4±0.1	0.9±0.2

We can observe that R_{HS} changes from 14.4 nm to 11.7 nm passing from 0.03 to 0.06 M NaCl sign of a compaction of the DNA due to the screening of the counterions present in the solution. At the same time we can observe a trend for ϵ_{HS} that starts from negative values (sign of a repulsive interaction) at low concentration of salt, reaching positive values (sign of an attractive interaction) at higher salt concentration confirming a better screening of the negative charges carried by the DNA backbone.

References:

- [1] Deka, J.; Měch, R.; Ianeselli, L.; Amenitsch, H.; Cacho-Nerin, F.; Parisse, P., Casalis, L. ACS Appl. Mater. Interfaces 7, 7033-7040 (2015)
- [2] Campolongo, M. J.; Tan, S. J.; Smilgies, D. M.; Zhao, M.; Chen, Y.; Xhangolli, I.; Cheng, W.; Luo, D. Crystalline Gibbs Monolayers of DNA-Capped Nanoparticles at the Air-Liquid Interface. ACS Nano 5, 7978-7985 (2011)

LOW RESOLUTION CRYSTALLOGRAPHY

M. De March¹, S. Onesti¹ and H. Amenitsch²

1.) Structural Biology Laboratory, Elettra-Sincrotrone Trieste, Italy

2) Graz University of Technology, Institute of Solid State Physics, Petersgasse 6, 8010 Graz, Austria

Crystals of large macromolecule assemblies grown from flexible proteins often show high mosaicity that is an indirect indication of intrinsic disorder. This phenomenon hinders the diffraction at high resolution and became difficult to be solved by standard protein crystallography. For this reason, diffraction data at low resolution can be used to collect also the critical information below 40 Å which is normally ignored in a standard crystallographic experiment.

In this view the aim of our low-resolution experiment was to increase the number of reflections between 100 Å and 10 Å in order to get complete data sets to use for ab-initio structure determination [1].

Basing on [2,3] we successfully set-up a new low-resolution crystallographic experiment at the AustroSAXS beamline in ELETTRA (Figure 1). The main difference to the previously implemented pilot experiment is the improved resolution from 20 Å before to 5 Å now and the better signal-to-noise ratio by using state-of-the-art detectors (Pilatus3 1M). Using the high brilliance synchrotron radiation we collected a number of datasets from standard protein Lysozyme and Avidin. Despite we were able to get a complete number of reflections between 200 Å and 5 Å of resolution (Figure 2a) data reduction process from these crystals revealed twinning and/or anisotropy. We also tested crystals obtained from proteins expressed and purified at the Structural Biology Laboratory at ELETTRA. These proteins have a fundamental role in cell replication [4] and their malfunctioning is often associated with tumors and cell disorders. Indeed, the impact in obtaining structural information from these key biological machines is clearly high. Most of our crystals were previously tested at the XRD1 beamline with a standard crystallographic experiment where we collected data between 30 Å and 7 Å. The high-resolution limit coming from these samples couldn't be improved both by crystal seeding and by using additives. For this reason and since no structural information were yet available they were used as a good probe for our experiments. Unfortunately, diffraction images revealed only few reflections (Figure 2b) that could be explained by intrinsic disorder and/or radiation damage. Beside the quality of the crystals tested during our experiments, which is often a limiting factor for a protein crystallographer, we succeeded to build a dedicated set-up at the AustroSAXS beamline as a useful installation for low resolution crystallographic experiments that can be integrated in the beamline skill and can be used for further data collections.

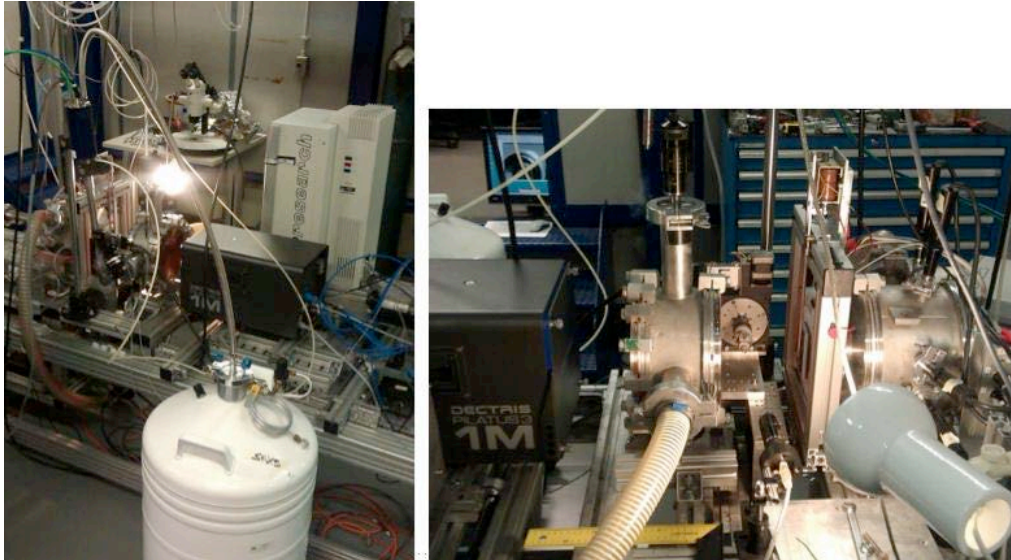


Figure 1. Low-resolution crystallography at the AustroSAXS beamline. The set-up consists of a Pilatus 1M detector ($2\theta=0^\circ$), a vacuum chamber with beam stop, a goniometer for the fine-angle slicing strategy (φ axis), an oxford cryostream to keep the collecting-temperature at 100K, and a camera-PC control system for crystal centering

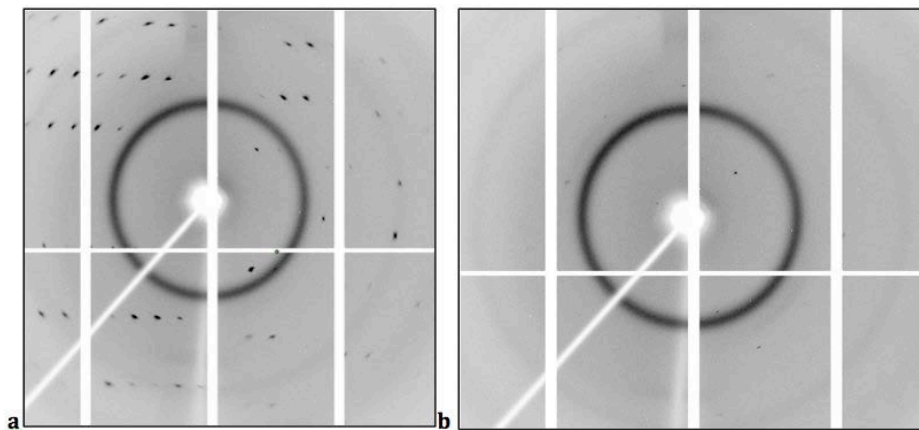


Figure 2. Low-resolution diffraction patterns ($200\text{\AA}-5\text{\AA}$) from **(a)** twinned and anisotropic crystals of Lysozyme and from **(b)** weakly-diffracting crystals of a bacterial replication factor RecJ^{Cdc45}

References:

- [1] V.Y. Lunin, N.L. Lunina, S. Ritter, I. Frey, A. Berg, K. Diederichs, A.D. Podjarny, A. Urzhumtsev & M.W. Baumstark. Low-resolution data analysis for low-density lipoprotein particle (2001) Acta Cryst. D57, 108-121
- [2] G. Evans, P. Roversi & G. Bricogne. In-house low-resolution X-ray crystallography (2000) Acta Cryst. D56, 1304-1311
- [3] R. Schwarzenbacher et al. in Annual Report of the Austrian SAXS beamline 99, ed. S. Bernstorff & H. Amenitsch, p66ff
- [4] S. Onesti & S.A. MacNeill. Structure and evolutionary origins of the CMG complex (2013) Chromosoma 122, 47-5

TIME-RESOLVED SIMULTANEOUS SAXS/WAXS AND DSC DETERMINATION OF LIPID MEMBRANES FLUIDITY IN THE PRESENCE OF OSMOLYTES (UREA AND TRIMETHYLAMINE N-OXIDE (TMAO))

S. Funari¹, J. Valerio¹ and S. Bernstorff²

1.) HASYLAB at DESY, Notkestraße 85, 22607 Hamburg, Germany

2.) Elettra-Sincrotrone Trieste, SS 14 km 163.5, 34149 Basovizza, Italy

In this project we intended to study the influence of the natural osmolytes urea and TMAO on the fluidity and stability of lipid model membranes as determined by the curvature in the lipid-water phases. In this way we expect to determine whether the dominant interaction of these solutes takes place on the lipids, or more indirectly by affecting the properties of water environment. Simultaneous DSC and SAXS/WAXS would enable us to determine the number of phases in each system, their transition temperatures and enthalpies and their reversibility. SAXS/WAXS would identify these structures and provide the dimensions of their lattices.

Lipid bilayers can display a wide range of morphologies [1-5] and are simple models for the cell membrane, that not only defines the cell limits but also provides a matrix for anchoring a variety of substances, e.g. membrane proteins, glycolipids, etc., that play an essential role in the cell. Moreover intracellular organelles are defined by their membrane boundaries. In particular the mitochondria, together with CoQ (ubiquinone) take part in the electron transport between the intra and extra cellular environments. Recently, we have been studying the structural effects of synthetic quinones on lipid model membranes as well as CoQ [6], in order to investigate their contribution to morphologies possibly involved in this transfer process. Summarizing, we can say that the insertion of these synthetic additives lower the temperature of the structural phase transitions comparative to pure lipids and in many cases induce the formation of cubic phases at low temperatures, e.g. 30 °C, which corresponds to an increase of the lipid matrix surface curvature. The scattering patterns of the cubic phases are clearly identifiable, despite their intrinsic low resolution. In some cases micellar cubic phases were observed.

It is accepted that urea and TMAO have antagonistic effects on the fluidity of lipid membranes [7-9]. In red blood cells, urea slightly increases the gel-phase domains, but this effect is counteracted by TMAO. We intended to determine how these organic solutes affect the lipid membrane and determine their contribution to fluidity, or curvature, induced on them. We note that these molecules are considerably smaller than the quinones previously studied, or ubiquinone. However previous thermal scans, on lipid matrices containing Urea or TMAO have shown morphologies of high curvature and upon temperature cycling the

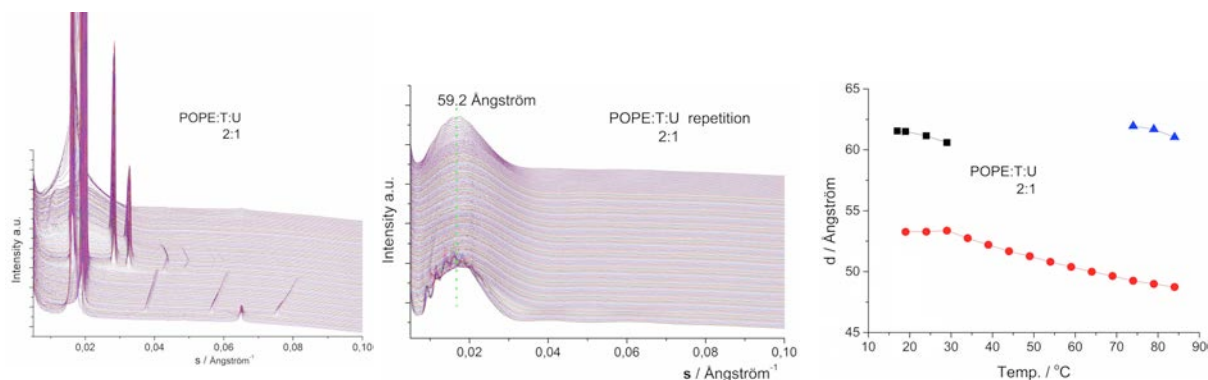


Figure 1. Sequence of diffraction patterns of POPE/TMAO/Urea. Left: initial scan. Middle: Scan repeated one day later with the sample subjected to several similar temperature cycles. Right: Spacings measured on the first scan

induction of cubic phases, whose unique structure could not be defined due to the lack of resolution or a significant number of samples.

In Figure 1, it can be seen already at the end of the first scan that the long range organization of the system is drastically reduced. Meantime an intermediate micellar cubic phase is temporarily formed, possibly with P4₃2 symmetry. After many temperature cycles, the cubic phase is much better resolved, however with a very low thermal stability.

The influence of TMAO, Urea and their mixtures is clearly different on both lipids, as shown in Figure 2. While POPE is barely affected, POPC is sensitive to their presence and the effect shows a composition dependence. Moreover the antagonistic effect of TMAO and Urea are clearly visible.

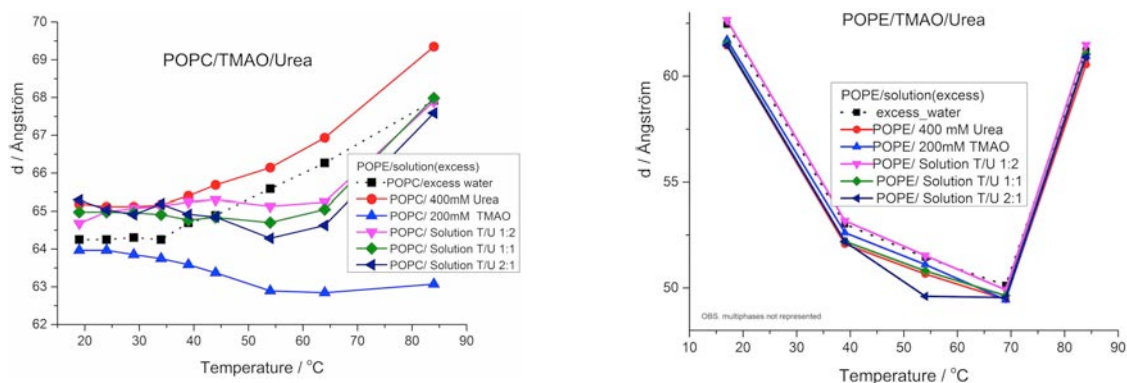


Figure 2. Repeat distances evolution upon heating for POPC:mixtures of TMAO:Urea and equivalent POPE/mixtures

Conclusions: The influence of the osmolytes TMAO and Urea on the fluidity and stability of lipid model membranes, is much different for POPC and POPE. Surely this reflects the polar head groups characteristics' of the lipids. We infer a poor miscibility of them, because these effects have been observed mostly after the samples were initially brought to higher temperatures. Upon cooling the long range order is significantly smaller and there is a tendency to form micelles, effect much stronger for POPE than POPC, and for TMAO than Urea.

References:

- [1] S.P. Gubin, A. Yu. Koksharov, G.B. Khomutov and G. Yu. Yurkov, Magnetic nanoparticles: preparation, structure and properties. *Russ. Chem. Rev.* **74**, 489–520 (2005)
- [2] J. I. Gittleman, B. Abeles and S. Bozowski, Superparamagnetism and relaxation effects in granular Ni-SiO₂ and Ni-Al₂O₃films. *Phys. Rev. B* **9**, 3891–3897 (1974)
- [3] M. Buljan, N. Radić, S. Bernstorff, G. Dražić, I. Bogdanović-Radović and V. Holý, Grazing incidence small angle X-ray scattering: application in study of quantum dot lattices. *Acta Cryst.* **A68**, 124–138 (2012)
- [4] M. Buljan, U. V. Desnica, G. Dražić, M. Ivanda, N. Radić, P. Dubček, K. Salamon, S. Bernstorff and V. Holý, Formation of three-dimensional quantum dot superlattices in amorphous systems: experiments and Monte Carlo simulations. *Phys. Rev. B* **79**, 035310 (2009)
- [5] M. Jerčinović, N. Radić, M. Buljan, J. Grenzer, I. Delač-Marion, M. Kralj, I. Bogdanović-Radović, R. Hübner, P. Dubček, K. Salamon and S. Bernstorff, Self-assembled growth of Ni nanoparticles in amorphous alumina matrix, *J. Nanopart. Res.* **16**, 2296 (2014)
- [6] M. Jerčinović, N. Radić, M. Buljan, J. Grenzer, I. Delač-Marion, M. Kralj, I. Bogdanović-Radović, R. Hübner, P. Dubček, K. Salamon and S. Bernstorff, Self-assembled growth of Ni nanoparticles in amorphous alumina matrix, *J. Nanopart. Res.* **16**, 2296 (2014)
- [7] M. Jerčinović, N. Radić, M. Buljan, J. Grenzer, I. Delač-Marion, M. Kralj, I. Bogdanović-Radović, R. Hübner, P. Dubček, K. Salamon and S. Bernstorff, Self-assembled growth of Ni nanoparticles in amorphous alumina matrix, *J. Nanopart. Res.* **16**, 2296 (2014)
- [8] M. Jerčinović, N. Radić, M. Buljan, J. Grenzer, I. Delač-Marion, M. Kralj, I. Bogdanović-Radović, R. Hübner, P. Dubček, K. Salamon and S. Bernstorff, Self-assembled growth of Ni nanoparticles in amorphous alumina matrix, *J. Nanopart. Res.* **16**, 2296 (2014)
- [9] M. Jerčinović, N. Radić, M. Buljan, J. Grenzer, I. Delač-Marion, M. Kralj, I. Bogdanović-Radović, R. Hübner, P. Dubček, K. Salamon and S. Bernstorff, Self-assembled growth of Ni nanoparticles in amorphous alumina matrix, *J. Nanopart. Res.* **16**, 2296 (2014)

CORE-SHELL STRUCTURE OF MONODISPERSE POLY(ETHYLENE GLYCOL)-GRAFTED IRON OXIDE NANOPARTICLES STUDIED BY SMALL-ANGLE X-RAY SCATTERING

T. A. Grünewald¹, A. Lassenberger², P. D. J. van Oostrum², H. Renzhofer¹, R. Zirbs², B. Capone³, I. Vonderhaid², H. Amenitsch⁴, H. C. Lichtenegger¹ and E. Reimhult²

- 1.) Department of Material Sciences and Process Engineering, University of Natural Resources and Life Sciences, Vienna, Austria
- 2.) Department of Nanobiotechnology, University of Natural Resources and Life Sciences, Vienna, Austria
- 3.) Faculty of Physics, University of Vienna, Austria
- 4.) Institute for Inorganic Chemistry, Graz University of Technology, Graz, Austria

Superparamagnetic Fe₃O₄ nanoparticles (NPs), with core diameters of 3-15 nm, are used in a rapidly expanding number of applications in the biomedical field; the most common include magnetic cell labeling, hyperthermia, drug delivery, and as contrast agents for magnetic resonance imaging. Rapid aggregation and precipitation of the iron oxide cores occurs without a sterically stabilizing shell; a grafted polymer brush shell is the most stable and one of the most common surface modifications to enable dispersion of NPs in aqueous solutions containing biomolecules.

With recent improvements in the synthesis of NPs [1], there has been a move towards more and more well-defined, core-shell particle architectures with ever increasing grafting density. A novel melt-grafting approach allows for achieving grafting densities approaching those limited by the footprint of the anchor molecule. These high grafting densities now allow overcoming the electron density contrast which usually hindered the application of SAXS for the direct characterization of the shell morphology.

In order to describe the morphology of the shell a mean-field scaling approach, based on the Daoud-Cotton model [2], was chosen which describes the polymer density in two distinct regions. Region 1 is termed the “melt” region. This region is located near the core. The polymer density here approaches that of a polymer melt due to the confinement of the chains by the high grafting density. The boundary of this region is given by the grafting density and the monomer length. The second region is called the “swollen” region where the polymer solvation is ideally self-avoiding. Here the volume occupied by each monomer segment is influenced by the solvent quality and the monomer length. An intermediate region usually described in literature cancels out in the case of PEG as its excluded volume parameter is 1. A more detailed deviation is given in Ref [3]. The model gives the monomer density which can be directly transferred into an electron density, which can be essentially used as a form factor after fourier transform. A graphical representation of the model and its application to scattering data in water is given in Figure 1.

In this study we applied SAXS to study the shell morphology and the changes herein induced by changing the solvent quality achieved heating of NPs in the vicinity of the lower critical solution temperature (LCST). In situ heating experiments were carried out at the Austrian SAXS beamline at Elettra synchrotron Trieste, Italy, with a fixed energy of 8.00 keV. For this experiment a Pilatus3 1M detector (Dectris, Switzerland) was used, giving access to a q-range from 0.01 to 0.65 Å⁻¹. Heating was carried out using custom made heating stage with water circulation. Measurement time was 2 s per scattering pattern. As visible in Fig. 1, the data shows a pronounced shoulder at about 0.15 Å⁻¹ which could be attributed to the radius of the polymer shell as a dilution did not affect the position of the shoulder as it would be expected for a structure factor. Another experiment carried out was the controlled heating in the

vicinity of the LCST. As the excluded volume parameter changes as a response to heating, also the shell radius of the NPs is responding.

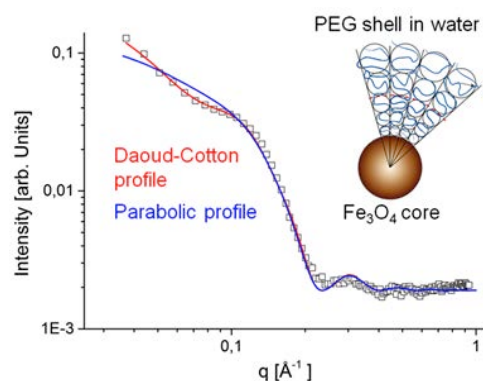


Figure 1. A graphical representation of the polymer density model (right-hand side). An x-ray scattering curve of core-shell NPs (open squares) is compared to the Daoud-Cotton profile (red) and a conventional parabolic profile (blue)

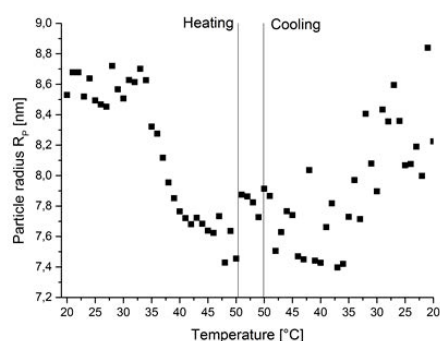


Figure 2. Total particle radius R_p of iron oxide core – melt-grafted PEG shell particles in response to temperature changes

Fig 2 shows the results of the heating experiment. After an initial phase of constant size the radius starts to decrease at about 34°C to find its minimal size at above 40°C. Upon cooling the system showed to a certain extent a reversible size increase. Our findings demonstrate that SAXS can be applied to structural studies of hybrid core-shell nanoparticle systems. The highly monodisperse nanoparticles allowed the fitting of the shell density profile to a mean-field scaling model first derived by Daoud and Cotton for star polymers and adapted by us to densely grafted spherical brush core-shell NPs. This model quantitatively fitted the experimental data for all observable states of the shell, including the temperature induced contraction of the shell in cloud-point buffer. In contrast, a parabolic brush-type density profile could not reproduce the clear shoulder defined by the shell. These results support a constant monomer density region comparable to the density of the corresponding polymer melt closest to the core followed by a region of monotonously decreasing monomer density corresponding to that of a star polymer to describe the internal structure and unique colloidal properties of ultra-densely grafted core-shell NPs.

This opens up new opportunities for the study of, e.g., fast changes in core-shell nanoparticle structure. For such studies, SAXS has important advantages over competing techniques such as SANS as the experiments can be carried out with laboratory equipment or high brilliance synchrotron sources with very high time resolution.

References:

- [1] R. Zirbs, A. Lassenberger, I. Vonderhaid, S. Kurzhals and E. Reimhult; Melt-grafting for the synthesis of core-shell nanoparticles with ultra-high dispersant density; *Nanoscale* **7**, 11216-11225 (2015)
- [2] M. Daoud and JP. Cotton; Star shaped Polymers – A model for the conformation and its concentration dependence; *Journa de Physique* **43**, 531-538 (1982)
- [3] T.A. Grünewald, A. Lassenberger, P.D.J. van Oostrum, H. Rennhofer, R. Zirbs, B. Capone, I. Vonderhaid, H. Amenitsch, H.C. Lichtenegger and E. Reimhult; Core-Shell Structure of Monodisperse Poly(ethylene glycol)-Grafted Iron Oxide Nanoparticles Studied by Small-angle X-ray scattering; *Chemistry of Materials*, accepted, DOI: 10.1021/acs.chemmater.5b01488

SELF-ASSEMBLED SUPRAMOLECULAR STRUCTURES AND MEMBRANE-ACTIVITY OF AMPHIPHILIC DESIGNER PEPTIDES

K. Kornmueller¹, B. Lehofer¹, H. Amenitsch² and R. Prassl¹

1.) Institute of Biophysics, Medical University of Graz, BioTechMed-Graz, Harrachgasse 21/VI, 8010 Graz, Austria

2.) Institute of Inorganic Chemistry, Graz University of Technology, Stremayrgasse 9/4, 8010 Graz, Austria

A very active area of research aims to use peptide-based nanostructured materials as biomimetic artificial matrices in nanomedicine [1]. Our studies focus on self-assembling amphiphilic designer peptides as building blocks. Being exclusively composed of amino acids, their amphiphilic nature derives from a sequence containing antagonistic hydrophilic and hydrophobic amino acid residues within the same molecule (e. g. V₄D is composed of four hydrophobic valine residues, followed by a negatively charged aspartic acid). Due to their amphiphilic nature, they self-assemble above a critical aggregation concentration into highly ordered supramolecular structures, like spherical micelles, extended fibers, tubes, rods, donuts, helical and twisted ribbons [2], or double helices [3]. To fully exploit the potential of these molecules in nanomedical applications, it requires a deep understanding of the peptides' individual, as well as their collective morphology, the underlying dynamic assembly mechanisms and how these materials act at the interface of synthetic and biological membranes.

Seven systematically varied amphiphilic designer peptides were subject of the present study, namely V₄WD₂, I₄WD₂, L₄WD₂, V₄WD, V₄D₂, V₄D, and V₃D. Their concentration dependent self-assembly, as well as their interaction with low density lipoprotein (LDL) and dipalmitoyl phosphatidylcholine (DPPC) multilamellar vesicles (MLVs) - two simple models of biologically relevant membrane structures - has been investigated by Synchrotron small angle X-ray scattering (SAXS) at the Austrian SAXS beamline at ELETTRA (Trieste, Italy). Samples were prepared by dissolving lyophilized peptides in double-distilled water. Supramolecular structure formation was investigated after 1 week of aging. For membrane-interaction studies, different ratios of peptides were applied on LDL and DPPC MLVs: 5:1, 10:1, 25:1, and 50:1 (mol lipid/mol peptide), respectively. Samples were measured in a 1.5 mm glass capillary. Measurements were performed at a wavelength of 0.154 nm and a sample-detector distance of 1.1 m. The photon energy was 8 keV. Data was recorded with a Pilatus detector (Pilatus3 1M, DECTRIS Ltd., Villigen PSI, Switzerland), calibrated with silver behenate. The scattering intensity was measured as a function of the scattering vector q where $q = 4\pi (\sin\theta)/\lambda$, with 2θ being the scattering angle and λ being the wavelength. Data analysis was done with Fit2D and Igor Pro (Version 6.22A, WaveMetrics Inc., USA). Experimental intensities were normalized and background corrected.

Preliminary results of this study show, that the peptide L₄WD₂ stood out from the other peptides, and should be highlighted at this point. Regarding the peptide's interaction with DPPC MLVs and LDL, L₄WD₂ showed to be least membrane-active. This might be due to the fact that - in contrast to all other peptides - it self-assembled into stable and highly ordered supramolecular structures already at very low concentrations (0.1-1 mM). The SAXS patterns show typical characteristics of a core-shell cylinder structure (see Figure 1A). The scattering curves of DPPC at 25 °C with different concentrations of L₄WD₂ are similar to those of pure DPPC, showing five reflection orders with sharp equidistant peaks and an associated lamellar spacing of $d = 6.38$ nm. When L₄WD₂ was added to obtain a 5:1 lipid:peptide molar ratio, we observed the formation of a second lamellar phase, independent of the original one, with a much smaller d -spacing of 4.48 nm. In addition, the amount of uncorrelated bilayered stacks

increased, whereas the peaks of the L_α phase decreased. LDL served as model to test the peptide's activity under physiological conditions. The scattering patterns of pure LDL and LDL in the presence of 50:1, 25:1 and 10:1 (mol lipid/mol peptide) L_4WD_2 were virtually superimposable, whereas the highest peptide concentration (5:1) resulted in an increase of intensity in the low q -range. This contribution was attributed to the presence of the self-assembled supramolecular cylinder structures.

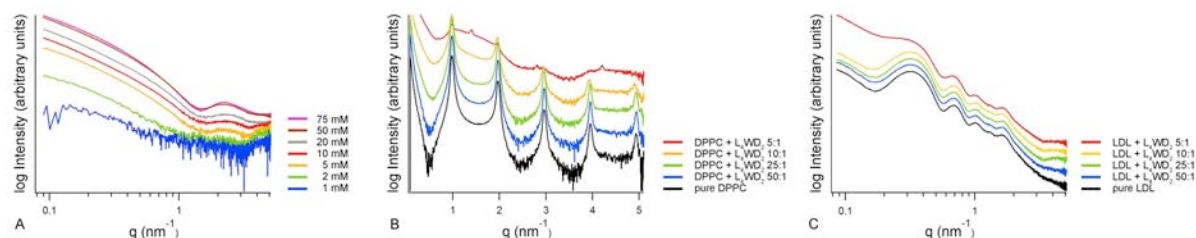


Figure 1. SAXS patterns of the concentration-dependent self-assembly of L_4WD_2 (A), and the peptide's interaction with DPPC MLVs (B) and LDL (C)

Figure 2 highlights the impact of all investigated peptides on DPPC MLVs at 25 °C. Figure 2A shows the effect of the lowest applied peptide concentration (50:1), whereas Figure 2B shows the effect of high peptide concentrations (5:1). It can be generalized, that – with the exception of L_4WD_2 as stated above – all peptides, even at the lowest concentration, result in a reorganization of the membrane structure. The SAXS patterns are characteristic for positionally weakly correlated bilayers of oligolamellar vesicles. The first three reflection orders of the original lamellar phase are still visible, but diminish as the diffuse scattering of the background increases. It appears that peptides which are lacking a tryptophane residue (V_3D (yellow), V_4D (red) and V_4D_2 (blue)) are less membrane-perturbing than tryptophane-containing peptides. Tryptophane is known to partition into the interface region of biomembranes, thus facilitating membrane-destabilization. When the peptide concentration increases, the remodeling of the membrane continues. Most peptides give rise to the formation of a second lamellar phase, by an intermediate state of increased uncorrelated bilayered stacks (Figure 2B). Only one peptide behaves differently: V_4D is the most hydrophobic one and results in the complete disappearance of the original lamellar structure.

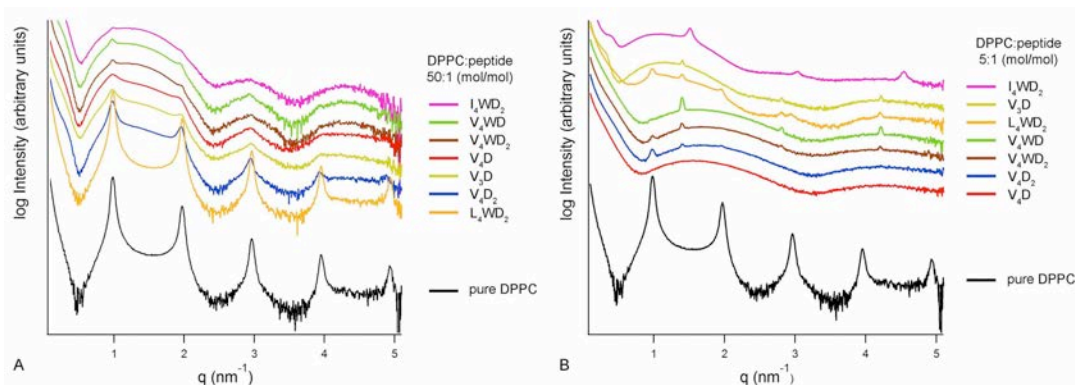


Figure 2. SAXS patterns of DPPC in the absence and presence of seven different amphiphilic designer peptides at two lipid:peptide molar ratios - 50:1 (A) and 5:1 (B)

References:

- [1] Luo, Z., Zhang, S. *Chem. Soc. Rev.* 41, 4736-4754 (2010)
- [2] Zhao, X., Pan, F., Xu, H.; Yaseen, M., Shan, H., Hauser, C. A., Zhang, S., Lu, J. R. *Chem. Soc. Rev.* 39, 3480-3498 (2010)
- [3] Kornmueller, K., Letofsky-Papst, I., Gradauer, K., Mikl, C., Cacho-Nerin, F., Leybold, M., Keller, W., Leitinger, G., Amenitsch, H., Prassl, R. *Nano Res.* 8 (6), 1822-1833 (2015)

EFFECTS OF HIGH HYDROSTATIC PRESSURE ON LOW DENSITY LIPOPROTEIN (LDL) AND ITS CORE LIPID TRANSITION

B. Lehofer¹, K. Kornmueller¹, M. Kriechbaum², J. Peters^{3,4}, N. Martinez^{3,4}, H. Amenitsch² and R. Prassl¹

- 1.) Medical University of Graz, Institute of Biophysics, Harrachgasse 21/VI, 8010 Graz, Austria
- 2.) Graz University of Technology, Institute of Inorganic Chemistry, Stremayrgasse 9, 8010 Graz, Austria
- 3.) Institut Laue-Langevin, 71 avenue des Martyrs, 38044 Grenoble, France
- 4.) Université Grenoble Alpes, IBS, 71 avenue des Martyrs, 38044 Grenoble, France

Human low density lipoprotein (LDL) particles are the principal cholesterol transporter in the blood circulation. The quasi-spherical LDL particles (~20 nm in diameter) are made up of a complex combination of various lipids (primarily cholesteryl esters, triglycerides and phospholipids) and a large single amphipathic protein moiety, named apolipoprotein B-100 (apoB-100). The surface of the particle is made up of a phospholipid monolayer and certain domains of apoB-100. The LDL core is basically made up by a mixture of cholesteryl esters and triglycerides. Each LDL particle has a defined transition temperature (T_m) depending on the individual lipid composition of its core. The phase transition of LDL corresponds to the melting of the cholesteryl esters in the inner lipid core from an ordered liquid crystalline phase to a disordered fluid phase. T_m was determined in advance for the measured samples with differential scanning calorimetry (DSC).

The structural behavior of different types of LDL (native, oxidized and triglyceride rich) was investigated under high hydrostatic pressure (HHP). The HHP conditions ranged from 50 to 3000 bar, whereas the temperature was adjusted in relation to T_m of each individual sample. The measured temperatures ranged from 10°C below T_m to 10°C above T_m of each sample.

Table 1. T_m for the individual LDL samples determined with DSC

	native LDL1	oxidized LDL1	native LDL2	oxidized LDL2	TG rich LDL3
T_m (°C)	28.3	28.5	21.2	22.6	12.6

The high pressure equipment consisting of a pressure generator with control unit (SITEC-Sieber Engineering AG, Maur, Switzerland) and a custom-built pressure cell (Resch Fertigungstechnik und Prototyping, Glojach, Austria) was successfully installed and adjusted at the beamline (see Fig. 1). This very special high pressure cell contains a cylindrical sample capillary, which is 2 cm long and 1.5 mm in diameter. The cell has a filling volume of approx.



Figure 1. The installed high pressure cell with temperature control unit at the SAXS beamline (left) and the control unit of the high pressure generator in the control cabin (right)

25 μL . It is made out of Kapton, which is a polymer of very high mechanical and thermal stability. Moreover this polymer is insensitive to radiation damage and has a high transmittance to X-rays. The sample was inserted and the capillary was sealed with two small Teflon plugs. A temperature unit covering the sample cell was attached and provided the possibility to adjust the temperature for the experiments as desired.

The SAXS pattern of LDL below T_m shows a characteristic peak at $q=1.7 \text{ nm}^{-1}$ corresponding to the ordered cholesteryl esters in the lipid core. When the temperature is raised above T_m these lipids undergo a phase transition so that the layered organization disrupts and an isotropic distribution dominates the core [1]. This behavior could be observed in a temperature scan at a constant pressure of 50 bar, where the peak at $q=1.7 \text{ nm}^{-1}$ completely fades (see Figure 2).

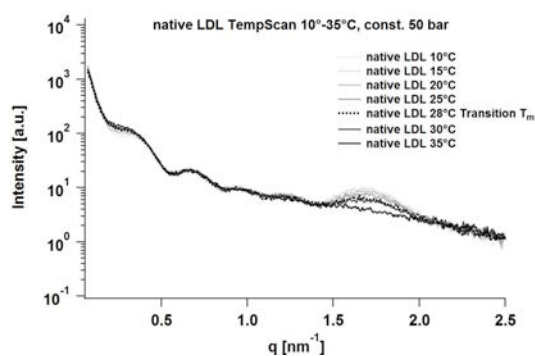


Figure 2. Temperature scan from 10°C – 35°C of native LDL1 at constant pressure of 50 bar

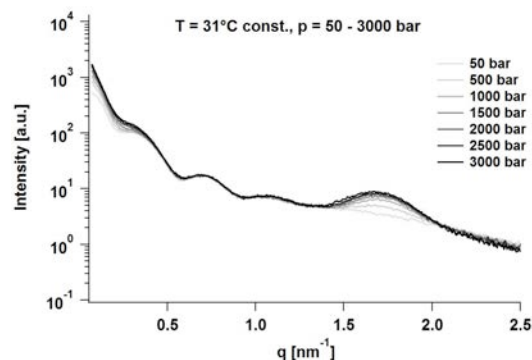


Figure 3. SAXS curves of native LDL measured 10°C above T_m (31°C) from 50-3000 bar

When we did pressure scans at constant temperature, we could show the pressure effects on the different samples. The measurements 10°C above T_m showed that the peak at $q=1.7 \text{ nm}^{-1}$ re-emerged continuously by increasing the pressure to 3000 bar (Figure 3). This finding confirms the close relation between temperature and pressure concerning the fluidity state of lipids, as has so far been demonstrated only for lipid/water systems [2].

On the contrary the scattering intensity around $q=0.25 \text{ nm}^{-1}$ increases with growing pressure but does not increase when lowering the temperature. Usually the intensity at small q -values decreases at lower temperatures as seen in the temperature scan (Figure 2). So this effect seems to be independent from the pressure induced phase transition of the lipid core and might reflect an overall particle shape alteration. Both observed effects occurred in all investigated LDL types, whereas the triglyceride rich LDL showed the least intensity changes in all q -regions. This might be due to a lack of a lamellar core lipid organization and a lack of ellipsoidal morphology of LDL below T_m [3].

Summing up we can say that high hydrostatic pressure has an impact on the structural characteristics of the LDL particle. On the one hand we could observe a pressure induced phase transition of the inner lipid core and on the other hand there is an additional structural element, which shows a modified SAXS pattern by applying pressure.

References:

- [1] Y. Liu, D. Luo and D. Atkinson; Human LDL core cholesterol ester packing: three-dimensional image reconstruction and SAXS simulation studies; *J. Lipid Res.* **52**, 256–262 (2011)
- [2] R. Winter; Synchrotron X-ray and neutron small-angle scattering of lyotropic lipid mesophases, model biomembranes and proteins in solution at high pressure; *Biochim. Biophys. Acta.* **1595**, 160-184 (2002)
- [3] M.B. Sherman *et al*; Structure of Triglyceride-Rich Human Low-Density Lipoproteins According to Cryoelectron Microscopy; *Biochemistry* **42**, 14988-14993 (2003)

KINETIC STUDY OF AMYLOID-LIKE OLIGOMERS FORMATION IN CONCAVALIN A

F. Librizzi, R. Carrotta, D. Bulone, S. Vilasi and P.L. San Biagio

Institute of Biophysics, National Research Council, Via Ugo La Malfa 153, 90146 Palermo, Italy

Protein aggregation is of extreme interest in many fields of scientific research, from physics to biotechnology and medicine. Several human pathologies, such as Alzheimer's and Parkinson's disease are related to the formation and the accumulation of proteinaceous deposits, mainly composed of ordered aggregates, known as amyloid fibrils [1,2]. The formation of amyloid fibrils is often detected by means of Thioflavin T (ThT) fluorescence. This dye is poorly fluorescent in aqueous solutions, but its quantum yield strongly increases when it intercalates into the intermolecular β -sheets structures arising during the formation of amyloid fibrils [3]. However, the exact mechanisms leading to ThT fluorescence enhancement need to be further clarified.

Concanavalin A (ConA) is a jack bean protein, often used as a model system for its ability to aggregate and form, in alkaline conditions, Thioflavin T sensitive, amyloid-like, aggregates [4-6]. It is also able to induce apoptosis on cells [7]. The aggregation process of ConA develops in different steps: starting from native tetramers, probably following a conformational change, protein molecules associate to build small aggregates; subsequently, coagulation of different species occurs and continues up to the formation of very large aggregates, up to the scale of tens of microns [5,6]. An intriguing aspect of the ConA aggregation process is that the first step, which is clearly and selectively detected by ThT, is substantially not dependent on the protein concentration [4,5] and, as we have very recently found, on the ionic strength of the solvent. On the contrary, the later steps of aggregation clearly depend on these parameters [5]. Accordingly, a suitable lowering of the ionic strength of the solvent gives the possibility to isolate the first step of aggregation by almost hindering the following ones.

Aim of the experiments performed at Elettra was the detection and characterization of the early small amyloid-like aggregates of ConA. We followed the kinetics of aggregation at 37 °C at two protein concentrations (0.5 and 1.0 mg/ml) and in two ionic strength conditions (10mM and 100mM buffer). We found that the most favorable conditions for our purposes were high protein concentration (1.0 mg/ml) and low buffer ionic strength (10mM buffer). In fact, ConA has a very strong tendency to aggregate, and at high ionic strength the measurements were partly impaired by the presence of aggregates since the beginning of the kinetics.

Fig. 1 reports in a Guinier plot some of the scattering curves at different times during the aggregation kinetics, and clearly shows the formation of aggregates. From the Guinier analysis we obtain an estimation of the average radius of gyration of the particles in solutions and, by comparison with a suitable Bovine Serum Albumin (BSA) reference measurement, their average mass. These parameters are reported in Fig. 2 (a and b, respectively), as a function of the aggregation time. In Fig.2c,d the same parameters are reported for comparison on a log-log scale, together with the average mass (c) and with the hydrodynamic radius (d), as obtained by dynamic light scattering (DLS). The difference observed between the gyration and the hydrodynamic radius at low ionic strength (panel d) appears a bit larger than expected. However, the data indicate that, also in SAXS experiments, at low ionic strength we have singled out the formation of the small amyloid-like (ThT sensitive) aggregates, which presumably constitute the building blocks for the extremely large aggregates observed in the high ionic strength conditions. Both from the average dimensions (Fig. 2a,c) and mass (Fig. 2b,d), these small aggregates seem to be composed by few tetramers; further work is

necessary to extract from the SAXS data more detailed information on their structure and nature, and on the properties which make them ThT-sensitive.

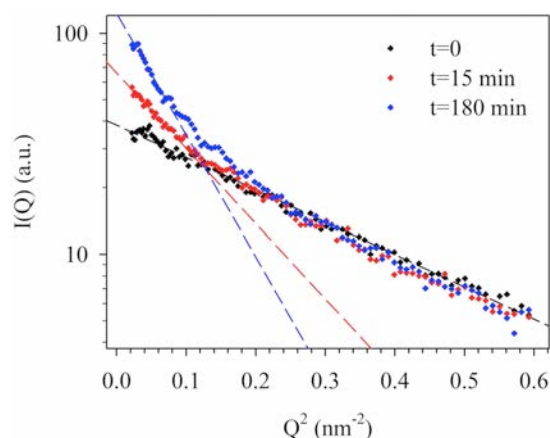


Figure 1. Guinier plot at different times during the aggregation process at 1.0 mg/ml, $T = 37\text{ }^{\circ}\text{C}$, pH 9 (10mM buffer)

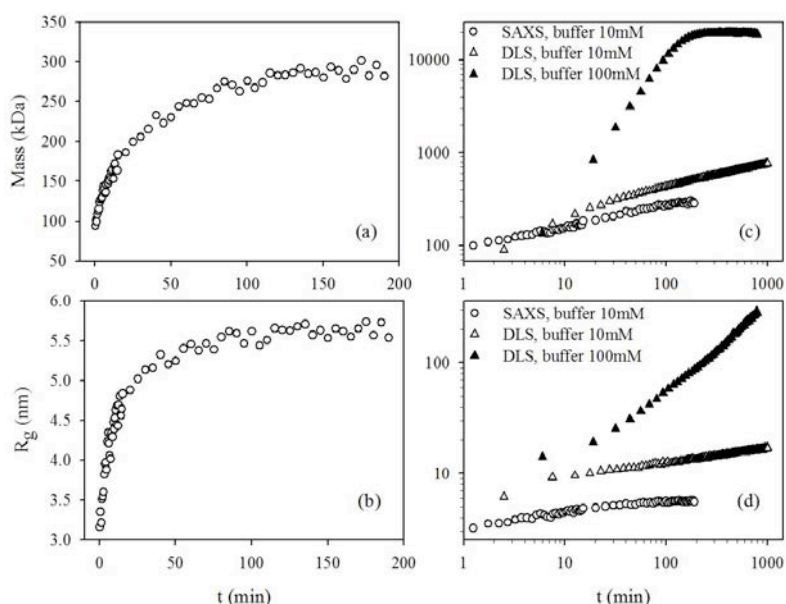


Figure 2. Average mass (a) and radius of gyration (b), as obtained from the Guinier analysis. In panels (c) and (d), the same parameters are reported for comparison together with the average mass (c) and with the hydrodynamic radius (d), as obtained by dynamic light scattering (DLS)

References:

- [1] C.M. Dobson; Protein folding and misfolding; *Nature* **426**, 884-890 (2003)
- [2] D.J. Selkoe; Folding proteins in a fatal way; *Nature* **426**, 900-904 (2003)
- [3] M. Groenning, M. Norrman, J.M. Flink, M. van de Weert, J.T. Bukrinsky, G. Schluckebier and S. Frokjaer; Binding mode of Thioflavin T in insulin amyloid fibrils; *J. Struct. Biol.* **159**, 483-497 (2007)
- [4] V. Vetri, C. Canale, A. Relini, F. Librizzi, V. Militello, A. Gliozzi and M. Leone; Amyloid fibrils formation and amorphous aggregation in Concanavalin A; *Biophys. Chem.* **125**, 184-190 (2007)
- [5] R. Carrotta, V. Vetri, F. Librizzi, V. Martorana, V. Militello and M. Leone; Amyloid fibrils formation of Concanavalin A at basic pH; *J. Phys. Chem. B* **115**, 2691-2698 (2011)
- [6] R. Carrotta, S. Vilasi, F. Librizzi, V. Martorana, D. Bulone and P.L. San Biagio; α -Casein inhibition mechanism in Concanavalin A aggregation process; *J. Phys. Chem. B* **116**, 14700-14707 (2012)
- [7] V. Vetri, R. Carrotta, P. Picone, M. Di Carlo and V. Militello; Concanavalin A aggregation and toxicity on cell cultures; *Biochim. Biophys. Acta* **1804**, 173-183 (2010)

DNA NANOSTARS: PHASE BEHAVIOUR AND STRUCTURAL INVESTIGATION BY SAXS

P. Mariani¹, F. Carducci¹, F. Spinozzi¹, M. G. Ortore¹, R. Cerbino², T. Bellini², F. Sciortino³ and F. Bomboi³

- 1.) Università Politecnica delle Marche, Dipartimento di Scienze della Vita e dell'Ambiente, Via Brecce Bianche, 60131 Ancona, Italy
- 2.) Università di Milano - Dipartimento di Biotecnologie Mediche e Medicina Traslazionale, via F.lli Cervi 93, 20090 Segrate, Italy
- 3.) Sapienza Università di Roma, Dipartimento di Fisica, Piazzale Aldo Moro, 2 00185 Roma, Italy

A new generation of micro- and nano-colloids, interacting via strongly anisotropic forces and based on the self-assembly of DNA oligomers, has been recently introduced [1,2]. Indeed, the rational design of the DNA sequences enables guiding the self-association of multiple DNA strands into a rich variety of nanosized objects, such as geometrical figures. In such framework, we were particularly attracted by “DNA-stars”, nanoscopic particles with a controlled number of interacting terminations formed by 49-base-long ssDNA molecules.

The structure of DNA-nanostars obtained by dissolving in water f distinct oligonucleotides is shown in Fig. 1: the $f=3$ and $f=4$ nanostars are formed by the self-assembly of three and four oligomers, respectively. Note that the arm tips terminate with one sticky overhang each, mimicking molecules with controlled limited valence. These DNA trimers and tetramers are considered as promising colloidal particles whose interactions and self-assembly could be predetermined [1]. In particular, fluorescent emission from a capillary tube containing a sample of EtBr-marked $f=4$ nanostars (see in Fig. 1 the capillaries photographed in *C* at the two different temperatures indicated by the green and magenta dots in *E*) shows that at low enough temperature (magenta-framed picture), the system phase separates into DNA-rich and DNA-poor phases. Molecular dynamics simulations showed an unconventional dynamic behavior: while the dynamics at high temperature is the one expected for free-diffusing DNA-

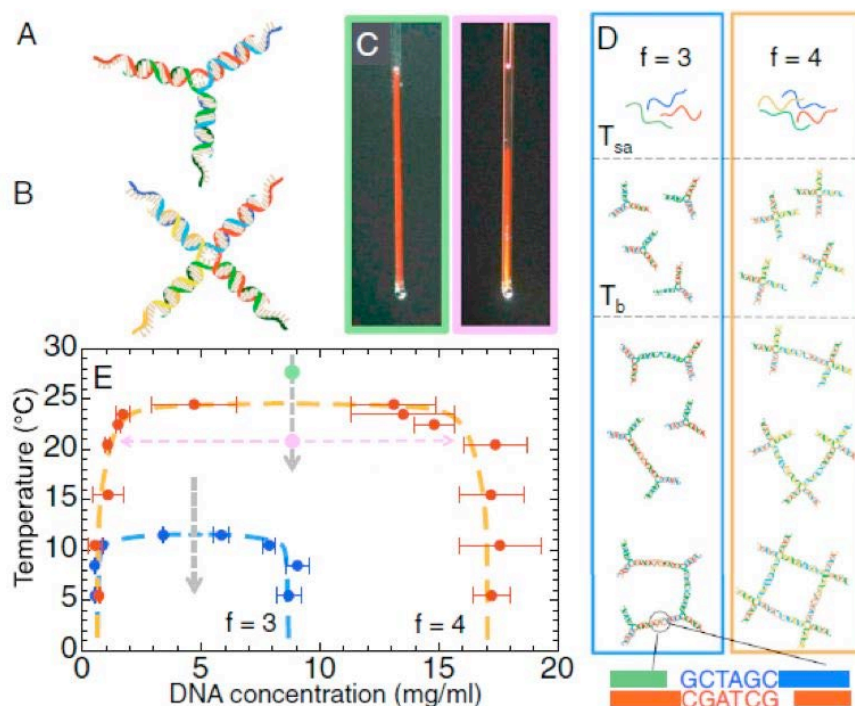


Figure 1. Structure and phase behavior of DNA nanostars with valence $f=3$ and $f=4$ [1]

nanostars, at lower temperature such relaxation develops continuously into the fast component, with the stretching exponent decreasing [3]. Static structure factors were obtained for several concentrations and temperature values [3], but a direct, experimental validation of the DNA-nanostar phase behavior and structural properties at different temperatures is still lacking.

To investigate both not-interacting systems and phases where the structure factor can be evidenced, Small Angle X-ray Scattering (SAXS) experiments have been performed at the SAXS beam-line at Elettra as a function of DNA-nanostar concentration and temperature (e.g., crossing in different positions the phase-boundary in the phase diagram of Fig.1). In particular, $f=3$ and $f=4$ nanostars were considered and the investigated concentrations were 1, 2, 6 and 18 mg/ml for tetramers and 1, 2 and 9 mg/ml for trimers. Nanostars were prepared by mixing equimolar quantities of the three and four strands, respectively. Note that each sample was prepared in sealed 1.0 mm quartz capillary: before the experiments, solutions have been kept at 90.8°C for 20 min and slowly cooled to the temperature of 5°C in about 3 h. A few results are reported in Fig. 2. Data analysis is still under progress, but results clearly show that it is possible to monitor the temperature-dependence of the structure factor and that a general picture of the gelation mechanism could be probably obtained.

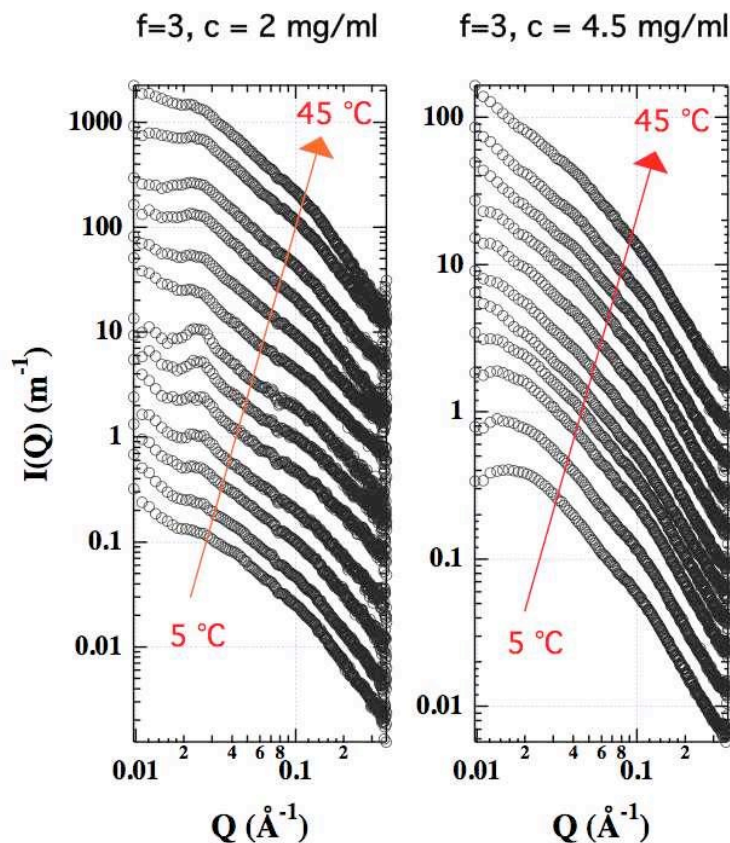


Figure 2. SAXS profiles obtained from DNA nanostars with valence $f=3$ at two different concentrations

References:

- [1] S. Biffi, R. Cerbino, F. Bomboi, E.M. Paraboschi, R. Asselta, F. Sciortino and T. Bellini. Phase behavior and critical activated dynamics of limited-valence DNA nanostars. PNAS (2013)
- [2] B. Wei, M. Dai, P. Yin. Complex shapes self-assembled from single-stranded DNA tiles. Nature 485, 623–626 (2012)
- [3] L. Rovigatti, F. Bomboi, F. Sciortino. Accurate phase diagram of tetravalent DNA nanostars. J.Chem.Phys. 140, 154903 (2014)

FEASIBILITY STUDY OF THE EARLY STAGE INTERACTION OF SILICA NANOPARTICLES WITH LYSOZYME USING A FREE JET MICROMIXER IN COMBINATION WITH SAXS

B. Marmiroli¹, J. Meissner², B. Sartori¹, G. Greci³, M. Girod⁴, G. H. Findenegg², and H. Amenitsch¹

1.) Graz University of Technology, Institute of Inorganic Chemistry, NAWI, Stremayrgasse 9/IV, 8010 Graz, Austria

2.) Technische Universität Berlin, Institut für Chemie, Strasse des 17. Juni 124, D-10623 Berlin, Germany

3.) National University of Singapore, Mechanobiology Institute (MBI), T-Lab 5A Engineering Drive 1, Singapore

4.) Elettra-Sincrotrone Trieste, Strada Statale 14, km 163.5, 34149 Basovizza / Trieste, Italy

The study of protein-induced clustering of nanoparticles is important in biotechnology and in the biomedical area due to the potentially bioadverse consequences of such particle aggregation processes [1]. Up to now, many studies have been devoted to examine protein adsorption and structural changes caused by adsorption at nanoparticles. Less attention has been paid to protein induced aggregation.

In this experiment, we investigated the interaction of silica nanoparticles with lysozyme, which is known to lead to heteroaggregation and flocculation within a wide pH range [2,3]. Our attention was focused on the early stages just after the mixing of the two components, as no information on the kinetics of the process is available yet. The aggregation is attributed to a bridging of silica particles by adsorbed protein molecules. Adsorption of lysozyme at hydrophilic silica surfaces is due mostly to electrostatic interactions between the negatively charged silica surface and the positive net charge of the protein, therefore it occurs rapidly. Previous investigation using a stop-flow apparatus indicated that the reaction is faster than 10 ms. Recently, we have combined the synchrotron SAXS technique, rapid mixing by means of microfluidics, and a free liquid microjet in air to push the limits of time resolved measurements of fast chemical reactions at and below the ms time range. We have designed, fabricated and tested a microfluidic device based on hydrodynamic focusing and a free-jet optimized for synchrotron SAXS time resolved measurements [4,5].

We have used the free jet micromixer directly at the beamline. A conceptual scheme of the measurement is shown in Fig. 1. Synchrotron SAXS measurements have first been conducted along the jet containing only one of the reagents (buffer, nanoparticles, buffer plus nanoparticles, protein). This is fundamental to determine the position (and therefore the time) of the jet instability, and have a reference curve for the subsequent measurements. In fact, we have already demonstrated that the jet itself produces a scattering signal that must be taken into account [6].

We have then performed the SAXS measurements of the real reaction of aggregation of silica nanoparticles due to protein adsorption with the micromixer. We have investigated one lysozyme concentration, one nanoparticle concentration, and one pH. The onset of aggregation has been detected, demonstrating the suitability of this technique for such kind of studies.

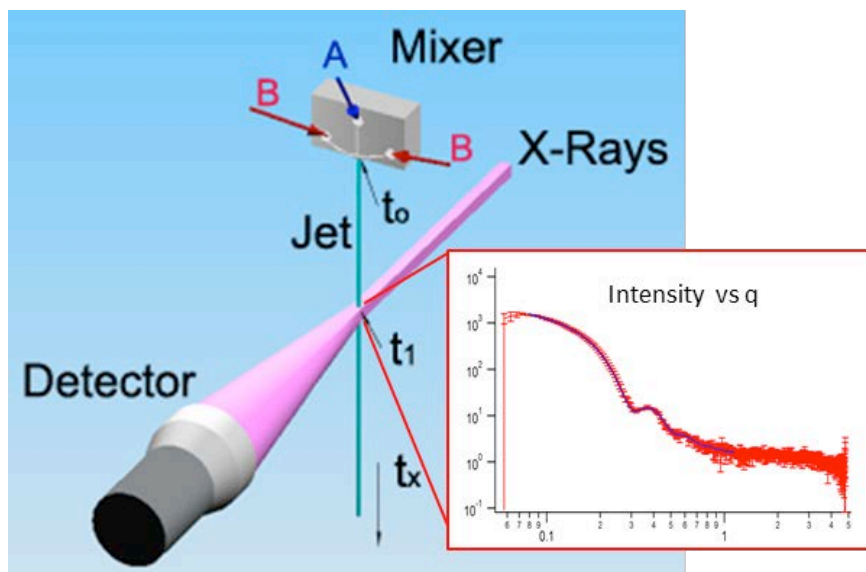


Figure 1. Conceptual scheme of time resolved measurements of nanoparticles/protein interaction by using the micromixer in combination with SAXS. Reagents A (nanoparticles) and B (protein) are injected in the device. The mixing is performed inside the microfluidic circuit, and at the exit of the device a free liquid jet in air is formed. The liquid jet is investigated by synchrotron SAXS

References:

- [1] A.E. Nel, L. Mädler, D. Velegol, T. Xia, E.M.V. Hoek, P. Somasundaran, F. Klaessig, V. Castranova, M. Thompson, Understanding biophysicochemical interactions at the nano–bio interface, *Nature Materials* 8, 543-557 (2009)
- [2] B. Bharti, J. Meissner, G.H. Findenegg, Aggregation of Silica Nanoparticles Directed by Adsorption of Lysozyme; *Langmuir*, 27, 9823 (2011)
- [3] B. Bharti, J. Meissner, S.H.L Klapp, G. H. Findenegg; Bridging interactions of proteins with silica nanoparticles: The influence of pH, ionic strength and protein concentration, *Soft Matter* 10, 718–728 (2014)
- [4] B. Marmiroli, G. Greci, F. Cacho-Nerin, B. Sartori, E. Ferrari, P. Laggner, L. Businaro, H.Amenitsch, Free-jet micromixer to study fast chemical reactions by small angle X-ray scattering; *Lab Chip* 9, 2063 (2009)
- [5] B. Marmiroli, G. Greci, F. Cacho-Nerin, B. Sartori, P. Laggner, L. Businaro, H.Amenitsch, Experimental set-up for time resolved small angle X-ray scattering studies of nanoparticles formation using a free-jet micromixer; *Nuclear Instruments and Methods in Physics Research B* 268, 329–333 (2010)
- [6] B. Marmiroli, F. Cacho-Nerin, B. Sartori, J. Perez, H. Amenitsch, Thorough small-angle X-ray scattering analysis of the instability of liquid micro-jets in air; *J. Synchrotron Rad.* 21, 193 (2014)

EFFECT OF PROTEIN LIPIDATION ON THE STRUCTURAL PROPERTIES OF EXOSOMES RELEASED BY SKELETAL MUSCLE CELLS

V. Martorana¹, S. Raccosta¹, R. Noto¹, V. Buffa², D. Romancino², A. Bongiovanni² and M. Manno¹

1.) National Research Council of Italy, Institute of Biophysics, via Ugo La Malfa 153, Palermo, Italy

2.) National Research Council of Italy, Institute of Biomedicine and Molecular Immunology, via Ugo La Malfa 153, Palermo, Italy

Exosomes are small extracellular membrane vesicles (40–100 nm in diameter) secreted by a variety of cell types [1]. They are composed of a lipid bilayer containing cell-specific collections of proteins, lipids, and genetic material. Their main function is related to cell–cell communication through the transport of protein, RNA and other signaling molecules. Also, they may act as mediators in the tumorigenesis and metastasis phenomena. Several factors are emerging as important regulator of exosome role and function, such as the lipidic composition of the bilayer itself as well as the composition of protein associated with exosome biogenesis [2]. Recently, we have shown that Skeletal muscle (SkM) cells can release Alix-positive EVs, suggesting a new paradigm for understanding how muscles communicate with other organs, such as adipose tissue, bones, the brain, or tumors. Alix downregulation or lipidation lead to alterations of exosome characteristics and composition [3].

In this context, we focused on protein lipidation (and specifically on protein palmitoylation) as possible post-translational modification of specific regulators of extracellular vesicles biogenesis. We study the structural features of exosomes secreted by skeletal muscles cells at different stages of their differentiation and upon treatment with specific inhibitors of protein palmitoylation (2-Br-Palmitate, 2BP). Exosome from the muscle cell line C2C12 were isolated by ultracentrifugation (10000 g for 30 min.), allowing removal/isolation of larger microvesicles, and resuspension in PBS. The total amount of protein content in the vesicles lysate was measured using the BCA assay [3], and regulated to 1 mg/ml.

We measured two sets of vesicle samples. (1) First set (Fig. 1, left): Exosomes from muscles cell lines, pelleted by ultracentrifugation and resuspended in PBS. More specifically, the following samples were selected: (1.i) exosomes secreted within the first day of cell culture (cellular proliferation); (1.ii) exosomes secreted at the third day of cell culture (cellular differentiation); (1.iii) exosomes secreted at the third day and treated with 2BP, an inhibitor of protein lipidation; (1.iv) exosomes secreted within the sixth day of cell culture (cellular contraction). (2) Second set (Fig. 1, right): Microvesicles from muscles cell lines; four samples have been prepared as in the first set.

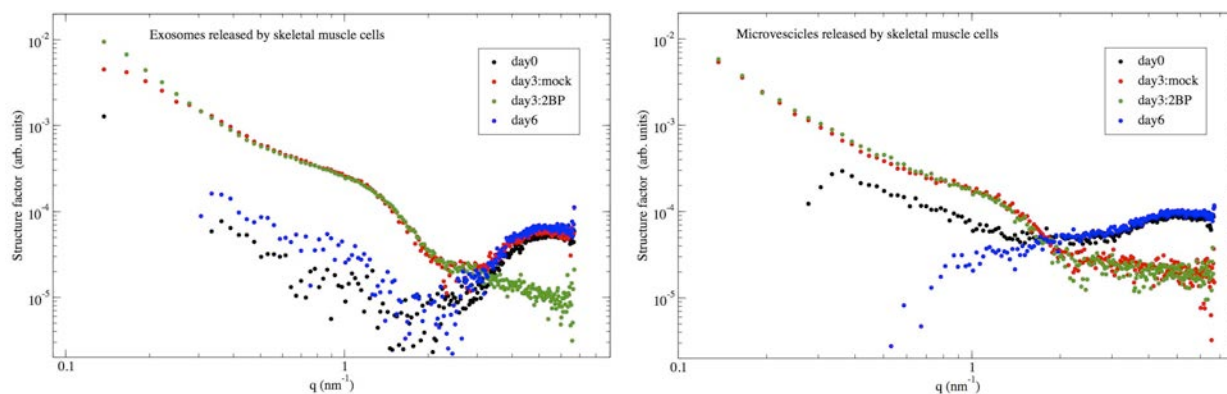


Figure 1. SAXS intensity profiles $I(q)$ for vesicles secreted by muscles cell lines with or without treatment with lipidation inhibitor 2BP and at different stages of differentiation. (a) nanoscale exosomes. (b) microvesicles

SAXS measurements were performed in the q range from 0.1 to 6.5 1/nm. For all the samples, several consecutive measurements of 60 seconds were performed. The data were averaged, since no evidence of radiation damage was observed. The buffer was measured for each vesicle sample by using the same capillary. The prepared concentration was at the lower limit available for recording a reliable signal. For some sample the signal was too low to allow a reliable background subtraction. In conclusion, we were able to optimise the experimental condition for such complex systems, in that we were able to identify the spectral range and the duration required for the measurements and to set the limit concentration. Notwithstanding the experimental limitations, the biological problem related to the effect of protein lipidation inhibitors was successfully addressed. Indeed we could observe a clear difference between exosomes secreted during cell differentiation and treated with lipidation inhibitors (Fig. 2, left). These differences are likely due to changes in the organisation level of lipid membrane. A deeper understanding of such a difference requires the interpolation of measured curves by currently available models of vesicles bilayers. [4]. This work is currently in progress.

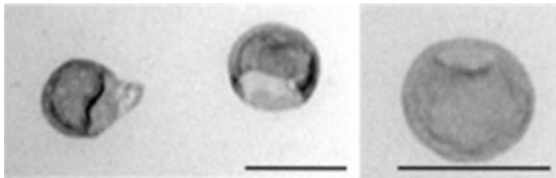


Figure 2. Electron-microscope analysis of vesicles purified from conditioned-media of C2C12 myotubes, scale bar 100 nm (redrawn from ref. [3])

References:

- [1] M. Simons and G. Raposo; Exosomes – vesicular carriers for intercellular communication. *Curr Opin Cell Biol* **21**, 575–81 (2009)
- [2] C. Théry, L. Zitvogel and S. Amigorena; Exosomes: composition, biogenesis and function. *Nature Reviews Immunology* **2**, 569–579 (2002)
- [3] D. Romancino, G. Paterniti, Y. Campos, A. De Luca, V. Di Felice, A. d’Azzo and A. Bongiovanni; Identification and characterization of the nano-sized vesicles released by muscle cells. *FEBS Lett.* **587**, 1379–1384 (2013)
- [4] S. Castorph, D. Riedel, L. Arleth, M. Sztucki, R. Jahn, M. Holt and T. Salditt; Structure Parameters of Synaptic Vesicles Quantified by Small-Angle X-Ray Scattering. *Biophys. J.* **98**, 1200–1208 (2010)

ANALYSIS OF SELF-ASSEMBLY PROPERTIES OF GUANOSINE IN AQUEOUS SOLUTION IN THE PRESENCE OF SILVER IONS

S. Moscatelli and P. Mariani

Università Politecnica delle Marche, Dipartimento di Scienze della Vita e dell'Ambiente, Via Brecce Bianche, 60131 Ancona, Italy

G-quadruplexes are helical structures formed by self-assembling of guanosine derivatives in water and in the presence of monovalent cations (Na^+ , K^+ or NH_4^+). G-quadruplexes are made by tetrads (G-quartets) stacked one on the top of the other at a distance of 3.4 Å, each of the tetrads consisting of four planar guanine molecules, arranged in a cyclic pattern according to the Hoogsteen scheme. Depending on concentration and temperature, G-quadruplexes exhibit an additional long-range organization, characterized by the formation of hexagonal and cholesteric lyotropic phases [1]. SAXS experiments demonstrated that G-quadruplexes are relatively short (typically, from 30 to 150 Å), but their length is strongly dependent on counter-ion concentration and on temperature. It has been suggested that counter-ions compete for quadruplex major and minor binding sites, stabilizing the final structure in different ways (see Figure 1) [2].

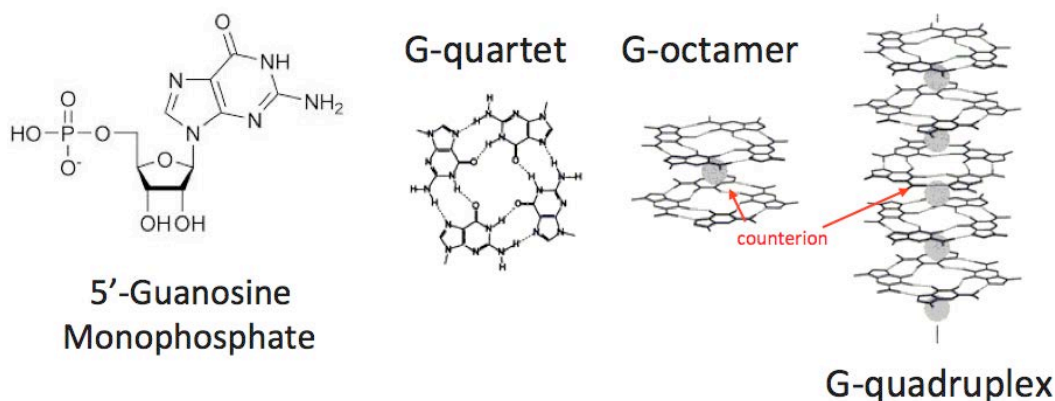


Figure 1. Schematic representation of the structure of GMP aggregates. From the left: monomer; G-quartet; G-octamer; G-quadruplex. The gray spheres represent the cations

The structural properties of GMP in solution and in the presence of silver ions are particularly interesting. In fact, on the basis of optical microscopy and X-ray diffraction results, it has been proposed that the presence of Ag^+ modifies the assembly of GMP at high concentration, with the formation of dimers [3]. Therefore, an alternative arrangement of nucleobases through the coordination of silver with electron-rich functional groups in respect to the other ions widely studied, such as Na^+ , K^+ or NH_4^+ that promote G-quartet self-association, has been proposed.

To derive information about self-assembling in dilute conditions and to obtain the size and shape of the species forming in the presence of Ag^+ , SAXS experiments were performed at the Elettra Synchrotron (Trieste, Italy) at the SAXS beam-line. Samples were prepared dissolving at $c = 1$ and $c = 5$ wt% (c is the GMP weight concentration, in %) the GMP salt powder in bi-distilled water containing different silver chloride solutions. The investigated temperature ranges from 20 to 50 °C. However, because the self-assembling process and the correlated polymorphism are strongly influenced by all the counterions present in solution, samples were prepared using different GMP salts, *e.g.* GMP/Na in NaCl, KCl or Ag_2SO_4 .

A few data are reported in the Figure 2.

Data analysis is still in progress, but SAXS data confirm the presence of a different GMP structure in the presence of large amount of silver ions and give evidence for the occurrence of a strong aggregation when the concentration of Ag^+ increases (see the broad band at $Q = 0.29 \text{ \AA}^{-1}$ in the case of GMP/K samples in Ag_2SO_4).

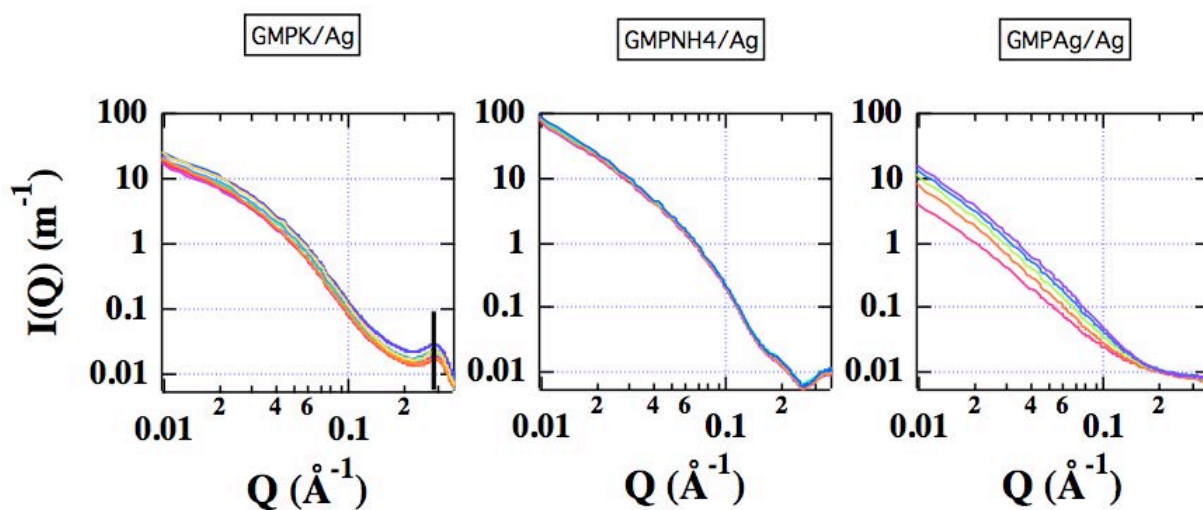


Figure 2. In-solution SAXS profiles observed for GMP at concentration of $c = 5 \text{ wt}\%$ at different temperatures (temperature increases from blue to red curves). The kind of sample is indicated in the frame

References:

- [1] A. Garbesi, G. Gottarelli, P. Mariani and G. P. Spada, *Pure & Appl. Chem.* **65**, 641-646 (1993)
- [2] P. Mariani, F. Spinuzzi, F. Federiconi, H. Amenitsch, L. Spindler and I. Drevensek-Olenik. *J. Phys. Chem. B*, **113**, 7934-7944 (2009)
- [3] K. Loo, N. Degtyareva, J. Park, B. Sengupta, M. Reddish, C.C. Rogers, A. Bryant, J.T. Petty, *J. Phys. Chem. B*, **114**, 4320-4328 (2010)

AMYLOID BETA PEPTIDE AGGREGATION INFLUENCED BY CURCUMIN-LIKE COMPOUNDS

M. G. Ortore¹, C. Ricci¹, S. Vilasi², M. R. Mangione², D. Bulone², A. Palumbo Piccionello³ and P.L. San Biagio²

1.) Università Politecnica delle Marche, via brecce bianche, Ancona, Italy

2.) Istituto di Biofisica, CNR, via U. La Malfa, Palermo, Italy

3.) Università degli Studi di Palermo, viale delle scienze, Palermo, Italy

Alzheimer's disease (AD) is a chronic and progressive syndrome characterized by the accumulation of a 40-42 aminoacids peptide, the amyloid-beta peptide (A β), in insoluble cerebral plaques, known as amyloid fibrils. Curcumin is considered a candidate drug for enhanced clearance of the toxic amyloid generated by the A β peptide. A recent study suggests that curcumin does not inhibit fibrillation of A β , but promotes amyloid fibril conversion by reducing the pre-fibrillar/oligomeric species of A β [1]. Although previous Small Angle X-ray Scattering (SAXS) experiments on the effects of curcumin on A β fibrillization evidenced that curcumin can modify the aggregation pattern, the molecular description of the effects of curcumin on intermediate and fibrillar species is still a matter of debate. Because the idea of using curcumin for therapeutic purposes in AD presents big limitations inherent to its poor solubility, stability and ability to permeate the blood-brain barrier (BBB), we synthesized compounds with the same ability of curcumin to bind A β peptide, but that do not present stability and bio-availability problems, allowing a real applicability in the treatment of AD. In this sense, the replacement of 1,3-dicarbonilic nuclei with heterocyclic isosteres is a promising strategy, which has already allowed to identify isoxazole and pyrazole [2] derivatives capable to bind A β in the same manner as curcumin. This background shows that, although A β /curcumin and A β /curcumin-like molecules interactions draw the attention of scientific communities ranging from medicine to biology, from chemistry to physics, a quantitative description of the influence of these molecules on the complex aggregation pattern of A β in solution, in conditions similar to those in vivo, is still lacking.

Because the A β peptide interaction with curcumin (and curcumin-like molecules) depends on its aggregate conformation, we investigated both the effect of the curcumin-like compounds on A β mature fibrils, and their effect on A β monomers whose aggregation was induced by gentle agitation at 37°C. While no effect of curcumin-like molecules was detected on mature fibrils, changes in the aggregation pattern with or without curcumin-like molecules were obtained.

A β peptide was let to fibrillate at 37°C for 7 hours at a concentration equal to 50 μ M, and then concentrated until the 200 μ M value. The same procedure was followed with A β peptide with the curcumin-like compound we nominated NV2034 at a final concentration of $c=186\mu$ M in the presence of 3% v/v DMSO. The low amount of DMSO was necessary to dissolve the curcumin-like compound in the aqueous buffer. SAXS experimental curves reported in Figure 1 suggest that, even though the final aggregated stages are not dramatically different, some changes can be appreciated.

In particular, the low- q range of the SAXS curves could be fitted by a Guinier approach, according to the equation $d\Sigma/d\Omega(q) = d\Sigma/d\Omega(0) \exp(-Rg^2q^2/3)$, and the results are reported in the caption of Fig. 1. The average dimensions of the globular objects in solution detected are bigger in the case of amyloid beta peptide aggregation without the curcumin-like compound. Although this approach provides information only on the wider compact species, it appears meaningful that the NV2034 compound is able to limit the presence of bigger aggregates.

Furthermore, the whole SAXS curves corresponding to samples aggregated with or without the curcumin-like compound (Figure 1), let us to evaluate that NV2034 modifies the aggregated species distribution.

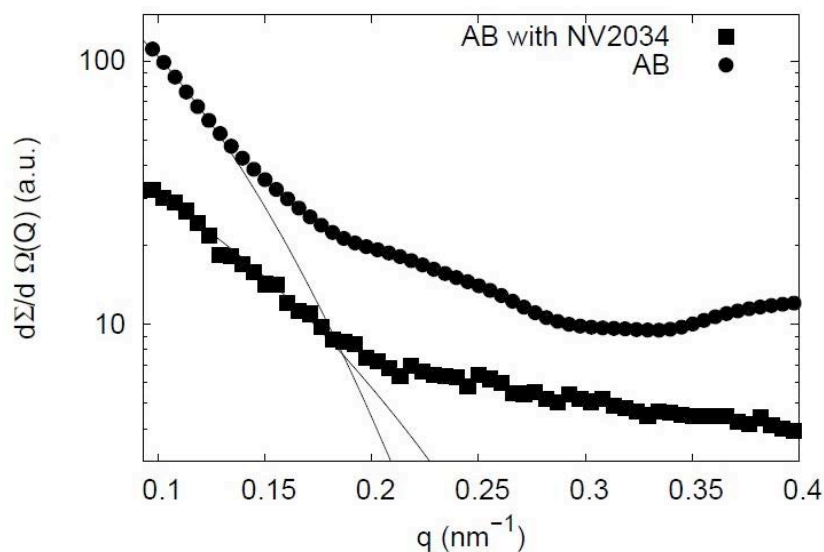


Figure 1. SAXS experimental curves corresponding to amyloid beta peptide aggregated for 7 hours at 37°C (circles), and to amyloid beta peptide aggregated in the same conditions together with the curcumin-like compound NV2034 at a concentration $c=186\mu\text{M}$ in presence of 3% v/v DMSO (squares). Theoretical fitting curves obtained by the Guinier approximation: the resulting radii of gyration are $R_g=(12.8\pm 0.2)$ nm for the amyloid beta peptide incubated with the curcumin-like compound and $R_g=(17.7\pm 0.2)$ nm for the amyloid beta peptide alone. The experimental curves are scaled for the sake of clarity

This result is comparable to the one obtained in a previous study with curcumin [2] and let us to suggest that the most toxic oligomeric species present in the amyloid beta peptide aggregation pattern, could be absent or quickly converted into fibrils in presence of this new soluble and not cytotoxic compound. Further analysis will take into account the presence of multiple species in solution, aimed to determine the consistency of our hypothesis. Also, the analysis of the effects of the other investigated curcumin-like compound is still in progress and complementary techniques are considered in order to clarify several molecular and environmental features of this delicate and promising effects.

References:

- [1] I. Caesar, M. Jonson, K. P. R. Nilsson, S. Thor and P. Hammarstrom. PLOS ONE. 2012. 7, 2: e31424
- [2] R. Narlawar, M. Pickhardt, S. Leuchtenberger, K. Baumann, S. Krause, T. Dyrks, S. Weggen, E. Mandelkow and B. Schmidt, Chem Med Chem. 2008, 3: 165

INVESTIGATION OF VIMENTIN ASSEMBLY BY COMBINING SAXS AND DROPLET MICROFLUIDICS

O. Saldanha¹, C. Hémonnot¹, R. Graceffa¹, B. Marmioli², B. Sartori², H. Amenitsch² and S. Köster¹

1.) Institute for X-ray Physics, Friedrich-Hund-Platz 1, 37077, Göttingen, Germany

2.) Institute of Inorganic Chemistry, Graz University of Technology, Stremayrgasse 9/IV 8010 Graz, Austria

Vimentin is an intermediate filament (IF) protein found in the cytoskeleton of mesenchymal cells, which plays an instrumental role in cell mechanics. Together with actin filaments and microtubules, vimentin IFs form an intricate network in cells which provides stability, enables motion and bears external forces. The hierarchical assembly from smaller subunits, namely tetramers, into extended, micrometer-long filaments occurs first laterally and then longitudinally [1]. The aim of this present experiment was to access the early stages of this assembly process in the presence of monovalent K^+ ions at a temporal resolution of milliseconds to seconds. For this purpose, we employed droplet microfluidics to encapsulate the assembling protein, thereby preventing adhesion to the microfluidic channel walls. In the past, we had performed bulk SAXS studies of vimentin filaments in the presence of mono- and divalent ions [2] as well as microscopy investigations of network formation from these filaments [3-5] and could thus relate our present measurements to those previous results.

X-ray compatible microfluidic devices fabricated as a PDMS (polydimethylsiloxane)-capillary ensemble were used for producing micron-sized aqueous drops in oil (see Fig. 1). These devices combined two advantages: within the PDMS part, controlled water-in-oil droplet generation was realized whereas the measurement region consisted of a X-ray compatible quartz capillary. By using microfluidics we take advantage of the reduction of radiation damage when sensitive biological material is probed, since the material flows by the beam. In our device design, three aqueous inlets 1,2,3 mix the protein with K^+ ions separated by a stream of buffer. The droplets are then pinched off by the oil phase flow (inlet 4) from adjacent channels [3,5]. These droplets flow down the outlet channel into the quartz capillary. Data were taken at several positions along the capillary enabling us to convert the spatial axis

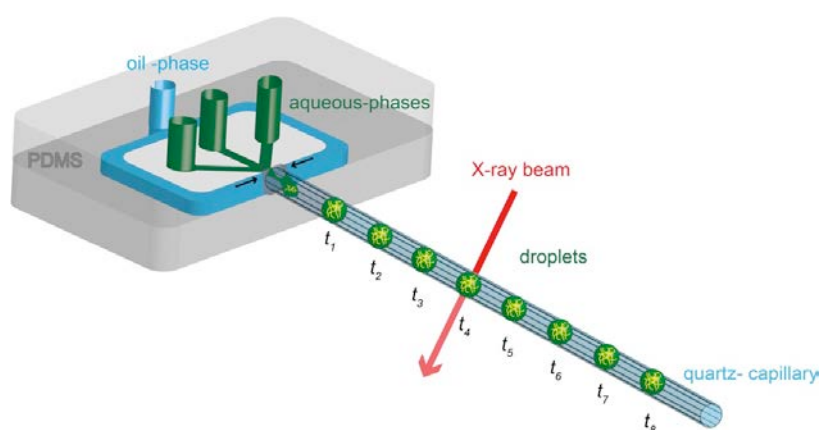


Figure 1. Schematic representation of the X-ray compatible composite PDMS- capillary device for droplet production

into a time axis and reaching a temporal resolution of milliseconds. Exposure times of 10 minutes were employed during which a large number of drops containing vimentin in the same assembly state were flowing by and were averaged. The beam spot was defined by a 50 μm diameter pinhole to fit in the capillary (inner diameter 80 μm) and avoid streaks stemming

from the capillary edges. The data were collected using a PILATUS 1M single-photon counting pixel detector.

Radial intensity curves $I(q)$ of vimentin at 4 different positions along the capillary, corresponding to 4 different time points, are plotted in Fig. 2. The intensity at the first position corresponds to the earliest time point with respect to the point of droplet pinch off i.e., at 0.09 s and then increases up 2.7 s. At this time point, vimentin tetramers have laterally assembled into so-called unit length filaments (ULFs). Thereafter, elongation starts and a shoulder at $\sim 0.3 \text{ q nm}^{-1}$ emerges; hinting at the developing form factor. However, no information can be obtained at lower q due to the absence of a well formed Guinier region. With this experiment, we have demonstrated that the study of assembly with droplets in flow by SAXS is feasible and the accessible time scales range from milliseconds to seconds, which is exactly what we need to understand the assembly of many biological macromolecules.

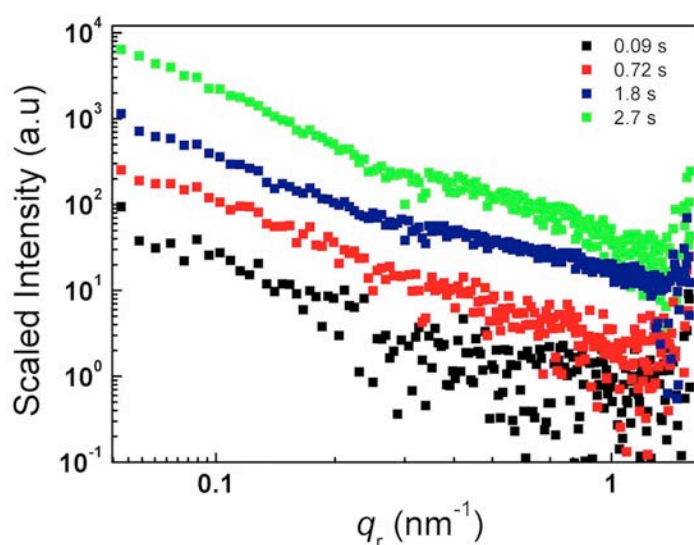


Figure 2. Radially integrated intensity profiles of the different stages of vimentin assembly

References:

- [1] M.E. Brennich, J.F. Nolting, C Dammann, B Nöding, H Herrmann, T Pfohl and S Köster; *Lab on a Chip* **11**, 708-716 (2011)
- [2] M.E Brennich, S Bauch, U Vainio, T Wedig, H Herrmann and S Köster; *Soft Matter* **10**, 2059 – 2068 (2014)
- [3] C Dammann and S Köster; *Lab on a Chip* **14**, 2681 – 2687 (2014)
- [4] C Dammann, H Herrmann and S Köster; *Israel Journal of Chemistry* 00212148, (2015)
- [5] C Dammann, B Nöding and S Köster; *Biomicrofluidics* **6**, 022009 (2012)

Material Science

APPLICATION OF SAXS TO THE STUDY OF BIOGENIC NANOPARTICLE FORMATION

P. S. Bauer¹, H. Amenitsch², and P. M. Winkler¹

1.) Faculty of Physics, University of Vienna, Boltzmanngasse 5, 1090 Wien, Austria

2.) Institute of Inorganic Chemistry, Graz University of Technology, Stremayrg. 9/IV, 8010 Graz, Austria

Gas-to-particle conversion is known to dominate the aerosol number concentration in the global atmosphere [1]. Besides sulfuric acid, oxidized organic molecules originating from biogenic emissions have been identified as major contributors to the growth of newly formed nanoparticles [2]. The rigorous study of airborne particles in the size range from 1 nm to 50 nm is hence crucial for a better understanding of the underlying nanoparticle formation mechanisms.

In this study we aimed at the characterization of biogenic nanoparticles that were formed in a flow tube from precursor gases after chemical reaction with ozone based on a set-up described in [3]. For the first time SAXS was applied to study in-situ particle evolution and dynamics. To this end, we constructed a glass tube (inner diameter 5.6 cm, 150 cm long) that was mounted in an aluminum block to allow positioning at the SAXS experimental stage. Figure 1 shows a picture of the main components of the experimental set-up. 20 cm from one end of the tube we cut openings into the glass to allow penetration of the x-ray beam perpendicular to the gas flow. Kapton windows (thickness 8 μm) were installed inside the aluminum block to separate ambient pressure of the tube from vacuum of the x-ray beam.

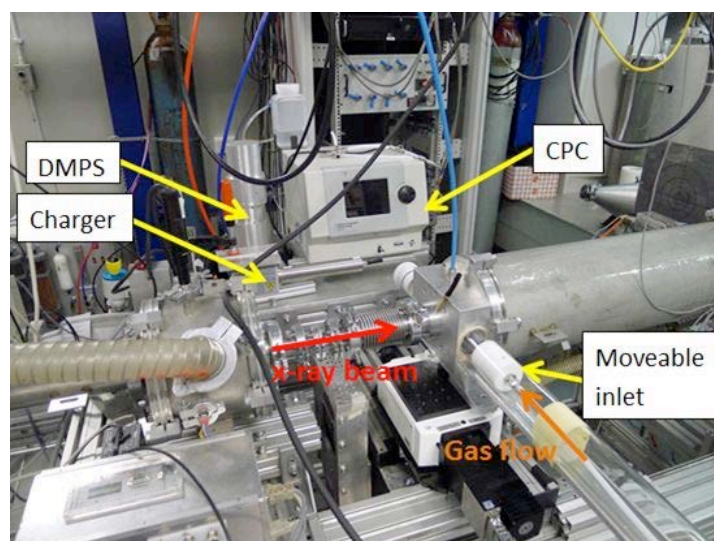


Figure 1. Experimental set-up of aerosol flow reactor at the SAXS beamline showing the main aerosol measurement devices. See text for explanation

Particles were generated by reacting α -pinene vapor with ozone in dry clean air. The vapor was introduced into the system by head space sampling at a flow rate of 60 ml/min over liquid α -pinene at room temperature. This flow was subsequently diluted by dry clean air at a flow rate of 6 l/min. Shortly before the inlet of the glass tube ozone was added from a discharge ozone generator at 1 l/min. Thereby, ozone concentrations between 0 and 2000 ppbv could be obtained, depending on the potentiometer settings of the ozone generator. The vapor-air-ozone mixture was then introduced into the flow tube to allow for a certain residence and hence reaction time. The residence time was adjustable by a moveable inlet allowing us to

control the particle size distribution in the measurement cell. Typical inlet positions relative to the front end of the aluminum block were ranging from 20 cm to 100 cm.

The experimental set-up was complemented by an ozone monitor and aerosol instrumentation at the exit of the flow tube to monitor ozone concentration and particle evolution. A differential mobility particle sizer (DMPS) together with a soft x-ray aerosol charger was used to measure particle size distributions. A condensation particle counter (CPC) simultaneously measured total particle number concentration.

After final alignment of the measurement cell we performed calibration tests with a silver behenate standard to check the pre-calculated scattering range and detector position. Thereby, the design of the optical ports as well as the size of the measurement cell was found to be appropriate for the planned experiments. However, first experiments soon revealed that substantial particle deposition on the Kapton windows prevented us from doing in-situ measurements of growing biogenic nanoparticles.

As a consequence, in a follow-up study we designed a similar flow tube equipped with a sheath air flow to protect the windows. However, more success was achieved by replacing the Kapton by aluminum coated, electrically conductive Kapton. Despite a higher background from the aluminum, the signal from deposition was reduced significantly. We then used tungsten oxide (WOx) particles to increase the scattering contrast to the gas. In a defined sequence regulated by a flow switching module we alternated SAXS measurements between pure gas and particle-laden air over a period of one and a half hours. Figure 2 illustrates background subtracted SAXS signals from WOx particles with a mean diameter of ~20 nm. As can be seen, the signal is still weak; however, there is some indication that we have now found a procedure and appropriate conditions that will allow us in-situ nanoparticle studies by SAXS. In a next step, we are aiming at a reduced carrier gas pressure to further increase the signal-to-noise ratio and identify conditions that will allow the characterization of biogenic nanoparticles. In the meanwhile, our experiment has been highlighted in the first Ceric-Eric-Newsletter [4].

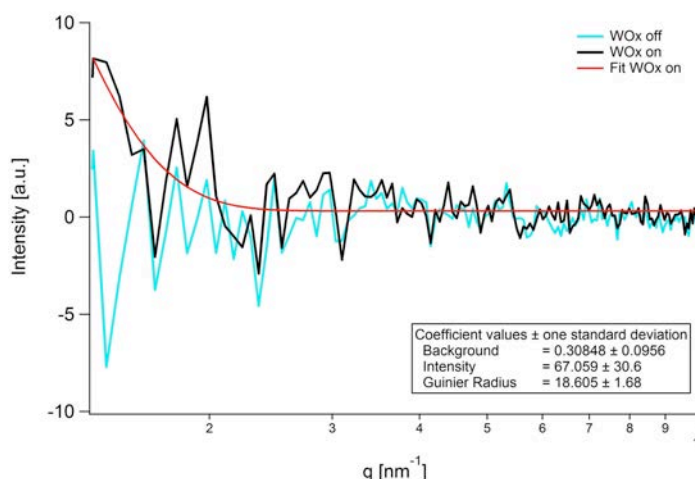


Figure 2. SAXS signals from WOx particles after background subtraction obtained by measuring pure air (WOx off) and particles (WOx on) alternately. The fit is a Guinier-Fit with a radius of gyration of 18.6 nm for the particle laden case (WOx on)

References:

- [1] M. Kulmala, et al., Formation and growth rates of ultrafine atmospheric particles: a review of observations, *J. Aerosol Sci.* 35, 143 (2004)
- [2] J. Jimenez, et al., Evolution of Organic Aerosols in the Atmosphere, *Science* **326**, 1525 (2009)
- [3] P. M. Winkler, et al., Identification of the biogenic compounds responsible for size-dependent nanoparticle growth, *Geophys. Res. Lett.* 39, L20815 (2012)
- [4]] https://www.ceric-eric.eu/uploads/Media/newsletter_n.1.pdf (April 2015)

FORMATION OF P123-MEDIATED AU-NANOPARTICLES IN AQUEOUS SOLUTION: IN-SITU X-RAY SCATTERING STUDY

M. Buljan¹, T. Car¹, N. Nekić¹, M. Jerčinović¹, I. Delač Marion², M. Kralj², I. Bogdanović-Radović¹, K. Salamon², S. Bernstorff³ and N. Radić¹

1.) Ruđer Bošković Institute, Bijenička cesta 54, 10000 Zagreb, Croatia

2.) Institute of Physics, Bijenička cesta 46, 10000 Zagreb, Croatia

3.) Elettra-Sincrotrone Trieste, SS 14 km 163.5, 34149 Basovizza, Italy

Films consisting of Ge quantum dots (QDs) embedded in conductive ITO matrix are very interesting since such films are widely used as transparent conducting films as well as for photovoltaic applications and touch-screen displays. However, in the literature exist only a very few studies of this system, and they all have a specific Ge/ITO multilayer structure in which the ITO-spacer layer was always much thicker than the Ge layer. For such geometry it is very likely that the transport properties of the films are mainly determined by the more-conductive ITO layers. In this work we investigate Ge-ITO systems consisting of Ge QDs embedded in layers that are very close to each other and also in continuously mixed Ge+ITO systems. These systems may be considered as 3D arrays of closely packed Ge QDs, so the transport properties in all directions are strongly affected by the Ge QDs. We show that the presence of Ge in these systems significantly influences the electrical properties of the material.

Four types of Ge+ITO films were produced by a magnetron sputter deposition system. Two film types consist of a (Ge/ITO)×30 multilayer and the other two of a Ge+ITO mixture, both of them were produced at a deposition temperature of RT and 300°C. All films were annealed in a separate furnace up to 500°C for 45 min. The films are denoted by the preparation method (Ge/ITO for the multilayer and Ge+ITO for the mixture) followed by the deposition temperature in parentheses. The structural properties of the films were determined by grazing incidence small angle X-ray scattering (GISAXS), atomic force microscopy (AFM), transmission electron microscopy (TEM), Raman spectroscopy and X-ray diffraction (XRD). The GISAXS and XRD measurements were simultaneously performed at the synchrotron Elettra, using a photon energy of 8 keV.

The GISAXS, TEM and AFM measurements on the as-grown films are demonstrated in Fig. 1. The GISAXS map of the multilayer Ge/ITO (RT) film and the corresponding AFM image of the film surface are shown in Figs. 1(a),(b) respectively. The GISAXS map exhibits a horizontal sheet centred at $(Q_y, Q_z) = (0.0, 2.7) \text{ nm}^{-1}$ and two vertical sheets centred at $|Q_y| = 0.23 \text{ nm}^{-1}$. The horizontal sheet is related to the multilayer structure of the film with a period of $2.3 \pm 0.1 \text{ nm}$. The vertical sheets show the presence of ordered nano-objects with a characteristic distance of 25 nm in the direction parallel to the surface. The measurements were performed at different grazing incidence angles of the x-rays, and indicate that the detected nano-objects are on the films surface. A similar conclusion can be drawn from the AFM measurement shown in Fig. 1(b). The surface morphology features visible in the AFM image have an ordering that can be described by a distorted hexagonal lattice, as follows from the self-correlation image shown in the inset of Fig. 1(b). The separation between them is $25 \pm 2 \text{ nm}$, as was found also by GISAXS analysis. Such surface morphology features are often related to the presence and specific ordering of Ge clusters below the surface (Buljan et al. 2009.; Buljan et al. 2013). The mixture Ge+ITO (RT) film (Fig. 1(c)) is showing a very similar surface morphology but with a larger separation of $37 \pm 2 \text{ nm}$. The GISAXS map of the Ge/ITO (300°C) film is shown in Fig. 1(d). It is interesting that the multilayer structure is not visible in the GISAXS map (the horizontal sheet is not visible). However, it is well visible in

the TEM image of the film's cross-section shown in Fig. 1(e). The multilayer period is found to be 2.4 ± 0.1 nm what is nearly equal to the period of the multilayer film deposited at RT. The measured GISAXS intensity for this film consists mainly of the semi-circular intensity originating from the shape (nearly spherical) of the embedded nanoparticles. A very similar GISAXS map (Fig. 1(f)) shows the Ge+ITO (300°C) film. No specific surface-related features are visible in the GISAXS map, only the semi-circular intensity originating from the QD shape properties.

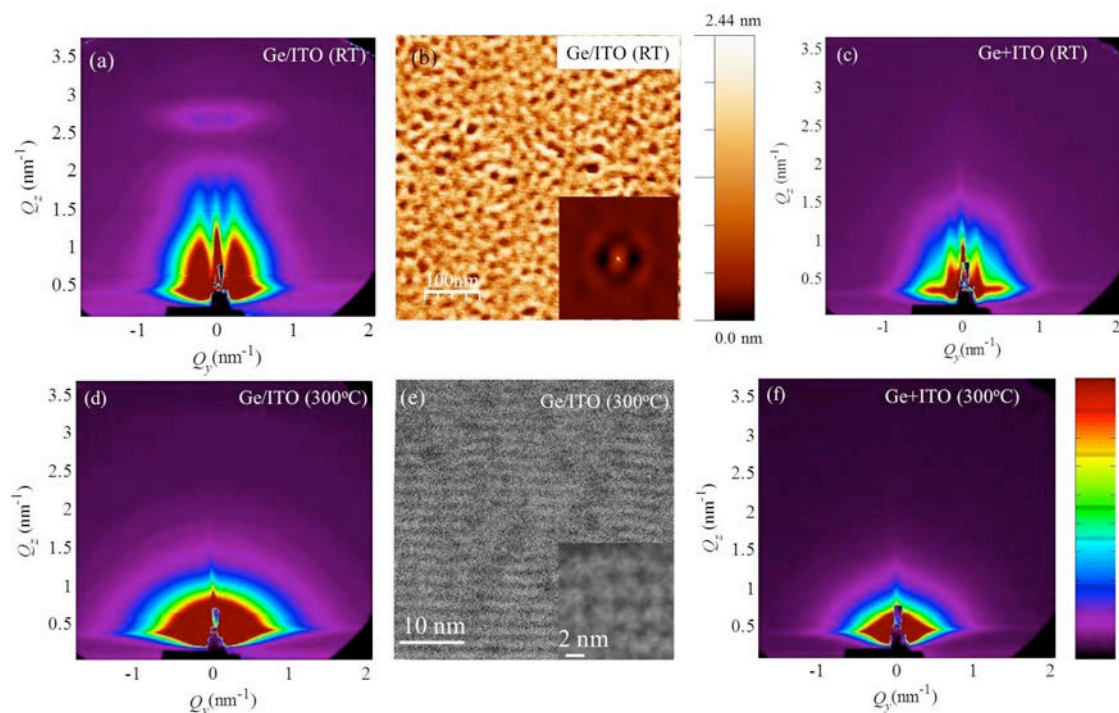


Figure 1. (a) GISAXS intensity map and (b) AFM amplitude image of Ge/ITO (RT) film. The inset shows a self-correlation map of the AFM image. (c) GISAXS map of Ge+ITO (RT) film. (d), (e) GISAXS map and cross-sectional TEM image of Ge/ITO (300°C) film. The inset shows an enlarged part of the multilayer cross-sectional TEM image where QDs are visible. (f) GISAXS map of Ge+ITO (300°C) film

The XRD and Raman analyses show that the crystallization of Ge occurs at 400°C for the films deposited at RT, and at 300°C for the films deposited at 300°C (not shown here). A very interesting influence of the Ge crystallization on the films electric properties is found and demonstrated in Fig. 2. In Fig. 2(a) we compare the resistivity of the closely packed Ge QDs formed in the Ge/ITO(RT) (thickness ratio 0.4 nm/1.8 nm) and Ge+ITO (RT) films with the resistivity obtained for the Ge/ITO (0.4 nm /17 nm) multilayer film from Ref. [1], which has nearly the same Ge thickness, but approximately 10 times wider ITO layers. From the figure it is obvious that the resistivity strongly drops for the crystalline Ge QDs, and the closely packed Ge QDs from the Ge/ITO layers investigated here are nearly 100 times more resistive than the films with thicker ITO spacers. The resistivity drop occurs at 400°C for both films deposited at RT (Fig. 2(a)), while the same change occurs at 300°C for the films deposited at 300°C (Fig 2. (b)). The effect is the most pronounced for the mixed Ge+ITO (300°C) film, for which a drop of nearly 7 orders of magnitude occurs after Ge crystallization. The pure ITO film, shown in Fig. 2(c) does not show such behavior, only a slow decrease of the resistivity is observed instead. The resistivity as a function of the Ge percentage in the as grown and $T_a=400^\circ\text{C}$ annealed films are shown in Figure 2(d). The resistivity of the as-grown films significantly increases with the Ge percentage. However, the resistivity of the fully crystalline

films ($T_a=400^\circ\text{C}$) are all significantly lower than for the as-grown, and have a peak for the Ge/ITO multilayer film

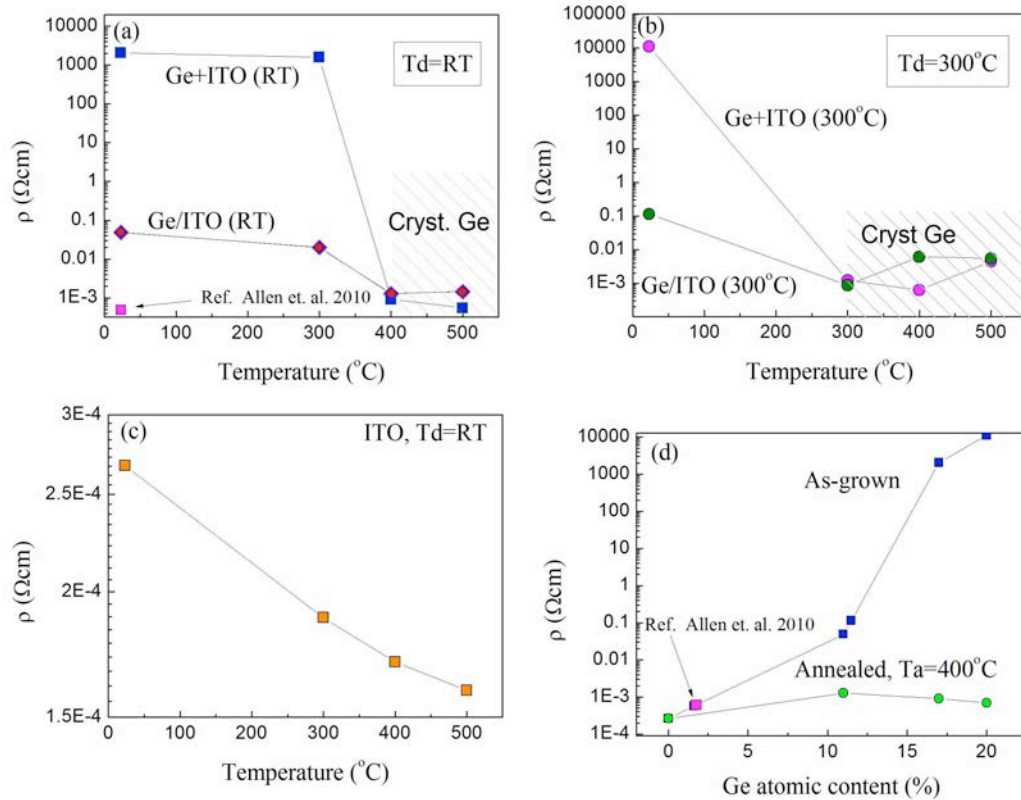


Figure 2. Resistivity as a function of the annealing temperature of: (a) Ge/ITO (RT) and Ge+ITO (RT), (b) Ge/ITO (300°C) and Ge+ITO (300°C). (c) Pure ITO films deposited at RT. (d) Resistivity of the as-grown films and annealed at $T_a=400^\circ\text{C}$ films as a function of the Ge percentage

This shows that the arrangement of the Ge QDs, i.e. the Ge/ITO thickness ratio has the main influence on their transport properties. Such finding is reasonable taking into account that ITO layers are significantly more conductive than Ge layers, so the transport occurs mainly through them. More details about these systems can be found in Ref. [2].

References:

- [1] C. G. Allen, G. H. Shih, and B. G. Potter, *Materials science and engineering B* **175** 150-158 (2010)
- [2] T. Car, N. Nekić, M. Jercinović, K. Salamon, I. Bogdanovic-Radović, I. Delač Marion, J. Dasovic, G. Dražić, M. Ivanda, S. Bernstorff, B. Pivac, M. Kralj, N. Radic and M. Buljan; under review (2015)

STRUCTURE OF SOFT NANOCOMPOSITES EXHIBITING CRYSTAL-TYPE ORDERING

G. Cordoyiannis^{1,2}, A. Abina³, U. Puc³, S. Kralj^{1,4}, A. Zidanšek^{1,3,4}

1.) Jozef Stefan Institute, Jamova cesta 39, 1000 Ljubljana, Slovenia

2.) Department of Physics, University of Athens, 15784 Athens, Greece

3.) Jozef Stefan International Postgraduate School, Jamova cesta 39, 1000 Ljubljana, Slovenia

4.) Faculty of Natural Sciences and Mathematics, University of Maribor, 2000 Maribor, Slovenia

In the past few years various types of colloids and nanoparticles (NPs) have been immersed in different soft matrices in order to substantially enhance effective material properties or to introduce qualitatively new properties and functionalities into systems. Pathways have been proposed towards tuneable soft metamaterials and self-healing mechanisms in polymers have been demonstrated [1, 2]. In particular, a rich diversity of possible behaviours is encountered in anisotropic soft materials, such as liquid crystals (LCs). The immersed particles could apparently disrupt soft LC structures and introduce long-range forces. In general, particles are attracted to locally elastically-distorted, non-singular or singular (topological defects) regions.

Our recent measurements (part of them performed at the Austrian SAXS Beamline of ELETTRA) demonstrate that the same kind of surface-functionalized CdSe quantum dots can be efficiently driven and trapped in cores of qualitatively different topological defects, stabilizing the resulting pattern [3]. The typical core sizes are comparable to the relevant order parameter correlation length ξ , which is in the nm scale. It is demonstrated that the trapped CdSe NPs efficiently stabilize both blue phase (BP) and smectic twist-grain boundary (TGB) defect lattice structures within the same chiral LC material. BP and TGB are characterized by lattices of topological defects in orientational and translational ordering, respectively. The stabilization of both defect structures is possible only if the NPs do not apparently disrupt these qualitatively different core structures, i.e., a NPs' surface needs to adapt to different environments. The stabilization of defects appears mainly due to a partial replacement of the singular defect core by the non-singular volume of trapped NPs. This points towards a universal character of this stabilization mechanism and its applicability to a rich variety of condensed matter systems exhibiting topological defects. Systematic experimental studies are needed to fully understand the mechanisms that govern the adaptability of the same type of NPs to various defect lattices, as well as to resolve the exact role of their size, shape and coating in the aforementioned phenomena.

In the experimental measurements performed at ELETTRA in July 2014 we have focused on two soft nanocomposites: liquid crystal CE8 + graphene oxide nanosheets decorated with small spherical nanoparticles (A) and CE8 + spherical Au nanoparticles (B).

The system (A) was studied in order to measure precisely the smectic layer periodicity and explore the possibility of graphene nanosheets being assembled among smectic layers. We have extracted the order parameter (i.e., tilt angle) evolution of the soft nanocomposite along the smectic-A to chiral-smectic-C transition. This is compared to the order parameter of the pure liquid crystal. Fits have been performed using the extended mean field model (i.e., a mean field behavior in the vicinity of a tricritical point).

The system (B) was studied at temperatures between the cholesteric and smectic-A phase, in order to see if the Au nanoparticles induce and stabilize the TGB structure. This was indeed confirmed by the characteristic trends in half-width at half-maximum as well as in the intensity of the quasi-Bragg smectic peaks. The use of Au nanoparticles is of particular

interest, in the search of novel soft metamaterials. The SAXS results from ELETTRA are combined with calorimetric ones as well as with measurements of the plasmon resonance of (B). Note that Au nanoparticles are of larger size compared to our older ones (CdSe, CdSSe) that were found to induce TGB structure in CE8 [4]. The stabilization of TGB structure supports the universal character of the proposed theoretical mechanism [3].

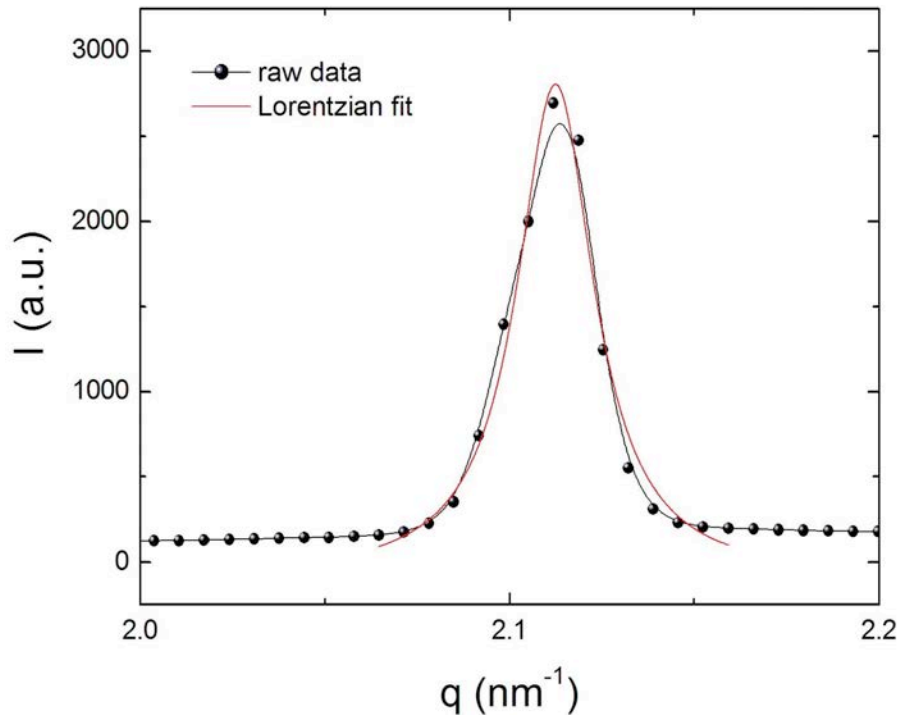


Figure 1. Intensity versus wavevector (I - q) plot in the smectic-A phase of system (B). The half-width at half-maximum and the maximum intensity are calculated by performing Lorentzian fitting of quasi-Bragg peaks

References:

- [1] A. C. Balazs, T. Emrick, T. P. Russell; Nanoparticle Polymer Composites: Where Two Small Worlds Meet; *Science* **314**: 1107-1110 (2006)
- [2] Q. Liu, Y. Cui, D. Gardner, X. Li, S. He, I.I. Smalyukh; Self-Alignment of Plasmonic Gold Nanorods in Reconfigurable Anisotropic Fluids for Tunable Bulk Metamaterial Applications; *Nano Lett.* **10**: 1347-1353 (2010)
- [3] G. Cordoyiannis, V.V. Rao Jampani, S. Kralj, S. Dhara, V. Tzitzios, G. Basina, G. Nounesis, Z. Kutnjak, C.S. Pati Tripathi, P. Losada-Perez, D. Jesenek, C. Glorieux, I. Muševič, A. Zidanšek, H. Amenitsch and J. Thoen; Different modulated structures of topological defects stabilized by adaptive targeting nanoparticles; *Soft Matt.* **9**, 3956-3964 (2013)
- [4] M. Trček G. Cordoyiannis, V. Tzitzios, S. Kralj, G. Nounesis, I. Lelidis and Z. Kutnjak; Nanoparticle induced twist grain boundary phase; *Phys. Rev. E* **90**, 032501 (2014)

PULSED LASER DEWETTING OF ALUMINIUM

P. Dubček¹, B. Pivac¹, N. Radić¹, N. Krstulović² and S. Bernstorff³

1.) Ruđer Bošković Institute, Bijenička 54, 10000 Zagreb, Croatia

2.) Institute for Physics, Bijenička 46, HR-10000 Zagreb, Croatia

3.) Elettra - Sincrotrone Trieste, SS 14, km 163.5, 34149 Basovizza (TS), Italy

Aluminium nanoparticles are good candidates for light absorption enhancement in future photovoltaics. When placed close to the photoactive layer or in the bulk of the heterojunction, they enhance the efficiency of photovoltaic devices, so that it can exceed 20%. However, this improvement requires a good control of the particles size and space distribution, which so far is only achievable at prohibitively high temperatures, which tend to damage the heterojunction structure itself. Therefore, laser dewetting is an alternative method of creating plasmonic nanoparticles, avoiding the need for excessive temperatures in the photovoltaic production.

Here we report on aluminium nanoparticle production by laser induced dewetting. Magnetron sputtering was used to produce 10 nm thick aluminum films which were sputtered onto Si(100) substrate, held at room temperature, under 1 mBar of pure Ar pressure. The dewetting was carried out in a vacuum chamber, pumped down to a base pressure of 10^{-3} mbar, using a nanosecond Q-switched Nd:YAG laser (Quantel Brilliant, 4 ns pulse length, 5 Hz repetition rate, output wavelength 1064 nm). An Al sample was placed in a target holder and kept at a floating potential and room temperature. The sample was rotated to avoid drilling and to treat the sample homogeneously. The laser pulse was defocused using a 10 cm lens in order to decrease the fluence to desired values giving a laser pulse spot area of 0.8 cm^2 . The distance between sample and lens was 35 cm. The sample was exposed to different laser pulse numbers, and a variety of laser output fluences ranging from 70 mJ/cm^2 to 200 mJ/cm^2 . The effects of irradiation/dewetting were investigated by GISAXS.

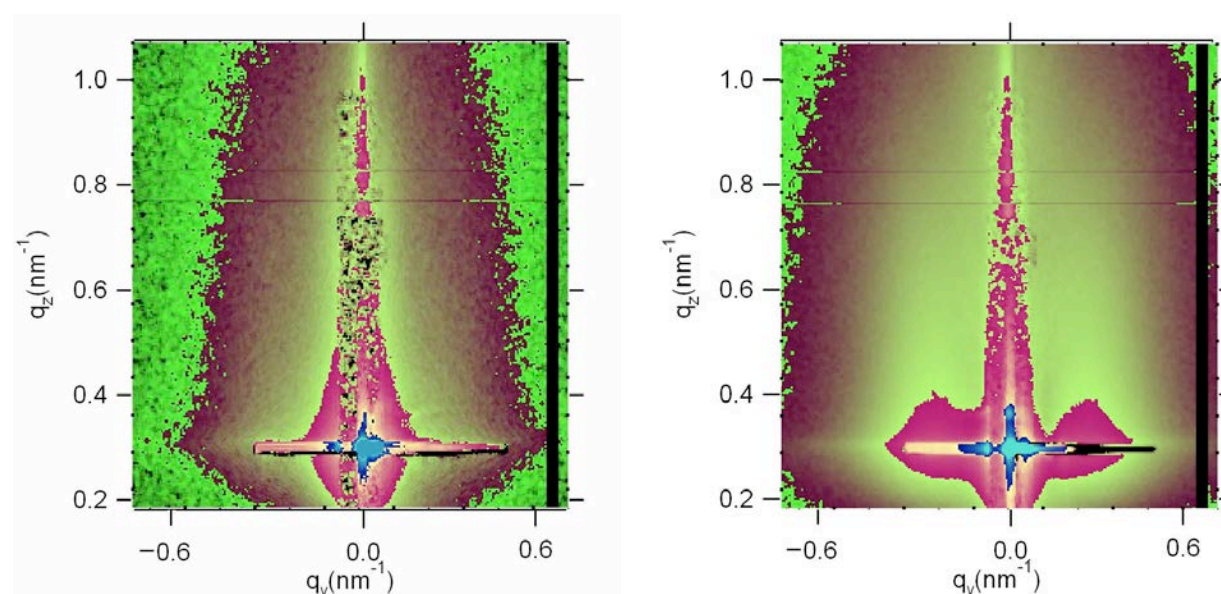


Figure 1. GISAXS from samples irradiated by 10000 pulses and 120 mJ/cm^2 (left) and 150 mJ/cm^2 (right) energy fluence

The surface of the as-received sample is characterized by a roughness resembling densely packed particles whose radii and heights fit well to a wide normal size distribution. The

equivalent disc radius distribution is centered at 10.0 nm and the distribution width is 3.9 nm. The particles height distribution is centered at 1.6 nm and the half width is 0.7 nm. After irradiating with 1000 pulses of 120 mJ/cm² energy fluence, evenly spaced larger particles are grown. However, these are surrounded by remnants of the initial rough surface features, i.e. the scattering contribution is resembling that from the not annealed sample is still present.

Increasing the fluence to 150mJ/cm² a more even particles distribution is produced. The lateral size distribution is significantly sharpened, while the height distribution remains relatively wide. Generally, an increment of the fluence increased the particle heights, while the lateral dimensions did not change significantly.

A TIME RESOLVED GISWAXS STUDY ON THE STRUCTURAL CHANGES IN NANOIMPRINTED POLYMER PATTERNS FOR THE PREPARATION OF INORGANIC/ORGANIC HYBRID SOLAR CELLS

S. Dunst¹, S. Leimgruber¹, V. Kaltenhauser¹, D. Reishofer¹, A. Radivo², E. Sovrnigo², M. Tormen², H. Amenitsch³, B. Marmiroli³, B. Sartori³, H. Ehmman¹, G. Trimmel¹

1.) Institute for Chemistry and Technology of Materials, Graz University of Technology, Stremayrgasse 9, 8010 Graz, Austria

2) IOM CNR, Laboratorio TASC Area Science Park - Basovizza, S.S. 14 Km 163.5, 34149 Trieste, Italy

3) Institute of Inorganic Chemistry, Graz University of Technology, Stremayrgasse 9, 8010 Graz, Austria

Hybrid solar cells have active layers consisting of conjugated polymers and inorganic semiconducting nanoparticles and combine the beneficial properties of inorganic solar cell materials with the easy processability of polymeric materials and show already encouraging efficiencies of up to 5% [1]. During the last years we have focused on CuInS₂/polymer hybrid solar cells via metal xanthates as precursors for the metal sulphide nanoparticles [2].

Two major prerequisites for optimal function include large interfaces between these two materials, providing effective charge separation, but also continuous pathways for transporting the separated charge carriers to the respective electrodes. A vertically bicontinuous and interdigitated heterojunction between the organic and inorganic phase is regarded to as an ideal structure for optimal charge separation as well as charge transport [3]. Such interdigitated structure can be prepared by nanoimprint lithography (NIL). In earlier studies, we have prepared NIL structures of the conjugated polymer PSiF-DBT (poly[2,1,3-benzothiadiazole-4,7-diyl-2,5-thiophene-diyl(9,9-dioctyl-9H-9-silafluorene-2,7-diyl)-2,5-thiophenediyl]). Subsequently, the corresponding metal xanthates were filled into the structures and thermally converted to the metal sulfide. In-situ GISWAXS experiments allowed the identification of the temperature window, where it is still possible to obtain defined nanostructures and additionally gave insights into the formation of the nanocrystalline metal sulfide. Finally, it was possible to build solar cells using this procedure which showed higher efficiencies as reference solar cells with flat interface. These results have already been published recently [4].

In this study we have focused our research towards smaller feature sizes below 100 nm by NIL using a new master stamp with a double line structure (line widths around 50 nm, widths between lines about 35/40 nm). Using the hot embossing method (high temperatures and pressure) nanostructures were imprinted into the conjugated polymer PSiF-DBT, see Figure 1.

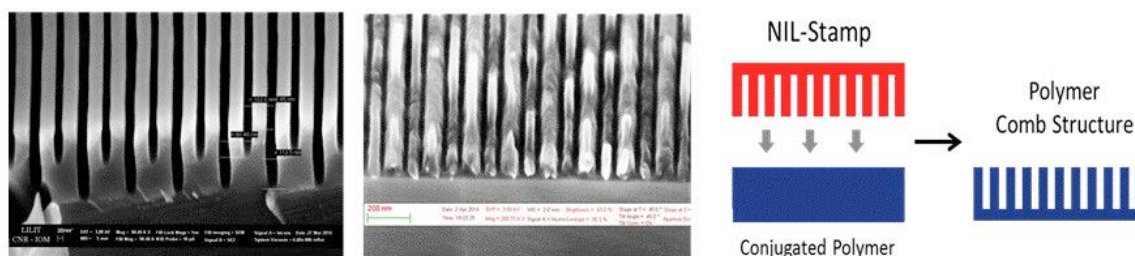


Figure 1. left image: SEM image of the new master stamp; middle image: SEM image of a nanoimprinted PSiF-DBT-film, right image: scheme of the NIL process

In a second approach, we prepared NIL structures in a film of metal xanthates in an inert polymer matrix (polyethylmethacrylate - PEMA). Afterwards the xanthates are converted into

the metal sulfide within the polymer matrix. For the time resolved GISWAXS investigations, the samples were mounted in an Anton Paar DHS 1100 heating cell with a specially designed dome. The GIWAXS signal was monitored using a Pilatus 100k detector and the GISAXS signal with a Pilatus 1M detector. The thermal stability was monitored in-situ by heating up the nanostructured polymer layers.

In Figure 2, typical 2D-images of nanoimprinted metal xanthates in PEMA at different temperatures are shown. Depending on the orientation of the line structure with respect to the beam, typically features, grating truncation rods (GTR), reflecting the periodicity can be observed. In perpendicular direction defined spots in q_z direction are observed, whereas in parallel direction a semicircle of defined spots is visible [5].

During the heating experiment, the alignment of the grating relative to the incoming beam reveals different information of the in situ investigations. The sample where the grating was perpendicular aligned with respect to the direct beam reveals that after a stepwise temperature increase to 170°C the distance between the GTR spots is shifted towards higher values of q , indicating a decrease in the periodic distance between the gratings. When the grating is aligned parallel with respect to the incoming beam, the semi-circular interference pattern of the GTR spots is visible. At a temperature of 130°C the infiltrated components start to convert into the corresponding metal-sulphides which is reflected by the alteration of the scattering pattern. When the temperature plateau at 170°C is reached and the conversion is completed, the semi-circular GTR ring is still visible. Both scattering experiments reveal the success of the infiltrated NIL structuring and that the lattice parameter do only differ slightly after the conversion. Further the dramatic increase of the Yoneda region indicates that the overall roughness of the investigated films increases in the course of the heating experiment

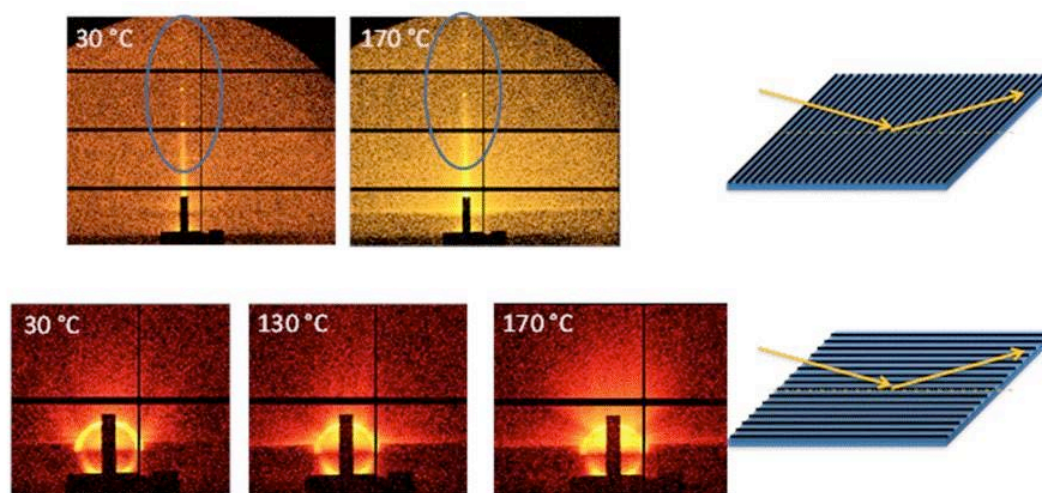


Figure 2. 2D- GIWAXS patterns of NIL structured PSiF-DBT films at different temperatures: first row: line structures perpendicular to the beam, second row: line structures parallel to the beam

References:

- [1] R. Zhou, J. Xue, Chem. Phys. Chem. 2012, 13, 2471-2481
- [2] T. Rath, M. Edler, W. Haas, A. Fischereder, S. Moscher, A. Schenk, R. Trattinig, M. Sezen, G. Mauthner, A. Pein, D. Meischler, K. Bartl, R. Saf, N. Bansal, S.A. Haque, F. Hofer, E.J.W. List, G. Trimmel, Adv. Energy Mater. 2011, 1, 1046-1050
- [3] Y. Yang, K. Mielczarek, M. Aryal, A. Zakhidov, W. Hu, ACS Nano, 2012, 6, 2877-2892
- [4] S. Dunst, T. Rath, A. Radivo, E. Sovrnigo, M. Tormen, H. Amenitsch, B. Marmiroli, B. Sartori, A. Reichmann, A.-C. Knall, G. Trimmel, ACS Appl. Mater. Interfaces, 6, 7633-7642)

SWIFT HEAVY ION TRACKS ON GAN SURFACE

M. Karlušić¹, M. Buljan¹, Z. Siketić¹, B. Šantić¹, M. Jakšić¹, H. Lebius², B. Ban d'Etat¹, T. Meisch³, F. Scholz³, S. Bernstorff⁴, M. Schleberger⁵

- 1.) Ruđer Bošković Institute, Bijenička cesta 54, 10000 Zagreb, Croatia
- 2) CIMAP, CEA-CNRS-ENSICAEN-UCBN, BP 5133, 14070 Caen Cedex 5, France
- 3) Universität Ulm, Institut für Optoelektronik, Albert-Einstein-Allee 45, 89081 Ulm, Germany
- 4) Elettra-Sincrotrone Trieste, SS 14 km 163.5, 34149 Basovizza, Italy
- 5) Fakultät für Physik and CENIDE, Universität Duisburg-Essen, D-47048 Duisburg, Germany

The passage of a swift heavy ion (SHI) through a solid material can result in permanent nanoscale damage called ion track. The most common description of the SHI track formation, the thermal spike model, suggests that the kinetic energy of the SHI projectile that is deposited as dense electronic excitation along the SHI trajectory, can lead to nanoscale melting of the material. Irradiation of flat solid surfaces by SHI under grazing incidence angle can result in the formation of surface SHI tracks. These ion tracks can be observed directly using atomic force microscopy (AFM) [1,2]. However, to extract statistical information (average ion track length, length distribution etc.), structural investigations of this type are very time consuming. For that purpose, we have shown that grazing incidence small angle X-ray scattering (GISAXS) can be utilized as well and allows short measuring times with an excellent statistics [3]. In the present work, we report the results of our investigations regarding SHI irradiation of GaN [4]. The grazing incidence SHI irradiation parameters were chosen to investigate the response of GaN surface in particular, by using AFM and GISAXS. Additionally, possible compositional changes were investigated by time of flight elastic recoil detection analysis (TOF-ERDA).

Wurzite GaN thin film samples were grown by low-pressure metalorganic vapor phase epitaxy on *c*-plane sapphire substrates. The layer thickness was 3 μm with a surface RMS roughness of <0.15 nm. SHI irradiations were performed at the IRRSUD beamline at GANIL using 92 MeV Xe^{23+} ions. A second set of SHI irradiations was done at the RBI using 23 MeV I^{6+} ions. Surface modifications were investigated using tapping mode AFM. The analysis of surface ion tracks was complemented by a novel approach using GISAXS. This experiment was carried out at the synchrotron facilities of Elettra-Sincrotrone Trieste, Italy on the SAXS beamline, using synchrotron radiation with wavelength $\lambda=0.154$ nm (photon energy of 8 keV). To investigate possible stoichiometric changes of the GaN, *in situ* TOF-ERDA measurements were performed at the RBI using the same 23 MeV I^{6+} beam.

After grazing incidence irradiation, chainlike surface ion tracks were observed [4]. In contrast to refs. [1,2] where nanohillocks were found, the morphology of 92 MeV Xe^{23+} ion tracks consists of both nanohillocks and nanoholes. For even higher energies only nanohillocks were observed previously [5]. But 23 MeV I^{6+} ion tracks consist only of nanoholes (Fig. 1). Samples irradiated at high fluence with 92 MeV Xe^{23+} ions, but still under conditions when ion tracks are not much overlapped, produce a strong GISAXS signal (Fig. 2.). TOF-ERDA measurement performed using 23 MeV I^{6+} at the same grazing incidence angle of 1° shows a significant loss of nitrogen already at the fluence of $2 \times 10^{11}/\text{cm}^2$ (Fig. 3). While the hillocks are generally interpreted as a signature of molten material, the occurrence of holes indicates a loss of material. Very recently, it was shown that in case of another wide band gap material, silicon carbide (SiC), grooves with a depth of ~ 0.3 nm instead of chains of nanohillocks appear [6] when irradiated by SHI under grazing incidence angle. In a broader context, the observation of nitrogen loss reported here and the loss of silicon from the SiC surface upon SHI irradiation reported in ref. [6] opens up the question of the composition of SHI tracks.

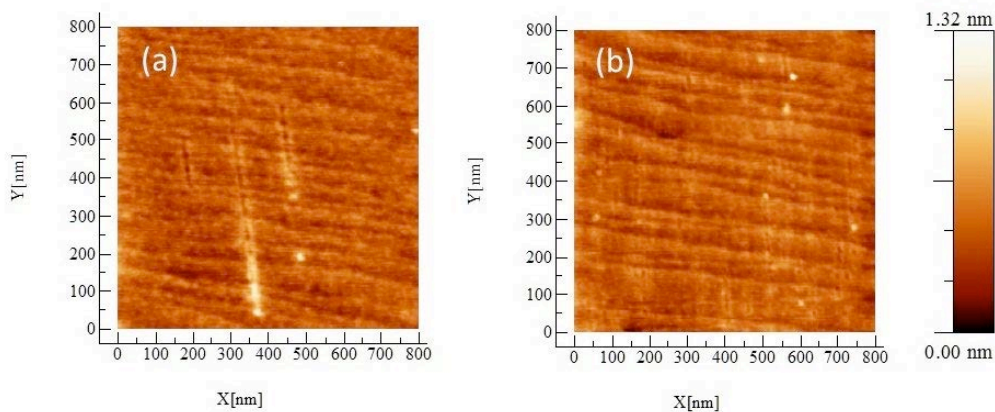


Figure 1. AFM images of irradiated GaN surface (a) IRRSUD, 92 MeV Xe^{23+} , $\theta = 1^\circ$; (b) IRB, 23 MeV I^{6+} , $\theta = 1^\circ$. Ions coming from the above

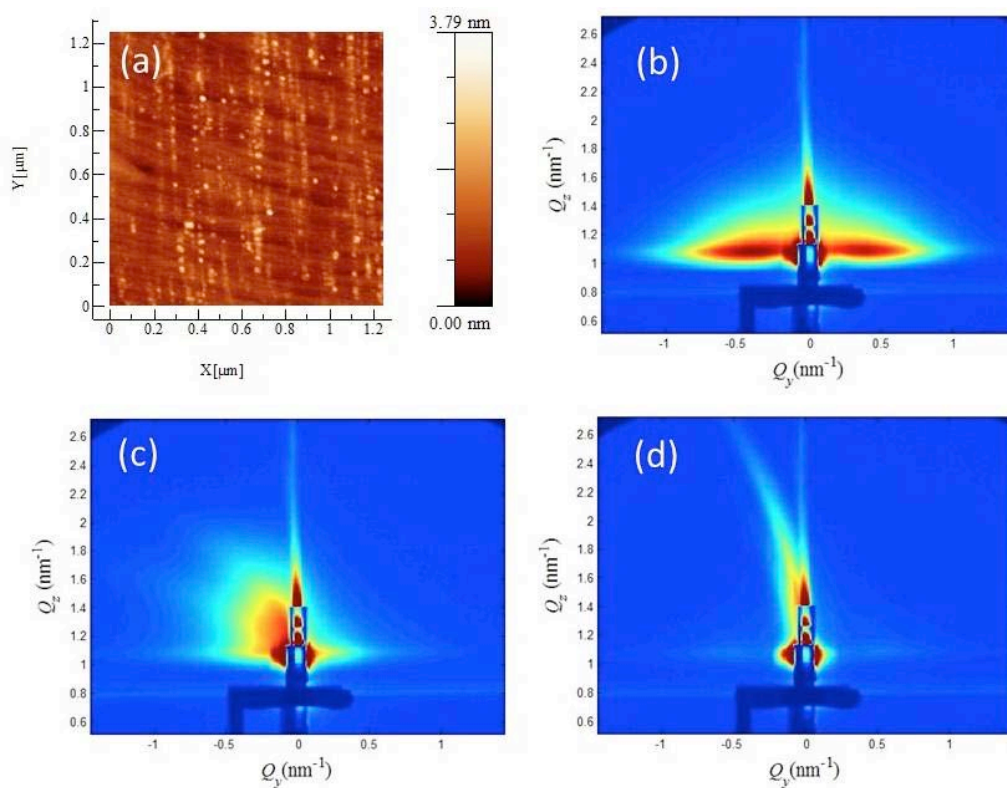


Figure 2. Irradiated GaN surface at IRRSUD with 92 MeV Xe^{23+} , $\theta = 1^\circ$, $\Phi = 100/\mu\text{m}^2$ (a) AFM image and GISAXS spectra taken at different azimuthal angles with respect to orientation of the surface ion tracks: 0° (b), 2° (c), 10° (d)

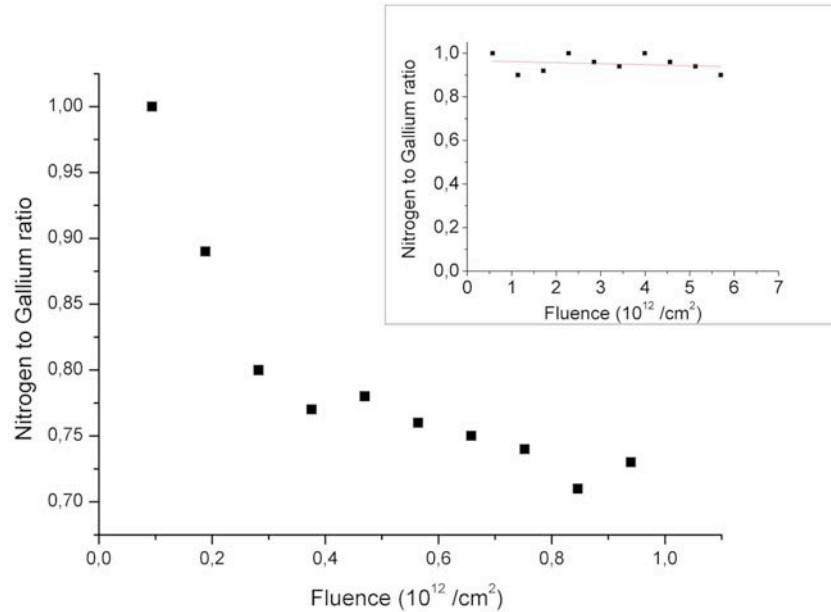


Figure 3. Nitrogen-to-Gallium ratio calculated from an offline analysis of in-situ TOF-ERDA measurements performed by 23 MeV I^{6+} ions at 1° grazing incidence angle. A significant loss of nitrogen is evident. In the inset are shown TOF-ERDA results performed by the same 23 MeV I^{6+} ions at 20° incidence angle, when nitrogen content is stable (red line is linear fit to the data)

The research leading to these results has received funding from the European Community's Seventh Framework Programme (FP7/2007-2013) -CALIPSO under grant agreement n° 312284.

References:

- [1] A. Akcöltekin et al., Creation of multiple nanodots by single ions, *Nature Nanotechnology* **2**, 90 (2007)
- [2] M. Karlušić et al., Energy threshold for the creation of nanodots on SrTiO_3 by swift heavy ions, *New J. Phys.* **12**, 043009 (2010)
- [3] M. Karlušić et al., Comparison of AFM and GISAXS capabilities for surface swift heavy ion track analysis, IBM Leuven 2014 (poster)
- [4] M. Karlušić et al., Response of GaN to energetic ion irradiation, *J. Phys. D: Appl. Phys.*, accepted (2015)
- [5] S. Mansouri et al., Swift heavy ions in Gallium Nitride, *Acta Electrotech.* **49**, 147 (2008)
- [6] O. Ochedowski et al., Graphitic nanostripes in silicon carbide surfaces created by swift heavy ion irradiation *Nature Comm.* **5**, 3913 (2014)

IN-SITU GROWTH STUDY OF ORGANIC HIERARCHIC NANOCRYSTALS BASED ON THE ORGANIC PIGMENT QUINACRIDONE

R.T. Lechner¹, M. Burian¹, M.Sytnik², W. Heiss^{2,3} and O. Paris¹

1.) Institute of Physics, Montanuniversitaet Leoben, 8700 Leoben, Austria

2.) Semiconductor and Solid State Physics, Johannes Kepler University Linz, 4040 Linz, Austria

3.) Materials for Electronics and Energy Technology, Friedrich-Alexander-University Erlangen-Nürnberg, 91058 Erlangen, Germany

Organic pigments such as indigos and quinacridones are widely produced industrially as colorants for everyday products like car finish and printing inks. Very recently a general procedure was developed to transform commercially available insoluble microcrystalline pigment powders into colloidal solutions of differently sized and shaped semiconductor micro- and nanocrystals. The synthesis is based on the transformation of the pigments into soluble dyes by introducing transient protecting groups, followed by controlled deprotection in solution [1].

In this work we studied with small and wide angle x-ray scattering (SAXS/WAXS) for the first time *in-situ* the growth of these quinacridone (QA) based hierarchic nanocrystal structures. In a first beamtime we were able to establish a setup that covers a large q -range from 0.1 up to 10 nm^{-1} using a Pilatus 1M detector. Moreover, with an additional Pilatus 100K we were able to record additional Bragg peaks of the quinacridone nanocrystals. This allowed us to follow the onset of the organic nanocrystals growth in the SAXS-regime and to record the evolution of the crystal phases in the WAXS range.

We could reveal that the crystalline phases of nanostructured QA depend on the used ligands during synthesis by recording SAXS/WAXS pattern in seconds to minutes time steps. Moreover, we could observe a not expected crystal phase transition in the time regime of several hours.

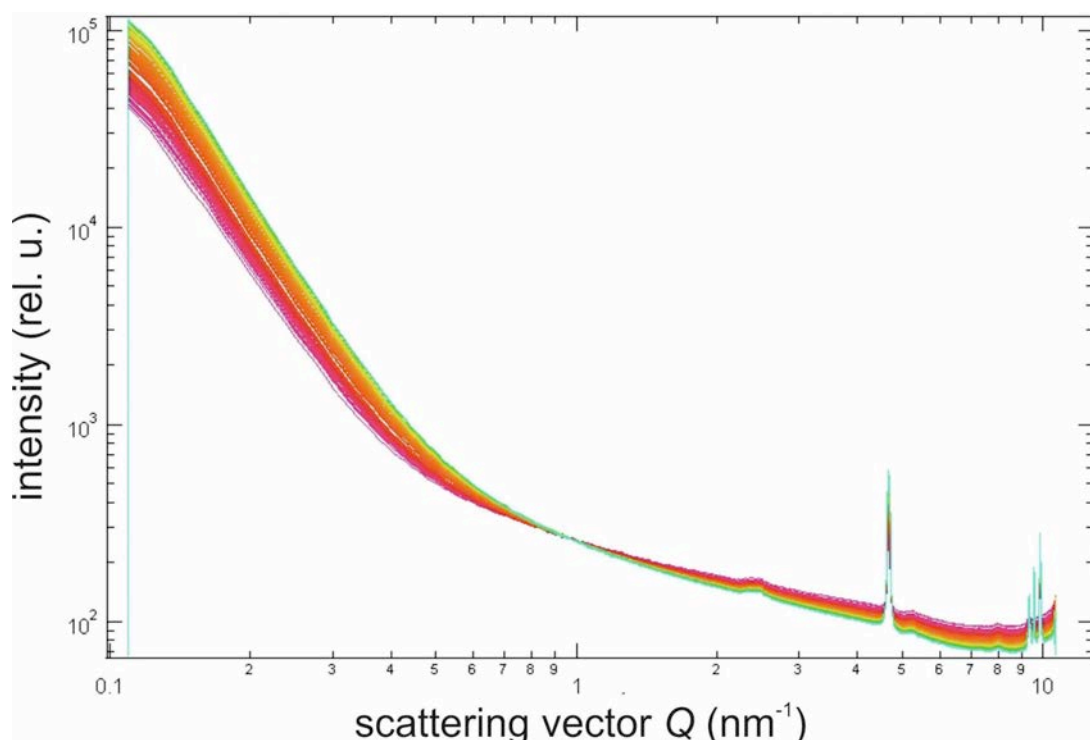


Figure 1. SAXS/WAXS pattern recorded during the QA-nanocrystals growth. The sharp peaks around 5 nm^{-1} and 10 nm^{-1} can be clearly related to the crystal structure of QA. This was a "slow" time series, where every 4 minutes one frame over 11 hours was recorded

In Fig. 1 the SAXS-regime recorded with the Pilatus 1M detector alone is shown. At higher q -values the crystals peaks of QA are visible being a fingerprint for α - β polymorphs of QA [1]. To follow this “slow” growth mode over 11 hours we recorded every 4 minutes a SAXS/WAXS pattern. The recorded in-situ SAXS/WAXS patterns together with a first analysis are exemplified for the case of quinacridone precursors solved in pyridine. After mixing with butyl acetate the QA-precursors are slowly destabilized and the growth of the nanocrystals starts. Right after this mixing we start to measure the solution filled in 1.5 mm capillaries that have been pre-aligned in the x-ray beam.

For a first analysis we concentrate in more detail on the first Bragg peak around 4.5 nm^{-1} . In Fig 2. the peak intensity I_0 (black), the peak position x_0 (red) as well as the peak width (FWHM) is plotted over time.

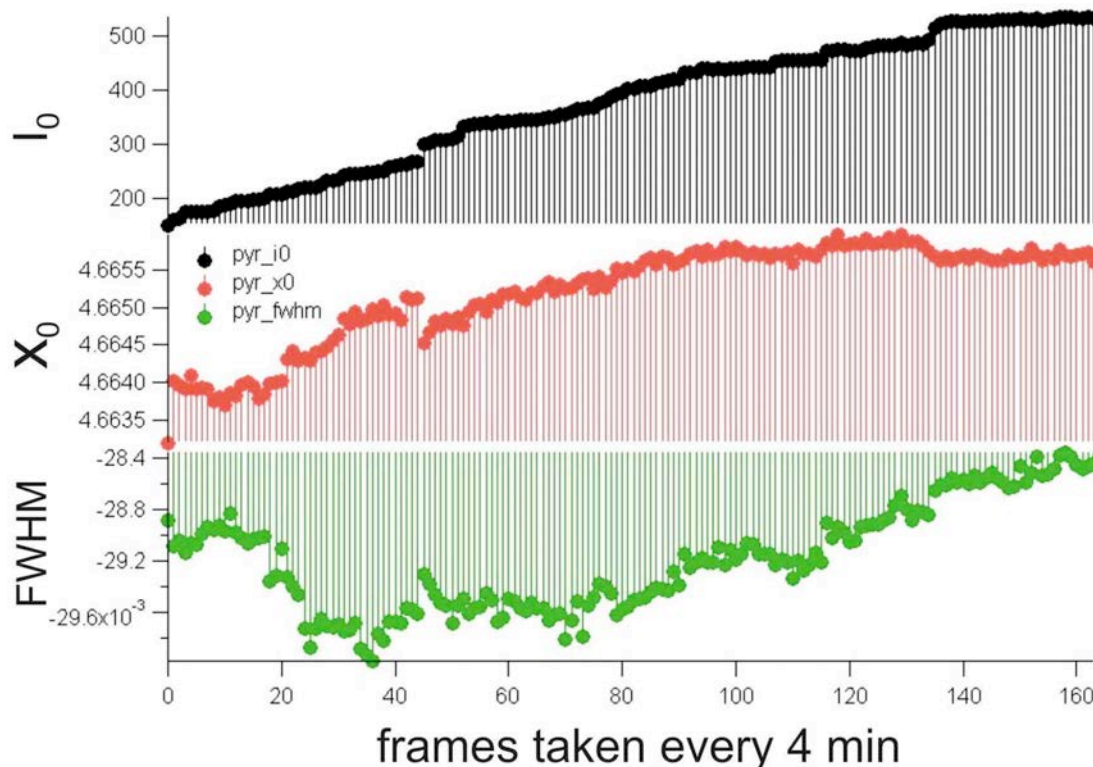


Figure 2. Analysis of the QA-peak at around 4.5 nm^{-1} as a function of growth time. One frame number corresponds to a 4 min time step

The increase of the intensity with time indicates the increasing amount of synthesized nanocrystals, whereas the increase in the peak position a change of the QA lattice constant towards smaller d -spacings. The FWHM of the Bragg peak is first broadened, but later is getting narrower again. This may be related to a change in the nanocrystals dimensions from 210 nm to around 221 nm.

The further detailed analysis of the various synthesis procedures studied *in-situ* will allow a better understanding of this newly developed synthesis method.

References:

- [1] M. Sytnyk, E. D. Głowacki, S. Yakunin, et al., J. Am. Chem. Soc. 2014, 136, 16522-16532

STRUCTURAL PROPERTIES AND LUMINESCENCE OF NANO-CRYSTALLINE ZNO THIN FILMS FORMED BY RF OXYGEN PLASMA ASSISTED PLD

D. Meljanac¹, N.Krstulovic², K. Juraić^{1,3}, K. Salomon², H.Skenderović², Z.Siketic¹, Z.Kregar², S.Bernstorff⁴, D. Gracin¹

1.) Ruđer Bošković Institute, Bijenička 54, 10000 Zagreb, Croatia

2.) Institute of Physics, Bijenička 46, 10000 Zagreb, Croatia

3.) Institute of Inorganic Chemistry, Graz University of Technology, Stremayrgasse 9/IV, 8010 Graz, Austria

4.) Elettra-Sincrotrone Trieste, SS 14, Km 163.5, in AREA Science Park, 34149 Basovizza (TS), Italy

The growth and properties of ZnO nanostructures are extensively studied because of many potential applications for example as transparent conductive electrodes in thin film solar cells, as a replacement for TiO₂ in dye sensitized solar cells, or in light emitting diodes. ZnO can be deposited in many ways using chemical and physical techniques.

The thin ZnO layers studied in this work were deposited by pulsed laser deposition (Figure 1) in vacuum or in oxygen atmosphere [1]. By changing the gas pressure between 10 and 70 Pa and by applying RF plasma at those pressures, various structural forms were obtained.

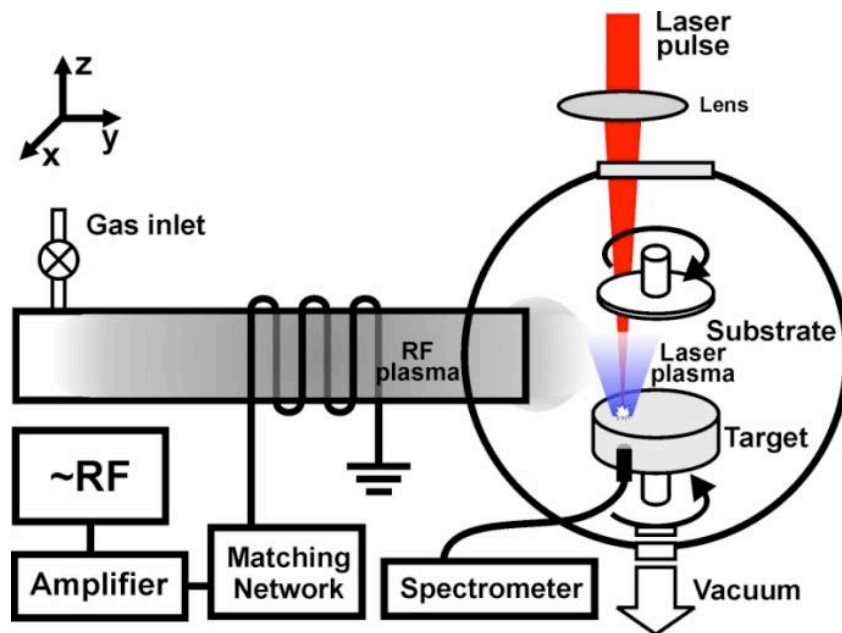


Figure 1. Experimental setup for thin film deposition

This study was focused on exploring the possibility to modify the ZnO thin film structure and luminescence properties by changing the atmosphere in the depositing chamber by adding neutral oxygen (10, 30 and 70 Pa) or by using RF plasma under the same gas pressure. The structural properties of the obtained ZnO thin films were studied by simultaneous grazing incidence small angle x-ray scattering (GISAXS) and grazing incidence x-ray diffraction (GIXRD) (Figure 2). Nanocrystal sizes were estimated from the diffraction peaks width (Figure 2a). The density and thickness were estimated by fitting GISAXS intensity cuts taken close to the Yoneda maximum (Figure 2b). The analysis results obtained within the Distorted Wave Born Approximation are summarized in Table 1.

These data show that increasing the oxygen pressure results in an increasing film roughness from 1.5 to 7 nm and a decreasing sample density. The size of the nanocrystals is around 20 nm for all samples. Films deposited under the same pressure exhibit different thicknesses: RF plasma yields slightly thicker films.

The photoluminescence spectra (Figure 3) consist of 3 well defined peaks: that in the UV corresponds to a band-to-band transition, the blue peak is due to Zn vacancies, and the red peak is probably due to oxygen interstitials. For all pressures the RF excitation lowered the defect level related to blue emission and resulted in a narrower UV luminescence peak indicating a better structural ordering. The red emission peak is only seen using RF excited oxygen atmosphere at 70Pa.

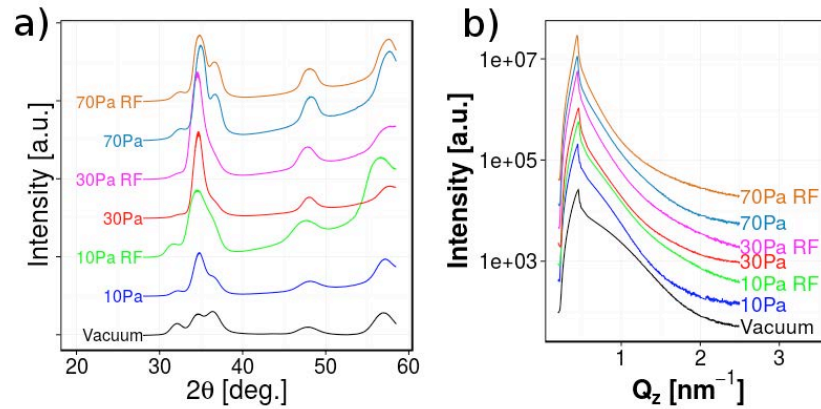


Figure 2. (a) GIXRD and (b) GISAXS 1D cuts taken perpendicular to the sample surface for ZnO thin films prepared by PLD as a function of the oxygen pressure and by applying RF plasma

Table 1. Sample parameters obtained by GISAXS

Sample	Thickness (nm)	Roughness (nm)	Density (g/cm ³)
Vacuum	91	1.5	5.69
10 Pa	128	2.4	5.56
10 Pa RF	138	2.5	5.60
30 Pa	77	3.0	5.27
30 Pa RF	105	3.5	5.31
70 Pa	/	7.5	5.02
70 Pa RF	/	7.1	5.11

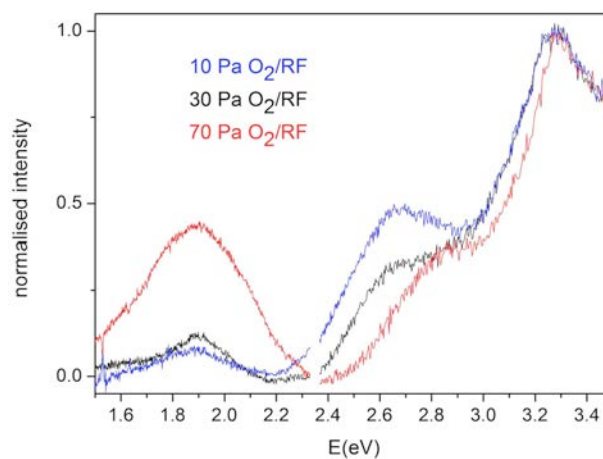


Figure 3. Luminescence of ZnO PLD samples as a function of the oxygen pressure and RF plasma

References:

- [1] N. Krstulović, N. Čutić, S. Milošević, SpectrochimActa B 63 (2008) 1233–1239

ION ELECTROSORPTION IN NANOPOROUS SUPERCAPACITORS STUDIED BY IN-SITU SAXS

C. Prehal¹, D. Weingarth², R. T. Lechner¹, H. Amenitsch³, V. Presser^{2,4} and O. Paris¹

1.) Institute of Physics, Montanuniversitaet Leoben, Franz-Josef Straße 18, 8700 Leoben, Austria

2.) INM - Leibniz Institute for New Materials, Campus D2 2, 66123 Saarbrücken, Germany

3.) Institute of Inorganic Chemistry, Graz University of Technology, Stremayrgasse 9/IV, 8010 Graz, Austria

4.) Department of Materials Science and Engineering, Saarland University, Campus D2 2, 66123 Saarbrücken, Germany

Supercapacitors are devices for efficient energy storage revealing higher power densities and longer cycle lifetimes than common batteries. When two electrically charged carbon electrodes are immersed in an electrolyte, an electrical double layer will form at the electrode-electrolyte interface. Energy is stored via ion electrosorption, where the opposite charge of electrons/holes on the electrode side and anions/cations on the electrolyte side reveal the capacitive behavior. A high specific capacitance requires a high surface area of the electrode material and a well-developed porosity. A large fraction of micropores in these carbons the pores have a size of ca. 1 nm, which is around the size of solvated ions. It was reported previously that the charge is stored most efficiently when the pores roughly match the desolvated ion size [1]. The exact understanding of ion behavior in the charged confinement of carbon nanopores is essential for improving power and energy densities in these devices. Hence, comprehensive in-situ techniques are required in order to directly probe ion arrangement as a function of an applied voltage [2].

We employed in-situ SAXS in combination with X-ray transmission (XRT) measurements on an in-operando supercapacitor cell using aqueous electrolytes and different nanoporous carbons as electrode material. The cell was built as a multilayer assembly consisting of Pt metal connections, carbon counter-electrode (CE), glass fiber spacer and carbon working electrode (WE). A small hole was cut into all materials except of the investigated working electrode. Hence, ion transport and arrangement as a function of applied voltage was studied within the working electrode only. While we applied various voltage signals every second, the SAXS pattern and the corresponding transmission value were recorded.

The transmitted intensity of the primary beam depends on the cation and anion concentration within the electrode weighted by their X-ray absorption coefficients. Combining the transmission signal with the measured electrical current signal, we are able to calculate cation and anion concentration changes independently from each other. As a major result, for 1 M aqueous electrolytes the electrode charge is counterbalanced via pure ion swapping over a large potential window (Fig. 1a). In other words, by applying a voltage to the electrode only the balance of cations and anions is disturbed, while the total number of cations plus anions remains constant [3].

Besides this global information on the ion flux in and out of the working electrode the SAXS signal allows to directly probe collective structural rearrangements of the ions within the carbon nanopores. The spherically averaged SAXS intensity of the studied activated carbon electrode in air and infiltrated with electrolyte (Fig. 1c) is decreased when infiltrating the electrode with electrolyte due to the decreased electron density difference between carbon matrix and pore-inside. In Fig. 1e (top) the relative SAXS intensity change as a function of time (or applied voltage) and the scattering vector length Q is given. The intensity corresponds to the SAXS intensity of all patterns measured during 2 cyclic voltammetry cycles (see applied voltage on the left), normalized by the first SAXS pattern at 0 V. It is not possible to fully explain the Q -dependent intensity changes (Fig. 1e) by assuming solely the electron density difference between carbon matrix and electrolyte to be changed. A simple, yet effective way to understand the rather complex change of the SAXS intensity is to

calculate the radius of gyration (or alternatively the correlation length given as the ratio between the 1st to the 2nd moment of the SAXS profile) in dependence on the applied charge (Fig. 1b). The magnitude of the correlation length change was found to correlate with the counter ion electron number. The Debye-Anderson-Brumberger (DAB) model [4] provides a reasonable analytical expression for the SAXS intensity of a random pore structure from activated carbons, revealing a relation between the radius of gyration and the pore volume fraction. Within a two-phase model the SAXS intensity change can be described consistently by a changing electron density difference as well as an apparent change of the pore width of the electron density structure due to the preferred adsorption of counter-ions close to the pore walls (see sketch of pore electron density profiles in Fig. 1d). Within this model, counter-ions undergo a mean, collective structural re-arrangement upon applying a voltage. The DAB-model was used to back-calculate the SAXS intensity changes, showing excellent agreement with the measured data (Fig. 1e top vs. bottom). Once the origin of the radius of gyration change is understood, a comparison of the ion transport on a *local* vs. the *global* scale is possible (comparing Fig. 1a and Fig. 1b). While the actual electrosorption is accommodated by ion swapping, involving both co-ion expulsion and counter-ion adsorption, *locally* counter-ions move preferably from the center towards the pore walls as a voltage is applied [3].

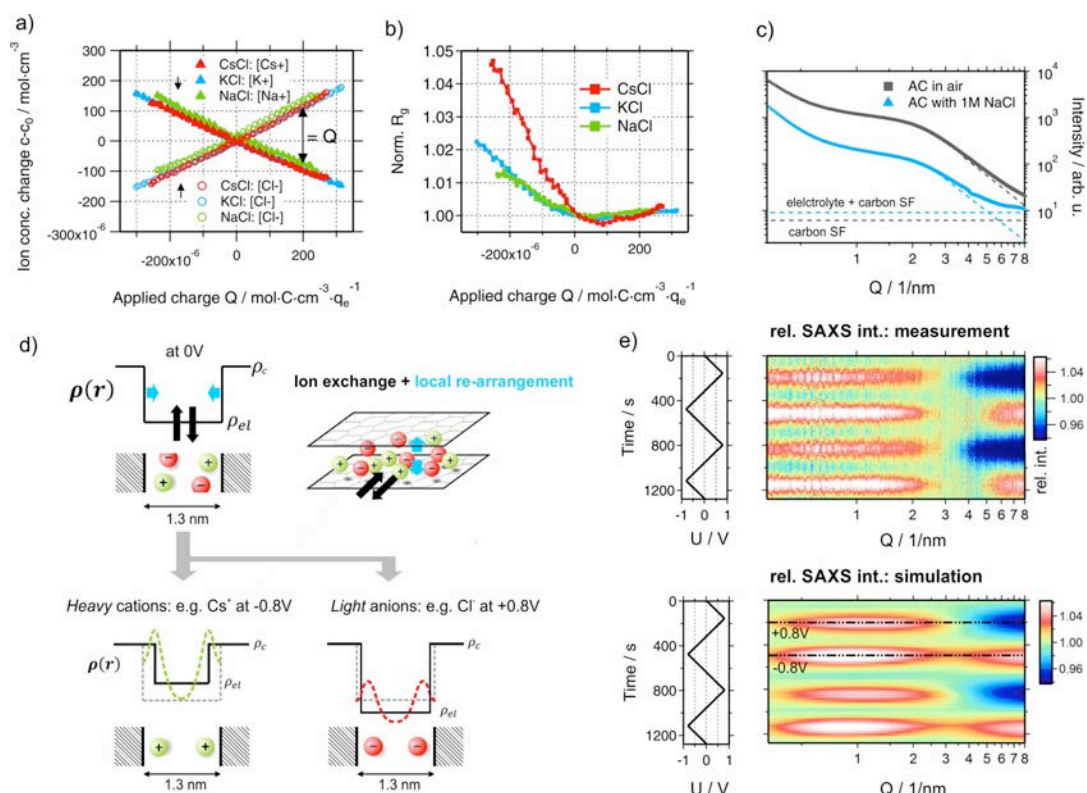


Figure 1. a) Cation and anion concentration change as a function of the applied charge, obtained from x-ray transmission measurements. In b) the radius of gyration from SAXS as a function of the applied charge is given. In c) the SAXS pattern of the activated carbon electrode in air and infiltrated with electrolyte is given. The relative SAXS intensity changes as a function of time and the scattering vector length Q are given right below in e). The simulated data (e, bottom) were obtained by considering a simple two-phase model picture as sketched in d). Reproduced from Ref. 2 with permission from the Royal Society of Chemistry

References:

- [1] J. Chmiola, G. Yushin, Y. Gogotsi, C. Portet, P. Simon and P. L. Taberna, *Science*, 2006, 313, 1760-1763
- [2] F. Béguin, V. Presser, A. Balducci and E. Frackowiak, *Adv. Mater.*, 2014, 26, 2219-2251
- [3] C. Prehal, D. Weingarh, E. Perre, R. T. Lechner, H. Amenitsch, O. Paris and V. Presser, *Energy Environ. Sci.*, 2015, 8, 1725-1735
- [4] P. Debye, H. R. Anderson and H. Brumberger, *J. Appl. Phys.*, 1957, 28, 679-683

GISAXS STUDIES OF THE STRUCTURAL CHANGE OF MESOPOROUS SILICA FILMS AFTER CONTROLLED X-RAY IRRADIATION

K. Salamon¹, N. Radić², I. Bogdanović Radović² and S. Bernstorff³

1.) Institute of Physics, Bijenička 46, HR-10000 Zagreb, Croatia

2.) Rudjer Bošković Institute, Bijenička cesta 54, HR-10000 Zagreb, Croatia

3.) Elettra-Sincrotrone Trieste, Strada Statale 14, km 163, in AREA Science Park, I-34149 Basovizza (TS), Italy

Transition metal nitrides show many interesting properties leading to their wide spread technological use, mostly in form of thin films. Tantalum nitrides (Ta-N) thin films are used as an effective Cu diffusion barrier/gate material in integrated circuitry and as a resistor due to their low temperature coefficient of resistance. Ta-N thin films are also important as wear resistant coatings, and functionalized optical coatings. Thus, the feasibility of growing Ta-N thin films has been extensively studied, particularly in terms of controlling their phase, electrical property and morphology. The binary Ta-N system is quiet rich with many crystalline phases, has a wide-ranging compositional range TaN_x ($0.41 < x < 1.67$) and oxidation states of tantalum.

Here we report on a structural and morphological study of Ta-N thin films produced with the magnetron deposition technique under various Ar/N₂ sputter conditions. We investigated the effect of the nitrogen fraction in the sputtering gas mixture defined as: $pN_2 = P_{N_2} / (P_{Ar} + P_{N_2})$ where P_{Ar} and P_{N_2} are the partial pressures of the Ar and N₂ gases, respectively. Furthermore, we investigated the thermal stability of the as grown Ta-N films up to $T_a = 950$ °C annealing temperature. The resulting pN_2 - T_a phase diagram is related with the morphological and electrical properties of these films. In the investigation, we employed X-ray techniques adapted for thin film analysis: grazing incidence X-ray diffraction (GIXRD), X-ray reflectivity (XRR) and grazing incidence X-ray small angle scattering (GISAXS) in combination with ERDA and four probe resistivity measurements.

Fig.1 shows the N/Ta atomic ratio and the deposition rate R as a function of pN_2 . As pN_2 increases, R monotonically decreases. In total, R drops by an order of magnitude when sputtering is performed with pure N₂, as compared by sputtering with pure Ar. In contrast, the N/Ta atomic ratio increases fast with pN_2 over the region 0-0.2, and then for $pN_2 > 0.7$ saturates at the value 2.1.

Figure 1. The N/Ta atomic ratio (left axis) and the deposition rate (right axis) as a function of pN_2

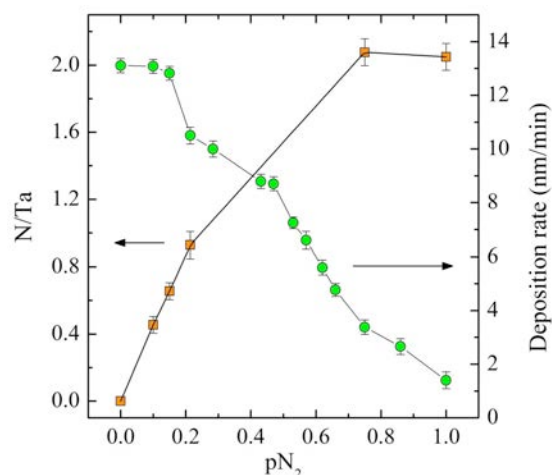


Fig.2 shows the series of GIXRD spectra of the Ta-N thin films grown for different pN_2 . The results show that the film deposited with pure Ar is metastable tetragonal β -Ta with a high degree of (001) preferred orientation. A slight addition of N₂ to the sputtering gas ($pN_2 < 0.15$) resulted in amorphous films. For higher pN_2 , up to $pN_2 = 0.45$, we found the rock-salt structure of δ - TaN_x with $x = 0.8-1.2$. Further addition of N₂ (films grown at $pN_2 = 0.43-0.8$) led to the

formation of an amorphous phase. For even higher partial pressures of N_2 , $pN_2 > 0.85$, deposited films are crystalline. The peaks of the two top-most GIXRD scans in Fig.2 are indexed as arising from the bixbyite- Ta_2N_3 phase. The calculation of the mean crystallite size, D from the full width at half maximum (FWHM) gives values in the nanometer range. We obtain $D=4-6$ nm for δ -TaN and $D=12-23$ nm for bixbyite- Ta_2N_3 crystallites.

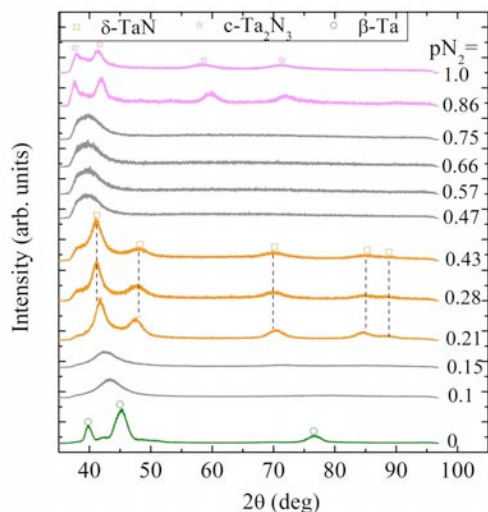


Figure 2. GIXRD spectra of the as grown Ta-N thin films for various pN_2

Selected 2D GISAXS intensity patterns corresponding to films deposited with $pN_2=0.1, 0.28, 0.53$ and 1.0 are displayed in Fig. 3(a). The qualitative difference in the patterns indicates that the film morphology is prominently influenced by the N_2 partial pressure. For low pN_2 (< 0.215), the most noticeable feature is a modulation of the scattering intensity along the q_z direction due to the thin surface layer. For $pN_2=0.28$, the scattering has nearly semi-circular shape, indicating spherical scatterers. The patterns for films with $pN_2=0.22-0.4$ are qualitatively similar. Interestingly, for $pN_2=0.5-0.7$, the GISAXS patterns becomes anisotropic, indicating scatterers which are elongated in the plane parallel with the surface. For $pN_2=0.8$ (and for $pN_2=1.0$), the scattering intensity again has a spherical-like shape, although somewhat more extended in the angles as compared with the pattern of the $pN_2=0.28$ sample. From the quantitative analysis shown in Fig. 3(b) and (c) we obtained that the sizes of the scattering objects in the crystalline Ta-N films are slightly larger or comparable with the sizes of crystallites.

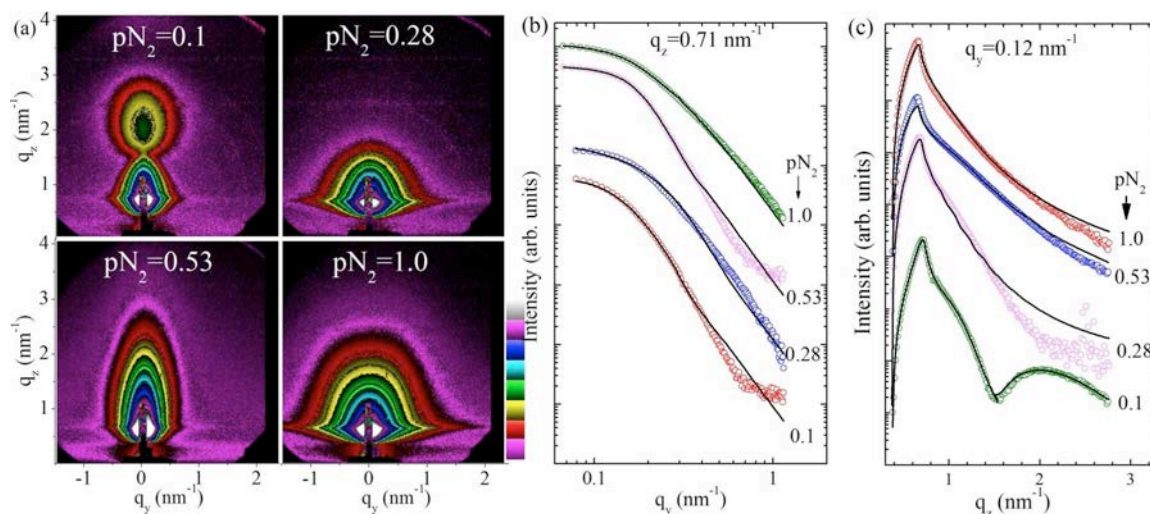


Figure 3. (a) 2D GISAXS patterns of selected as deposited Ta-N films. (b) and (c) show 1D profiles taken from the 2D GISAXS patterns along the q_y axis ((b)) and q_z axis ((c)) with the corresponding fits

IN-SITU SAXS STUDY OF THE EFFECT OF SALTS ON THE MESOSTRUCTURE OF SILICA NANOPARTICLES SYNTHESIZED IN THE GAS PHASE

B. Sartori¹, B. Marmiroli¹, F. Cacho-Nerin² and H. Amenitsch¹

1.) Graz University of Technology, Institute of Inorganic Chemistry, Stremayrgasse 9/IV, Graz, Austria
2.) Diamond Light Source Ltd, Diamond House, Harwell Science and Innovation Campus, Didcot, UK

Evaporation induced self-assembly (EISA) is a low-cost and environmentally benign processes which requires a limited number of preparation steps and allows to synthesize well ordered mesoporous materials [1]. In aerosol EISA, every spherical aerosol drop acts as a single reaction chamber in which the condensing solution rearrange continuously while the solvent evaporates radially from the external to the inner part of the sphere [2]. At high temperature, the fast solvents evaporation drives the formation and organization of the surfactant in micelles that act as templates for the mesopores. The final topology and organization of the pores is governed by the dimension and mesostructural order of the micelles; removal of the template leaves an ordered porous structure.

To understand the connection between the synthesis conditions and the chemistry of the chosen reaction characterization techniques that allow to follow in-operando the evolution of the mesostructured material from the aerosol droplet to the final powder are required [3].

As we previously demonstrated, with our custom-built aerosol setup it is possible to study in detail with SAXS the silica condensation ab-initio, from the sol-gel precursor solution to the final nanoparticles. With further experiments, we have shown how the process parameters, like temperature or humidity, influence the evolution of the mesostructure and the architecture of the mesoporous nanoparticles [4, 5].

In this experiment, we characterized in real time the silica condensation in presence and absence of two salts, $(\text{NH}_4)_2\text{SO}_4$, CeCl_3 , to study the effect of these additives on the final mesostructure.

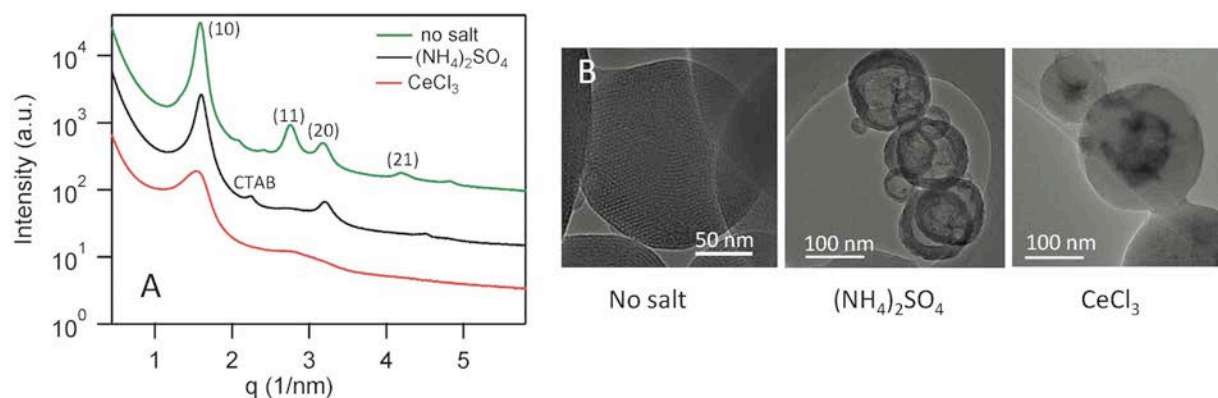


Figure 1. (A) SAXS pattern of aerosol-synthesized nanoparticles collected at the end of the reaction chamber; data are shifted vertically for clarity. (B) from left to right: TEM images of the nanoparticles synthesized in absence of salt, with $(\text{NH}_4)_2\text{SO}_4$, and CeCl_3 respectively

The time-resolved characterization of the hierarchical structure of the outer silica shell demonstrated that the presence of salts affects the silica mesostructure and influences the evolution as well as the order of the final mesostructure, as shown in Figure 1A. The TEM images in Figure 1B show that in presence of ammonium sulfate, the thin silica shell that surrounds the salt crystal has a better ordered mesostructure if compared to the one of the

nanoparticles synthesized in presence of CeCl_3 . A possible explanation is that, due to its high solubility in water, during EISA the ammonium sulfate remains in solution and only in the later stages of solvents evaporation forms few crystallization nuclei inside the external, ordered silica shell [6]. On the contrary, CeCl_3 is hydrolyzed and subsequently oxidized to CeO_2 at high temperature: thus it condenses in small nanocrystals throughout the silica matrix, reducing the mesostructural order.

References:

- [1] Brinker, C.J. et al., *Adv.Mater.*, 11 (7), 579-585 (1999)
- [2] Jiang, X. et al., *J. Nanomater.*, 760237 (2011)
- [3] Boissiere, C. et al., *Adv. Mater.*, 23, 599-623 (2011)
- [4] Shyjumon I., et al., *Langmuir*, 27, 5542-5548 (2011)
- [5] Jungnikl K., et al., *Aerosol Science and Technology* 45, 7, 795-800 (2011)
- [6] Jiang, X. et al., *chem Comm* 46, 3019-3021 (2010)

THE ROLE OF SOLVENT-ADDITIVES ON THE CRYSTALLIZATION BEHAVIOR OF POLYMER-FULLERENE LAYERS FOR ORGANIC PHOTOVOLTAIC

C. J. Schaffer¹, J. Schlipf¹, B. Su¹, Y. Rui¹, S. Bernstorff² and P. Müller-Buschbaum¹

1.) Technische Universität München, Physik-Department, Lehrstuhl für Funktionelle Materialien, James-Frank-Str. 1, 85748 Garching, Germany

2.) Sincrotrone Trieste Elettra, S.S. 14 km 163.5 in Area Science Park, 34012 Basovizza, Trieste, Italy

While organic photovoltaics evolve more and more as a highly versatile source of renewable energy, improving their efficiency, stability and the ease of processing crystallize as the three key issues to render them applicable in a large scale. In the case of polymer:fullerene bulk-heterojunction solar cells, the active layer where the conversion from light to electricity takes place, forms from a mutual polymer:fullerene solution. This approach allows for cheap and easy processing based on large-scale processing methods such as roll-to-roll slot die coating. For certain polymers, the use of solvent-additives has proven to allow for boosting solar cell efficiencies while not affecting the fabrication process, as shown e.g. by Peet et al. [1]. Therefore, the use of solvent-additives together with so called low bandgap polymer offers a highly interesting approach.

Within this work, the specific system consisting of the polymer PCPDTBT (poly[2,6-(4,4-bis-(2-ethylhexyl)-4H-cyclopenta [2,1-b;3,4-b']dithiophene)-alt-4,7(2,1,3-benzothiadiazole)]) and the C₇₀-based fulleren-derivative PC₇₁BM ([6,6]-Phenyl C₇₁ butyric acid methyl ester) is examined for the crystallization behavior in dependence of the mixing ratio and the presence of 3% vol. 1,8-octanedithiol (ODT) in the solvent chlorobenzene (CB). In order to access the crystallite structure, grazing incidence wide angle X-ray scattering (GIWAXS) has been proven to be a very powerful method [2]. The GIWAXS measurements were performed at the Austrian SAXS beamline at Elettra-Sincrotrone, Trieste. An incident angle of 0.25° has been chosen at a sample-to-detector distance of 104 mm (Dektris Pilatus 100k) with a photon energy of 8 keV.

The two dimensional scattering data have been corrected for the experimental geometry (using the GIXSGUI 1.6.1. software of the Argonne National Laboratory developed by Z. Jiang [3]) and are shown in Figure 1. In order to gain more detailed information, cake cuts are integrated between 5° and 15° with respect to the specular plane. These cuts are displayed together with their fits in Figure 2. Thereby, the data was fitted using an exponentially decaying background and three Lorentzian peaks. The Lorentzian center positions and widths then give information about stacking distances and crystallite sizes via the Scherrer-equation of polymer crystallites (lamellar and π - π stacking) and fullerene agglomerates.

The data reveal that the use of ODT strongly enhances the lamellar crystallization of PCPDTBT and therefore is assumed to drive micro-phase separation. Hereby, larger amounts of polymer also lead to larger crystallites. All other quantities display to be rather independent of the blending ratio.

Based on the scattering data and absorption data (not shown) we conclude that ODT enhances micro-phase separation and polymer crystallization, leading to both, improved light absorption and charge carrier mobility. Both effects would lead to enhanced solar cell efficiencies as shown by Peet et al. [1] and provide an important understanding on how solvent additives influence morphology and efficiency of polymer:fullerene solar cells..

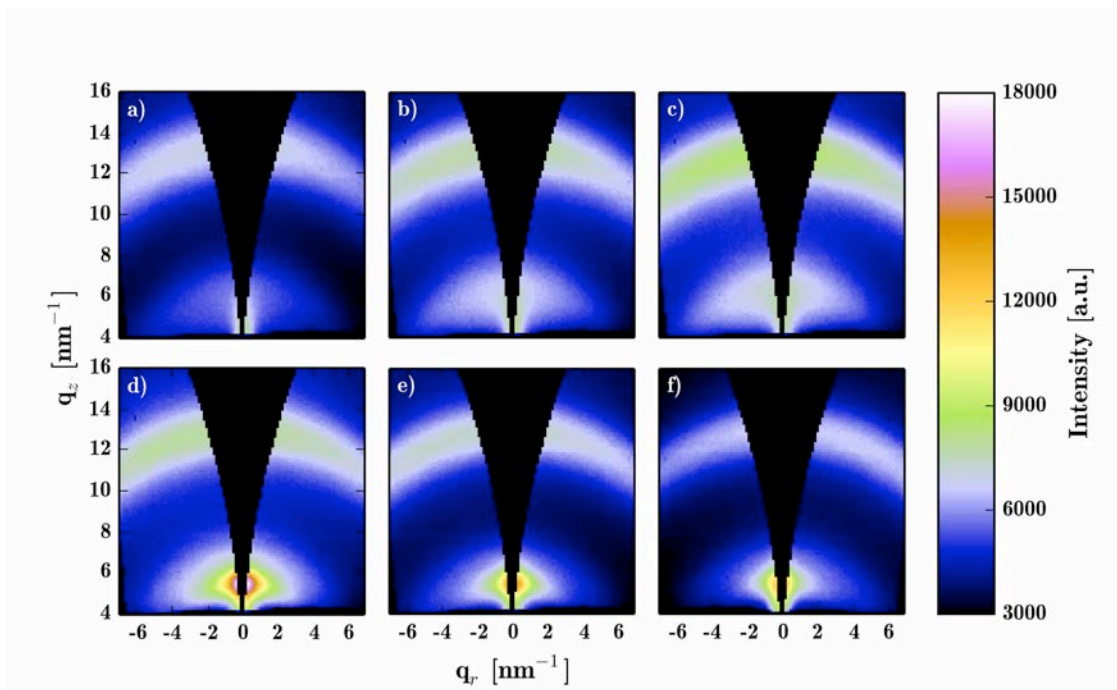


Figure 1. 2D GIWAXS data of PCPDTBT:PC71BM thin films processed with (lower row) and without (upper row) 3% vol. ODT with a polymer:fullerene blend ratio of 1:1.5 (left column), 1:2.0 (center column) and 1:2.7 (right column)

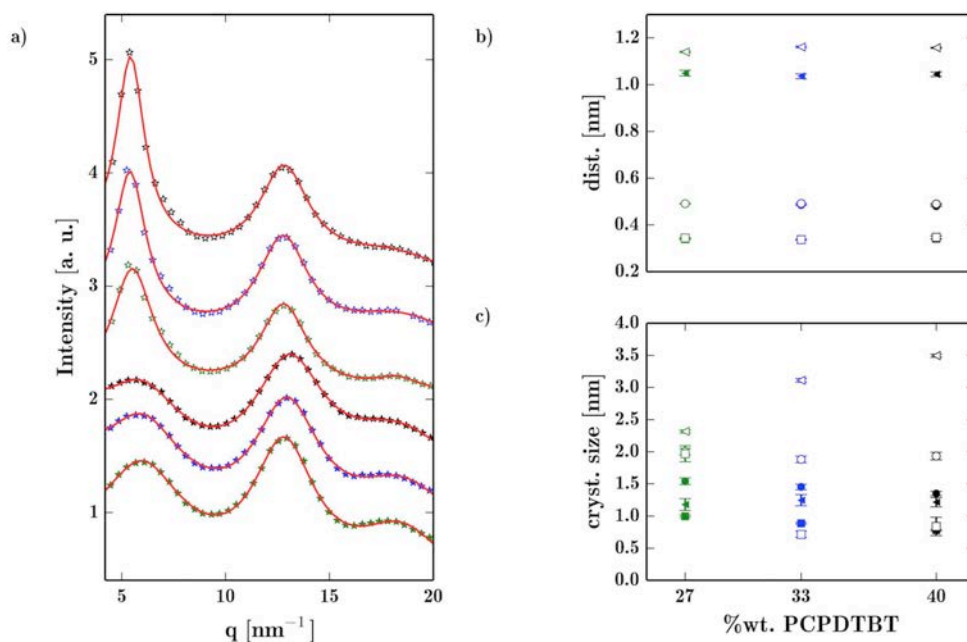


Figure 2. Reduced GIWAXS data: (a) Scattering data integrated from 5° ... 15° with respect to the specular plane. Open symbols refer to the films processed with 3% vol. ODT, full symbols refer to films w/o ODT. The colors denote the blending ratios 1:1.5 (black), 1:2.0 (blue) and 1:2.7 (green). (b, c) Stacking distances and estimated crystallite sizes from the Lorentzian peak center positions. The different markers denote PCPDTBT lamellar stacking (triangles), Fullerene agglomerations (circles) and PCPDTBT n-n stacking (squares)

References:

- [1] J. Peet, J. Y. Kim, N. E. Coates, W. L. Ma, D. Moses, A. J. Heeger, G. C. Bazan; Efficiency Enhancement in Low-Bandgap Polymer Solar Cells by Processing with Alkane Dithiols; *Nature Materials* **6**, 497–500 (2007)
- [2] P. Müller-Buschbaum; The active layer morphology of organic solar cells probed with grazing incidence scattering techniques; *Adv. Mater.* **26**, 7692–7709 (2014)
- [3] Z. Jiang, GIXSGUI is available for download:
<http://www.aps.anl.gov/Sectors/Sector8/Operations/GIXSGUI.html>

MORPHOLOGY OF HYBRID PEROVSKITE THIN FILMS BY 2-STEP SYNTHESIS

J. Schlipf¹, P. Docampo², C.J. Schaffer¹, V. Körstgens¹, L. Bießmann¹, F. Hanusch², S. Bernstorff³, T. Bein² and P. Müller-Buschbaum¹

- 1.) Lehrstuhl für Funktionelle Materialien, Physik-Department, Technische Universität München, James-Frank-Str. 1, 85748 Garching, Germany
- 2.) Department of Chemistry and Center for NanoScience (CeNS), University of Munich (LMU), Butenandtstr. 5-13, 81377 München, Germany
- 3.) Elettra-Sincrotrone Trieste S.C.p.A., Strada Statale 14, km 163,5 in AREA Science Park, 34149 Basovizza, Italy

Organic-inorganic compound materials with the perovskite crystal structure ABX_3 have received much attention as promising absorber materials for future photovoltaics in the past years. The most commonly used representative of this material class, $MAPbI_3$, incorporates the organic cation methylammonium (MA) inside an inorganic framework of iodine and lead. Comparable to organic and dye-sensitized solar cells, perovskite solar cells (PSC) can be processed from solution and nowadays already exhibit power conversion efficiencies (PCE) around 20 %. However, hysteretic behavior during current-voltage sweeps, as well as overall performance vary substantially and are strongly linked to the preparation protocol. Therefore, fundamental understanding has to be gained of the impact of synthesis processes on film morphology and device operation.

In this work we have prepared perovskite thin films with an established 2-step synthesis method known to exhibit highly efficient PSC over 15 % [1]. It comprises the deposition of a precursor layer (PbI_2) from solution by spin-coating and the subsequent conversion to perovskite. We have investigated both films with grazing incidence small angle X-ray scattering (GISAXS) at the Austro SAXS beamline at Elettra-Sincrotrone Trieste. Simultaneous wide angle scattering measurements (GIWAXS) at the same sample spot allowed us to confirm the perovskite crystal structure in tetragonal phase. We modeled the GISAXS data within the distorted wave born approximation (DWBA) by assigning three form factors (FF) to contemplate for different crystal sizes in the films [2].

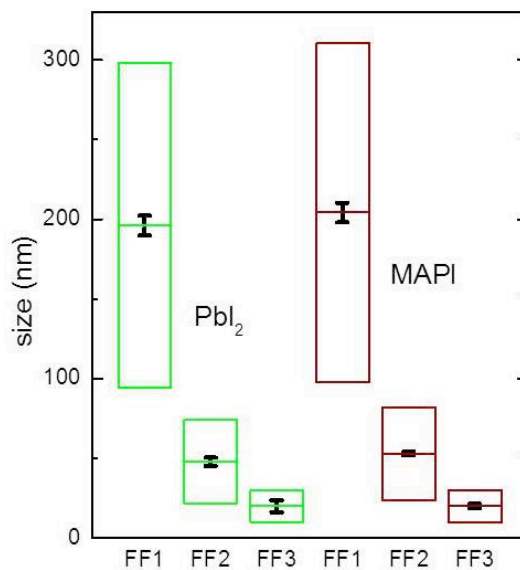


Figure 1. Form factors FF1-3 extracted from modeling the data for PbI_2 (green) and perovskite (brown). Despite the wide distribution, the crystal sizes in both films show a strong correlation.

We observe a strong correlation of lateral crystal sizes before and after conversion which we attribute to constrained crystal growth due to dense packing of crystals in the precursor film (cf. Figure 1). This result already explains the importance of optimizing the precursor films for achieving high performing PSC with a 2-step method. Additionally, we measured GISAXS images at different incident angles: one close to the critical angle of the materials with a high sensitivity to the film surface and one at a higher angle, so the beam penetrates the entire film. Thus, by contemplating the intensities of individual FF, we find an accumulation of smaller crystals within the film in contrast to the surface. The ratio of small to large crystals is higher in the perovskite film revealing vertically differing conversion processes: As the MA ions have to be incorporated into the metal halide framework, the crystal unit cell has to expand. Crystals close to the film surface can grow freely, smaller grains might even be included into larger ones by Ostwald-type ripening. However, due to the confinement close to the substrate, the strain induced by lattice expansion leads to cracking of larger crystals into smaller units. This observation is further confirmed by scanning electron microscopy of sample cross-sections and powder X-ray diffraction, where the latter revealed considerable strain in the perovskite crystals.

As the investigated 2-step method forms the basis for a range of different methods, our results can be useful to understand and further improve a range of 2-step methods, which may eventually lead to reproducible high PCE.

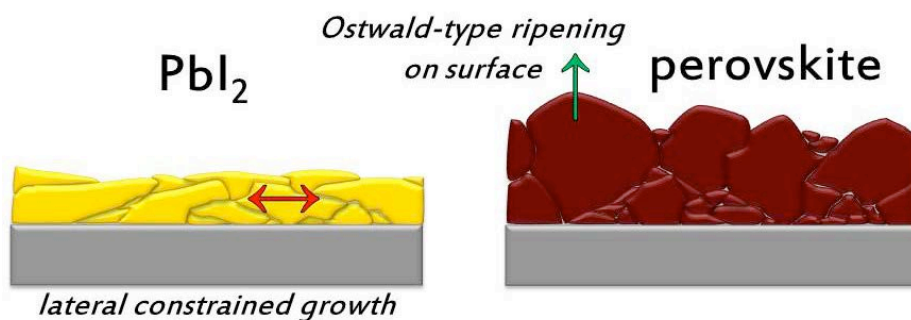


Figure 2. Model for the film morphology of both PbI_2 precursor and perovskite film

References:

- [1] P. Docampo, F. Hanusch, S.D. Stranks, M. Döblinger, J.M. Feckl, M. Ehrensperger, N.K. Minar, M.B. Johnston, H.J. Snaith and T. Bein; Solution Deposition-Conversion for Planar Heterojunction Mixed Halide Perovskite Solar Cells; *Adv. Energy Mater.* **4**, 1400355 (2014)
- [2] A. Hexemer and P. Müller-Buschbaum; Advanced Grazing-Incidence techniques for Modern Soft-Matter Material Analysis; *IUCrJ* **2**, 106-125 (2015)
- [3] J. Schlipf, P. Docampo, C.J. Schaffer, V. Körstgens, L. Bießmann, F. Hanusch, N. Giesbrecht, S. Bernstorff, T. Bein and P. Müller-Buschbaum; A Closer Look into Two-Step Perovskite Conversion with X-ray Scattering; *J. Phys. Chem. Lett.* **6**, 1265-1269 (2015)

STUDY OF KINETICS OF L₁₀ TRANSFORMATION IN FECUPT ALLOY FILM AND FE(CU)/PT(CU) MULTILAYER

K. Sharma¹, G. Sharma¹, A. Gupta¹, M. Gupta², V.R. Reddy², and S. Bernstorff³

1.) Amity Center for Spintronic Materials, Amity University UP, Sector 125, Noida 201 313, India

2.) UGC-DAE Consortium for Scientific Research, University Campus, Khandwa Road, Indore 452 001, India

3.) Elettra-Sincrotrone Trieste, 34149 Basovizza, Trieste, Italy

Films of L₁₀ phase of FePt possess one of the highest known magnetic anisotropy and are potential candidates for high density recording media. Extensive studies have been done in the literature to reduce the ordering temperature which for equiatomic alloy lies in the range of 500°C. Alloying with various non magnetic species like Au, Cu is known to reduce the ordering temperature [1]. Use of Fe/Pt multilayer as a starting structure has also been tried [2]. Post deposition annealing of such multilayers results in formation of the L₁₀ phase at reduced temperature. In the present work, a multilayer of Fe_{0.85}Cu_{0.15}/Pt_{0.85}Cu_{0.15} is used as a starting structure. It is envisaged that a combination of a multilayer structure along with impurity incorporation will further reduce the ordering temperature. Therefore the kinetics of L₁₀ ordering in FePtCu alloy film and [Fe_{0.85}Cu_{0.15}/Pt_{0.85}Cu_{0.15}]_{x10} multilayer were studied using *in situ* XRD at elevated temperatures.

Two films, one consisting of a 60 nm thick single layer of (Fe₅₀Pt₅₀)_{0.85}Cu_{0.15} and the other in the form of a multilayer [Fe_{0.85}Cu_{0.15} (2.4 nm) /Pt_{0.85}Cu_{0.15} (2.7 nm)]_{x10} have been studied. In situ x-ray diffraction measurements at elevated temperatures were done at the SAXS beamline of Elettra. The sample was kept in a miniature furnace under flowing N₂ atmosphere. The furnace was mounted on a New Port tilting stage in order to align the sample in grazing incidence geometry. Diffraction pattern in a limited q range were acquired using a 100 K Pilatus detector covering an angular range of 22° to 52° 2θ. Films were annealed at 300°C and diffraction patterns were recorded continuously with the data accumulation time for each diffraction pattern being equal to 121 sec. Thus the evolution of the structure was monitored with a time resolution of 121 seconds.

Fig. 1a gives the evolution of diffraction patterns of alloy film. One can see that in pristine sample only two diffraction peaks are observed which may be attributed to the (111) and (200) reflections of the FePt alloy phase. With thermal annealing an additional peak starts appearing and after 10 minutes of annealing a small peak around 2θ = 24 degree starts appearing which corresponds to (100) superlattice reflection of L₁₀ phase. With further annealing time, the superlattice peak grows in intensity and reaches saturation around an annealing time of 14 min.

The diffraction pattern of the multilayer film also exhibits a qualitatively similar trend of evolution with annealing time at 300°C (Fig. 1b). However, one can see that in this sample the superlattice peak starts appearing already after annealing for 6 minutes. One can clearly see that kinetics of L₁₀ transformation is significantly faster in multilayer as compared to alloy film.

The present study shows that a combination of multilayer structure with impurity incorporation can be used to further enhance the kinetics of L₁₀ transformation in a FePt system.

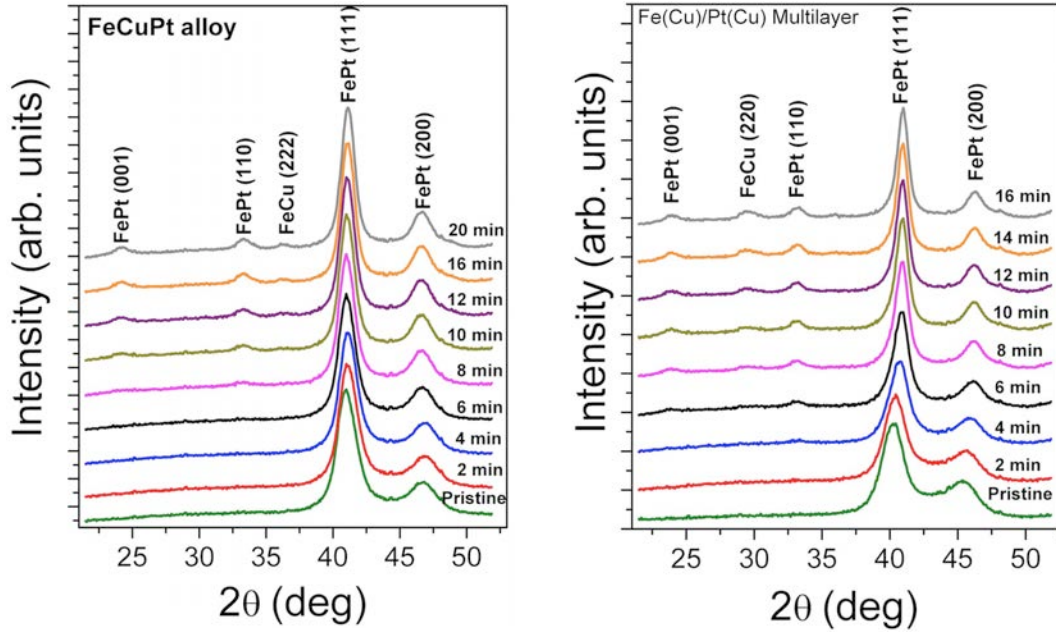


Figure 1. left: XRD pattern of $(\text{Fe}_{50}\text{Pt}_{50})_{0.85}\text{Cu}_{0.15}$ alloy film as a function of annealing time at 300°C ; right: XRD pattern of $[\text{Fe}_{0.85}\text{Cu}_{0.15}/\text{Pt}_{0.85}\text{Cu}_{0.15}]_{\times 10}$ multilayer film as a function of annealing time at 300°C

References:

- [1] Tom A. George, Zhen Li, Minglang Yan, Yingfan Xu, Ralph Skomski, and David J. Sellmyer, *J. Appl. Phys.* **103**, 07D502 (2008)
- [2] V. Raghavendra Reddy, S. Kavita, and Ajay Gupta, *J. Appl. Phys.* **99**, 113906 (2006)

STRUCTURE AND TRANSPORT PROPERTIES OF GE QUANTUM DOTS IN SiO₂ MATRIX

R. Slunjski¹, P. Dubček¹, N. Radić¹, S. Bernstorff², B. Pivac¹

1.) Ruđer Bošković Institute, Bijenička 54, 10000 Zagreb, Croatia

2.) Elettra-Sincrotrone Trieste, Strada Statale 14, km 163.5, 34149 Basovizza (TS), Italy

Superlattices consisting of Ge QDs embedded in amorphous SiO₂ layers were prepared by magnetron sputter deposition of 20 bilayers, each consisting of 4 nm of pure SiO₂ and 4 nm SiO₂+Ge (Ge was simultaneously cosputtered with SiO₂ from a separate source), plus an additional capping layer of 10 nm SiO₂, on a cleaned and etched p-type Si (1 0 0) substrate held at RT. After deposition, the samples were annealed at different temperatures ranging from 350° to 900°C for 1 h in flowing N₂ atmosphere to induce Ge nanocrystals formation. We have observed that 700°C was the optimum temperature where we obtained the best results and therefore only these results will be presented and analysed.

Structural properties: The GISAXS pattern of as-grown and annealed films for a grazing incidence angle larger than the critical angle are given in Fig. 1 a) and b) with arbitrary color coding. These patterns reveal the details of the layered structure of the samples

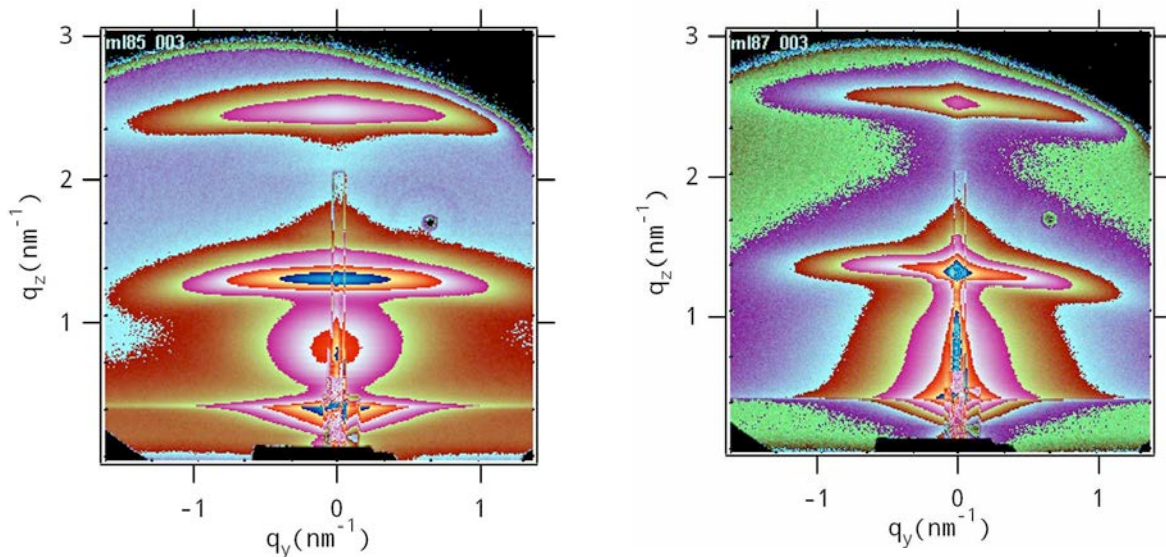


Figure 1. GISAXS patterns of an as-received sample (a) and annealed at 700°C for 1 h in N₂ atmosphere (b)

Due to the critical angle scattering, the Yoneda contribution is visible as a strong intensity peak extended in horizontal direction at $q_z=0.4 \text{ nm}^{-1}$. Furthermore, the first and the second Bragg peaks are placed at $q_z=1.25 \text{ nm}^{-1}$ and 2.5 nm^{-1} , respectively, corresponding to the multilayer structure. From these, the actual bilayer thickness is found to be 5.2 nm. An interference from the 10 nm capping layer contribution results in a broad peak centered at $q_z=0.8 \text{ nm}^{-1}$ in the as-received sample. It is less pronounced in the annealed sample due to the stronger particle scattering contribution.

The obtained radius of gyration value is $R_G=1.9 \text{ nm}$ for the annealed sample, and assuming spherical shape one can calculate the sphere radius as $R=\sqrt{5/3} R_G=2.4 \text{ nm}$. This is in good

agreement with the size obtained from the simultaneously performed diffraction experiment [1].

Transport properties: The logarithm of the absolute value of the current I measured across the oxide layer with Ge QDs is shown in Fig. 2 as a function of the applied gate voltage V . The analyzed sample has been found to be moderately conductive and rectifying. The I - V characteristics resemble that of a p - n junction diode, the poor quality of the diode is reflected in an ideality factor (which gives the slope of the forward-biased I - V in the straight region) that deviates significantly from unity. A hysteresis is observed for low forward voltages. This hysteresis originates from the charge accumulated in the SiO_2 layer with embedded Ge QDs. As it will be discussed below this accumulated charge is the charge trapped near the nanocrystal interfaces with the oxide layer. The large reverse-bias current is due to the presence of electron traps (electron generation centers) in the QDs layer. The reverse current increases linearly with small increasing bias values. It is noteworthy that the I - V characteristics under the forward bias shows a kink at the gate voltage around 0.5 V. We associate this kink with the energy barrier height at the interface between the silicon substrate and the active SO_2 layer.

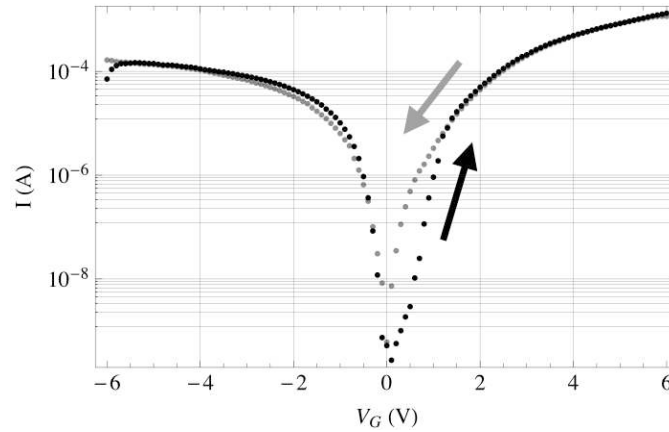


Figure 2. I-V curves of an annealed sample; arrows denote the scanning direction

Charge trapping occurs when the injected carriers are transported along the tunneling paths. The injected carriers could be trapped in the individual Ge nanocrystals. Moreover, it is well known that nc-Ge/ SiO_2 films contain a high density of oxygen-related defects at and close to the nc-Ge/ SiO_2 interface, such as neutral oxygen vacancy ($\text{O}_3\equiv\text{Si}-\text{Si}\equiv\text{O}_3$, where a Si atom is bonded to three oxygen atoms) and a non-bridging oxygen hole center ($\equiv\text{Si}-\text{O}$ which represents an unpaired electron). These defects could also trap carriers. In either case, charge trapping is associated with the existence of nc-Ge. Furthermore, charge trapping affects the carrier transport across the oxide layer in a number of ways: firstly, charge trapping in nc-Ge or a defect increases the resistance of the tunneling paths due to the electrostatic interaction of the transported carriers with the trapped carriers. Secondly, the tunneling paths related to the charged nc-Ge could be broken due to the Coulomb blockade effect, providing suppressing of the carrier transport across the oxide layer.

Fig. 3 shows the C - V characteristics measured on the same sample as described above. The C - V curve (when scanned to negative values) exhibits a distorted shoulder-like shape. This shoulder might be attributed to the mechanism of charge trapping at the nc-Ge/ SiO_2 interface or near the interface region [2–4]. However, there is another interpretation based on the mechanism of charge tunneling into the nanocrystals, which is similar to the observations on

quantum dots in compound semiconductors [2]. As the hysteresis is counterclockwise (the arrows in the Fig. 3 indicate the voltage scanning direction), that suggests that the net positive charge is accumulated in the oxide layer with Ge QDs. The C - V hysteresis correlates well with the hysteresis observed in the I - V characteristic, shown in Fig. 2. The observed C - V hysteresis is due to the trapping and detrapping of injected electrons at the nc-Ge/SiO₂ interface rather than charging and discharging of germanium nanocrystals itself.

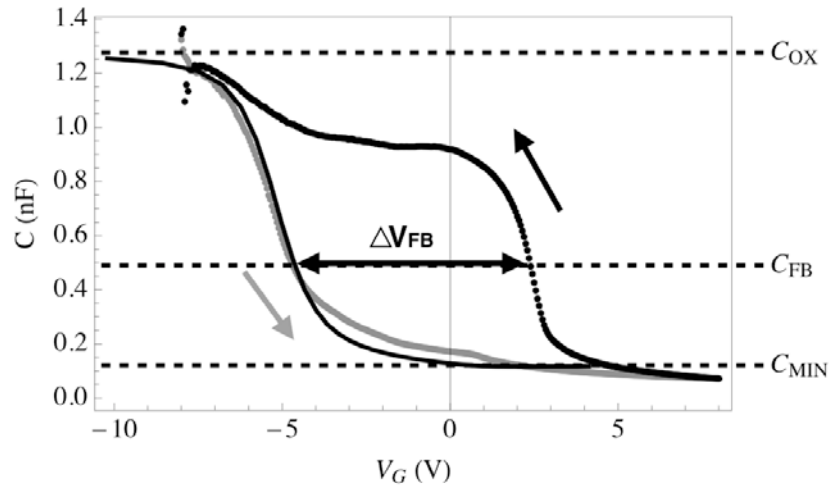


Figure 3. The hysteresis of the capacitance-voltage characteristic for the annealed sample. Dark dots represent scanning from $V=10$ V to -10 V and gray spots scanning from $V=-10$ V to 10 V. Also shown is the best fit (full dark line) $CV_{ID} + \Delta V_{FB} + D_{it}$. Where CV_{ID} is the calculated CV curve for an ideal MOS structure, and $D_{it} = 2.6 \times 10^{12} \text{ cm}^{-2} \text{ eV}^{-1}$, $\Delta V_{FB} = 7$ V. D_{it} are the defects at the interface

References:

- [1] R Slunjski, P Dubcek, N Radić, S Bernstorff and B Pivac, J. Phys. D: Appl. Phys. **48** (2015) 235301
- [2] Y. Ishikawa, M. Kosugi, M. Kumezawa, T. Tsuchiya, and M. Tabe, Thin Solid Films 369 (2000) 69-72
- [3] J. Shi, L. Wu, X. Huang, J. Liu, Z. Ma, W. Li, X. Li, J. Xu, D. Wu, A. Li, K. Chen, Solid State Commun. 123 (2002) 437-440
- [4] D. N. Kouvatsos, V. Ioannou-Sougleridis, A. G. Nassiopoulou, Appl. Phys. Lett. 82 (2003) 397-399

Chemistry

GRAZING INCIDENCE SMALL ANGLE SCATTERING (SAXS) AND DEEP X-RAY LITHOGRAPHY (DXRL) OF 9-ANTHRACENYL₂SiH₂ IN PMMA

J. Binder, C. Zeppek, A. Torvisco, B. Marmiroli, H. Amenitsch and F. Uhlig

TU Graz, Institute of Inorganic Chemistry, Stremayrgasse 9/IV, 8010 Graz, Austria

To study the effect of high radiation doses on hydrogen rich silanes, 9-anthracenyl₂SiH₂ was embedded into a PMMA (polymethylmethacrylate) matrix and irradiated with hard X-ray radiation between 2 and 20 keV at the Deep X-ray Lithography Beamline of the electron storage ring ELETTRA, Trieste, Italy [1]. The sample was prepared, first, by mixing the silane and the polymer and second, the mixtures were spin coated on a Si-wafer (2000 rpm for 1 minute followed by soft bake for 2 minutes at 150 °C). The thickness of the resulting film is about 690 nm. Irradiation was performed with increasing radiation doses up to 250 kJ/cm³ and analyzed with Grazing incidence Small Angle Scattering at the Austrian SAXS beamline at ELETTRA [2]. The incidence angle was set to 0.5°. Figure 1 shows the vertical cuts of the GISAXS images of PMMA and in comparison with the silane containing PMMA sample. In the latter, a growth of nanostructures can be observed instantly with beginning of the irradiation. In case of the sole polymer, a formation of larger structures (>10 nm) can as well be detected but with a much slower rate.

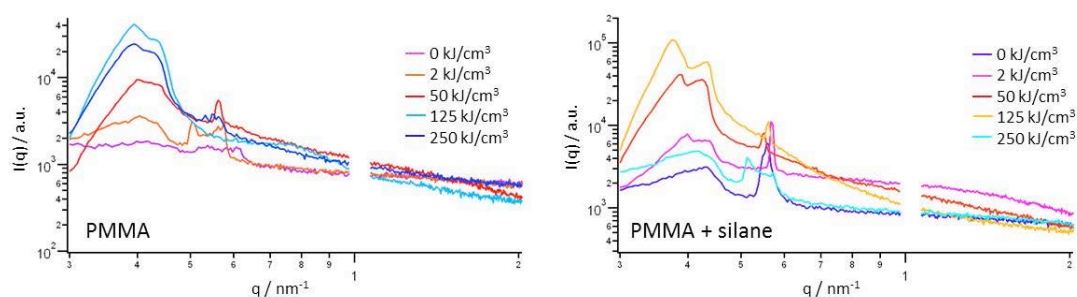


Figure 1. Vertical cuts of the GISAXS images of PMMA (left) and silane containing PMMA (right) at different radiation doses

A curve fit of the GISAXS data of the silane containing polymer (Figure 2) allows a more detailed description of the irradiation induced nanostructure formation. For the analysis a model consisting of spherical particles with a Schultz distribution for the particle sizes and a sticky hard sphere model for the structure factor was used. Additionally a general Porod term was added for the large structures [3,4].

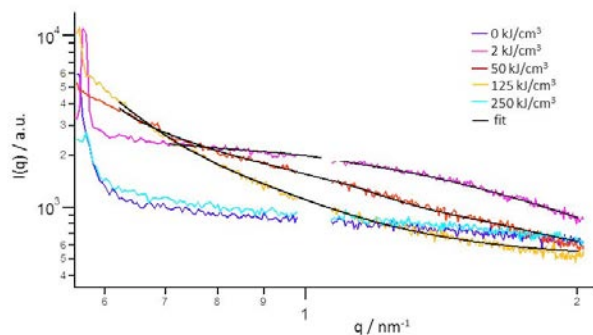


Figure 2. Vertical cuts of the GISAXS data of silane containing PMMA with the resulting fits of the model (described in the text)

At a dose of about 2 kJ/cm^3 , particles with a diameter of approximately 3 nm with a spacing of 7 nm can be detected (Figure 3). Upon continued irradiation an increase of size (5 nm) alongside with a wider spacing (11 nm) is observed, which might be attributed to the growth of larger nanostructures by aggregation of the initial smaller ones. The nanostructures continuously grow, until they reach a diameter larger than 10 nm at the highest irradiation dose, which was limited by the resolution of the technique.

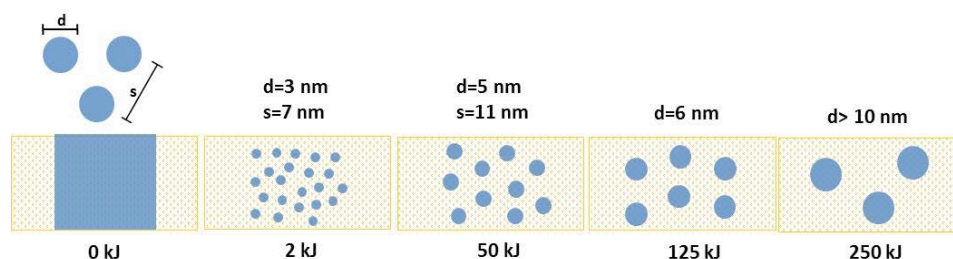


Figure 3. Formation of nanostructures in irradiated silane containing PMMA; d = diameter of particle, s = spacing between particles

The obtained GISAXS data supplements the UV irradiation experiments of 9-anthracenyl $_2$ SiH $_2$ that led to an intramolecular [4+4] adduct, which rapidly decomposes due to the unstable silacyclopropane structure (Figure 4) [5]. In the PMMA films, it seems that the anthracene structure stays unaltered since its typical blue fluorescence can still be observed after the highest irradiation dose. A formation of silicon nanostructures and the anthracene dimer *via* Si-C bond cleavage seems to be probable and is supported by $^1\text{H-NMR}$ data and GISAXS measurements.

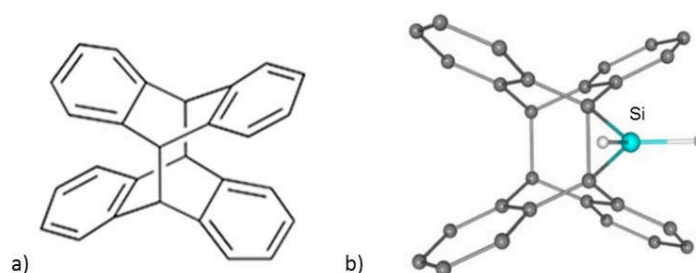


Figure 4. a) photodimer of anthracene; b) proposed structure of irradiation product of 9-anthracenyl $_2$ SiH $_2$

References:

- [1] <https://www.elettra.trieste.it/elettra-beamlines/dxrl.html>. Trieste
- [2] Amenitsch, H.; Rappolt, M.; Kriechbaum, M.; Mio, H.; Laggner, P.; Bernstorff, S.: First performance assessment of the small-angle x-ray scattering beamline at ELETTRA. *J. Synchrotron Radiat.* 1998, 5, 506-508
- [3] Pedersen, J. S.: Analysis of small-angle scattering data from colloids and polymer solutions: modeling and least-squares fitting. *Adv. Colloid Interface Sci.* 1997, 70, 171-210
- [4] Kinning, D. J.; Thomas, E. L.: Hard-sphere interactions between spherical domains in diblock copolymers. *Macromolecules* 1984, 17, 1712-18
- [5] Binder, J.: Synthesis, Characterization and Reactivity of novel Arylsilanes - steps towards new materials. PhD thesis, Graz University of Technology, 2015

TIME RESOLVED *IN SITU* GISAXS OF 9-ANTHRACENYL₂SiH₂ IN PMMA

J. Binder, C. Zeppek, A. Torvisco, B. Marmioli, H. Amenitsch and F. Uhlig

TU Graz, Institute of Inorganic Chemistry, Stremayrgasse 9/IV, 8010 Graz, Austria

For investigating the thermolysis of unaltered and irradiated 9-anthracenyl₂SiH₂ an *in situ* structural study was performed under grazing incidence conditions. Therefore 9-anthracenyl₂SiH₂ was embedded into a PMMA (polymethylmethacrylate) matrix and spin coated on a Si-wafer (2000 rpm for 1 minute followed by soft bake for 2 minutes at 150 °C). The final film (unaltered and with 250 kJ/cm³ dose) was heated to 440 °C with an Anton Paar DHS 1100 under argon atmosphere. The reaction was monitored by *in situ* GISAXS measurement.

Figure 1 shows the vertical cuts of the GISAXS pattern of PMMA and silane containing PMMA. A different reaction behavior can be observed. In case of the silane containing sample a sudden formation of particles is detected, which is independent from the irradiation dose.

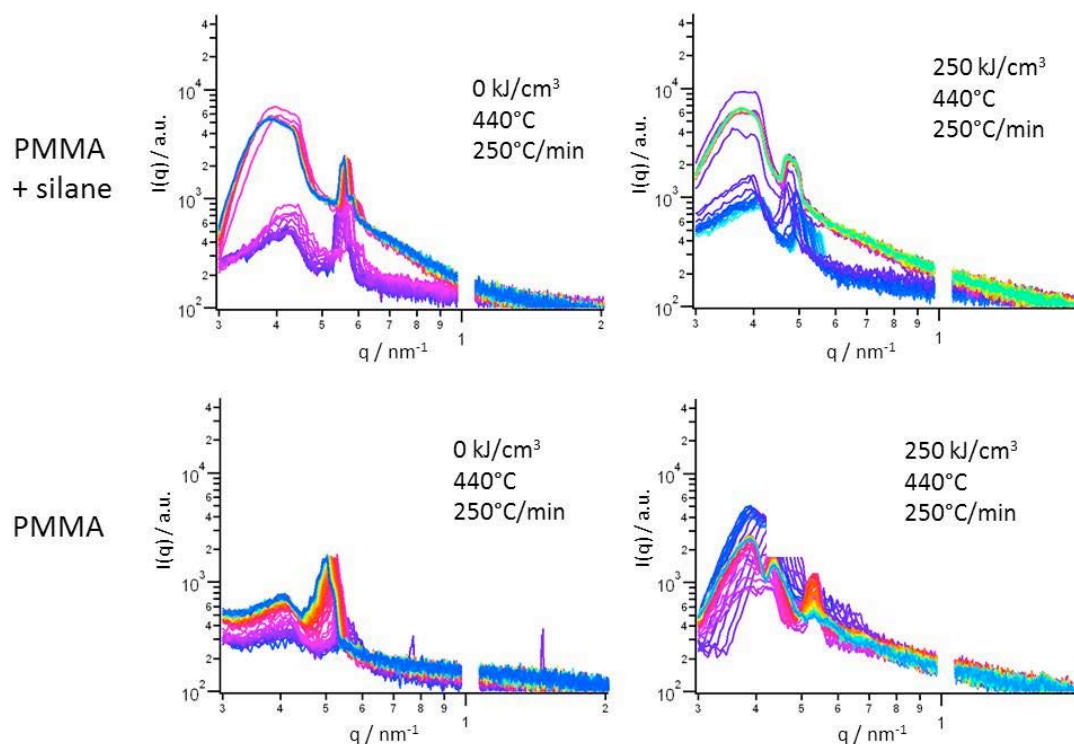


Figure 1. GISAXS of silane containing PMMA (top) and PMMA (bottom) and at different energy doses and heating to 440 °C

An easy accessible quantity is the correlation length of the particles derived by dividing the moments of the scattering pattern [1]. As a sensitive indicator the differential correlation length given by the difference of the correlation length to its initial value was used.

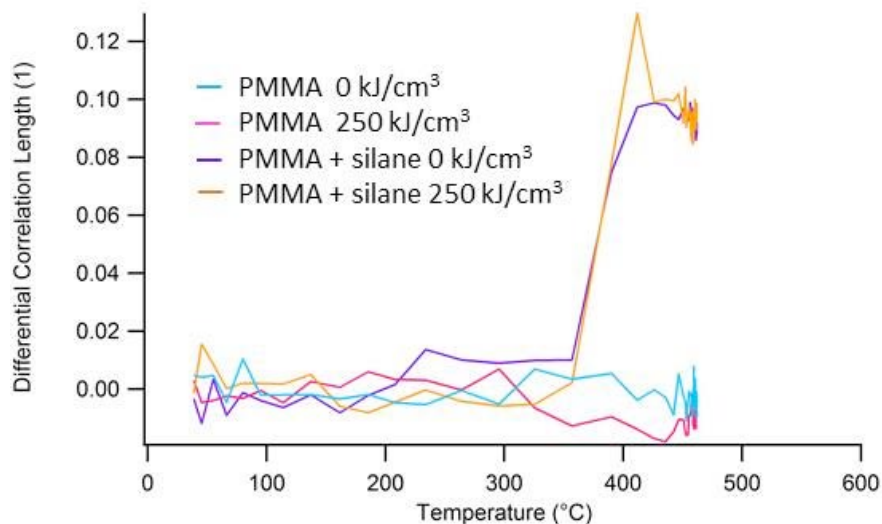


Figure 2. Correlation lengths of observed particles

The plot of the differential correlation lengths against the temperature (Figure 2) shows the rapid formation of particles in the range of 380-400 °C, which fits very well to the observed decomposing temperature of 9-anthracenyl₂SiH₂ detected by TGA/DSC analysis. These findings match the detected particle formation observed in thermolysis experiments [2].

References:

- [1] Glatter, O.; Kratky, O.: *Small Angle X-ray Scattering*; Academic Press, 1982
- [2] Binder, J.: *Synthesis, Characterization and Reactivity of novel Arylsilanes - steps towards new materials.* PhD thesis, Graz University of Technology, 2015

AUTOCATALYSIS IN SELF-HEALING POLYMERS: INVESTIGATION OF TIME-DEPENDENT NANO-CLUSTER FORMATION VIA SAXS MEASUREMENTS

W. Binder¹, P. Michael¹, S. Neumann¹, D. Döhler¹, J. Akbarzadeh² and S. Bernstorff³

- 1.) Institute of Chemistry, Chair of Macromolecular Chemistry, Faculty of Natural Sciences II (Chemistry, Physics and Mathematics), Martin-Luther University Halle-Wittenberg, von Danckelmann-Platz 4, Halle 06120, Germany
- 2.) Faculty of Physics, Dynamics of Condensed Systems, University of Vienna, Strudlhofgasse 4, 1090 Vienna, Austria
- 3.) Elettra-Sincrotrone Trieste S.C.p.A., Strada Statale 14, km 163.5, in Area Science Park, I-34149 Basovizza / Trieste, Italy

Due to thermal, chemical or physical stress, polymers will experience damage, degradation, and failure as a natural consequence of their material applications. Traditionally, the engineering and processing research has been mainly focused on the development and design of new, even more sophisticated materials in order to increase their service-lifetime. Inspired by biological systems the development of self-healing materials has gained significant importance focusing on a damage management concept *vs.* damage prevention. Thus, self-healing polymers belong to a group of emerging new “smart materials” with the ability to repair occurring damage themselves, therefore healing nano- or microscopic cracks within the material as a dynamic response to an external, applied stress and thus to mechanical deformation.

Following the goal to design self-healing polymers [1], we have investigated the network formation between various multivalent polymeric azides and alkynes based on poly(isobutylene)s (PIBs) and poly(acrylate)s *via* copper(I)-catalyzed alkyne-azide “click” cycloaddition reactions proceeding at room temperature [2]. Within the crosslinking process an autocatalytic effect was observed which was attributed to triazole ring formation further promoting network formation *via* nano-clustering effects. Furthermore, a significant influence of the molecular weight and therefore the functional group density was noticed showing a stronger autocatalytic effect with decreasing functional group density therefore linking “click” reactivity and polymer dynamics.

Accordingly, the project aims to investigate “click” reactions between multivalent, random copolymers composed of propargyl acrylate and *n*-butyl acrylate and poly(isobutylene)s (PIBs) functionalized with azide- and alkyne-moieties, respectively to gain detailed information of the crosslinking process and therefore a deeper understanding of the kinetics of nanocluster formation in self-healing polymers [1]. Within the “click” crosslinking reaction [3] transient nanosized 1,2,3-triazole-clusters are induced, proposed to act as nuclei for the complexation of copper(I)-ions and thus the acceleration of the reaction itself [2].

In order to investigate the formation of transient 1,2,3-triazole-clusters multivalent azide- and alkyne-functionalized polymers have been mixed in an equimolar ratio and the “click” network formation was started by the addition of a Cu(I)-source. The so obtained polymer mixture was immediately put between commercially available aluminum foil and was investigated *via* SAXS-measurements in defined time intervals. Therefore, an asymmetric set-up of the camera in vertical direction with a sample to detector distance of 135 cm in combination with a 2D Pilatus3 1M detector system was used, leading to an accessible *q*-range of 0.3 – 3.5 nm⁻¹ (8 keV photon energy beam).

In Table 1 the different investigated polymer mixtures and the corresponding molecular weights are summarized. Beside the molecular weight, the functional group density and the

composition of the polymers and also the amount of added copper(I) source ($\text{CuBr}(\text{PPh}_3)_3$) was varied in order to investigate the influence on the added amount of copper(I) on the size of the formed 1,2,3-triazole-clusters. Furthermore, multivalent star-shaped PIBs suitable for an all-in-one self-healing system have been investigated. Therefore, an azide-functionalized star-shaped PIB was mixed with a similar alkyne-functionalized star-shaped PIB still covered with protecting groups which first should be cleaved off by the addition of the catalyst, namely $\text{CuF}(\text{PPh}_3)_3$, followed by the “click” crosslinking reaction itself (see Table 1, Mixture 5).

Table 1. Overview of equimolar polymer mixtures prepared by mixing an azide- and an alkyne-functionalized polymer (molecular weights, added amount of copper(I) source).

Sample 1	M_n of azide-functionalized polymer [g/mol]	M_n of alkyne-functionalized polymer [g/mol]	Added amount of copper(I) / functional group [equ.]
Mixture 1: PIB-azide + Poly(propargyl acrylate- <i>co</i> - <i>ran</i> - <i>n</i> -butyl acrylate) (1:6)	6,300	6,800	0.1
Mixture 1: PIB-azide + Poly(propargyl acrylate- <i>co</i> - <i>ran</i> - <i>n</i> -butyl acrylate) (1:6)	6,300	6,800	0.5
Mixture 2: PIB-azide + Poly(propargyl acrylate- <i>co</i> - <i>ran</i> - <i>n</i> -butyl acrylate) (1:12)	6,300	9,400	0.1
Mixture 2: PIB-azide + Poly(propargyl acrylate- <i>co</i> - <i>ran</i> - <i>n</i> -butyl acrylate) (1:12)	6,300	9,400	0.25
Mixture 2: PIB-azide + Poly(propargyl acrylate- <i>co</i> - <i>ran</i> - <i>n</i> -butyl acrylate) (1:12)	6,300	9,400	0.5
Mixture 2: PIB-azide + Poly(propargyl acrylate- <i>co</i> - <i>ran</i> - <i>n</i> -butyl acrylate) (1:12)	6,300	9,400	1.0
Mixture 3: PIB-azide + Poly(propargyl acrylate- <i>co</i> - <i>ran</i> - <i>n</i> -butyl acrylate) (1:24)	6,300	8,500	0.1
Mixture 3: PIB-azide + Poly(propargyl acrylate- <i>co</i> - <i>ran</i> - <i>n</i> -butyl acrylate) (1:24)	6,300	8,500	0.5
Mixture 4: PIB-azide + PIB-alkyne	5,500	6,900	0.1
Mixture 4: PIB-azide + PIB-alkyne	5,500	6,900	0.5
Mixture 5: PIB-azide + PIB-alkyne (protected)	5,500	13,700	0.1

The prepared polymer mixtures were measured about 30 to 100 seconds each. Directly after the preparation the resulting mixture was measured continuously followed by larger time intervals in between (up to 10 minutes). Due to a home-made and complex sample holder

geometry several polymer mixtures could be measured one after another just by adjusting the sample holder and without changing the sample. All measurements were performed at room temperature.

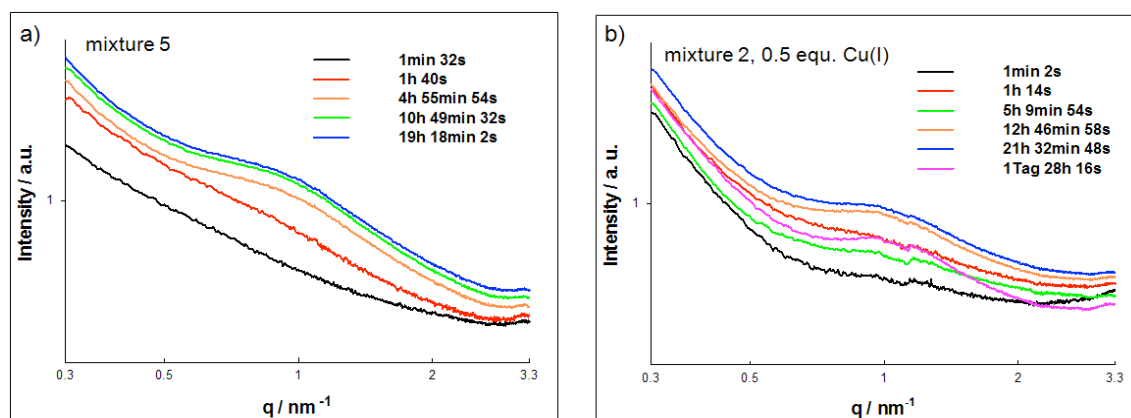


Figure 1. Time-resolved SAXS-measurements of polymeric mixtures of a) three-arm star-shaped azide- and protected alkyne-functionalized PIBs which undergo crosslinking *via* CuAAC after deprotection introduced by the addition of $\text{CuF}(\text{PPh}_3)_3$ (mixture 5) and b) three-arm star-shaped azide-functionalized PIBs and alkyne bearing poly(acrylate)s (1:12) which undergo crosslinking *via* CuAAC introduced by the addition of $\text{CuBr}(\text{PPh}_3)_3$ (0.5 equ., mixture 2).

Whereas the polymer mixture resulting from mixing three-arm star-shaped azide-functionalized PIB and three-arm star-shaped protected alkyne-functionalized PIB (Figure 1a) showed no scattering signal directly after mixing (black curve) as well as one hour after mixing (red curve), a broad scattering peak around 1.0 nm^{-1} emerged over time (orange, green and blue curve). Accordingly, the deprotection of the trimethyl-silyl protection groups followed by the click-crosslinking reaction itself was successfully started by the addition of $\text{CuF}(\text{PPh}_3)_3$. Due to the broadness of the scattering peak an exact evaluation of the exact position proved to be challenging.

The polymer networks formed between three-arm star-shaped azide-functionalized PIBs and alkyne-functionalized poly(acrylate)s (1:12) were analyzed in a similar manner (Figure 1b). Similar to mixed PIBs a scattering signal around 1.0 nm^{-1} was observed for the first time five hours and 10 minutes (green curve) after adding the copper(I) catalyst whereas the intensity increased with increasing reaction time of crosslinking. However, also for this polymer mixture an exact determination of the peak position proved to be challenging and therefore the detailed analysis of all obtained SAXS data of all polymer mixtures (see Table 1) and their relation to the click-crosslinking mechanism are still ongoing in cooperation with the Faculty of Physics of the University of Vienna.

References:

- [1] W. H. Binder, Wiley-VCH Verlag GmbH & Co. KGaA, Weinheim, 2013, p. 425
- [2] a) D. Döhler, P. Michael, W. H. Binder, *Macromolecules* 2012, 45, 3335; b) M. Gragert, M. Schunack, W. H. Binder, *Macromol. Rapid Commun.* 2011, 32, 419
- [3] a) V. O. Rodionov, V. V. Fokin, M. G. Finn, *Angew. Chem.* 2005, 117, 2250; b) T. R. Chan, R. Hilgraf, K. B. Sharpless, V. V. Fokin, *Org. Lett.* 2004, 6, 2853

PORE ORGANISATION INTO CRYSTALLINE MESOSTRUCTURED THIN FILMS BASED ON 3-GLYCIDOXY-PROPYL-TRIMETHOXYSILANE

D. Carboni¹, A. Pinna¹, H. Amenitsch², D. Loche³, M.F. Casula³, L. Malfatti¹ and P. Innocenzi*¹

- 1.) Laboratorio di Scienza dei Materiali e Nanotecnologie, CR-INSTM, Università di Sassari, Palazzo Pou Salid, Piazza Duomo 6, 07041 Alghero (SS), Italy
- 2.) Institute of Inorganic Chemistry, Graz University of Technology, Stremayrgasse 9/IV, 8010 Graz, Austria
- 3.) Dipartimento di Scienze Chimiche e Geologiche, Università di Cagliari, 09042 Monserrato (CA), Italy

Crystalline walls are easily obtained in mesostructured films based on transition metal oxides, such as titania, and recently also silica walls of mesostructured films were crystallized using a seeding process with strontium or barium, elements capable of assisting the nucleation and growth of quartz. The crystals growth inside mesostructured oxide films is generally achieved by a controlled thermal treatment while crystals of dimensions up to few nanometers could form their crystalline walls. The level of complexity increases in the case of organic–inorganic films obtained through sol–gel reactions of organically modified alkoxides. In fact, a crystalline organization in hybrid materials is usually observed only if preformed bridged species are allowed to self-assemble into ordered layered structures. To date, one of the few exceptions reported in literature is given by materials based on 3-glycidioxy-propyl-trimethoxy-silane (GPTMS), which is not a bridged alkoxide. This hybrid precursor is, in fact, capable of favouring, in highly basic conditions, the dimerization of two GPTMS molecules, through reaction of the terminal epoxides that, with controlled opening and condensation, can form *p*-dioxane rings [1].

The present work aimed at obtaining crystalline mesostructured hybrid films by using hybrid layered crystals as nano building blocks for the pore walls. These units have been let to form in the precursor sol and then have been incorporated within the pore walls to give an ordered mesophase. GPTMS has been selected as chemical precursor because of its chemical tunability; under highly basic conditions is, in fact, able to form bridged structures, via opening and coupling of two epoxy rings, which self-organize into lamellar structures. In order to acquire a deep insight of the structural evolution of the hybrid matrix, the micelles organization was followed through *in situ* Grazing Incidence Small and Wide Angle X-ray Scattering (GISAXS-WAXS). The sol was deposited onto a silicon substrate by using a dip-coater set up inside the SAXS experimental hutch and analysed using the synchrotron light source. This set-up has allowed us to follow the formation of the mesostructure in a time-resolved scale (Figure 1) by using a configuration performing the measure in a 2-theta range spanning from 1.5 to 14°. The reason for such a choice has been dictated by the need of having simultaneous information on the mesophase organization (low angular range) and further evidence of the hybrid crystallinity (high angular range) exploiting the higher definition attainable with the high brilliance source of the synchrotron light. The evolution of the time-resolved GISAXS experiment has been followed every 12 seconds starting 10 seconds after the deposition. A synoptic overview is illustrated by Figure 1, where the images (a–d) describe the acquisitions performed after 10, 34, 46 and 134 seconds from film deposition. Figure 1a gives a representation of the structural film organization at time zero, which is 10 seconds after the deposition. At this stage the solvent just started evaporating and no spots indicating any order have been detected. In Figure 1b, 34 seconds after the deposition, a faint halo depicting an arc starts appearing, indicating a mesostructural organisation lacking of defined order, which, instead, emerges 12 seconds after in Figure 1c (46 seconds after deposition) as soon as the solvent evaporation induced the self-assembly. Figure 1c shows, in fact, two defined and four faint spots indicating an ordered structure. The organisation is further confirmed after 88 seconds (Figure 1d), corresponding to 134 seconds

after deposition, where the spots defining the ordered mesostructure are more visible. The radial integration of the GISAXS-WAXS image has also shown the presence of a peak at 9° that can be placed in relationship with the presence of lamellar structures, confirming therefore the crystalline nature of the hybrid matrix.

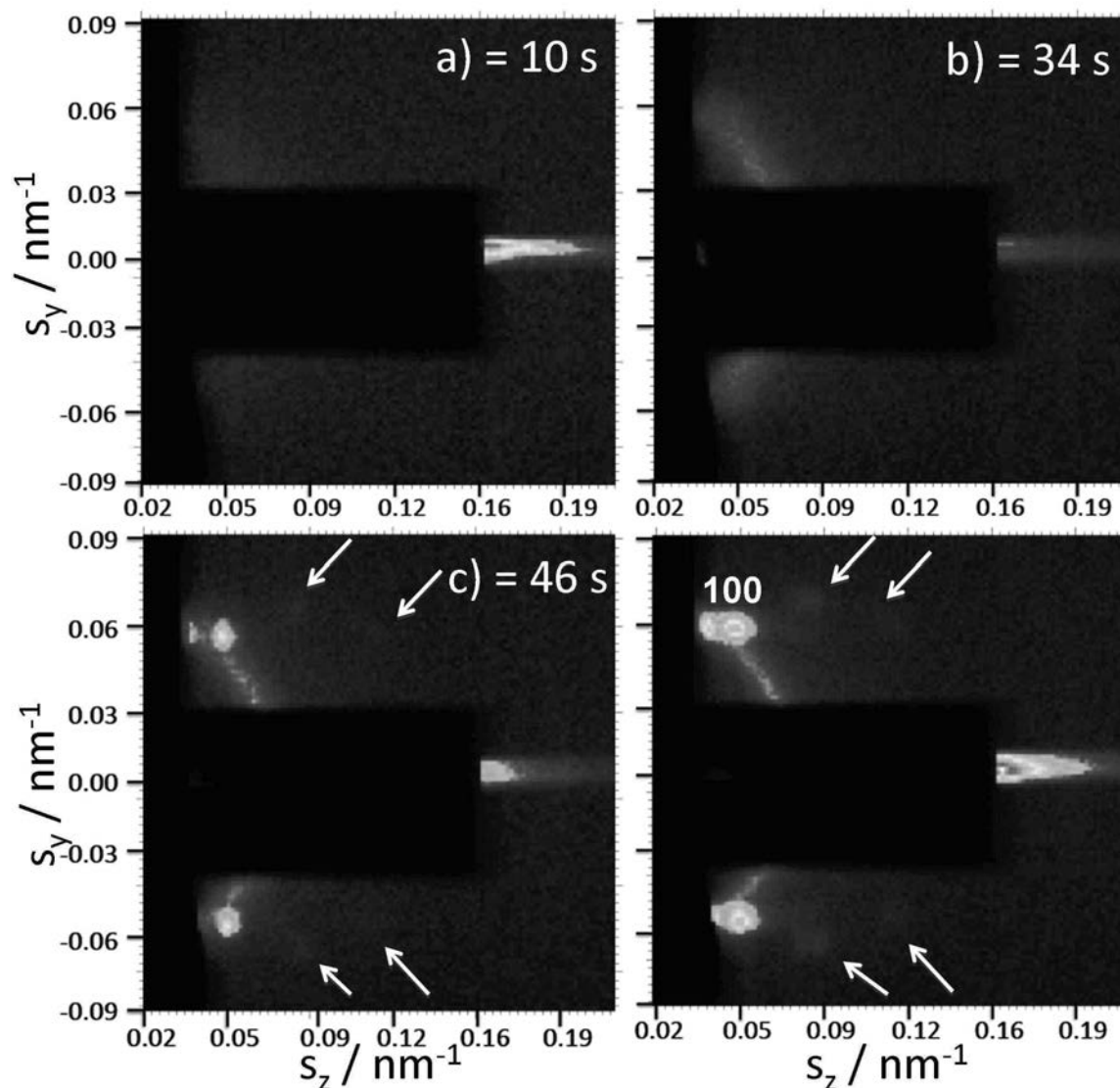


Figure 1. GI-SAXS-WAXS images of a mesostructured crystalline GPTMS film deposited on Si wafer. The patterns were acquired after 10, 34, 46 and 134 seconds

The organization at the mesoscopic level has been further investigated by TEM analysis (Figure 2a) that has revealed a highly organized mesostructure formed by large domains of cylindrical channels arranged in a 2D-hexagonal fashion. These results are not in agreement with the space group attributed to the mesostructure by GISAXS characterization, however it should be considered that the TEM characterization requires the films to be thermally treated before measurement (150°C under inert atmosphere). The change in the mesophase organization, therefore, is likely due to the thermal treatment, which is necessary to increase the contrast between pores and pore walls. A close examination of the TEM images also allows detecting a fine *texture*, which is due to the self-organization of the bridged moieties into a crystalline lamellar structure. A drawing of the final material is shown in Figure 2b: the

film exhibits a long-range pore organization and ordered hybrid lamellar structures embedded in the pore walls [2].

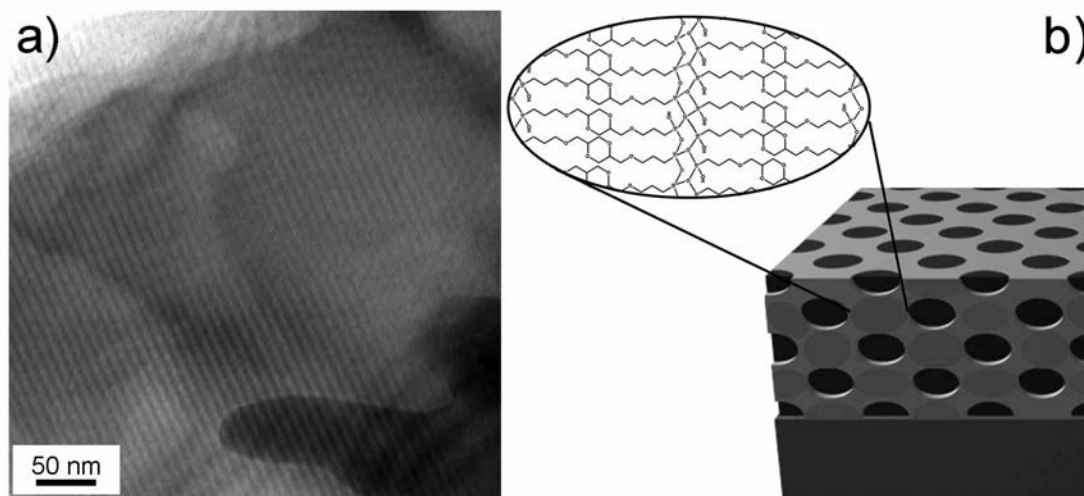


Figure 2. (a) Representative TEM image of the mesostructured film; (b) Schematic representation of the hybrid film containing lamellar layered hybrid crystals within a long-range close-packed mesostructure

The present work has explored the possibility of synthesizing crystalline periodic mesostructured organosilica starting entirely from a hybrid monosilicate precursor which is capable of forming new bridged species *in situ*. These self-assemble and grow up into hybrid crystals forming lamellar structures by controlled aging of the highly basic precursor sol. The addition of surfactant Pluronic F127 as a micellar template and a pH modification enables the deposition of a self-organised crystalline mesostructured hybrid film. The possibility of controlling the evolution of the epoxide opening allows the synthesis of hybrid films that can be further functionalised after the formation of an ordered matrix, giving rise to a versatile crystalline hybrid mesostructured platform.

References:

- [1] B. Mena, M. Takahashi, P. Innocenzi and T. Yoko; Crystallization in Hybrid Organic–Inorganic Materials Induced by Self-Organization in Basic Conditions; *Chem. Mater.*, **19**, 1946- 1953, (2007)
- [2] D. Carboni, A. Pinna, H. Amenitsch, M. F. Casula, D. Loche, L. Malfatti and P. Innocenzi; Getting order in mesostructured thin films, from pore organization to crystalline walls, the case of 3-glycidoxypropyltrimethoxysilane; *Phys. Chem. Chem. Phys.*, **17**, 10679-10686, (2015)

IN SITU MONITORING OF THE FORMATION AND ORIENTATION OF MESOPORES IN H₁-EPT FILMS BY GISAXS DURING TEMPLATED ELECTRODEPOSITION

B. Gollas¹, L. Vieira¹ and H. Amenitsch²

1.) Institute for Chemistry and Technology of Materials, Graz University of Technology, Graz, Austria

2.) Institute of Inorganic Chemistry, Graz University of Technology, A-8010 Graz, Austria

Lyotropic liquid crystal templating is a versatile and facile way of producing mesoporous materials [1], either chemically [2] or electrochemically [3, 4]. The types of materials range from inorganic materials to polymers from semiconductors and metal oxides to metals and alloys as well as hybrid materials. With the ability to control structure and accessibility, the high surface area of mesoporous materials makes their successful application in fields such as catalysis; analysis separation technology, optical devices, and biomedical science. Materials with controlled pore alignment will exhibit long range order in addition to local order and the ability to produce films containing aligned pores is thus highly desirable. However, the fabrication of a highly oriented and perfectly aligned mesoporous material is a challenge.

In 1997 Attard demonstrated that metallic mesoporous films (H₁-ePt) could be produced simply by electrodeposition from the desired mesophase [3] and based on STM measurement it was reported that the mesopores appeared to be “on average, at an angle of 20° with respect to the normal to the plane of the electrode”. Templated electrodeposition was frequently used to produce mesoporous metal films [5], but it was neither possible to control the orientation of the pores, nor could their orientation be monitored during film growth. The ability to electrodeposit a film with controlled pore orientation after shear alignment of the lyotropic liquid crystalline template was for the first time demonstrated by Asghar et al. [6]. They were able to electrodeposit H₁-ePt films with biaxial pore alignment, where the pores all lie in the plane of the electrode and all point in the same direction as shown by GISAXS.

We have monitored the formation and orientation of the mesopores in a growing Pt film during electrodeposition by GISAXS. As exemplary results, data of a film after deposition and after removal of the template are shown in Fig. 1.

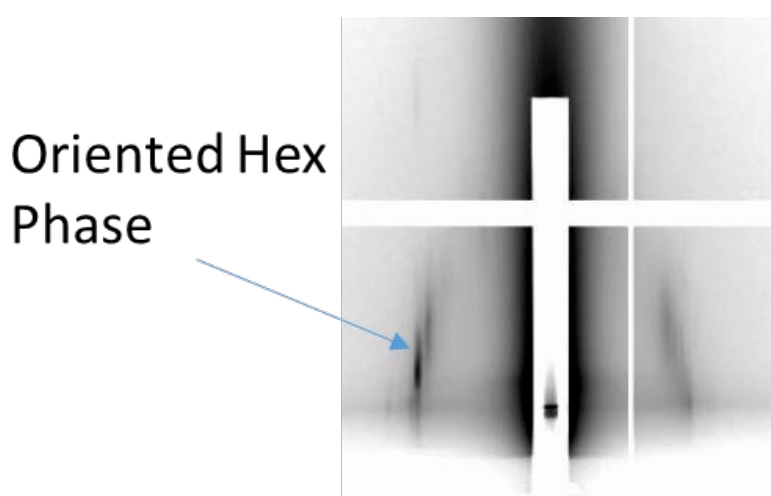


Figure 1. GISAXS pattern of the H₁-ePt film after electrodeposition and removal of the template. The reflections highlighted with an arrow indicate partially vertically aligned mesopores

In the experiment, we used a home-made Teflon cell containing a Au-sputtered glass slide as working electrode, a saturated calomel reference (SCE) electrode and a Pt wire (\varnothing 0.5 mm) auxiliary electrode. The lyotropic liquid crystalline electrolyte template consisted of a mixture of aqueous 0.2 M H_2PtCl_6 and C_{16}EO_8 (50:50 wt.%) mounted as a 0.5 mm thin column between two Kapton foils on the working electrode and contacted at the side to the SCE and at the top to the auxiliary electrode.

An Autolab PGSTAT128N was used to control the potential of the working electrode. The initial GISAXS scan before electrodeposition was carried out at open circuit potential (ca. 0.5 V vs. SCE). The potential was then stepped to -0.1 V (vs. SCE) for 30 minutes and the current recorded. During the electrodeposition GISAXS pattern were measured every 20 seconds.

References:

- [1] J. Y. Jing, C. P. Mehnert and M. S. Wong, *Angew. Chem. Int. Ed.* 38 (1999) 56-77
- [2] G. S. Attard, J. C. Glyde and C. G. Göltner, *Nature* 378 (1995) 366-368
- [3] G. S. Attard, P. N. Bartlett, N. R. B. Coleman, J. M. Elliott, J. R. Owen and J. H. Wang, *Science*, 1997, 278, 838-840
- [4] B. Gollas, J. M. Elliott and P. N. Bartlett, *Electrochim. Acta*, 2000, 45, 3711-3724
- [5] P. N. Bartlett, B. Gollas, S. Guerin and J. Marwan, *Phys. Chem. Chem. Phys.*, 2002, 4, 3835-3842
- [6] K. A. Asghar, J. M. Elliott and A. M. Squires, *J. Mater. Chem.*, 2012, 22, 13311-13317

MECHANISM OF FORMATION OF HKUST-1, A COPPER CONTAINING METAL-ORGANIC FRAMEWORK (MOF) DEPENDING ON REAGENTS AND SOLVENTS

C. C. Webb Jr.¹, M. Kriechbaum², A. Torvisco², H. Amenitsch² and K. Ruhlandt-Senge¹

1.) Department of Chemistry, CST 1-014, Syracuse University, Syracuse, NY, 13244-4100, USA

2.) Institute of Inorganic Chemistry, Graz University of Technology, A-8010 Graz, Austria

The mechanism of formation of the copper-based metal-organic framework (MOF) HKUST-1 has been studied by combined small-/wide-angle X-ray scattering (S/WAXS). The role of the solvent system on the formation of the final product and on the reaction kinetics has been investigated using a recently published facile *in-situ* synthetic pathway [1,2]. A copper salt solution of either $\text{Cu}(\text{NO}_3)_2 \cdot 2\text{H}_2\text{O}$, $\text{Cu}(\text{OAc})_2 \cdot \text{H}_2\text{O}$, CuSO_4 , and $\text{CuCl}_2 \cdot 2\text{H}_2\text{O}$ was added to a stirring solution of the 1,3,5-benzenetricarboxylic acid (H_3BTC) ligand in a 6:4 (3.57 mmol to 2.38 mmol) molar ratio, while systematically changing the solvent system for each experiment. The solvents used were water, methanol, ethanol, and isopropanol, which vary in size, polarity, and Lewis basicity. Experiments were performed at constant room temperature and under atmospheric pressure. The stirring reaction mixture was continuously pumped through Neoprin tubes into a 1.5 mm flow-through capillary, where the sample was irradiated by X-ray light, and then pumped back in to the reaction vessel [3].

The reactions performed at the Austro-SAXS beamline at ELETTRA are summarized in Table 1. The experimental strategy was limited by several factors including the limited solubility of $\text{Cu}(\text{OAc})_2 \cdot \text{H}_2\text{O}$ and CuSO_4 in alcohols, the lack of reactivity of $\text{CuCl}_2 \cdot 2\text{H}_2\text{O}$ with H_3BTC in entirely alcohol solvent systems, the non-homogeneous mixing environment, and the insufficient time resolution for some reactions where the product formed nearly instantaneously. Despite these limitations, this work collected results allowing us to compare the role of the anion for different copper salts and the role of the solvent system in the mechanism of formation of HKUST-1.

Table 1. Summary of *in-situ* reactions with solvent variation for the synthesis of HKUST-1 by combining a copper salt solution and a H_3BTC solution. The solvents listed in the far left column correspond to the solvent of a H_3BTC solution. The row below each copper salt gives the solvent for the corresponding copper salt solution. A red space in the table indicates a completed reaction with the associated reagents. Black spaces indicate a reaction did not occur.

	$\text{Cu}(\text{NO}_3)_2 \cdot 2.5 \text{H}_2\text{O}$				$\text{CuCl}_2 \cdot 2\text{H}_2\text{O}$				$\text{Cu}(\text{OAc})_2 \cdot \text{H}_2\text{O}$	CuSO_4
	H_2O	MeOH	EtOH	$^i\text{PrOH}$	H_2O	MeOH	EtOH	$^i\text{PrOH}$	H_2O	H_2O
H_2O										
MeOH										
EtOH										
$^i\text{PrOH}$										

A typical SAXS pattern for the experiment with CuSO_4 in water and H_3BTC in water is shown in Figure 1(A) with the Bragg peak enlarged in Figure 1(B). Examining the development of the first-order Bragg peak in the SAXS regime provided an effective analysis for the nucleation kinetics in the synthesis of HKUST-1. Additionally, calculation of the correlation length in the low-q region of the SAXS spectra provided structural information of the amorphous particle behavior.

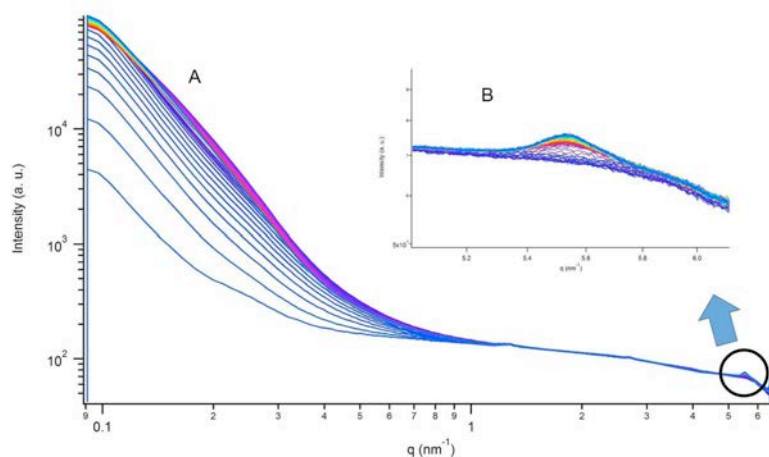


Figure 1. (A) Temporal evolution of the scattering pattern and (B) an enlarged view of the first-order Bragg peak at $q=5.52 \text{ nm}^{-1}$ for the reaction of CuSO_4 in water and H_3BTC in water. Note that the intensity is in arbitrary units

Data analysis from measurements in the WAXS regime provided insight into the structural effects of the solvent onto the larger crystalline framework. As one example, Figure 2 shows several characteristic WAXS patterns from a series of reactions between H_3BTC and $\text{Cu}(\text{NO}_3)_2 \cdot 2.5\text{H}_2\text{O}$ in homogenous solvent systems. The variation of the solvent system produced different lattice types while all other synthetic variables were held constant. Furthermore, simultaneous collection of SAXS and WAXS measurements afforded a direct correlation between the two MOF growth processes, nucleation and framework growth.

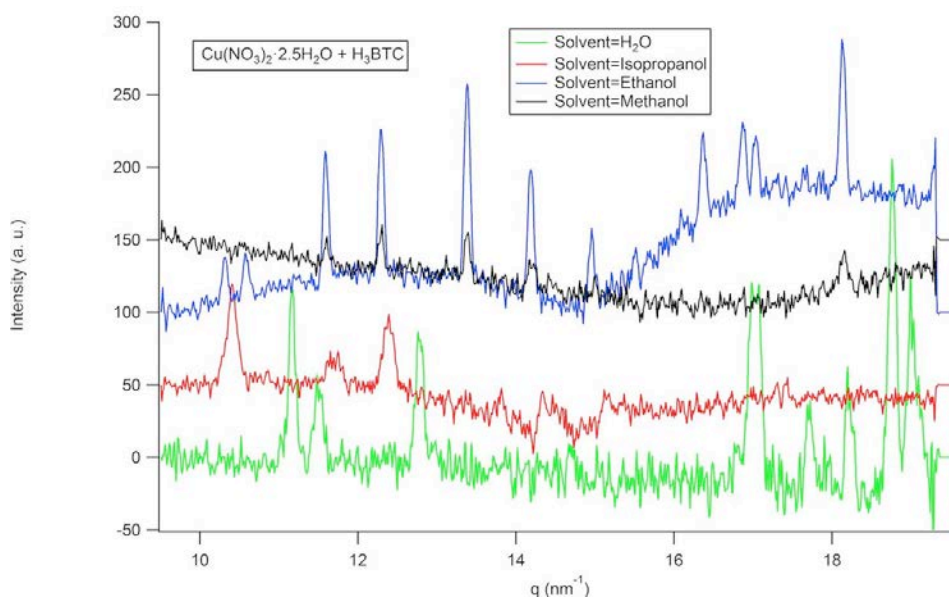


Figure 2. Typical WAXS pattern collected from the synthesis of HKUST-1 with solvent manipulation

References:

- [1] S. Loera-Serna, L. L. Núñez, J. Flores, R. López-Simeon, H. I. Beltrán; An alkaline one-pot metathesis reaction to give a $[\text{Cu}_3(\text{BTC})_2]$ MOF at r.t., with free Cu coordination sites and enhanced hydrogen uptake properties; *RSC Adv.* **3**, 10962-10972 (2013)
- [2] J. Huo, M. Brightwell, S. El Hankari, A. Garai, D. Bradshaw; A versatile, industrially relevant, aqueous room temperature synthesis of HKUST-1 with high space-time yield; *J. Mater. Chem. A* **1**, 15220-15223 (2013)
- [3] P. Ånggrin, M. Lindén, J. B. Rosenholm, R. Schwarzenbacher, M. Kriechbaum, H. Amenitsch, P. Laggner, J. Blanchard, F. Schüth; Kinetics of Cosurfactant-Surfactant-Silicate Phase Behavior. 1. Short-Chain Alcohols; *J. Phys. Chem. B* **103**, 5943-5948 (1999)

Publications

Publications in Journals and Reviewed Proceedings 2014

J. Akbarzadeh, S. Puchegger, A. Stojanovic, H.O.K. Kirchner, W. H. Binder, S. Bernstorff, P. Zioupos, H. Peterlik

*Timescales of self-healing in human bone tissue and polymeric ionic liquids
Bioinspired, Biomimetic and Nanobiomaterials Vol. 3, pp. 123-130 (2014)*

Naureen Akhtar, Alexey O. Polyakov, Aisha Aqeel, Pavlo Gordiichuk, Graeme R. Blake, Jacob Baas, Heinz Amenitsch, Andreas Herrmann, Petra Rudolf and Thomas T. M. Palstra

*Self-Assembly of Ferromagnetic Organic-Inorganic Perovskite-Like Films
Small 10 (23), pp. 4912-4919 (dec2014)*

Akhtar N, Blake GR, Felici R, Amenitsch H, Palstra TTM, Rudolf P

*Design of molecule-based magnetic conductors
Nano Research, Vol. 7 - 12, pp. 1832-1842 (2014)*

S. Bernstorff, V. Holý, J. Endres, V. Vales, J. Sobota, Z. Siketic, I. Bogdanovic-Radovic, M. Buljan and G. Drazic

*Co nanocrystals in amorphous multilayers - a structure study
J. Appl. Cryst. (2013). 46, 1711-1721*

J. Borges, M. Buljan, J. Sancho-Parramon, I. Bogdanovic-Radovic, Z. Siketic, T. Scherer, C. Kübel, S. Bernstorff, A. Cavaleiro, F. Vaz, A.G. Rolo

*Evolution of the surface plasmon resonance of Au:TiO₂ nanocomposite thin films with annealing temperature
Journal of Nanoparticle Research, Vol. 16 - 12, article 2790, 14 pages (2014)*

Carlo Carboni, David G. Carboni, Dražan Jozić, Sigrid Bernstorff, Michael

Rappolt & Samia Al-Mahrazi (2014)

Synchrotron X-ray investigation of the layer spacing in a series of low molar mass bi-mesogen organosiloxane smectic materials

Phase Transitions: A Multinational Journal, 04/2014 pp. 739-745 (7 pages)

Carboni, D., Marongiu, D., Rassu, P., Pinna, A., Amenitsch, H., Casula, M., Marcelli, A., Cibin, G., Falcaro, P., Malfatti, L., Innocenzi, P.

*Enhanced photocatalytic activity in low-temperature processed titania mesoporous films
Journal of Physical Chemistry C, 118 (22), pp. 12000-12009 (2014)*

B.T. Doan, S. Crauste-Manciet, C. Bourgaux, H. Dhotel, L. Juge', D. Brossard, D. Scherman, M. Bessodes, C.-A. Cuenod and N. Mignet

*Lipidic spherulites as magnetic resonance imaging contrast agents
New J. Chem. 38, 5190-5197 (2014)*

Drasler B, Drobne D, Novak S, Valant J, Boljte S, Otrin L, Rappolt M, Sartori B, Igljic A, Kralj-Igljic V, Sustar V, Makovec D, Gyergyek S, Hožicevar M, Godec M, Zupanc J

*Effects of magnetic cobalt ferrite nanoparticles on biological and artificial lipid membranes
International Journal of Nanomedicine, Vol. 9 - 1, pp. 1559-1581 (2014)*

S. Dunst, T. Rath, A. Radivo, E. Sovernigo, M. Tormen, H. Amenitsch, B. Marmiroli, Barbara Sartori, A. Reichmann, A.-C. Knall, G. Trimmel
Nanoimprinted Comb Structures in a Low Bandgap Polymer: Thermal Processing and Their Application in Hybrid Solar Cells
ACS Appl Mater Interfaces 6 (10), pp. 7633 - 7642 (May 28 2014)

Matko Erceg; Dražan Jozić; Irena Banovac; Sanja Perinović Jozić; S. Bernstorff
Preparation and characterization of melt intercalated poly(ethylene oxide)/lithium montmorillonite nanocomposites
Thermochimica Acta 579 (2014) 86–92

Esposito E, Ravani L, Mariani P, Huang N, Boldrini P, Drechsler M, Valacchi G, Cortesi R, Puglia C
Effect of nanostructured lipid vehicles on percutaneous absorption of curcumin
European Journal of Pharmaceutics and Biopharmaceutics, Vol. 86 - 2, pp. 121-132 (2014)

Heftberger P, Kollmitzer B, Heberle FA, Pan J, Rappolt M, Amenitsch H, Kucerka N, Katsaras J, Pabst G
Global small-angle X-ray scattering data analysis for multilamellar vesicles: the evolution of the scattering density profile model
Journal of Applied Crystallography, Vol. 47 - 1, pp. 173-180 (2014)

Heftberger, P.; Kollmitzer, B.; Rieder, A.; Amenitsch, H.; Rappolt, M.; Pabst, G.
Temperature Dependence of Lo/Ld Domain Thickness and Elasticity by Global Saxs Data Analysis
Biophysical Journal Volume 106, Issue 2, Supplement 1, p512a (28.1.2014) (Conf. abstract)

M Jerčinović, N Radić, M Buljan, J Grenzer, I Delač Marion, M Kralj, I Bogdanović Radović, R Hübner, P Dubček, K Salamon and S Bernstorff
Self-assembled growth of Ni nanoclusters in amorphous alumina matrix
J Nanopart Res 16, 2296 (2014)
Journal of Nanoparticle Research 16, 2296 (1-10), 2014

K. Kornmueller, I. Letofsky-Papst, F. Cacho-Nerin, G. Leitinger, H. Amenitsch, R. Prassl
Self-Assembly of an Amphiphilic Designer-Peptide into Double Helical Superstructures
Biophysical Journal 106(2). 58a (2014) (Published abstract)

Lepeltier E., Bourgaux C., Maksimenko A., Meneau F., Rosilio V., Sliwinski E., Zouhiri F., Desmaele D., Couvreur P.
Self-assembly of polyisoprenoyl gemcitabine conjugates : influence of supramolecular organization on their biological activity
Langmuir, 30, 22, 6348-6357 (2014)

Malfatti L, Falcaro P, Pinna A, Lasio B, Casula MF, Loche D, Falqui A, Marmiroli B, Amenitsch H, Sanna R, Mariani A, Innocenzi P
Exfoliated graphene into highly ordered mesoporous titania films: Highly performing nanocomposites from integrated processing
ACS Applied Materials and Interfaces, Vol. 6 - 2, pp. 795-802 (2014)

B. Marmiroli, F. Cacho-Nerin, B. Sartori, J. Pérez, H. Amenitsch
Thorough small-angle X-ray scattering analysis of the instability of liquid micro-jets in air
Journal of Synchrotron Radiation, Vol. 21 - 1, pp. 193-202 (2014)

M Mozetic , K Ostrikov , D N Ruzic , D Curreli , U Cvelbar , A Vesel , G Primc , M Leisch , K Jousten , O B Malyshev , J H Hendricks , L Koeber , A Tagliaferro , O Conde , A J Silvestre , J Giapintzakis , M Buljan , N Radic , G Drazic , S Bernstorff , H Biederman , O Kylian , J Hanus , S

Milosevic , A Galtayries , P Dietrich , W Unger , M Lehocky , V Sedlarik , K Stana-Kleinschek , A Drmota-Petric , J J Pireaux , J W Rogers , M Anderle
Recent advances in vacuum sciences and applications
Journal of Physics D: Applied Physics, Vol. 47 - 15, pp. 153001 (2014)

Pozzi D, Cardarelli F, Salomone F, Marchini C, Amenitsch H, Barbera GL, Caracciolo G
Role of cholesterol on the transfection barriers of cationic lipid/DNA complexes
Applied Physics Letters 105 (7), article 073701 (5 pages) (2014)

Pozzi D, Colapicchioni V, Caracciolo G, Piovesana S, Capriotti AL, Palchetti S, De Grossi S, Riccioli A, Amenitsch H, Laganà A
Effect of polyethyleneglycol (PEG) chain length on the bio-nano- interactions between PEGylated lipid nanoparticles and biological fluids: From nanostructure to uptake in cancer cells
Nanoscale, Vol. 6 - 5, pp. 2782-2792 (2014)

T. Rath, J. Novák, H. Amenitsch, A. Pein, E. Maier, W. Haas, F. Hofer, G. Trimmel
Real time X-ray scattering study of the formation of ZnS nanoparticles using synchrotron radiation
Materials Chemistry and Physics, Vol. 144 - 3, pp. 310-317 (2014)

Sekhar, K.C., Levichev, S., Buljan, M., Bernstorff, S., Kamakshi, K., Chahboun, A., Almeida, A., Agostinho Moreira, J., Pereira, M., Gomes, M.J.M.
Effect of bi-layer ratio in ZnO/Al₂O₃ multilayers on microstructure and functional properties of ZnO nanocrystals embedded in Al₂O₃ matrix
Applied Physics A: Materials Science and Processing, 115 (1), pp. 283-289 (April 2014)

P. Sharifi, B. Marmiroli, B. Sartori, F. Cacho-Nerin, J. Keckes, H. Amenitsch, O. Paris
Humidity-driven deformation of ordered mesoporous silica films
Bioinspired, Biomimetic and Nanobiomaterials 3, 183 - 190 (2014)

T. Sibillano, L. De Caro, D. Altamura, D. Siliqi, M. Ramella, F. Boccafoschi, G. Ciasca, G. Campi, L. Tirinato, E. Di Fabrizio & C. Giannini
An Optimized Table-Top Small-Angle X-ray Scattering Set-up for the Nanoscale Structural Analysis of Soft Matter
SCIENTIFIC REPORTS 4: 6985 (2014) (7 pages)

Sinturel C, Grosso D, Boudot M, Amenitsch H, Hillmyer MA, Pineau A, Vayer M
Structural transitions in asymmetric poly(styrene)-block -poly(lactide) thin films induced by solvent vapor exposure
ACS Applied Materials and Interfaces, Vol. 6 - 15, pp. 12146-12152 (2014)

F. Spinozzi, C. Ferrero, M.G. Ortore, A. De Maria Antolinos, P. Mariani
GENFIT: software for the analysis of small-angle X-ray and neutron scattering data of macromolecules in solution
Journal of Applied Crystallography 47 (3), 1132-1139, 2014

V. Valeš, M. Buljan, V. Janicki, S. Bernstorff, S. Mangold, Z. Siketić, O. Schneeweiss, V. Holy
Fe₂O₃/TiO₂ nanoparticles—a complex structural study
Thin Solid Films 564 (2014) 65–72

V. Vales, J. Vejpravova, B. Pacakova, V. Holy, S. Bernstorff and M. Kalbac
Self-ordering of iron oxide nanoparticles covered by graphene
Physica Status Solidi B, Vol. 251 - 12, pp. 2499-2504 (2014)

F. Valle, N. Zuliani, B. Marmiroli, H. Amenitsch und R. Taccani
SAXS analysis of catalyst degradation in high temperature PEM fuel cells subjected to accelerated ageing tests
Fuel Cells, Vol. 14 - 6, pp. 938-944 (2014)

S. Vilasi, R. Carrota, M. R. Mangione, C. Campanella, F. Librizzi, L. Randazzo, V. Martorana, A. Marino Gammazza, M. G. Ortore, A. Vilasi, G. Pocsfalvi, G. Burgio, D. Corona, A. Palumbo Piccionello, G. Zummo, D. Bulone, E. Conway de Macario, A. J. L. Macario, P. L. San Biagio, F. Cappello
Human Hsp60 with Its Mitochondrial Import Signal Occurs in Solution as Heptamers and Tetradecamers Remarkably Stable over a Wide Range of Concentrations.
PLoS One. 9(5):e97657, doi: 10.1371/journal.pone.0097657. eCollection 2014

A. Yaghmur, J. Østergaard, S. Weng Larsen, H. Jensen, C. Larsen, and M. Rappolt
Drug Formulations Based on Self-Assembled Liquid Crystalline Nanostructures
In: Liposomes, Lipid Bilayers and Model Membranes. From Basic Research to Application. G. Pabst, N. Kučerka, M.-P. Nieh, and J. Katsaras (eds.), CRC Press, pp. 341-360 (2014)
(Print ISBN: 978-1-4665-0709-8; eBook ISBN: 978-1-4665-0711-1)
Bookchapter 17, DOI: 10.1201/b16617-20

Publications January to Aug 2015

Addiego F, Patlazhan S, Wang K, André S, Bernstorff S, Ruch D
Time-resolved SAXS study of void fraction evolution in HDPE during stress unloading and strain recovery
Polymer International 64 (11), pages 1513–1521, (2015)

M. Buljan, N. Radić, J. Sancho-Paramon, V. Janicki, J. Grenzer, I. Bogdanović-Radović, Z. Siketić, M. Ivanda, A. Utrobičić, R. Hübner, R. Weidauer, V. Valeš, J. Endres, T. Car, M. Jerčinović, J. Roško, S. Bernstorff and V. Holy
Production of three-dimensional quantum dot lattice of Ge/Si core-shell quantum dots and Si/Ge layers in an alumina glass matrix
Nanotechnology 26, 065602, 9 pages (2015)

Carla Cannas, Andrea Ardu, Anna Musinu, Lorenza Suber, Gabriele Ciasca, Heinz Amenitsch, and Gaetano Campi
Hierarchical Formation Mechanism of CoFe₂O₄ Mesoporous Assemblies
ACS Nano 9 (7), Pages 7277-7286 (2015)

Caracciolo G, Pozzi D, Capriotti AL, Cavaliere C, Piovesana S, Amenitsch H, Laganà A
Lipid composition: a key factor for the rational manipulation of the liposome - protein corona by liposome design
RSC Advances, Vol. 5 - 12, pp. 5967-5975 (2015)

Carboni D, Pinna A, Amenitsch H, Casula MF, Loche D, Malfatti L, Innocenzi P
Getting order in mesostructured thin films, from pore organization to crystalline walls, the case of 3-glycidoxypropyltrimethoxysilane
Physical Chemistry Chemical Physics 17 (16), pp. 10679-10686 (2015)

Valentina Colapicchioni, Sara Palchetti, Daniela Pozzi, Elettra Sara Marini, Anna Riccioli, Elio Ziparo, Massimiliano Papi, Heinz Amenitsch and Giulio Caracciolo
Killing cancer cells using nanotechnology: novel poly(I:C) loaded liposome–silica hybrid nanoparticles

J. Mater. Chem. B, Vol. 3 - 37, pp. 7408-7416 (2015)

Jashmini Deka, Rostislav Mech, Luca Ianeselli, Heinz Amenitsch, Fernando Cacho-Nerin, Pietro Parisse, and Loredana Casalis
Surface Passivation Improves the Synthesis of Highly Stable and Specific DNA-Functionalized Gold Nanoparticles with Variable DNA Density
ACS Appl. Mater. Interfaces, Vol. 7 - 12, pp. 7033-7040 (2015)

Ida Delač Marion, Danijel Grgičin, Krešimir Salamon, Tomislav Vuletić
I. Delač Marion, D. Grgičin, K. Salamon, S. Bernstorff, T. Vuletić
Polyelectrolyte Composite: Hyaluronic Acid Mixture with DNA
Macromolecules 48 (8), 2686–2696 (2015)

Dordevic L, Marangoni T, Miletic T, Rubio-Magnieto J, Mohanraj J, Amenitsch H, Pasini D, Liaros N, Couris S, Armaroli N, Surin M, Bonifazi D
Solvent Molding of Organic Morphologies Made of Supramolecular Chiral Polymers
J. Am. Chem. Soc., Vol. 137 - 25, pp. 8150-8160 (2015)

Barbara Drasler, Damjana Drobne, Amin Sadeghpour, Michael Rappolt
Fullerene up-take alters bilayer structure and elasticity: A small angle X-ray study
Chemistry and Physics of Lipids, Vol. 188, pp. 46-53 (2015)

Heike M. A. Ehmman, Oliver Werzer, Stefan Pachmajer, Tamilselvan Mohan, Heinz Amenitsch, Roland Resel, Andreas Kornherr, Karin Stana-Kleinschek, Eero Kontturi, and Stefan Spirk
Surface-Sensitive Approach to Interpreting Supramolecular Rearrangements in Cellulose by Synchrotron Grazing Incidence Small-Angle X-ray Scattering
ACS Macro Letters 2015, 4, pp 713–716

T.A. Grünewald, A. Lassenberger, P.D.J. van Oostrum, H. Rennhofer, R. Zirbs, B. Capone, I. Vonderhaid, H. Amenitsch, H.C. Lichtenegger and E. Reimhult
Core-Shell Structure of Monodisperse Poly(ethylene glycol)-Grafted Iron Oxide Nanoparticles Studied by Small-angle X-ray scattering
Chem. Mater., Vol. 27 - 13, pp. 4763-4771 (2015)

Heftberger P, Kollmitzer B, Rieder A, Amenitsch H, Pabst G
In Situ Determination of Structure and Fluctuations of Coexisting Fluid Membrane Domains
Biophysical Journal, Vol. 108 - 4, pp. 854-862 (feb. 2015)

A Iglıc, CV Kulkarni, M Rappolt
Preface to
Advances in Planar Lipid Bilayers and Liposomes, Vol. 21, page ix (2015)

S. Joseph, M. Rappolt, M. Schoenitz, V. Huzhalska, W. Augustin, S. Scholl, and H. Bunjes
Stability of the Metastable α -Polymorph in Solid Triglyceride Drug- Carrier Nanoparticles
Langmuir 31(24) 6663-74 (2015)

Kaper, Helena; Djerdj, Igor; Gross, Silvia; Amenitsch, Heinz; Antonietti, Markus; Smarsly, Bernd M
Ionic liquid- and surfactant-controlled crystallization of WO₃ films
Physical chemistry chemical physics : PCCP (2015) 17 (27) 18138-45

M. Karlušić, R. Kozubek, H. Lebius, B. Ban d'Etat, R.A. Wilhelm, M. Buljan, Z. Siketić, F. Scholz, T. Meisch, M. Jakšić, S. Bernstorff, M. Schleberger, and B. Šantić
Response of GaN to energetic ion irradiation: conditions for ion track formation
J. Phys. D: Appl. Phys. 48 (2015) 325304 (12pp)

- B. Kollmitzer, P. Heftberger, R. Podgornik, J.F. Nagle, and G. Pabst
Bending rigidities and interdomain forces in membranes with coexisting lipid domains
Biophysical Journal 108, 2833-2842 (2015)
- Karin Kornmueller, Ilse Letofsky-Papst, Kerstin Gradauer, Christian Mikl, F. Cacho-Nerin, Mario Leybold, Walter Keller, Gerd Leitinger, H. Amenitsch and R. Prassl
Tracking morphologies at the nanoscale: Self-assembly of an amphiphilic designer peptide into a double helix superstructure
Nano Research 8 (6), pp. 1822-1833 (2015)
- A.J. MacLachlan, T. Rath, U.B. Cappel, S.A. Dowland, H. Amenitsch, A.C.Knall, C. Buchmaier, G. Trimmel, J. Nelson, S. A. Haque
Polymer/Nanocrystal Hybrid Solar Cells: Influence of Molecular Precursor Design on Film Nanomorphology, Charge Generation and Device Performance
Advanced Functional Materials, Vol. 25 - 3, pp. 409-420 (2015)
- Elise Lepeltier, Claudie Bourgaux, Heinz Amenitsch, Véronique Rosilio, Sinda Lepetre-Mouelhi, Fatima Zouhiri, Didier Desmaële, Patrick Couvreur
Influence of the nanoprecipitation conditions on the supramolecular structure of squalenoyled nanoparticles
Eur J Pharm Biopharm. 96, Pages 89-95 (30 July 2015)
- Martin Loncaric, Jordi Sancho-Parramon, Hrvoje Zorc, Suzana Segota, Pavo Dubcek, S. Bernstorff
M. Loncaric, J. Sancho-Parramon, H. Zorc, S. Segota, P. Dubcek and S. Bernstorff
Optical and structural characterization of gold island films on glass substrates
Thin Solid Films 591, part B, pp. 204–209 (2015)
- Helena Kaper, Igor Djerdj, Silvia Gross, Heinz Amenitsch, Markus Antonietti and Bernd Smarsly
Ionic Liquid- and Surfactant-Controlled Crystallization of WO₃ films
Phys. Chem. Chem. Phys. 17, pp. 18138-18145 (2015)
- Nicastro MC, Spigolon D, Librizzi F, Moran O, Ortore MG, Bulone D, Biagio PLS, Carrotta R
Amyloid beta-peptide insertion in liposomes containing GM1-cholesterol domains
Biophysical Chemistry, pp. in print,-available online (30 sept. 2015)
- G. Polt, F. Spieckermann, H. Wilhelm, Ch. Fischer, E. Schafner, S. Bernstorff, M. Zehetbauer
Crystalline plasticity in isotactic polypropylene below and above the glass transition temperature
eXPRESS Polymer Letters Vol.9, No.10 (2015) 894–900
- C. Prehal, D. Weingarh, E. Perre, R. T. Lechner, H. Amenitsch, O. Paris and V. Presser
Tracking the structural arrangement of ions in carbon supercapacitor nanopores using in situ small-angle X-ray scattering
Energy Environ. Sci.8, 1725-1735 (2015)
- D. Ribitsch, E. Herrero Acero, A. Przylucka, S. Zitzenbacher, A. Marold, C. Gamerith, R. Tscheließnig, A. Jungbauer, H. Rennhofer, H. Lichtenegger, H. Amenitsch, K. Bonazza, C.P. Kubicek, I.S. Druzhinina, G.M. Guebitz
Enhanced cutinase-catalyzed hydrolysis of polyethylene terephthalate by covalent fusion to hydrophobins
Appl Environ Microbiol. 81(11), 3586-3592 (2015)
- Ricci C, Ortore MG, Vilasi S, Carrotta R, Mangione MR, Bulone D, Librizzi F, Spinozzi F, Burgio G, Amenitsch H, San Biagio PL
Stability and disassembly properties of human naïve Hsp60 and bacterial GroEL chaperonins
Biophysical Chemistry, pp. in print,-available online (2015)

A. Sadeghpour, M. Rappolt, D. Ntountaniotis, P. Chatzigeorgiou, K. Viras, G. Megariotis, M. Papadopoulou, E. Siapi, G. Mali, T. Mavromoustakos
Comparative Study of Interactions of Aliskiren and ATI Receptor Antagonists with Lipid Bilayers
Biochimica et Biophysica Acta, Vol. 1848 - 4, pp. 984-994 (2015)

Christoph J. Schaffer, Johannes Schlipf, Efi Dwi Indari, Bo Su, Sigrid Bernstorff †, and Peter Müller-Buschbaum
Effect of blend composition and additives on the morphology of PCPDTBT:PC₇₁ BM thin films for organic photovoltaics
ACS Applied Materials & Interfaces 2015, 7, 21347-21355 (Sept.2015)

J. Schlipf, P. Docampo, C. J. Schaffer, V. Körstgens, L. Bießmann, F. Hanusch, N. Giesbrecht, S. Bernstorff, T. Bein, and P. Müller-Buschbaum
A Closer Look into Two-Step Perovskite Conversion with X-ray Scattering
J. Phys. Chem. Lett. 6 (7), 1265–1269 (2015)

K.C. Sekhar, K. Kamakshi, S. Bernstorff and M.J.M. Gomes
Effect of annealing temperature on photoluminescence and resistive switching characteristics of ZnO/Al₂O₃ multilayer nanostructures
Journal of Alloys and Compounds, Vol. 619 - 1, pp. 248-252 (2015)

Robert Slunjski
R. Slunjski, P. Dubček, N. Radić, S. Bernstorff, B. Pivac
Structure and transport properties of Ge quantum dots in a SiO₂ matrix
J. Phys. D: Appl. Phys. **48** article 235301 (6pp) (2015)

W. Wang, C.J. Schaffer, L. Song, V. Koerstgens, S. Proeller, E.D. Indari, T. Wang, A. Abdelsamie, S. Bernstorff, P. Müller-Buschbaum
In-Operando Morphology Investigation of Inverted Bulk Heterojunction Organic Solar Cells with GISAXS
J. Mater. Chem. A3 (16), pp. 8324-8331 (2015)

S. Vilasi, R. Carrota, M.R. Mangione, C. Campanella, F. Librizzi, L. Randazzo, V. Martorana, A. Marino Gammazza, M.G. Ortore, A. Vilasi, G. Pocsfalvi, G. Burgio, D. Corona, A. Palumbo Piccionello, G. Zummo, D. Bulone, E. Conway de Macario, A.J. Macario, P.L. San Biagio, F. Cappello
Human Hsp60 with Its Mitochondrial Import Signal Occurs in Solution as Heptamers and Tetradecamers Remarkably Stable over a Wide Range of Concentrations.
PLoS One. 9(5):e97657. doi: 10.1371/journal.pone.0097657. eCollection 2014

International Conferences and Workshops in 2014

H. Amenitsch
The Austrian SAXS beamline as tool in Energy
Energy ESRF/ELETTRA, Trieste, Italy, 22.-23.5.2014 (talk)

H. Amenitsch, I. Hanzu, M. Flock, F. Uhlig, M. Wilkening, J.M. Biedermann, J. Binder, A. Torvisco Gomez, M. Wolf, C. Zeppek
From Molecules Towards Energy Related Materials
"10 Years Nawi Graz", Graz, Austria, 10.7.2014 (poster)

H. Amenitsch
Why is SAXS so sexy?
NanoSimposio 2014, San Benedetto del Tronto, Italy, 19.-20.8.2014 (talk)

Amenitsch H,
The Austrian SAXS beamline and Life Science Research
International Life Science Advisory Panel (LSP), Elettra, Trieste, Italy, 14 October 2014 (talk)

I. D. M. Azmi, C. Nilsson, J. Østergaard, S. M. Moghimi, S. Stürup, B. Gammelgaard, A. Urtili, A. Yagmur
Cubosomes and Hexosomes as Soft Nano-Carriers for Loading the Platinum-Based Anticancer Drug Cisplatin
Liposomes Research Day. Copenhagen, Denmark. 4-7.8.2014

I. D. M. Azmi, C. Nilsson, J. Østergaard, S. M. Moghimi, S. Stürup, B. Gammelgaard, A. Urtili, A. Yagmur
Cubosomes and Hexosomes as Soft Nano-Carriers of Cisplatin
20th International Symposium on Surfactants in Solution, University of Coimbra Coimbra, Portugal, 22-27.6.2014

I. D. M. Azmi, C. Nilsson, J. Østergaard, S. M. Moghimi, S. Stürup, B. Gammelgaard, A. Urtili, A. Yagmur
Cubosomes and Hexosomes as Soft Nano-Carriers for Loading the Platinum-Based Anticancer Drug Cisplatin
11th International Conference on Nanosciences & Nanotechnologies (NN14), Thessaloniki, Greece, 8-11.7.2014

P. S. Bauer
In-situ investigations of biogenic nanoparticle formation utilizing small angle x-ray scattering
Aerosol Seminar, University of Vienna, 22.10.2014 (seminar talk)

P. S. Bauer
SAXS at aerosols or In-situ investigations of biogenic nanoparticle formation utilizing small angle x-ray scattering (SAXS)
DCS Seminar, University of Vienna, 21.11.2014 (seminar talk)

S. Bernstorff
Grazing Incidence Small Angle X-ray Scattering (GISAXS)
SAXS school on “Application of SAXS to the study of biological and nanoscale systems”, Melbourne, Australia, 19. May 2014 (Invited lecture)

S. Bernstorff
GISAXS analysis of quantum dot lattices
SAXS school on “Application of SAXS to the study of biological and nanoscale systems”, Melbourne, Australia, 19. May 2014 (Invited lecture)

S. Bernstorff
Synchrotron radiation scattering methods for structural determinations on the nanoscale
The 6th Biannual Italian-Australian Bilateral Workshop on “Photon and Neutron Applications to Biology and Nanoscale Systems”, Melbourne, Australia, 20.+21.5.2014 (invited talk)

S. Bernstorff
The Austrian SAXS beamline: Science Highlights, and beamline statistics
International Life Science Advisory Panel (LSP), Elettra, Trieste, Italy, 14 October 2014 (talk)

A. Bonasera

Perylene Derivatives in Water Splitting Process: One Step Further
Nanosolar Project meeting, Ferrara, Italy, 17-18.2.2014

M. Buljan, N. Radić, M. Ivanda, I. Bogdanović-Radović, M. Karlušić, J. Grenzer, S. Prucnal, G. Dražić, G. Pletikapić, V. Svetličić, M. Jercinović, S. Bernstorff, V. Holy

Ge quantum dot lattices in Al₂O₃ multilayers

15th Joint Vacuum Conference (JVC15) Vienna, Austria, June 15-20, 2014

M. Buljan, N. Radić, I. Bogdanović-Radović, Z. Siketić, K. Salamon, M. Jerčinović, M. Ivanda, G. Dražić and S. Bernstorff

Influence of annealing conditions on the structural and photoluminescence properties of Ge quantum dot lattices in continuous Ge + Al₂O₃ films

E-MRS 2014 Spring Meeting, Lille, France, May 26-30, 2014 (talk)

M. Buljan, N. Radić, M. Jerčinović, I. Bogdanović-Radović, M. Karlušić, T. Car, S. Bernstorff

Self-assembly of quantum dots in glasses: design of amorphous materials by magnetron sputtering deposition

ICTF-16: International Conference on Thin films, Dubrovnik, Croatia, 13-19.10. 2014 (invited, talk)

M. Buljan, M. Karlušić, I. Bogdanović-Radović, I. Mekterović, D. Mekterović, M. Schleberger, S. Bernstorff, N. Radić

A model for GISAXS characterization of ion-beam induced tracks in the surface region of thin films

IBMM 19th International Conference on Ion Beam Modification of Materials, Leuven, Belgium, 14-19.9.2014 (oral)

M. Buljan, N. Radić, T. Car, I. Bogdanović-Radović, M. Jerčinović, S. Bernstorff

Tuning the structural properties of Ge nanowire networks in glass Al₂O₃ matrix

21. International Scientific Meeting on Vacuum Science and Techniques, Samobor, Croatia, 8-9 May 2014 (poster)

M. Burian, H. Amenitsch, G. Fritz-Popovski, M. Yarema, W. Heiss, M. Kovalenko, O. Paris, R.T. Lechner

In-situ Synchrotron Studies of Colloidal Crystallization and the Influence of the Nanocrystal Shape

Nanoscience with Nanocrystals NaNaX 6, Bad Hofgastein, Austria, 18-23.5.2014 (oral presentation)

Jashmini Deka

Synthesis of highly stable ssDNA-Gold Nanoparticle conjugates for application in bio-sensing

New Advances and Horizons in Nanoscience and Nanotechnology, National Seminar held in IASST, Guwahati, Assam, India, 20th-21st December 2014 (invited talk)

Jashmini Deka

DNA and Gold nanoparticles based scaffold for sensing and catalyses

Research Seminar (GRS) and Gordon Research Conference (GRC) on 'Noble Metal Nanoparticles', held in Mount Holyoke College, South Hadley, M.A, USA, 14th to 20th June 2014 (poster)

I. Delač Marion, K. Salamon, D. Grgičin, S. Bernstorff, and T. Vuletić

SAXS study of binary mixtures of DNA and HA

XVI Linz Winter Workshop, Linz, Austria 31.01-03.02.2014

I. Delač Marion, D. Grgičin, K. Salamon, S. Bernstorff, and T. Vuletić

Polyelectrolyte composite: Hyaluronic acid mixture with DNA

9th Christmas Biophysics workshop of the Croatian Biophysical Society, WBW2014, Buzet, Croatia, 15.-16.12.2014 (talk)

P. Dubcek, B. Pivac, N. Radic, and S. Bernstorff
Aluminium nano particles for future photovoltaic applications
E-MRS 2014 Spring Meeting, Lille, France, May 26-30, 2014 (poster)

P. Dubcek, B. Pivac, N. Radic, S. Bernstorff
Aluminium nano particles grown for applications in photovoltaics
ICTF-16: International Conference on Thin films, Dubrovnik, Croatia, 13-19.10. 2014 (invited talk)

Ehmann, H.; Werzer, O.; Reishofer, D.; Hribernik, S.; Mohan, T.; Stana-Kleinschek, K.; Amenitsch, H.; Resel, R.; Spirk, S.
Following In Situ Regeneration and Pore Rearrangement of Trimethylsilylcellulose Thin Films via GISAXS
EUSIP 2014, Maribor, Slovenia, 21.09.2014 (poster)

Tilman Grünewald
Core-shell nanoparticles – Insights in their growth and dynamic behavior by small-angle x-ray scattering
6th ÖGMBT Annual Meeting, 15-18. 9. 2014 (oral presentation)

P. Heftberger, B. Kollmitzer, A. Rieder, G. Pabst
Influence of domain size on structure and elastic fluctuations in complex lipid mixtures
9th Christmas Biophysics Workshop, Buzet, Croatia, 15.12.2014

P. Heftberger, B. Kollmitzer, G. Pabst
Temperature Dependence Of Lo/Ld Domain Thickness And Elasticity By Global SAXS Data Analysis
Annual Meeting of the German Biophysical Society, Lübeck, Germany, 14.8.2014

P. Heftberger, B. Kollmitzer, G. Pabst
Temperature dependence of Lo/Ld domain thickness and elasticity by global saxs data analysis
International Workshop on Biomembranes, Helsinki, Finland, 19.8.2014

P. Heftberger, B. Kollmitzer, A. Rieder, H. Amenitsch, M. Rappolt, G. Pabst
Temperature dependence of Lo/Ld domain thickness and elasticity by global SAXS data analysis
58th Annual Meeting, San Francisco, CA., USA, 17.2.2014

M. Jerčinović, N. Radić, M. Buljan, J. Grenzer, I. Delač Marion, M. Kralj, I. Bogdanović Radović, R. Hübner, P. Dubček, K. Salamon and S. Bernstorff
Self-assembled growth of Ni nanoparticles in amorphous alumina matrix
E-MRS Spring Meeting 2014, Lille, France, May 26-30, 2014 (poster)

M. Karlušić, R. Kozubek, H. Lebius, R.A. Wilhelm, M. Buljan, Z. Siketić, F. Scholtz, T. Meizsch, M. Jakšić, S. Bernstorff, M. Schleberger, B. Šantić,
Energy threshold for swift heavy ion tracks in GaN
19th International Conference on “Ion Beam Modification of Materials” (IBMM 2014), Leuven, Belgium, September 14-19, 2014 (poster)

M. Karlušić, M. Buljan, I. Bogdanović - Radović, M. Jakšić, N. Radić, B. Šantić, M. Schleberger, S. Bernstorff
Comparison of AFM and GISAXS capabilities for surface swift heavy ion track analysis
19th International Conference on “Ion Beam Modification of Materials” (IBMM 2014), Leuven, Belgium, September 14-19, 2014 (poster)

O. Karzazi, A. Chahboun, S. Levichev, K.C. Sekhar, M. Buljan, S. Bernstorff, M.J.M. Gomes
GISAXS characterisation of Co doped ZnO nanostructures
6th Francophone Conference on Electron Spectroscopy, Fez-Morocco, 19-24th May 2014

- B. Kollmitzer, P. Heftberger, H. Amenitsch, R. Podgornik, J.F. Nagle, G. Pabst
Membrane domain interactions by Monte Carlo type analysis of osmotic stress data
 9th Christmas Biophysics workshop of the Croatian Biophysical Society, WBW2014, Buzet, Croatia, 15.12.2014 (talk)
- B. Kollmitzer, P. Heftberger, M. Rappolt, G. Khelashvili, D. Harries, G. Pabst
Protein Partitioning in Liquid-Ordered (Lo) / Liquid-Disordered (Ld) Domains Depends on Lipid Composition and Protein Shape
 Annual Meeting of the German Biophysical Society. Lübeck, Germany, 15.9.2014
- B. Kollmitzer, P. Heftberger, M. Rappolt, G. Pabst
Monolayer spontaneous curvature of raft-forming membrane lipids
 Biophysical Society 58th Annual Meeting, San Francisco, CA, 17.2.2014
- B. Kollmitzer, P. Heftberger, M. Rappolt, G. Khelashvili, D. Harries, G. Pabst
Protein partitioning in liquid-ordered (Lo) / liquid-disordered (Ld) domains depends on lipid composition and protein shape
 4th International Meeting on Antimicrobial Peptides, Graz, Austria. 30.9.2014
- K. Kornmueller, I. Letofsky-Papst, F. Cacho-Nerin, G. Leitinger, H. Amenitsch, and R. Prassl
Self-Assembly of an Amphiphilic Designer-Peptide into Double Helical Superstructures Biophysical Society 58th Annual Meeting, San Francisco, USA, 15. – 19. 2. 2014 (poster, received a Student Research Achievement Award)
- K. Kornmueller, I. Letofsky-Papst, G. Leitinger, H. Amenitsch, and R. Prassl
Peptide-based architectures: morphology of a self-assembled double helical superstructure
 BioNanoMed 2014, 5th International Congress, Nanotechnology, Medicine & Biology”, Krems, Austria, 26. – 28. 3. 2014 (poster)
- K. Kornmueller
Designer-peptides as next-generation biomaterials: morphology of a novel double helix superstructure
 Seminar Presentation, Graz, Austria, 23. 1. 2014 (talk)
- K. Kornmueller
Morphology of a novel double helix superstructure revealed by Synchrotron SAXS
 Lecture “Structure and Matter II”, Graz, Austria, 31. 3. 2014 (talk)
- K. Kornmueller
Peptide-based architectures: self-assembly of amphiphilic designer peptides
 Zentrum für Physiologische Medizin Meeting, Graz, Austria, 13. 5. 2014 (seminar talk)
- Andrea Lassenberger
A closer look at hydrophilic core-shell iron oxide nanoparticles for medical applications
 18th International Microscopy Conference, Prague, Czech Republic, 7-12.9.2014 (Poster presentation)
- R.T. Lechner, M. Burian, C. Prehal, M. Yarema, H. Amenitsch, W. Heiss, and Oskar Paris
In-situ Synchrotron Studies of Colloidal Crystallisation and the Influence of the Nanocrystal Shape
 DPG-Fruehjahrstagung der Sektion
 Kondensierte Materie (SKM)2014, Dresden, Germany, 30.3.-4.4. 2014 (oral presentation)
- M. Lucić Lavcević, P. Dubcek, S. Bernstorff, M. Marušić and L. Matković
Simultaneous GISAXS/GIWAXS measurements of ZnO nanowires grown on ZnO seeding substrates
 15th Joint Vacuum Conference (JVC15) Vienna, Austria, June 15-20, 2014

Luca Malfatti, Paolo Falcaro, Alessandra Pinna, Barbara Lasio, Maria F. Casula, Danilo Loche, Andrea Falqui, Benedetta Marmiroli, Heinz Amenitsch, Roberta Sanna, Alberto Mariani, Plinio Innocenzi
Exfoliated graphene doped mesoporous titania films: functional nanocomposites from integrated processing

E-MRS 2014 Spring Meeting, Lille, France, May 26-30, 2014 (talk)

L. Malfatti

Top-down and bottom-up approach towards the synthesis of nanocomposite mesoporous films
SiO₂ Advanced Dielectrics and Related Devices congress, Cagliari, Italy, 16-18 June 2014

L. Malfatti

Getting order into matter: a top-down and bottom-up approach towards the processing of hierarchical porous thin films

Junior Euromat (FEMS award invited talk), Lausanne, Switzerland, 21-25 July 2014

L. Malfatti

Highly Performing Nanocomposite Porous Films from Integrated Processing

ICNM 2014, Flic en Flac, Mauritius, 31 August- 5 September 2014

L. Malfatti

Exfoliated graphene into sol-gel based thin films: highly performing nanocomposites from integrated processing

China-Italy Bilateral Workshop on Graphene 2014, Dalian, China, 20-21 September

M. Manno

Electrostatic repulsion mimics molecular crowding and selects the fibrillation pathways in fibril-forming protein solutions

2nd Workshop on "The Physics of Protein Folding and Aggregation" (organized by G. Tiana and A. Trovato), Bressanone (BZ), Italy, February 06-08 2014 (invited lecture)

B. Marmiroli, B. Sartori and H. Amenitsch

Tuning mesoporous silica films properties by Deep X-ray Lithography for fluidics applications

64. Annual Meeting of the Austrian Physical Society, Pöllau, Austria, 24.-27. 9.2014 (poster)

Marmiroli, B.; Han, S. H.; Sartori, B.; Falcaro, P.; Amenitsch, H.

Tuning materials meso/microporosity by deep X-ray lithography for fluidics applications

MNE (Micro Nano Engineering) 2014, Lausanne, Switzerland, 22.09.2014 (poster)

M. Očko¹, M. Buljan², N. Radić², K. Salamon¹, T. Car², S. Bernstorff³

Transport properties of multilayers composed of germanium nanowires grown in alumina deposited on glass covered with ITO nanolayer

ICTF-16: International Conference on Thin films, Dubrovnik, Croatia, 13-19.10. 2014

B. Pivac, P. Dubcek, V. Janicki, R. Slunjski, J. Dasovic, S. Bernstorff

Si QDs formation in dielectric matrix: A defect study

E-MRS 2014 Spring Meeting, Lille, France, May 26-30, 2014 (poster)

Gerald Polt, Florian Spieckermann, Harald Wilhelm, Michael Kerber, Erhard Schafner, Sigrid Bernstorff, Michael Zehetbauer

Thermal Stability of Deformation Induced Dislocations in PP

6th International Conference on Polymer Behaviour (ICPB6), Vienna, Austria, Sept 22-26 2014

C. Prehal

In-situ SAXS/WAXS as a novel method to study ion transport in microporous systems

Symposium on "Ion Dynamics in Confined systems", University of Cambridge, 09.07.2014 (talk)

Christian Prehal, Daniel Weingarth, Emilie Perre, Rainer T. Lechner, Heinz Amenitsch, Oskar Paris and Volker Presser

In-situ SAXS/WAXS as a novel method to study ion transport phenomena in confined geometry

64. Annual Meeting of the Austrian Physical Society, Pöllau b. Hartberg, Steiermark, Austria, 24.–27.9.2014 (talk)

S. Raccosta, V. Martorana, M. Manno

Electrostatic repulsion promotes molecular crowding and selects the fibrillation pathways in fibril-forming protein solutions

Int. Meeting “Biophysics of Amyloids and Prions”, Naples, Italy, May 25-26, 2014 (oral contribution)

Nikola Radić, Maja Buljan, Pavo Dubcek, Marko Jercinović, Iva Bogdanović-Radović, Marko Marciuš, Jordi Sancho Parramon, Krešimir Salamon, Sigrid Bernstorff

Structure, optical, and electrical properties of Al- and Ag-doped ZnO thin films prepared by magnetron sputtering

15th Joint Vacuum Conference (JVC15) Vienna, Austria, June 15-20, 2014

N. Radic, K. Salamon, M. Ocko, I. Bogdanovic-Radovic, S. Bernstorff

Structural, morphological and electrical properties of TaxN thin films

E-MRS 2014 Spring Meeting, Lille, France, May 26-30, 2014 (poster)

T. Rath, A. MacLachlan, H. Amenitsch, S. Dowland, A.-C. Knall, G. Trimmel, S. A. Haque

Polymer/nanocrystal hybrid solar cells: Influence of precursor structure on film nanomorphology, charge generation and device performance

Spring meeting of the European Materials Research Society, Lille, France, 26–30.5.2014 (talk)

T. Rath, A. MacLachlan, H. Amenitsch, S. Dowland, A.-C. Knall, G. Trimmel, S.A. Haque

Influencing nanomorphology formation and charge generation in ligand-free prepared hybrid absorber layers by variation of the alkyl moiety in the precursors

EMRS 2014 Spring Meeting, Lille, France, 29.05.2014 (talk)

C. Ricci, M.G. Ortore, S. Vilasi, R. Carrotta, M.R. Mangione, D. Bulone, H. Amenitsch, F. Spinozzi, P.L. San Biagio

Stability and disassembly of the bacterial chaperonin protein GroEL and of its human homolog Hsp60

XXII Congresso Nazionale della Società Italiana di Biofisica Pura e Applicata. Palermo, Italy, 21-24.9.2014 (poster)

A.G. Rolo, C. Kubel, M. Buljan, S. Bernstorff, N. P. Barradas, N. Franco, and E. Alves

Rapid thermal annealing effect on the optical properties of Au-doped ZnO thin films grown by rf-sputtering

E-MRS 2014 Spring Meeting, Lille, France, May 26-30, 2014 (poster)

D. Romancino, V. Buffa, A. Lavanco, S. Raccosta, V. Martorana, M. Manno, A. Bongiovanni

Characterization of skeletal muscle-derived extracellular vesicles: Protein lipidation for cargo selection and/or exosome biogenesis

SIBPA XXII Nat'l Congress, Palermo (Italy), 21-24.9.2014 (Oral contribution)

K. Salamon, O. Milat, N. Radić, M. Očko, I. Bogdanović-Radović, S. Bernstorff

The effects of deposition conditions and annealing temperature on the structure and morphology of Ta-N thin films

16th International Conference on Thin Films, Dubrovnik, Croatia, 13-16 October, 2014

K. Salamon, O. Milat, N. Radić, M. Očko, S. Bernstorff

X-ray study of defects and nanomorphology in Tantalum Nitride thin films

21st International Scientific Meeting on Vacuum Science and Technique, Samobor, Croatia, 8-9.5.2014

- L. Sapir, C. Stanley, and D. Harries
DNA in Choline-Chloride/Urea Deep Eutectic Solvent
 American Conference on Neutron Scattering, Knoxville, Tennessee (USA), 1-5, June, 2014
- B. Sartori, B. Marmiroli, F. Cacho-Nerin and H. Amenitsch
Effect of humidity and salts on the mesostructure of silica nanoparticles synthesized in the gas phase
 64. Annual Meeting of the Austrian Physical Society, Pöllau, Austria, 24.–27. 9.2014 (poster)
- C. J. Schaffer, J. Schlipf, B. Su, Y. Rui, S. Bernstorff and P. Müller-Buschbaum
On the Morphology of PCPDTBT:PC71BM Thin Films for Organic Photovoltaics
 EuroTech Meeting, 27-28.10.2014, Brussels, Belgium
- J. Schlipf
Hybrid Perovskites for Application in Solar Cells – A Morphological Investigation
 Seminar of Chair for Functional Materials, Physics-Department, TUM, München; 16.12.2014
- KC.Sekhar, S.Levichev, S. Bernstorff, M. Buljan A. Almeida, J. A. Moreira, M.J.M. Gomes
Zinc oxide (ZnO) based nanostructures for memory applications
 NanoTP: Final Scientific meeting held at Nantes, France, 2-5th April 2014
- Parvin Sharifi, Benedetta Marmiroli, Barbara Sartori, Fernando Cacho-Nerin, Heinz Amenitsch, Christian Ganser, Christian Teichert, Oskar Paris
Humidity Driven Pore Lattice Deformation of Ordered Mesoporous Thin Films
 2014 Spring Meeting of the German Physical Society, Dresden, 30.3 - 4.4.2014 (poster)
- R. Slunjski, P. Dubček, N. Radić, S. Bernstorff, B. Pivac
Structure and transport properties of Ge quantum structures in SiO₂ matrix
 ICTF-16: International Conference on Thin films, Dubrovnik, Croatia, 13-19.10. 2014 (poster)
- F. Spieckermann, G. Polt, H. Wilhelm, E. Schafler, S. Bernstorff and M. Zehetbauer
The Thermal Stability of Dislocations in α -Phase Polypropylene
 Workshop on Recent Advances in Polymer Crystallization, Tsinghua University Beijing, China, 9-10 January 2014 (poster)
- Z. Syrgiannis
Supramolecular nanostructures of ruthenium photosensitizer and polyoxometalate dyads: The role of the water
 Nanosolar Project meeting, Ferrara, Italy, 17-18.2.2014
- A. Turkovic, K. Juraic, P. Dubcek, S. Bernstorff
In-situ SAXS/DSC/WAXD Study of the Temperature Evolution in Nanocomposite Polymer Electrolytes with Different Nanofillers
 E-MRS 2014 Spring Meeting, Lille, France, May 26-30, 2014 (poster)
- Francesco Valle, Benedetta Marmiroli, Heinz Amenitsch, Rodolfo Taccani
PEM fuel cells degradation study through catalyst layer SAXS nano-morphology mapping
 Fuel Cells 2014 Science & Technology, Amsterdam 3 – 4.4.2014 (poster)
- Vilasi S. Carrotta R., Rappa G.C., Ortore M.G., Canale C., San Biagio P.L., Bulone D.
Chaperon-like activity of intrinsically disordered caseins in A β fibrillogenesis
 Biophysics of amyloid and prions, Naples, Italy, 25-26 May 2014

S. Vilasi, M.G. Ortore, M.R. Mangione, R. Passantino, C. Marino, D. Spigolon, F. Cappello, D. Bulone and P.L. San Biagio

Effect of chaperones with intrinsically disordered regions (IDRs) on the fibrillogenesis of A β amyloid peptide.

Gordon Conference Understanding Intrinsically Disordered Regions (IDRs) at Different Scales: From Single Molecules to Complex Systems Stonehill College Easton, MA, USA, July 6-11, 2014

C. Webb Jr., M. Kriechbaum, H. Amenitsch, A. Torvisco and K. Ruhlandt-Senge
In-situ Formation of the Cu-Based MOF HKUST-1 Studied by Time-Resolved SAXS
23rd Congress of the IUCr, Montreal, Canada, 5.-12.8.2013 (poster)

A. Yaghmur, M. Rappolt, S. W. Larsen
In situ formation of drug delivery systems based on lyotropic liquid crystalline phases ESCDD 2014, Egmond aan Zee, The Netherlands, April 16-18 (poster)

A. Yaghmur
Lipidic Soft self-assembled drug nanocarriers: cubosomes, hexosomes, and in situ formation of cubic and hexagonal liquid crystalline phases
"Trends in Drug Research": The 32nd Cyprus Noordwijkerhout Camaerino Symposium, Cyprus, 18-22 May 2014 (Invited talk)

ELETTRA Highlights 2013-2014

S. Dunst, T. Rath, A. Radivo, E. Sovernigo, M. Tormen, H. Amenitsch, B. Marmiroli, B. Sartori, A. Reichmann, A.-C. Knall and G. Trimmel
Investigation of the thermal stability of nanoimprinted comb structures in a conjugated polymer and their application in hybrid solar cells
Elettra Research Highlight, pp. 18-19 (2013-2014)

M. Rittman, H. Amenitsch, M. Rappolt, B. Sartori, B. M. D. O'Driscoll and A. M. Squires
Nanomaterial coatings: controlling and analyzing thin films of lipid cubic phase
Elettra Research Highlight, pp. 34-35 (2013-2014)

Contributions to "communicate science in public"

Friday 4.4.2014 took place the "Sechste lange Nacht der Forschung" (sixth long night of research) - an open day at Austrian research facilities. 1.789 Stations at 234 different places attracted 136.500 visitors from all over Austria. Also the Austrian SAXS-beamline at Elettra participated with presentations from the members of the SAXS beamline, by connection via Skype to the Technical University in Graz / Austria.

Benedetta Marmiroli and Christian Morello participated at the third "Trieste Next", Piazza Untita' di Trieste, Italy, 27 September 2014, which a contribution to "Science explained for kids". Trieste Next is a scientific fair, organized by the city of Trieste in collaboration with the university and many of the scientific research institutes of Trieste, among them also Elettra-Sincrotrone. The theme of this year was "energy", which was explained to the public, based on over 100 program points: discussions, conferences, lectures, presentations, "hands-on" laboratories and entertainment.

SAXS training courses

The 4th tutorial on “Advanced Synchrotron Radiation Applications” organized by the Graz University of Technology and the Montan University of Leoben on the days from 26th to 28th May 2014. A group of 22 Austrian students, divided in subgroups of 4 -6 students, participated “hands-on” in some demonstrative experiments performed on the SAXS, DXRL, XRD, MCX, SISSI and XAFS beamlines. On Tuesday 27th morning, after a short presentation of the Synchrotron, the students visited also ELETTRA and FERMI, and afterwards SYRMEP and TWINMIC beamlines. On Tuesday afternoon, and in the morning of Wednesday 28th, the students attended a series of lectures on the data treatment.

PhD Theses 2014

Aurelio Bonasera

Design and Synthesis of Perylene-Based Supramolecular Hybrids for Novel Technological Applications
University of Trieste, Italy, 2014

Stefania Corvaglia

Nanoscale platform to study unstructured proteins interactions
University of Trieste, Italy, 27.3.2014

M. Jerčinović

Self-organization and characterization of nickel nanoparticles in dielectric matrix
University of Zagreb, Croatia, 21.5.2014

Thesis di Laurea / Diplomarbeit / Master 2014

Efi Dwi Indari

Morphology Changes of Organic Solar Cells Introduced via Aging
Master Thesis, Physik-Department, Lehrstuhl für Funktionelle Materialien,
Technical University München, Germany, 29.8.2014

Christian Prehal

In-situ SAXS study on the ion dynamics in microporous carbon based supercapacitors
Diploma Thesis at Institute of Physics, Montanuniversität Leoben, Austria (2014)

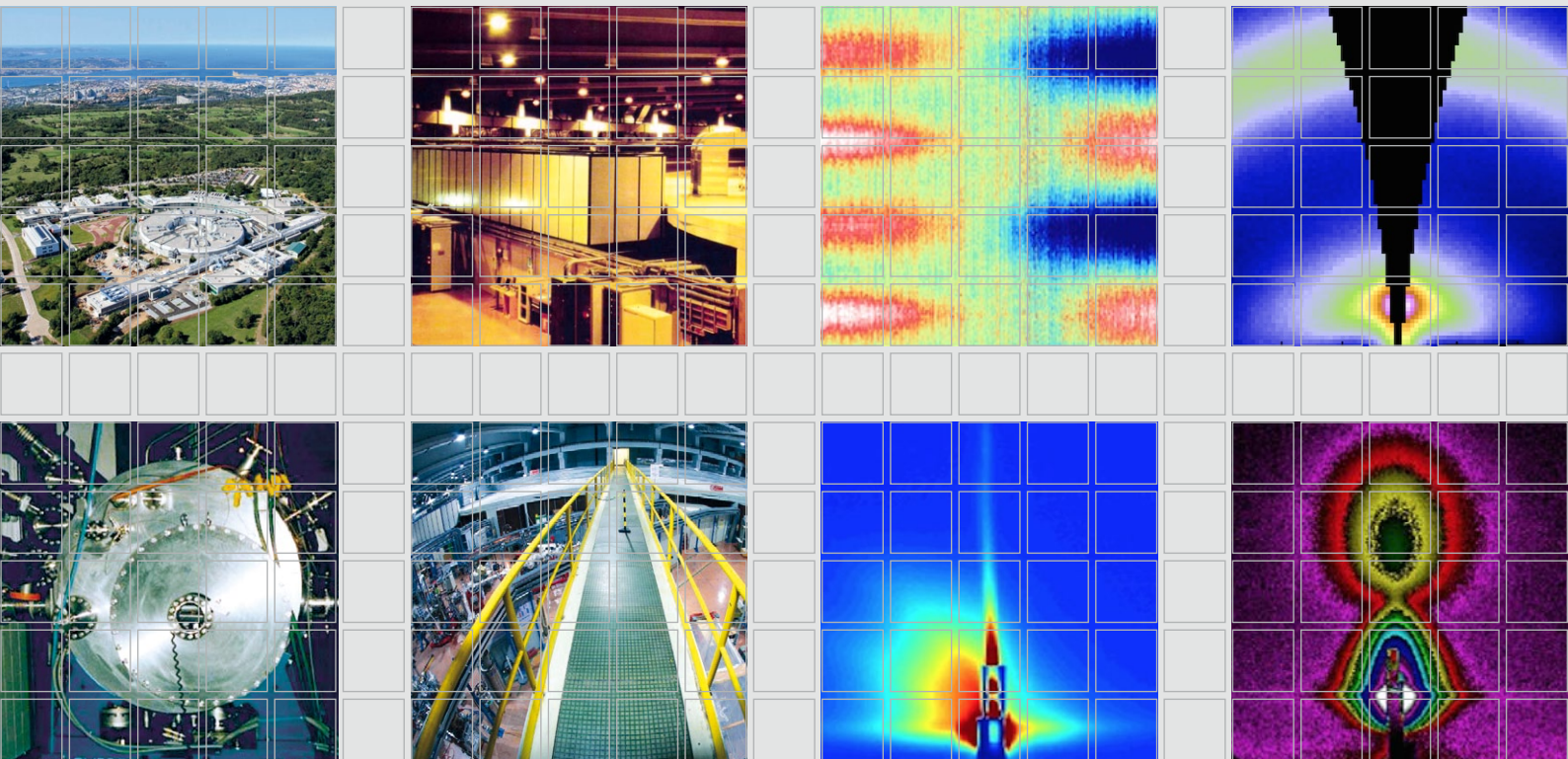
Authors Index

Abina A.	88
Akbarzadeh J.	121
Amenitsch H.	47, 51, 54, 56, 58, 62, 64, 66, 72, 80, 83, 92, 101, 105, 117, 119, 124, 127, 129
Azmi I. D. M.	47
Ban d'Etat B.	94
Bauer P. S.	83
Bein T.	109
Bellini T.	70
Bernstorff S.	60, 85, 90, 94, 99, 103, 107, 109, 111, 113, 121
Bießmann L.	109
Binder J.	117, 119
Binder W.	121
Bogdanović Radović I.	85, 103
Bomboi F.	70
Bongiovanni A.	74
Búcsi A.	49
Buffa V.	74
Buljan M.	85, 94
Bulone D.	68, 78
Burian M.	97
Cacho-Nerin F.	56, 105
Capone B.	62
Car T.	85
Caracciolo G.	51, 54
Carboni D.	124
Carducci F.	70
Carrotta R.	68
Casalis L.	56
Casula M.F.	124
Cerbino R.	70
Colapicchioni V.	54
Cordoyiannis G.	88
De March M.	58
Deka J.	56
Delač Marion I.	85
Devínsky F.	49
Docampo P.	109
Döhler D.	121
Dubček P.	90, 113
Dunst S.	92
Ehmann H.	92
Findenegg G.H.	72
Funari S.	60

Gammelgaard B.	47
Girod M.	72
Gollas B.	127
Graceffa R.	80
Gracin D.	99
Grenci G.	72
Grünewald T.A.	62
Gupta A.	111
Gupta M.	111
Hanusch F.	109
Heiss W.	97
Hémonnot C.	80
Hubčík L.	49
Ianeselli L.	56
Innocenzi P.	124
Jakšić M.	94
Jerčinović M.	85
Juraić K.	99
Kaltenhauser V.	92
Karlušić M.	94
Kornmueller K.	64, 66
Körstgens V.	109
Köster S.	80
Kralj M.	85
Kralj S.	88
Kregar Z.	99
Kriechbaum M.	66, 129
Krstulović N.	90, 99
Lassenberger A.	62
Lebius H.	94
Lechner R. T.	97, 101
Lehofer B.	64, 66
Leimgruber S.	92
Librizzi F.	68
Lichtenegger H.C.	62
Loche D.	124
Malfatti L.	124
Mangione M.R.	78
Manno M.	74
Mariani P.	70, 76
Marmiroli B.	72, 76, 80, 92, 105, 117, 119
Martinez N.	66
Martorana V.	74
Měch R.	56
Meisch T.	94
Meissner J.	72
Meljanac D.	99
Michael P.	121

Moghimi S. M.	47
Moscatelli S.	76
Müller-Buschbaum P.	107, 109
Nekić N.	85
Neumann S.	121
Noto R.	74
Onesti S.	58
Ortore M.G.	70, 78
Østergaard J.	47
Palchetti S.	54
Palumbo Piccionello A.	78
Paris O.	97, 101
Parisse P.	56
Peters J.	66
Pinna A.	124
Pivac B.	90, 113
Pozzi D.	51, 54
Prassl R.	64, 66
Prehal C.	101
Presser V.	101
Puc U,	88
Raccosta S.	74
Radić N.	85, 90, 103, 113
Radivo A.	92
Reddy V.R.	111
Reimhult E.	62
Reishofer D.	92
Rennhofer H.	62
Ricci C.	78
Romancino D.	74
Ruhlandt-Senge K.	129
Rui Y.	107
Salamon K.	85, 99, 103
Saldanha O.	80
San Biagio P.L.	68, 78
Šantić B.	94
Sartori B.	72, 80, 92, 105
Schaffer C. J.	107, 109
Schleberger M.	94
Schlipf J.	107, 109
Scholz F.	94
Sciortino F.	70
Sharma G.	111

Sharma K.	111
Siketic Z.	94, 99
Skenderović H.	99
Slunjski R.	113
Sovernigo E.	92
Spinozzi F.	70
Stürup S.	47
Su B.	107
Sytnik M.	97
Tormen M.	92
Torvisco A.	117, 119, 129
Trimmel G.	92
Uhlig F.	117, 119
Uhríková D.	49
Urtti A.	47
Valerio J.	60
van Oostrum P.D.J.	62
Vieira L.	127
Vilasi S.	68, 78
Vonderhaid I.	62
Webb Jr. C.C.	129
Weingarh D.	101
Winkler P. M.	83
Yaghmur A.	47
Zeppek C.	117, 119
Zidanšek A.	88
Zirbs R.	62



Institute of Inorganic Chemistry
 Graz University of Technology
 Faculty of Technical Chemistry,
 Chemical and Process Engineering,
 Biotechnology – TCVB
 Stremayrgasse 9/IV, 8010 Graz, Austria
 Tel.: +43 316 873 32145
 Fax: +43 316 873 32102
 E-mail: amenitsch@tugraz.at
 Web: <http://ac.tugraz.at>

Austrian SAXS Beamline
 Outstation of the Institute of
 Inorganic Chemistry
 Graz University of Technology
 c/o Elettra-Sincrotrone Trieste
 Strada Statale 14, km 163.5
 34149 Basovizza (TS) Italy
 E-mail: amenitsch@tugraz.at



Elettra-Sincrotrone Trieste
 Strada Statale 14, Km 163,5
 34149 Basovizza (TS), Italy
 Tel.: +39 040 375 8572
 Fax: +39 040 9380 902
 E-mail: bernstorff@elettra.eu
 Web: www.elettra.eu